The Pennsylvania State University

The Graduate School

The College of Earth and Mineral Sciences

THE EFFECT OF DISSIMILATORY IRON REDUCTION, NITRATE REDUCTION AND MICROBIAL GROWTH ON ELECTRICAL CONDUCTIVITY

A Dissertation in

Geosciences

by

Aaron B. Regberg

Submitted in Partial Fulfillment

of the Requirements
for the Degree of

Doctor of Philosophy

May 2011

The dissertation of Aaron Benjamin Regberg was reviewed and approved* by the following:

Susan L. Brantley
Professor of Geosciences
Dissertation Co-Advisor
Co-Chair of Committee

Kamini Singha
Assistant Professor of Geosciences
Dissertation Co-Advisor
Co-Chair of Committee

James D. Kubicki
Professor of Geosciences

Ming Tien
Professor of Biochemistry

Chris J. Marone
Professor of Geosciences
Associate Department Head of Graduate Programs of Geosciences

*Signatures are on file in the Graduate School

ABSTRACT

In this dissertation changes in measured electrical conductivity are related to measured changes in aqueous concentrations of ions. In previous work anomalous increases in electrical conductivity measured in and around contaminated aquifers have been associated with biogeochemical activity. The respiration and growth of micro-organisms has been suggested as a possible cause of these conductivity signals. However, a quantitative link between the activity of micro-organisms and electrical conductivity has not been established. Normally, the bulk electrical conductivity (σ_b) of a water-saturated sediment responds to changes in concentrations of ions in solution. If micro-organisms in the subsurface are catalyzing mineral dissolution or precipitation, σ_b may be affected by changing concentration of ions in the pore fluids.

In this dissertation changes in the fluid electrical conductivity (σ_f) and σ_b are related to changes in chemical concentrations at multiple scales. Changes in σ_f can be interpreted as reaction rates if the stoichiometry of the reaction is understood. Results from batch experiments demonstrate that measured changes in σ_f over time document rates of abiotic and biotic reduction of goethite. Rates of change in conductivity are related quantitatively to rates of reduction.

In two column reactors packed with sediments from Oyster Virginia and fed with a flowing input containing dissolved acetate, measured changes in σ_b initially document biogeochemical reaction rates of iron reduction or nitrate reduction in the sediment. Eventually, σ_b becomes decoupled from changes in chemical concentrations and increases significantly. Fe(II) adsorption does not cause σ_b to become decoupled from aqueous chemistry. Instead, this decoupling is attributed to the growth and presence of an electrically conductive biofilm. Reactive transport modeling is used to constrain the amount of biomass produced in each reactor. A value for electrical conductivity is estimated that depends on the calculated growth in biomass and the assumed density of that biomass. For iron-reducing conditions biofilms, the model is consistent with values of biofilm conductivity > 2.2 S/m, and for nitrate reducing conditions, with conductivity > 300 S/m. The value for biofilm conductivity for iron-reducing conditions seems reasonable, but the value for nitrate-reducing conditions, ~ 60 times more conductive than sea water, may be unreasonably large. Nonetheless, these values are the first estimates for biofilm electrical conductivity based on column reactor experiments.

The results of a field-scale tracer test involving nitrate reduction are also presented. The results suggest that electrical conductivity may be able to track biogeochemical activity if the tracers are large enough and conductive enough to be detectable. Finally, results of preliminary electrochemical experiments designed to directly measure the conductivity of biofilms are presented. Methods for improving the accuracy of these experiments are proposed.

The research presented in this dissertation provides examples for when quantitative relationships between measured changes in σ_f and σ_b and measured changes in aqueous chemistry can be defined. In situations where σ_b increases at rates faster than observed changes in fluid chemistry, conductive biofilms are suggested as a theoretical explanation for this phenomenon. This research lays the groundwork for further investigations into the existence of electrically conductive biofilms. Additionally, methods for constructing field-scale experiments are suggested. A framework for interpreting electrical conductivity data with respect to biogeochemical reactions is also described.

TABLE OF CONTENTS

LIST OF FIGURES

LIST OF TABLES

ACKNOWLEDGMENTS

I acknowledge National Science Foundation Grants CHE-0431328 to Susan L. Brantley and Ming Tien for the Center for Environmental Kinetics Analysis at Penn State and EAR-0525069 to Flynn Picardal, as well as Department Of Energy Grant No. DE-FG02-08ER64520 to Kamini Singha and Susan L. Brantley. An NSF equipment grant to Jurgen Schieber (EAR-0318769) provided funds for the purchase of the FEI Quanta 400 FEG ESEM that was used for acquiring the images used in Chapter 2. I acknowledge Andy Binley for assistance with the spectral induced polarization equipment and Flynn Picardal and Quanxing Zheng for constructing and maintaining the iron-reducing column reactor and the nitrate-reducing reactor and Eric Roden for discussions involving the interpretation of these experiments. I wish to thank Doug Kent, Dick Smith, Jenn Underwood and Deb Repert for their extensive expertise at the field site on Cape Cod and for allowing me to collaborate with them on their reactive tracer experiment. I wish to thank Denis LeBlanc for organizing logistics on the MMR and for facilitating the drilling of new monitoring wells. Jesse Robertson also assisted with fieldwork at the MMR. Jiayun Zhang and Jeffery Catchmark helped to design and build a set of gold electrodes that could be built into a microfluidics device and used to grow microbial biofilms and measure the resulting conductivity inside and outside the biofilm. The microfluidics device was fabricated at the Penn State nano-fab facility. The proof-of-concept experiments in Chapter 5 were conducted with the assistance of Daniel Bond at the University of Minnesota. Finally I had many helpful discussions with Dan Ross, Tim Fischer, Jochen Nuester, and Laura Liermann.

.

Chapter 1

INTRODUCTION

This dissertation focuses on the effects of microbiological growth and respiration on the electrical properties of subsurface aquifers. Respiration is the series of chemical reactions cells use to obtain energy from substrates. Previous work has qualitatively linked measureable changes in the electrical properties of aquifers to microbiological activity [e.g., *Abdel-Aal et al.*, 2004; *Atekwana and Atekwana*, 2005; *Ntarlagiannis et al.*, 2005; *Slater et al.*, 2009]. The goal of this dissertation is to develop and test techniques to quantitatively link microbiologically induced changes in subsurface chemistry to measurable changes in electrical properties. Linking chemical changes to measureable changes in electrical properties will allow us to monitor biogeochemical activity in a novel, non-invasive manner that is faster and cheaper than traditional chemical methods.

Heterotrophic bacteria are bacteria that derive energy by removing electrons from (i.e. oxidizing) organic carbon compounds and transferring those electrons to (i.e. reducing) an electron accepting compound or molecule. The energy released by these oxidation and reduction reactions is used to synthesize a compound capable of storing energy called adenosine triphosphate (ATP). The synthesis of ATP coupled to the oxidation of organic carbon and the reduction of an electron-accepting compound is respiration. At the Earth's surface, O_2 gas is a very good terminal electron acceptor (TEAP) because it is abundant and because transferring electrons to oxygen from high-energy electron-rich compounds releases a relatively large amount of energy compared to other possible TEAPs (Fig. 1.1). At the Earth's surface, bacteria oxidize organic carbon and transfer electrons to O_2 gas forming two O^{-2} anions. Generally, these O^{-2} anions react with the newly oxidized carbon to form CO_2. In subsurface aquifers with abundant sources of organic carbon, microbial respiration often consumes all of the available O_2 [*Christensen et al.*, 2001]. When O_2 is unavailable as a TEAP, bacteria are forced to utilize alternative TEAPs. Transferring electrons to these alternative TEAPs (e.g., NO_3^- and, Fe(III)) generally does not release as much energy as transferring electrons to oxygen (Fig. 1.1), but the alternative TEAPs are often abundant in subsurface aquifers when oxygen is not [*Christensen et al.*, 2001].

Reducing these alternative TEAPs can cause large changes in the chemistry of subsurface aquifers due to the dissolution of solid minerals, changes in pH and precipitation of other minerals that occur in conjunction with these reduction reactions. In this dissertation I focus on Fe(III) and NO_3^- as TEAPs. Bacteria that dissolve solid Fe(III)-containing minerals increase the concentration of ions in solution. Larger concentrations of ions in solution may increase the ability of that solution to conduct electricity (electrical conductivity). Bacteria that reduce NO_3^- to N_2O or N_2 decrease the concentration of ions in solution and may decrease the electrical conductivity. In this dissertation I investigate the chemical changes that accompany bacterial use of Fe(III) and NO_3^- as TEAPs and attempt to relate those chemical changes to measured changes in electrical conductivity.

Geochemical characterization of microbiological activity in the subsurface requires the drilling and sampling of multiple wells. Analyzing the chemical samples collected from these wells is time consuming and expensive [e.g., *LeBlanc et al.*, 1991]. Electrical conductivity as measured by inserting electrodes into the ground or down wells is usually faster and cheaper than chemical measurements. I demonstrate that changes in electrical conductivity are consistent with microbiologically driven changes in aqueous chemistry, but in some instances, films of bacteria, called biofilms, also affect measured electrical conductivity. I estimate biofilm electrical conductivity from chemical and electrical measurements. Future work to further constrain this link may allow researchers to use changes in electrical conductivity to monitor biogeochemical activity at contaminated sites in the subsurface.

Electrical methods utilized in this dissertation

Electrical resistivity/conductivity is one of the oldest methods in exploration geophysics. Resistivity measurements have been utilized to identify mineral deposits since the beginning of the 20th century [*Kunetz*, 1966]. Although the technology surrounding electrical resistivity measurements has increased vastly since the technique's inception, the basic measurement has remained the same. A direct-current (D.C.) resistivity measurement utilizes four electrodes. To make the measurement, current is injected through two of the four electrodes (electrodes A and B) (Fig 1.2). This current flow creates a voltage field throughout the sample. The difference in voltage between two points is measured by means of the two additional electrodes (electrodes M and N). Voltage measurements are converted to resistances using Ohm's Law:

$$R = V / I \tag{1.1}$$

where R is resistance in Ohms, V is voltage in volts and I is current in amps. Resistance is a value that represents the ability of a material to oppose current flow. A material's resistance is dependent on its length and the cross sectional area as well as its composition. Resistivity is also a measure of how strongly a material can oppose current flow, but it is not dependent on the size or shape of the material. Resistivity is an intrinsic property. To obtain a resistivity value for natural materials, it is vital to know the location and distance separating the electrodes from one another. Resistance is converted to apparent resistivity with a geometric factor κ having units of length in meters as shown in the equation below:

$$\rho = \kappa R = 1 / \sigma \, . \tag{1.2}$$

Apparent resistivity (ρ) has units of ohm-m and is the inverse of apparent conductivity (σ), which has units of S/m. For electrodes inserted into the ground at the earth's surface, κ can be calculated using the following formula:

$$\kappa = \frac{2\pi}{\frac{1}{AM} - \frac{1}{BM} - \frac{1}{AN} + \frac{1}{BN}} \tag{1.3}$$

where *AM, BM, AN* and *BN* are the distances between the four electrodes (m) (Fig. 1.2). A detailed explanation of how to calculate geometric factors can be found in Keller and Frischknecht [1966]. The true resistivity of the subsurface can be obtained by using the apparent resistivity measurements to generate an inverse model of resistivity.

Electrodes used to measure electrical conductivity can be made of any metal but usually stainless steel, graphite, copper or Ag/AgCl is used [*Vanhala and Soininen*, 1995]. Contrary to the name, D.C. resistivity measurements actually require a very low frequency (generally between 0.5 and 2 Hz) alternating current (A.C.) [e.g., *Binley and Kemna*, 2007]. The A.C. current prevents the electrodes from becoming polarized. A polarized electrode will result in incorrect voltage measurements because it will measure the background voltage of the material in addition to the voltage created by the induced current. Another issue with direct versus alternating current is spontaneous or self-potential (SP), an inherent background voltage that can be very large (hundreds of millivolts) in certain situations. Using a low frequency A.C. current causes the SP signal to change sign when the direction of current flow is switched thereby canceling itself out [*Koefoed*, 1979].

The electrical conductivity of an aqueous solution (fluid electrical conductivity, σ_f) is a function of the concentration of dissolved ions in that solution:

$$\sigma_f = F\sum_j \left|Z_j\right| C_j \mu_j \tag{1.4}$$

where σ_f is the fluid electrical conductivity (S/m), F is Faraday's constant (9,6485 C mol^{-1}), C_j is the concentration of each ion (mol/m^3), Z_j is the charge of each ion (unitless) and μ_j is the electrical mobility of each ion ($m^2(V\ s)^{-1}$). A change in concentration will cause a change in measured σ_f

$$d\sigma_f = F\sum_j |Z_j| \mu_j dC_j \ . \qquad (1.5)$$

In a sediment saturated with fluid bulk electrical conductivity (σ_b) is measured instead of σ_f. In natural and laboratory settings, σ_b is a function of σ_f as well as changes in lithology, mineralogy [*Keller and Frischknecht*, 1966], temperature [*Sen and Goode*, 1992], porosity, and the degree to which the sample is saturated [*Knight and Endres*, 2005]. In this work, the first assumption when measuring the σ_b of a fluid-saturated sediment is that σ_b is dominated by σ_f because the electrical conductivity of the fluid is orders of magnitude greater than the electrical conductivity of the sediments. Archie's law, an empirically derived relationship, describes the effect of σ_f on σ_b:

$$\sigma_b = a^{-1}\sigma_f \phi^m \qquad (1.6)$$

where ϕ is porosity, and *a* and *m* are empirical parameters related to tortuosity and cementation [*Archie*, 1942]. An excellent discussion of how *a* and *m* respond to changes in lithology can be found in *Glover* [2010].

Eqs. 1.4 and 1.6 can be used to interpret changes in D.C. conductivity as well as spectral induced polarization (SIP) or complex conductivity in terms of changes in concentration. SIP measurements are similar to D.C. resistivity measurements in that they require four electrodes. As with D.C. resistivity, two electrodes are used to drive an electrical current and the remaining two electrodes are used to measure the resulting voltage field. The primary difference between the two methods is the type of electrical current utilized. Where D.C. electrical resistivity uses a very low frequency alternating current, SIP methods employ an alternating current of varying frequency [*Vanhala and Soininen*, 1995]. Typically, a wide range of A.C. frequencies are employed with data collected from kHz to MHz frequencies.

An SIP measurement consists of two values. At any given current frequency, a voltage is recorded as well as a phase lag. The phase lag, measured in degrees or radians, represents the difference in phase between the induced current oscillations and the resulting voltage oscillations (Fig. 1.3). Larger phase lag values indicate that a given material is more polarizable. A polarizable material has the ability to temporarily store charge. When a current is applied across a polarizable material it behaves like a capacitor, storing charge and releasing it when the current is removed. This release of charge causes the measured voltage curve to be out of phase with the induced current curve in an SIP measurement. Historically, large polarization responses in SIP measurements of natural systems have been attributed to sulfidic-mineral deposits because some sulfidic minerals behave as semi-conductors and temporarily hold electrical charge [e.g. *Sumner*, 1976]. More recently, changes in the magnitude of the phase lag, measured on samples of unconsolidated sediments, have been attributed to mineral precipitation [e.g., *Wu et al.*, 2005] and bacterial attachment to mineral surfaces [e.g., *Abdel-Aal et al.*, 2010]. Mineral precipitation and bacterial attachment may decrease the average diameter of the pore throats connecting the pores or voids in a porous material. Changes in the size of these pore throats has been shown to affect the frequency at which the maximum phase lag occurs [*Scott and Barker*, 2003].

SIP, commonly referred to as complex conductivity, can be reported in terms of its real and imaginary components. The real and imaginary components of complex conductivity are mathematical combinations of the measured conductivity and phase lag. Changes in the real and imaginary components of complex conductivity have been correlated to changes in the physical and chemical parameters discussed above. Real conductivity is defined as

$$\sigma' = |\sigma| \cos(\varphi) \tag{1.7}$$

where σ' is the real component (S/m) of the complex conductivity (σ, S/m) and φ is the phase lag (degrees or radians). σ' is equivalent to D.C. conductivity and responds to changes in σ_f following Eqs. 1.4 and 1.5 [e.g., *Slater and Lesmes*, 2002]. Imaginary conductivity (σ'', S/m) is defined as

$$\sigma'' = |\sigma| \sin(\varphi). \tag{1.8}$$

σ'' responds to changes in the polarizability of the material as described above. As a material becomes more polarizable φ will increase causing σ' to decrease while σ'' increases. In this dissertation I will focus on σ'.

The electrical techniques discussed above have been used to investigate near-surface aquifers containing organic contaminants. In some cases these contaminated zones are more electrically conductive than would traditionally be expected based on Eq. 1.6 [e.g. *Werkema et al.*, 2003; *Atekwana et al.*, 2004a; 2004b; 2004c; 2004d; *Atekwana and Atekwana*, 2005]. These researchers were able to culture more bacteria from areas with higher electrical conductivity, and thus hypothesized that microbiological activity was affecting electrical conductivity. These preliminary findings spurred further experiments. In laboratory experiments SIP measurements on sediments containing live bacteria have been linked to increases in microbial biomass and to cells attaching to sediment surfaces [e.g. *Ntarlagiannis et al.*, 2005; *Davis et al.*, 2006; *Abdel Aal et al.*, 2009]. In this dissertation, I used laboratory experiments to develop an approach to interpret geochemical changes in terms of changes in electrical conductivity. This is a novel quantitative approach. Previous work has not been able to link changes in electrical conductivity directly to changes in chemical calculations. Additionally, my goal is to understand anomalous electrical conductivity and increased polarization observed in aquifers. Combining electrical and chemical techniques may allow researchers to use electrical measurements like resistivity and SIP to monitor contaminated zones without drilling as many monitoring wells. It is possible that changes in electrical conductivity over time can be related to changes in biogeochemistry and can be used to measure biogeochemical reaction rates.

Geochemical methods for measuring reaction rates

Measuring geochemical reaction rates requires several pieces of information. Changes in chemical concentration with respect to changes in time can be used to calculate a reaction rate if the stoichiometry of the reaction is understood. The stoichiometry of a chemical reaction is the relative ratio at which chemical reactants are consumed and chemical products are generated. The concept of reaction extent illustrates how changes in concentration relate to reaction rates. A differential change in reaction extent ($d\xi$) is defined as follows:

$$d\xi = \frac{dn_j}{v_j} \tag{1.9}$$

where n_j is the moles of species j and v_j is the stoichiometric coefficient for species j in the reaction (> 0 for products; < 0 for reactants). A chemical reaction rate (R) is defined as a change in reaction extent with respect to time. For an experimental system at constant volume (V) (m^3),

$$R = \frac{d\xi}{dt} = \frac{VdC_j}{v_j dt} \tag{1.10}$$

where C_j is the concentration of species j in the pore fluid (mol/m^3). At the field scale it may be difficult, time consuming and or prohibitively expensive to collect concentration versus time data for an experimentally meaningful time period. Furthermore, many geochemical reaction rates are so slow that measureable changes in concentration may take hundreds if not thousands of years. In those cases spatial changes can often be used as a proxy for changes in time. Samples collected from different depths in a single well or from different areas above a single rock type may represent unique changes in time that can be combined to infer reaction rates [e.g. *Bau et al.*, 2004; *Porder et al.*, 2007].

Because measuring changes in chemical concentrations can be difficult and time consuming we suggest that changes in σ_f and thus σ_b can be related to changes in concentration and thus chemical reaction rates. Eqs. 1.10 and 1.5 can be combined to describe the relationship between reaction rates and changes in σ_f

$$R = \frac{d\sigma_f}{dt}\frac{V}{F}\frac{1}{\sum_j \mu_j |Z_j| v_j} \quad . \tag{1.11}$$

This relationship allows us to interpret changes in σ_f as reaction rates assuming we understand the stoichiometry of the chemical reactions occurring. When σ_b is coupled to σ_f, changes in σ_b can also document reaction rates. In Chapter 2 I also discuss experiments where σ_b is not coupled to σ_f. This decoupling is concurrent with biomass growth. If biofilms are more electrically conductive than their surroundings, they could cause σ_b to become decoupled from σ_f. In this dissertation I suggest that biofilms have high electrical conductivity and are causing σ_b to increase above predictions based only on porous media and fluids within the pore space. Previous research has also suggested electrically conductive biofilms to explain decoupled σ_f and σ_b measurements [*Atekwana et al.*, 2004b; *Slater et al.*, 2009], but no one has attempted to calculate the electrical conductivity of that biomass. Measurements of organic carbon consumption are used to estimate the extent of biomass growth and the electrical conductivity necessary to describe measured increases in σ_b. This is the first time such an estimate of biofilm conductivity has been attempted using electrical conductivity measurements for a column reactor.

The rate and amount of biomass production can be inferred from the measured reaction rates of the consumption of certain chemical species, using the concept of yield coefficients. For a flow-through column reactor with a dissolving or precipitating component *x*, a reaction rate can be calculated as follows:

$$R_x = ([x]_{in} - [x]_{out})Q \tag{1.12}$$

where R_x is the reaction rate (moles time^{-1}), $[x]_{in}$ and $[x]_{out}$ and are the concentrations of species x (M) in the influent and effluent respectively. $R_x < 0$ indicates precipitation or sorption of x while $R_x > 0$ indicates dissolution or desorption that releases x to solution. Q is the flow rate (L time^{-1}). Yield coefficients relate the measureable rate of substrate consumption to an inferred rate of biomass production:

$$R_{biomass} = -\gamma \nu R_{substrate} \quad . \tag{1.13}$$

Here $R_{biomass}$ is the rate of biomass production (M time^{-1}), γ is the yield coefficient (unitless), $R_{substrate}$ is the rate of substrate consumption (M time^{-1}) and ν is the stoichiometric coefficient of the chemical reaction describing biomass growth [*Rittmann and McCarty*, 2001]. Eq. 1.13 is written specifically for a substrate that can be used both as a carbon source and as an electron donor. In this dissertation, acetate is the substrate and so the chemical reaction describing biomass growth is written as follows:

$$0.05NH_4^+ + 0.125CH_3COO^- + 0.075H^+ \rightarrow 0.05C_5H_7O_2N + 0.15H_2O. \tag{1.14}$$

Biomass is written as $C_5H_7O_2N$, an empirical formula that describes the relative ratios of C, H, O and N measured in biomass containing multiple species of bacteria collected from a sewage treatment plant [*Rittmann and McCarty*, 2001]. γ has a value between 0 and 1 and represents the fraction of substrate being converted to new biomass. A γ value of 1 indicates that all of the substrate consumed is used to generate new biomass. A γ value of 0 indicates that none of the substrate consumed is used to generate new biomass. In cases where $\gamma \neq 1$ the remaining substrate (1-γ) is used for respiration and cellular maintenance. Eqs. 1.13 and 1.14 are used extensively in this dissertation to describe the amount of biomass produced inside flow-through column reactors.

The value for γ can be estimated by comparing the rate of acetate consumption to the rates at which respiration byproducts are produced (e.g. Fe(II), NO_2^-, CH_4, CO_2). This method is effective if a pure strain of bacteria is being studied or all the respiration byproducts are easily measurable. In an experimental system containing multiple species this may not be possible. Another possibility is to compare acetate consumption rates to the consumption rate of a species only utilized to produce new biomass. In our experiments, NH_4^+ was added as a N source to facilitate cell growth. We assume NH_4^+ is only consumed for biomass growth and that acetate is consumed for respiration and biomass growth [*Rittmann and McCarty*, 2001]. Therefore, γ can be estimated by comparing the rates of acetate consumption to the rates of NH_4^+ consumption:

$$\gamma = \frac{R_{NH_4^+}}{R_{acetate}} \frac{0.125}{0.05} \quad . \tag{1.15}$$

Here R_x is the rate of consumption (mol/time) of either NH_4^+ or acetate. The values 0.125 and 0.05 represent the stoichiometric coefficients for NH_4^+ and acetate from Eq. 1.13. Using Eq. 1.15 we are able to estimate γ, and thus estimate the amount of biomass produced in flow experiments. An estimate of the amount of biomass produced in a column allows us to model the electrical conductivity of biomass necessary to describe measured changes in σ_b in our experiments. This is a novel approach to calculating biofilm electrical conductivity and may be applicable to other systems as well.

Dissertation Summary

There are four research chapters in this dissertation. The first research chapter (Chapter 2) describes laboratory experiments designed to examine changes in σ_f due to the reduction and dissolution of Fe(III) oxides. We show that changes in σ_f can be interpreted as reaction rates in batch experiments containing no bacteria (abiotic), batch experiments containing the enzymes responsible for iron reduction (*in vitro*) and batch experiments containing live cells (*in vivo*). We also interpret changes in effluent chemical concentrations and changes in σ_b measured from a flow through column reactor. The column reactor was constructed and maintained by Flynn Picardal and Quanxing Zheng at Indiana University. I installed conductivity electrodes in the reactor and interpreted all the conductivity data. The reactor contained iron-reducing bacteria as well as bacteria that produce methane (methanogens). Initially, in the column experiment we were able to interpret σ_b changes as chemical reaction rates. Later in the experiment, σ_b changes became decoupled from changes in effluent chemical concentrations. We hypothesize that this decoupling was due to the growth of an electrically conductive biofilm. Using the concept of yield coefficients we were able to estimate the amount of biofilm present in the column and suggest a conductivity value necessary to describe the measured increase in σ_b. This is the first estimate of biofilm conductivity to be calculated from measured chemical changes in a column reactor. This chapter was written with Susan L. Brantley, Kamini Singha, Ming Tien, Eric Roden, Flynn Picardal, Quanxing Zheng and Jurguen Schieber as co-authors and is in press at Water Resources Research.

In Chapter 3, I revisit the column reactor experiment from Chapter 2 and use reactive transport modeling to better constrain the amount of biomass produced inside the reactor. Reactive transport models consist of sets of equations that describe the transport and reactions of chemical species within a porous medium like unconsolidated sediments. The model we utilized, for the column experiment PHREEQC [*Parkhurst and Appelo*, 1999] like PHAST, [*Parkhurst et al.*, 2004] the model we used for the field experiment in Chapter 4, can simulate mineral dissolution, precipitation, adsorption, cation exchange, biomass growth and oxidation-reduction reactions. All of these chemical reactions can be modeled as equilibrium reactions, which occur instantaneously, or as kinetic reactions, which have a time dependence. Reactive transport models are useful in complicated chemical systems where there are tens if not hundreds of reactions occurring simultaneously. I found that reactive transport modeling could be used to more accurately describe the chemical reactions occurring in the column reactor. I also present the results from an iron-adsorption column experiment in Chapter 3 that demonstrates that abiotic sorption of Fe(II) onto Fe(III)-oxide coated sediments does not produce a large increase in σ_b. I present a new estimate of biofilm electrical conductivity that is consistent with the reactive transport modeling.

In Chapter 4 we focus on a different respiration pathway, NO_3^- reduction. We present chemical and electrical data from a flow-through column reactor in which the influent was amended with NO_3^- and acetate to encourage NO_3^- reduction. Again the reactor was constructed and maintained by Flynn Picardal and Quanxing Zheng. In this experiment σ_b again became decoupled from σ_f in the same manner as described for the Fe-reducing column in Chapter 2. I use reactive transport modeling to describe the measured changes in effluent concentrations and to interpret measured changes in σ_b as a function of biofilm formation. Based on the results of these reactive transport models I suggest that biofilms may be electrically conductive. The present the requisite conductivity value of these biofilms necessary to describe the measured σ_b increase is presented. Additionally, we present the results from a field-scale experiment in which NO_3^- was injected into an aquifer to encourage NO_3^- reduction. For the field experiment Dick Smith and Deb Repert measured N_2O and anion concentrations in samples. Doug Kent measured cation concentrations on those same samples. For the field experiment, I also used reactive transport modeling to describe the microbially driven consumption of NO_3^- as it is transported through the aquifer. I used electrical forward models to describe the measured changes in σ_b due to NO_3^- reduction and dispersion. In general, modeling of the nitrate reduction was more problematic than modeling Fe-reduction, because of the many redox reactions that can occur in the N system. Additionally, the field experiment was particularly difficult to interpret because the concentrations we used for injection in the field experiment were too low to be detected with the electrical conductivity measurements. Therefore, I discuss some these shortcomings in our experimental design and suggest modifications for future field scale experiments.

In Chapter 5, we present the results of an attempt to directly measure the electrical conductivity of a microbial biofilm. We discuss the construction of a micro-fluidic microbial fuel cell in which biofilms of iron-reducing bacteria are grown on gold electrodes. We present the preliminary results of these experiments and discuss shortcomings in the experimental design that could be improved upon in the future. Several suggestions are offered for improving the results of these experiments.

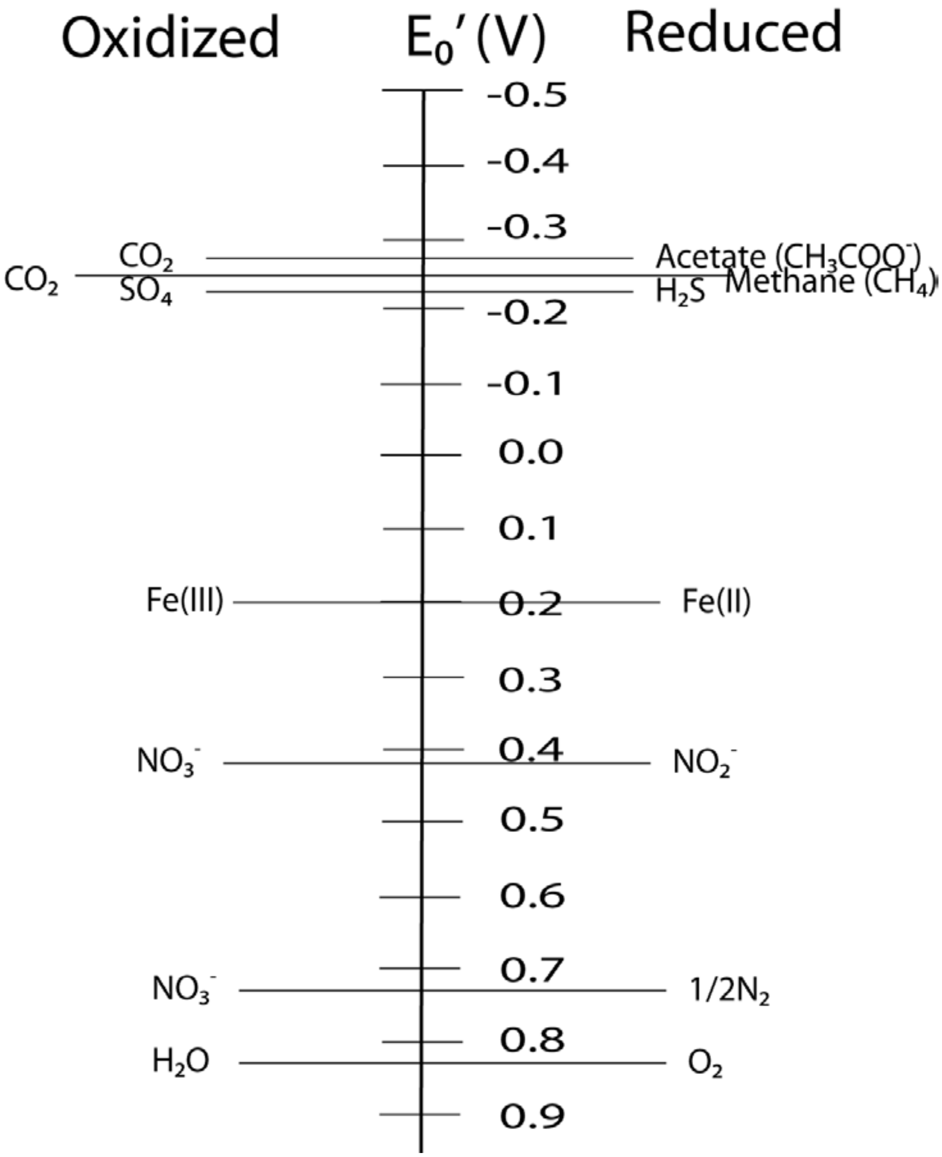

Figure 1.1: A redox ladder demonstrates the potential energy (E_o') at STP and pH =7 in volts for different pairs of electron donors and terminal electron acceptors. The farther apart the electron donor and the terminal electron acceptor are the greater the potential energy. In this ladder acetate oxidation coupled to O_2 reduction has the greatest potential energy [e.g., *Madigan et al.*, 2003].

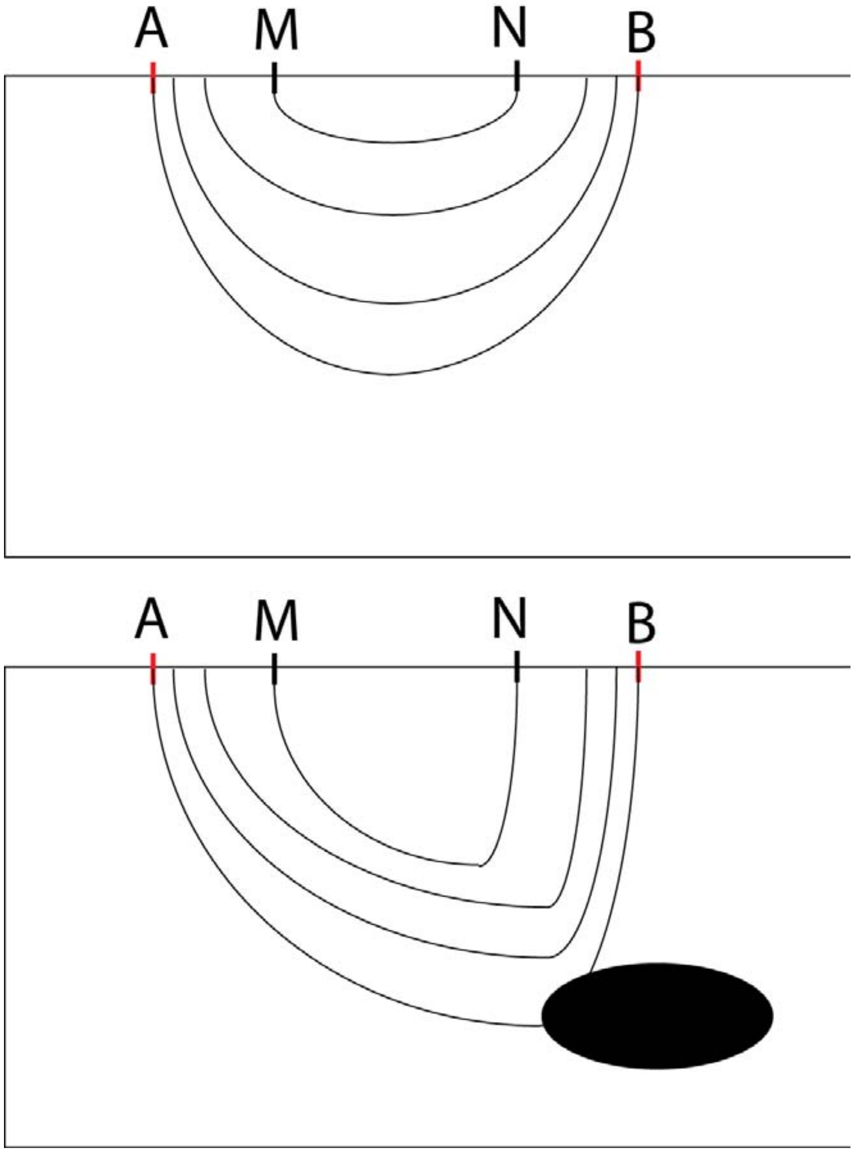

Figure 1.2: This cartoon illustrates how a typical electrical conductivity measurement is made. Current is injected across two electrodes (A and B) and the resulting voltage is measured at two additional electrodes (M and N). If current flow (solid lines) intersects a conductive body it will deflect toward areas of higher electrical conductivity (black ellipse, bottom panel).

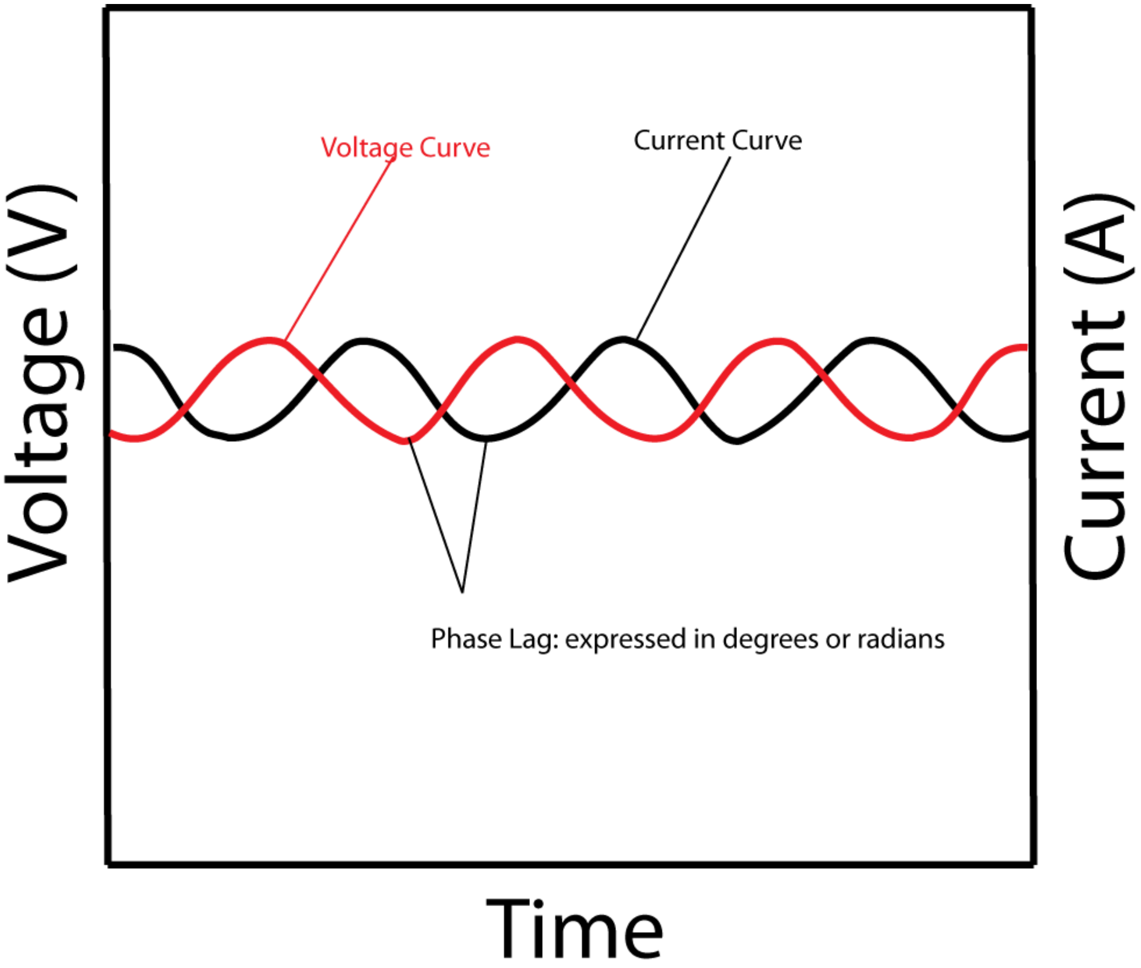

Figure 1.3: A cartoon exhibiting the relationship between induced current curves and measured voltages for SIP measurements. The more polarizable a material is the more the voltage curve (red line) will lag behind the current curve (black line).

Works Cited

Abdel Aal, G., E. Atekwana, S. Radzikowski, and S. Rossbach (2009), Effect of bacterial adsorption on low frequency electrical properties of clean quartz sands and iron-oxide coated sands, *Geophysical Research Letters*, *36*(L04403).

Abdel-Aal, G. Z., E. A. Atekwana, L. D. Slater, and E. A. Atekwana (2004), Effects of microbial processes on electrolytic and interfacial electrical properties of unconsolidated sediments, *Geophysical Research Letters*, *31*(12).

Abdel-Aal, G. Z., E. A. Atekwana, S. Rossbach, and D. D. Werkema (2010), Sensitivity of geoelectrical measurements to the presence of bacteria in porous media, *Journal of Geophysical Research-Biogeosciences*, *115*(G03017), 1-11.

Archie, G. E. (1942), The electrical reisistivity log as an aid in determining some reservoir characteristics, *Petroleum Transactions of AIME*, *146*, 54-62.

Atekwana, E., E. Atekwana, F. Legall, and R. Krishnamurthy (2004a), Field evidence for geophysical detection of subsurface zones of enhanced microbial activity, *Geophysical Research Letters*, *31*(23), L23603.

Atekwana, E., E. Atekwana, R. Rowe, D. Werkema, and F. Legall (2004b), The relationship of total dissolved solids measurements to bulk electrical conductivity in an aquifer contaminated with hydrocarbon, *Journal of Applied Geophysics*, *56*(4), 281-294.

Atekwana, E., and Atekwana (2005), Biodegradation and mineral weathering controls on bulk electrical conductivity in a shallow hydrocarbon contaminated aquifer, *J. Contam. Hydrol.*, *80*(3-4), 149-167.

Atekwana, E. A. E., E. A. Atekwana, D. Werkema, J. P. Allen, L. A. Smart, J. W. Duris, D. P. Cassidy, W. A. Sauk, and S. Rossbach (2004c), Evidence for microbial enhanced electrical conductivity in hydrocarbon-contaminated sediments, *Geophysical Research Letters*, *31*(23), 20.

Atekwana, E. A. E., D. Werkema, J. W. Duris, S. Rossbach, E. Atekwana, W. A. Sauk, D. P. Cassidy, J. Means, and F. D. Legall (2004d), In-situ apparent conductivity measurements and microbial population distribution at a hydrocarbon-contaminated site, *Geophysics*, *69*(1), 56-63.

Bau, M., B. Alexander, J. Chesley, P. Dulski, and S. Brantley (2004), Mineral dissolution in the cape cod aquifer, Massachusetts, USA: I. reaction stoichiometry and impact of accessory feldspar and glauconite on strontium isotopes, solute concentrations, and REY distribution, *Geochim. Cosmochim. Acta*, *68*(6), 1199-1216.

Binley, A., and A. Kemna (2007), DC Resistivity and Induced Polarization Methods, in *Hydrogeophysics*, edited by Y. Rubin and S. Hubbard, pp. 129-156, Springer, AA Dordrecht, The Netherlands.

Christensen, T., P. Kjeldsen, P. Bjerg, D. Jensen, J. Christensen, A. Baun, H. Albrechtsen, and G. Heron (2001), Biogeochemistry of landfill leachate plumes, *Appl. Geochem.*, *16*(7-8), 659-718.

Davis, C. A., E. Atekwana, E. Atekwana, L. D. Slater, S. Rossbach, and M. R. Mormile (2006), Microbial growth and biofilm formation in geologic media is detected with complex conductivity measurements, *Geophysical Research Letters*, *33*(18), L18403.

Glover, P. W. J. (2010), A generalized Archie's law for n phases, *Geophysics*, *75*(6), E247-E265.

Keller, G. V., and F. C. Frischknecht (1966), *Electrical Methods in Geophysical Prospecting*, 1 ed., 523 pp., Pergamon Press, Oxford.

Knight, R. J., and A. L. Endres (2005), *An Introduction to Rock Physics for Near-Surface Application in Near Surface Geophysics, Volume 1: Concepts and Fundamentals*, 31-70 pp., Society of Exploration Geophysicists, Tulsa.

Koefoed, O. (1979), *Geosounding Principles, 1 Resistiivity Sounding Measurements*, Elsevier Scientific Publishing Company, New York.

Kunetz, G. (1966), *Principles of Direct Current Resistivity Prospecting*, 103 pp., Gerbruder Borntraeger, Berlin.

LeBlanc, D. R., S. P. Garabedian, K. M. Hess, L. W. Gelhar, R. D. Quadri, Stollenwerk, K. G;, and W. W. Wood (1991), Large-scale natural gradient tracer test in sand and gravel, Cape Cod, Massachusetts; 1, Experimental design and observed tracer movement, *Water Resour. Res.*, *27*(5), 895-910.

Madigan, M. T., J. M. Martinko, and J. Parker (2003), *Brock Biology of Microorganisms*, 10th ed., 1019 pp., Prentice Hall, Upper Saddle River.

Ntarlagiannis, D., N. Yee, and L. Slater (2005), On the low-frequency electrical polarization of bacterial cells in sands, *Geophysical Research Letters*, *32*(24).

Parkhurst, D. L., and C. Appelo (1999), User's guide to PHREEQC (Version 2) - A Computer program for speciation, batch-reaction, one-dimensional transport, and inverse geochemical calculations, *Water-Resources Investigations Report*, *99-4259*.

Parkhurst, D. L., K. L. Kipp, P. Engesaard, and S. R. Charlton (2004), PHAST - A Program for Simulating Ground-Water Flow, Solute Transport, and Multicomponent Geochemical Reactions, *U.S. Geological Survey Techniques and Methods 6-A8*, 154.

Porder, S., G. E. Hilley, and O. A. Chadwick (2007), Chemical weathering, mass loss, and dust inputs across a climate by time matrix in the Hawaiian Islands, *Earth. Planet. Sci. Lett.*, *258*(2007), 414-427.

Rittmann, B. E., and P. L. McCarty (2001), *Environmental Biotechnology: Principles and Applications*, 754 pp., McGraw Hill, Boston.

Scott, J. B. T., and R. D. Barker (2003), Determining pore-throat size in Permo-Triassic sandstones from low-frequency electrical spectroscopy, *Geophysical Research Letters*, *30*(9), 1450.

Sen, P., and P. Goode (1992), Influence of temperature on electrical conductivity on shaly sands, *Geophysics*, *57*(1), 89-96.

Slater, L., and D. Lesmes (2002), Electrical-hydraulic relationships observed for unconsolidated sediments, *Water Resour. Res.*, *38*(10), 1213.

Slater, L. D., F. D. Day-Lewis, D. Ntarlagiannis, M. O'Brien, and N. Yee (2009), Geoelectrical measurement and modeling of biogeochemical breakthrough behavior during microbial activity, *Geophysical Research Letters*, *36*.

Sumner, J. (1976), *Principles of Induced Polarization for Geophysical Exploration*, 1 ed., 277 pp., Elsevier Scientific Publishing Company, Amsterdam.

Vanhala, H., and H. Soininen (1995), Laboratory technique for measurement of spectral induced polarization response of soil samples, *Geophysical Prospecting*, *43*(5), 655-676.

Werkema, D. D., E. A. Atekwana, A. L. Endres, W. A. Sauck, and D. P. Cassidy (2003), Investigating the geoelectrical response of hydrocarbon contamination undergoing biodegradation, *Geophysical Research Letters*, *30*(12), 1647.

Wu, Y., L. Slater, and N. Korte (2005), Effect of precipitation on low frequency electrical properties of zerovalent iron columns, *Environ. Sci. Technol*, *39*(23), 9197-9204.

Chapter 2

ELECTRICAL CONDUCTIVITY AS AN INDICATOR OF IRON REDUCTION RATES IN ABIOTIC AND BIOTIC SYSTEMS

Microorganisms impact subsurface chemistry in ways that may affect fluid and bulk electrical conductivity (σ_f and σ_b) [*Atekwana et al.*, 2004a; 2004b; 2004c]. For instance, study of an aquifer contaminated with hydrocarbons at the Crystal Refinery in Carson City, MI revealed a zone of increased σ_b near the hydrocarbon-water interface that corresponds to increased microbial activity [*Werkema et al.*, 2003]. A conceptual model has been suggested to explain conductivity increases at contaminated sites [*Sauck*, 2000] and specific microbial processes like iron reduction, methanogenesis, sulfate reduction and sulfide oxidation have been identified [*Allen et al.*, 2007].

To date, field-scale σ_b measurements have been difficult to interpret mechanistically due to the complicated nature of larger systems. Even laboratory measurements of σ_b in biogeochemical systems have been difficult to interpret. Bulk conductivity has been measured in biogeochemical systems containing environmental consortia (i.e., a culture containing all the bacterial species from a natural system) [*Abdel Aal*, 2004; *Davis et al.*, 2006] and in some cases additional electrical measurements of complex conductivity [*Ntarlagiannis et al.*, 2005; *Abdel Aal et al.*, 2009] and self potential [e.g. *Ntarlagiannis et al.*, 2007] were collected to provide further insights. Despite this work, many unanswered questions remain regarding the effect of microbial growth and respiration on σ_b in natural systems and in laboratory experiments.

In this paper we describe a series of simple experiments focusing on specific microbial processes to elucidate the effects of these processes on changes in chemistry, σ_f and σ_b. Specifically, we investigate if it is possible to quantify biogeochemical reaction rates from changes in electrical conductivity measured in systems with dissimilatory iron-reducing bacteria (DIRB). Dissimilatory iron-reducing organisms commonly impact subsurface water chemistry under the anoxic conditions associated with organic-contaminated aquifers [*Christensen et al.*, 2001]. Furthermore, DIRB are ubiquitous [e.g., *Abrams and Loague*, 2000; *Bennett et al.*, 2000; *Scheibe et al.*, 2006] because iron oxides are an abundant terminal electron acceptor [*Christensen et al.*, 2001]. We report experiments of increasing complexity from abiotic batch experiments to batch experiments using a pure culture of a DIRB (*Shewanella oneidensis* MR-1) to a column experiment. We chose to use a pure culture in the batch experiments for ease of interpretation. For the column experiment, we switched to an environmental consortium to better mimic natural systems.

Our experiments were designed to build the capability to combine chemical measurements (e.g. pH, [Fe(II)]) from a limited number of locations with geophysical measurements of electrical conductivity to yield models of subsurface biogeochemical activity. Currently, understanding biogeochemical reactions in aquifers requires extensive sample collection at many locations (e.g., monitoring wells) followed by time-consuming laboratory analyses for each sample. In contrast, geophysical methods may provide data that can map out reactions over spatially broader zones. To quantify reaction rates, it will be necessary to attribute spatially integrated changes in electrical measurements to discrete changes in fluid chemistry. Here, we demonstrate how inferred reaction stoichiometries (Table 2.1) can be used in increasingly complex experimental systems to determine reaction rates; this development should provide a framework for future research in natural systems.

We demonstrate a link between changes in concentrations and electrical conductivity versus time in the batch experiments. We are able to convert a change in conductivity versus time into a change in concentration versus time, which can then be used to calculate a geochemical reaction rate. Similarly, in the column experiment, concentrations in effluent change with time and document reaction rate. Due to the spacing of electrodes in the column, the electrical measurements represent an average conductivity of the entire volume. Early in the column experiment, σ_b correlates to effluent chemistry and can be converted to an inferred reduction rate for the column. At later times, σ_b is influenced by another process – hypothesized here to be biofilm growth -- and no longer reflects iron oxide reduction rates.

Electrical conductivity and reaction rates

Below, we demonstrate how electrical conductivity methods are useful for measuring biogeochemical reaction rates. For a defined chemical reaction, the differential change in reaction extent, $d\xi$, is defined as a function of n_j, the moles of species j :

$$d\xi = \frac{dn_j}{v_j} \tag{2.1}$$

where v_j is the stoichiometric coefficient of the reaction (> 0 for products; < 0 for reactants). The rate of the reaction (R) is defined at constant volume (V) as

$$R = \frac{d\xi}{dt} = \frac{VdC_j}{v_j dt} \tag{2.2}$$

where C_j is the concentration of species j in the pore fluid (mol/m^3). For species that are ions in solution, the following relation can be written to define σ_f (S/m):

$$\sigma_f = F\sum_j \left|Z_j\right| C_j \mu_j \tag{2.3}$$

where F is Faraday's constant (C/mol) and Z_j and μ_j (m^2 (V s)$^{-1}$) are the charge and electrical mobility of ion j. Combining Eqs. 2 and 3 yields

$$d\sigma_f = F\sum_j |Z_j|\mu_j dC_j = \frac{F}{V}\sum_j |Z_j|\mu_j v_j d\xi \tag{2.4}$$

and

$$R = \frac{d\sigma_f}{dt}\frac{V}{F}\frac{1}{\sum_j \mu_j |Z_j| v_j}. \tag{2.5}$$

Combining Eqs. 2 and 5, separating variables, and integrating over time yields:

$$C_j = C_j^0 + \frac{v_j}{F\sum_j \mu_j |Z_j| v_j}(\sigma_f - \sigma_f^0) \tag{2.6}$$

where C_j^0 and σ_f^0 are initial ion concentrations and fluid conductivity, respectively. Equation 2.5 can be used to calculate a chemical reaction rate from a change in σ_f if the stoichiometry of the reaction is known. As shown in Eq. 2.4, the change in σ_f is directly related to the change in reaction extent. Equation (2.6) demonstrates that the term $\frac{v_j}{F\sum_j \mu_j |Z_j| v_j}$ will control the slope of a plot of σ_f versus concentration C_j

The bulk conductivity of a fluid-saturated porous medium, σ_b, can often be described as a function of σ_f with the following equation:

$$\sigma_b = a^{-1}\sigma_f \phi^m \ , \tag{2.7}$$

where ϕ is porosity [e.g. *Archie*, 1942; *Balberg*, 1986]. Here *a* (generally varying from 0.62 to 3.5) and *m* (from 1.37 to 1.95) are empirical factors related to the extent of cementation and tortuosity. The primary assumption behind Eq. 2.7 is that the solid phase is nonconductive relative to the liquid phase. When this is the case, σ_b is expected to vary predictably as a function of σ_f according to equation (2.7).

However, in some settings, especially in the presence of clays, the assumption of a single non-conductive solid phase may be incorrect. For such cases where σ_b does not vary with σ_f as described by Eq. 2.7, the expression is often modified to include a surface conductivity term (σ_{surf}):

$$\sigma_b = a^{-1}\sigma_f \phi^m + \sigma_{surf} \ . \tag{2.8}$$

The term σ_{surf} is sometimes attributed to the presence of clay coatings on grains or, at larger scales, the presence of shale in the porous media [*Juhasz*, 1981; *Sen and Goode*, 1992; *Revil and Glover*, 1998]. Alternately, at the grain scale, σ_{surf} is attributed to conduction through the electrical double layer around mineral grains [e.g. *Waxman and Smits*, 1968; *Juhasz*, 1981; *Johnson et al.*, 1987; *Schwartz et al.*, 1989; *Revil and Glover*, 1997; *Revil et al.*, 1998].

Another approach used to modify Eq. 2.7 is to assume the presence of two conductive phases with bulk electrical conductivities σ_1 and σ_2 contributing to σ_b [e.g. *Glover et al.*, 2000]:

$$\sigma_b = \sigma_1 \chi_1^m + \sigma_2 \chi_2^p \ . \tag{2.9}$$

Here χ is the volume fraction of phase 1 or 2 and m and p are treated as fitting factors related to the tortuosities of phases 1 and 2 respectively. Notably, for both Eqs. 2.8 and 2.9, conductivity terms are summed to describe σ_b. If surface conduction or secondary phases become significant contributors to σ_b, then the interpretation of chemical reaction rates from changes in σ_b using Eq. 2.5 becomes difficult or impossible.

One goal of this research is to identify criteria that describe when biogeochemical conditions are favorable for interpreting subsurface reaction kinetics from electrical conductivity measurements. With such a mechanistic understanding, geophysical measurements might be interpreted more accurately for field systems.

Laboratory Experiments

We first conducted a series of abiotic, *in vitro* and *in vivo* batch experiments to test the effect of iron oxide reduction on σ_f with as few reactions and confounding variables as possible. In each case, synthetic goethite (4.5 mg/ml) [*Cornell and Schwertmann*, 2003] was reduced in reactors in triplicate. The goethite was synthesized in two batches and surface area was measured with a Micromeritics ASAP 2000 BET surface area analyzer. Each reactor was a continuously stirred 50 ml flask maintained at ambient temperature. The concentration of electron donor was varied to change the reaction rate.

Abiotic experiments contained 0.01 or 0.1 M ascorbic acid solution and goethite [*Zinder et al.*, 1986]. *In vitro* experiments allowed exploration of biological Fe reduction catalyzed by bacterial cell membranes without the complication of live cells; experiments were conducted with aliquots of total membrane fraction (TM) from *Shewanella oneidensis MR-1* (0.1 mg/ml) with 0.001, 0.01 or 0.1 M Na-formate as the reductant [*Ruebush et al.*, 2006] in 100mM HEPES buffer (pH = 7) under a 5% H_2 - 95% N_2 headspace. *In vivo* experiments were inoculated with 0.8 mg cells ml^{-1} of *S. oneidensis* in buffered solution with 0.01 or 0.1 M Na-formate as the reductant under non-growth conditions [*Ruebush et al.*, 2006]. To inhibit cell growth, neither nitrogen nor phosphorus were added.

For all batch experiments, pH was measured *in situ*. Aliquots of the slurry were collected every 20 minutes, filtered through a 0.2 μm filter, and analyzed for Fe(II) concentration, $[Fe(II)_{(aq)}]$, using ferrozine [*Stookey*, 1970; *Violier et al.*, 2000]. Solid-associated (adsorbed and/or precipitated) Fe(II) was extracted by adding 100 μl of 2N HCl to 300 μl of unfiltered slurry to obtain a final concentration of 0.5 N HCl. The resulting solution was immediately centrifuged at 13,200 r.p.m. for 1 minute to pellet the suspended solids. A 50 μl sample was removed from the supernatant for analysis with ferrozine [*Lovley and Phillips*, 1986]. Additionally, σ_f was measured every 10 minutes (±0.0005 S/m) with an Orion conductivity cell and every minute with an IRIS Syscal Pro meter with 4 electrodes (Wenner array, 1 cm spacing) designed for field geophysical measurements. The Orion cell consists of a set of graphite electrodes embedded in plastic. In contrast, the geophysical electrodes consist of Ag/AgCl wire insulated such that only the tip of the wire is conductive. The σ_f measurements with either the Orion cell or the field instrument take <1 second to collect and involve injecting small amounts of current (~0.1 mA) into the solution. Changes in σ_f versus time were compared to changes in aqueous and adsorbed Fe(II) concentrations versus time and were used to calculate reaction rates.

To scale up from the batch experiments, iron reduction rates were measured in a flow-through column experiment. The column reactor (20.3 cm long, 7.6 cm I.D.) was constructed from an acrylic tube with walls 1.27 cm thick packed with 1552 g of air dried, sieved, iron mineral-bearing sediment (2 wt. % Fe) from the subsurface at Oyster, VA [*Penn et al.*, 2001]. The sediment was not sterilized by autoclave or exposure to radiation to avoid alteration of the sediment mineralogy. The large aspect ratio and thick walls of this column preclude significant O_2 diffusion [*Kjeldsen*, 1993]. The effluent end of the column was loosely packed with glass wool to prevent the transport of fine particles out of the column. The sediment was mixed with a microbial inoculum of shallow subsurface sediment from Dorn Creek in Madison, WI (9:1 ratio by mass). Such an environmental consortium contains all the species present in the natural system and was used instead of a pure culture to mimic natural conditions. The initial effective porosity was 0.33 and was measured with a NaBr tracer by determining when 50% of the tracer had exited the column [*Knutsson*, 1966; *Freeze and Cherry*, 1979]. Sterile, anoxic, PIPES-buffered artificial groundwater (PBAGW) with 1 mM acetate and < 5μM $Fe(II)_{aq}$ (hereafter $[Fe(II)_{(aq)}]_{in}$) was pumped at 2 ml hr^{-1} through Teflon-tubing using a glass syringe pump. The PBAGW contains NaCl (0.15 g L^{-1}), $CaCl_2$ (0.30 g L^{-1}), $MgCl_2$-$6H_2O$ (0.50 g L^{-1}), KH_2PO_4 (0.006 g L^{-1}), NH_4Cl (0.01 g L^{-1}), $NaHCO_3$ (0.25 g L^{-1}) PIPES (3.35 g L^{-1}), trace elements and vitamins. All effluent was collected daily in a N_2-purged tube and analyzed for acetate concentration, $[acetate]_{out}$, using high performance liquid chromatography; $[Fe(II)_{(aq)}]_{out}$ using ferrozine; and $[NH_4^+]_{out}$ using *o*-phthaldialdehyde [*Holmes et al.*, 1999]. The flow rate was confirmed by measuring the volume of effluent collected each day.

A Ag/AgCl wire electrode inside a glass tube filled with KCl-saturated agar was inserted 3.8 cm into the center of the column at a point 2.96 cm from the inlet at the bottom. Three more identical electrodes were inserted every 4.8 cm along the rest of the column axis (Fig. 2.1). Only the tips of the electrodes were designed to be conductive. These electrodes are adequately non-polarizable and resistant to reaction [*Vanhala and Soininen*, 1995]. To make σ_b measurements, current (I) was injected across the outer two electrodes at large enough levels (0.1 – 0.2 mA) so that voltage could be measured across the inner electrodes but low enough to avoid inducing electrochemical reactions. We began these measurements on day 70, as the concentrations in the column effluent were approaching steady state. An IRIS Syscal R2E resistivity meter was used to measure the voltage twice daily. Each σ_b measurement takes <1 min. From the measured voltage (V), σ_b was calculated using Ohm's law, $V = I/S$, where S is conductance. A geometric factor K (m) was used to convert S (in Siemens) to σ_b (S/m):

$$\sigma_b = K^{-1}S \quad . \tag{2.10}$$

Here K for the column was calculated to equal 10.7 m using COMSOL Multiphysics (COMSOL, Inc., Burlington, MA), a finite element analysis software package [2008]. Measurements of σ_b collected for the column experiment represent a volume-weighted conductivity value over the area encompassed by the electrodes.

At the conclusion of the experiment at 198 days, sediment was removed and examined with a FEI Quanta 400 FEG environmental scanning electron microscope (ESEM). Sediment samples were placed on 0.5" diameter Al sample stubs, allowed to air dry for 30 minutes, and then immediately examined with scanning electron microscopy (SEM) under vacuum. All samples were examined in low vacuum mode at 90 Pa chamber pressure. The operating voltage of the SEM was 15 kV. Samples were imaged simultaneously in secondary electron (SE) and backscatter electron (BSE) mode, and selected areas were also examined for elemental composition by energy dispersive X-ray spectroscopy (PGT Spirit EDS system).

To extract sorbed Fe(II), 0.5 N HCl was incubated for 24 hours with 10 g portions of the unwashed sediment from the top, bottom and middle of the column following published experimental protocols [*Heron et al.*, 1994]. A separate analysis was also used to determine the amount of siderite and vivianite precipitation. In this latter extraction, the masses of CO_2, Fe, Ca, Mg, and P released were measured after the reaction of 10 ml of 1 N HCl with 10 g of acetone-washed, post-reaction column sediment for 24 hours in a sealed vessel [*White et al.*, 1999]. It was assumed that all the Ca and Mg extracted with 1 N HCl was derived from solubilized carbonate minerals. The moles of CO_2 released were attributed to calcite and dolomite based on the Ca and Mg concentrations in the 1 N HCl extraction, and the remainder of the CO_2 was attributed to siderite. A minor amount of excess Fe could be attributed to vivianite precipitation based on the amount of P released. However, thermodynamic calculations performed with the geochemical speciation code PHREEQC using the default database [*Parkhurst and Appelo*, 1999] indicated that vivianite ($Fe(PO_4)_2 * 8H_2O$) was undersaturated (SI = -0.23) therefore we assumed no vivianite precipitation. Any remaining Fe from the 1 N HCl extraction was considered as adsorbed onto mineral surfaces.

Instantaneous Fe(II) release rates normalized to sediment surface area, $R_{release}$ (mol Fe m^{-2} day^{-1}), were calculated as follows:

$$R_{release} = \frac{([Fe(II)_{(aq)}]_{out} - [Fe(II)_{(aq)}]_{in})Q}{A\ M} \tag{2.11}$$

where Q is the flow rate (L/day), A is the specific surface area of sediment (m^2 g^{-1}), and M is the column sediment mass (g). $[Fe(II)_{(aq)}]_{in}$ was observed to be below detection ($\leq$ 5 µM). As discussed later, instantaneous Fe release rate can be calculated for aqueous Fe alone based on equation (11) or a cumulative total release rate can be calculated from the sum of sorbed + aqueous + precipitated Fe(II), $Fe(II)_{TOT}$:

$$R_{release}^{total} = \frac{mFe(II)_{TOT}}{AMt} = \frac{\left(mFe(II)_{(aq)out} + mFe(II)_{(sorbed)} + mFe(II)_{(siderite)}\right)}{AMt} \qquad (2.12)$$

Here *m* is the cumulative moles of $Fe(II)_{aq}$ released from the column, the total Fe(II) sorbed, or total Fe(II) precipitated as siderite by the end of the experiment at time $t = 298$ days. The specific surface area of the sediment, A, was set equal to ~1.48 $m^2\ g^{-1}$ as measured in a previous study [*Knapp et al.*, 2002].

Results

Batch experiments

Electrical conductivity measured with the field and laboratory electrodes in the batch experiments agreed within ±15% (Fig. 2.2A). The noise using the field instrumentation is attributed to small changes in electrode spacing caused by removing aliquots from the flask for chemical measurements. As expected, the laboratory instrument, with fixed electrode spacing, demonstrated better precision.

Given the low reactivity of goethite, no change in σ_f was observed when the reductant was absent in the abiotic experiments; however, when ascorbate was present, σ_f increased with time and the rate of increase accelerated with increasing concentration of ascorbate (Fig. 2.2A). Note that in Fig. 2.2 all experiments are plotted such that $\sigma_f = 0$ at time 0 i.e., the starting σ_f was subtracted from all subsequent σ_f measurements. The pH in the abiotic experiments started at 3.2 and increased to 4.6 at experiment termination.

For i*n vitro* and *in vivo* experiments, no conductivity change was observed, even in the presence of reductant (formate) unless TM or whole cells were present to catalyze the reaction (Fig. 2.2 B,C).

When the reductant and catalyst were present, σ_f (Fig. 2.2) and $[Fe(II)_{aq}]$ (Fig. 2.3) increased with time and the rates of change in σ_f increased with greater concentrations of formate (Fig. 2.2 B,C). The pH remained constant *in vitro* and *in vivo* due to the presence of HEPES buffer. At experiment termination, the concentration of sorbed Fe(II) per L of solution was < 1%, 97 ± 3%, and 80 ± 2% of the total [Fe(II)] for abiotic, *in vitro*, and *in vivo* experiments, respectively (Table 2.2).

Column experiment

In the column experiment, $[Fe(II)_{(aq)}]_{in}$ was below detection ($\leq$ 5 µM) and $[Fe(II)_{(aq)}]_{out}$ increased to a steady-state value of 0.18 mM by day 50. The release rate at day 50 was equal to 8.64 µmol $Fe(II)_{aq}$ day^{-1} and was equivalent to $R_{release}$ = 0.0038 ±0.0002 µmol $Fe(II)_{aq}$ $m^{-2}day^{-1}$ (Eq. 2.11, Fig. 2.4).

Measured $[acetate]_{out}$ decreased below detection ($\leq$ 0.05 mM) after day 75 (Fig. 2.4), consistent with a steady-state instantaneous consumption rate of ≤ 39.1 µmol acetate day^{-1}. $[NH_4^+]_{out}$ also attained steady-state values (0.16 mM) at day 75, consistent with an instantaneous consumption rate of 1.8 µmol NH_4^+ day^{-1} (Fig. 2.4). Acetate consumption is necessary for microbial respiration and growth. In contrast, NH_4^+consumption only occurs for cell growth. Cell growth into biofilms is consistent with observations by SEM on the reacted sediments that revealed carbon-rich coatings (Fig. 2.5).

At the conclusion of the experiment, the average of the 0.5 N HCl extractable Fe(II) for four samples was 7.61 ± 0.59 mmol (equivalent to 0.0049 mmol / g sediment). There was a noticeable trend in the 0.5 N HCl-extractable Fe(II) measured in these four samples. Sediment samples collected along the length of the column showed a decrease in concentration from 0.0067 mmol Fe(II) g^{-1} sediment at 4 cm from the inlet to 0.0063 mmol Fe(II) g^{-1} sediment at 8 cm from the inlet to 0.0030 mmol Fe(II) g^{-1} sediment at 12 cm from the inlet to 0.0050 mmol Fe(II) g^{-1} 16 cm from the inlet. These values were corrected for the initial concentration in sediment, observed to equal 0.001 mmol Fe(II) per gram. The average value of all four samples is reported in Table 2.2.

At the conclusion of the experiment, 16.45 ± 0.002 mmol sorbed ± precipitated Fe(II) (equivalent to 0.0106 mmol/ g sediment) were extracted with 1 N HCl. Of this total, 1.4 ± 5.16 mmol of Fe(II) were attributed to sorbed Fe(II) based on the argument described in the next paragraph. This value was the same within two standard deviations as the $Fe(II)_{sorbed}$ measured in the 0.5 N extraction (7.61± 0.59 mmol). The 0.5 N HCl probably extracted some siderite [*Heron et al.*, 1994] also.

The 1 N HCl extraction released 39 µmoles CO_2 g sediment^{-1} (equivalent to 60.5 mmoles CO_2 for the entire reactor). Of this, 46.1 mmoles were attributed to Mg and Ca carbonates (based on Ca and Mg measurements in the extractant) and the remaining 14.4 ± 5.16 mmol of CO_2 to siderite. However, this extraction released 16.45 mmol Fe, leaving 2.05 mmol non-carbonate Fe. Since we calculated vivianite to be undersaturated we did not include it in our mass balance. Therefore the remaining 2.05 ± 5.16 mmol of Fe(II) was present as sorbed Fe(II). No siderite or vivianite were detected in fresh sediment before the experiment.

Based on these data, a total of 18.10 mmol of Fe (released Fe_{aq} + 1N HCl extracted Fe) were reduced over 198 days. This includes the cumulative release of aqueous Fe(II) determined by summing the mass of Fe(II) in each sample, i.e., 1.653 mmol over 198 days. Therefore, of the 18.10 mmoles of Fe reduced, >90% was retained in the column. These values are equivalent to 91.4 µmol $Fe(II)_{TOT}$ day^{-1} or 0.0398 µmol Fe_{TOT} m^{-2} day^{-1} of reduction, assuming a constant reduction rate over the entire experiment (Eq. 2.12).

Similarly, the cumulative consumption of acetate was determined to be 8.08 mmol by summing the mass of acetate in each outlet sample and subtracting this value from the total mass of acetate introduced to the column over the entire experiment. This corresponds to a cumulative acetate consumption rate of 40.8 µmole day^{-1}. Note that this value is very similar to the instantaneous acetate consumption rate calculated previously from effluent chemistry and flow rate.

Influent σ_f equaled 0.276 S/m throughout the experiment and steady-state effluent σ_f after day 70 equaled 0.281 S/m, as calculated from measured ionic concentrations. In contrast, measurements of σ_b across the column remained constant (~0.055 S/m) only from day 70 to 120 but after day 120, σ_b began to increase to ~0.18 S/m (Fig. 2.4). The ionic strength of the effluent remained constant at 26 mM during this increase in σ_b.

Discussion

The intent of this research was to develop an approach to interpret field measurements of electrical conductivity in terms of biogeochemical reaction rates. This is an inverse problem and will yield non-unique, model-derived reaction rates that must be constrained by chemical measurements. With these chemical measurements, the reaction stoichiometries can be identified allowing interpretation of the geophysical data. We demonstrate this general approach hereafter. Reaction models will be iteratively proposed and tested against measured conductivity until discrepancies between the model predictions and the measured data are minimized. Here, we iterate by using investigator-written geochemical models; however, inverse modeling modules in geochemical codes such as PHREEQC can also be used [*Parkhurst and Appelo*, 1999] to constrain more complicated field systems.

For the batch experiments, composite reaction stoichiometries (numbered equations, Table 2.1) were proposed and used to compare the measured values of $d\sigma_f/dt$ to measured concentrations using Eqs. 2.5 and 2.6. It is easy to see that the batch experiments (abiotic, *in vitro* and *in vivo*) have different stoichiometries describing different reactions by comparing the slopes of the lines in Fig. 2.3. The relationship between σ_f and Fe(II) is different for each experimental condition. Different reactions were tested until a stoichiometry was found that fit the observed rate of change in conductivity and the measured chemistry. For example, in the abiotic batch experiment, the stoichiometry of the redox reaction (Reaction A, Table 2.1) incorporating ascorbic acid ($C_6H_8O_6$) oxidation, and goethite reduction was initially written as follows:

$$C_6H_8O_6 + 2FeOOH + 4H^+ \rightarrow 2Fe^{2+} + 4H_2O + C_6H_6O_6 . \qquad (2.13)$$

Given that the initial pH of the experiments (pH=3.2) was less than the pKa of ascorbic acid [*Kumler and Daniels*, 1935], pKa = 4.12, no deprotonation of ascorbic acid was included in the proposed reaction. However, the stoichiometry of Eq. 2.13 is inconsistent with the change in σ_f as documented in Fig. 2.6A. This inconsistency led us to conclude that an additional acid-base reaction (Reaction B in Table 2.1) was missing from Eq. 2.13. Furthermore, the pH values of the abiotic experiments increased from starting values of 3.2 to 4.6 at experiment termination, well above the pKa of ascorbic acid. When the appropriate acid-base reaction for ascorbic acid was added to Eq. 2.13, Reaction I in Table 2.1 was the result. Using Reaction I, the calculated changes in σ_f from measured changes in ionic concentrations for the abiotic experiments were similar to the measured increases in σ_f (Fig. 2.6B). Importantly, we did not need to make measurements of the ascorbate ion concentrations once the reaction stoichiometry was inferred from the slope of Fig. 2.6A. Consistency is demonstrated in Fig. 2.6B where the measured conductivity is plotted along with the summed contributions of conductivities for all ions. Using Eq. 2.5 and the stoichiometry from Reaction I (Table 2.1), the calculated reduction rate from measured values of $d\sigma_f/dt$ is 0.12 nmol Fe(II) m^{-2} min^{-1} for the 0.01 M ascorbic acid experiment, consistent with a reduction rate from measured values of $d[Fe(II)_{aq}]/dt$ of 0.10 nmol m^{-2} min^{-1} as summarized in Table 2.2 (ionic mobilities summarized in Table 2.3). Sorption in these abiotic experiments was less than 1%, as measured with a 0.5 N HCl extraction. This is consistent with the pH value below 4.5.

In contrast to these abiotic experiments, the pH was greater than 7 in the *in vitro* and *in vivo* experiments and sorption was significant. Therefore, composite reactions used to interpret *in vitro* and *in* *vivo* data had to include a reduction reaction (Reaction A, Table 2.1), an acid-base reaction (Reaction B, Table 2.1), and a sorption reaction (Reaction C, Table 2.1). Chemical measurements to determine the extent of Fe(II) adsorption were also necessary. With measured adsorption, composite reactions II or III were written. For example, in the *in vitro* experiment, a measured change in σ_f can be converted to a change in Fe(II) concentration using Eq. 2.6. A change in σ_f is partitioned to changes in the relevant ionic species (in this case Fe(II), $HCOO^-$, and HEPES anion) using stoichiometry from reaction II. Using this method, the inferred rate of change of total Fe(II) based on measured changes in σ_f matched measured changes in total Fe(II) within error (Eq. 2.5) (Table 2.2, Fig. 2.6C). Error in the *in vitro* and *in vivo* experiments was primarily due to uncertainty surrounding the ionic mobility for the HEPES anion.

With this inverse approach, the batch experiments were described within error with composite reactions I, II and III that summed redox (Reaction A), acid-base (B), and sorption (C) reactions. We were able to predict biogeochemical reaction rates from changes in σ_f in these well constrained systems. The same approach was then pursued to interpret the column experiment. To create a composite reaction that describes the column experiment (Reaction IV), additional reactions occurring in the column were included as described in the next section.

Interpreting the column experiment

In addition to reactions A,B, and C, in Table 2.1 the composite reaction for the column must also incorporate biomass growth. Since NH_4^+ and acetate consumption are both at steady state after day 70, the biomass growth rate was inferred to be constant after that point as well. Biomass growth in the column was estimated from acetate and ammonium consumption rates using the concept of yield coefficients (γ) [*Rittmann and McCarty*, 2001]. Every mole of $C_5H_7O_2N$ (a generic formula for biomass) consumes 2.5 moles of acetate and 1 mole of N. However, the observed ratio of NH_4^+ to acetate consumption was 0.05 much less than the 0.4 required by this stoichiometry. This is expected because most of the acetate was oxidized and converted to HCO_3^- during dissimilatory iron reduction. Assuming NH_4^+ is only consumed by biomass growth, the ratio obtained by dividing the ammonia consumption rate (moles NH_4^+ day^{-1}) by the acetate consumption rate (moles acetate day^{-1}) is related to the growth yield γ. The growth yield expresses the relative partitioning of electrons from the electron donor into two sinks, new biomass or the terminal electron acceptor (in this case ferric iron), and can theoretically have a value between 0 and 1. In the column experiment, $\gamma = 0.12$ based on rates of NH_4^+ consumption divided by the steady state instantaneous acetate consumption rate (γ = 1.8 µmol NH_4^+ day^{-1}/(39.1 µmol acetate day^{-1} * 0.4)).

However, the observed rate of Fe reduction is not consistent with these interpretations. Specifically, if Fe(III) is the only terminal electron acceptor, and assuming 8 e- released per mole of acetate oxidized, then $8(1-\gamma)$ moles of Fe(II) are produced per mole of acetate consumed (Table 2.1, Eq. A). In contrast, the observed ratio of the rate of Fe(III) reduction (91.4 µmol day^{-1}) to the cumulative acetate consumption rate (40.8 µmol day^{-1}) is too low, consistent with a higher growth yield of $\gamma = 0.72$. This value is inconsistent with literature values for growth yields: γ = 0.12-0.15 for growth of *Geobacteraceae* species on amorphous Fe(III) oxides [*Lovley and Phillips*, 1988; *Roden and Lovley*, 1993; *Caccavo Jr et al.*, 1994].

Therefore, another process in addition to Fe reduction and biomass production was inferred to consume acetate. Mass balance dictates that the cumulative consumption of acetate released 64.6 meq e^-. Iron reduction accounts for 28% of the 61.9 meq e^- released, (based on the summed total of $Fe_{(aq)}(II)_{out}$ + 1 N HCl extractable Fe(II))and biomass production accounts for another 12% (based on the mass of NH_4^+ consumed and the stoichiometry in Eq. D in Table 2.1). The remaining 60% of electrons released from acetate could have produced methane if methanogenesis (Table 2.1, Eq. E) occurred in the column. Methanogenesis is the only reasonable respiration pathway in this system given that no additional ionic solutes were measured in the column effluent. HCO_3^- produced via methanogenesis presumably precipitated as siderite. The column was effectively impermeable to O_2 diffusion inward from the atmosphere and so O_2 is not a reasonable sink for electrons released from acetate [*Kjeldsen*, 1993]. Reactions for biomass growth and methanogenesis were added to the composite reaction (see equation IV) based on these arguments.

Thermodynamic calculations with PHREEQC [*Parkhurst and Appelo*, 1999] are consistent with chemical oversaturation of siderite in the effluent by day 50. Furthermore, extractions with 1N HCl were also consistent with the presence of siderite. The composite reaction that includes Fe(III) reduction, acid-base buffering, Fe(II) sorption, methanogenesis, biomass growth, and siderite precipitation (Eq. IV, Table 2.1) is consistent with the relative changes in concentrations of all measured species between influent and effluent. Based on the cumulative consumption of acetate and using Eq. IV in Table 2.1, biomass production was calculated as a function of time and plotted on Figure 2.4.

Electrical Conductivity

For the column experiment, measured values of σ_b were compared to σ_f using Eq. 2.7. To do this, we assumed values of *a* within the range of 0.63 to 3.5 and *m* within the range of 1.37 to 1.95 based on literature values [e.g. *Archie*, 1942; *Balberg*, 1986]. Values of σ_b calculated from Eq. 2.7 and effluent chemistry with $a = 1$ and $m = 1.5$ were consistent with measured σ_b before day 120. Furthermore, the Fe(II) release rate calculated from measured σ_b, 0.0041 μmol $Fe(II)_{aq}$ m^{-2} day^{-1}, using equations 5, 7 and composite reaction IV (Table 1), is consistent with the rate calculated from the measured $[Fe(II)_{aq}]$ (0.0038 μmol $Fe(II)_{aq}$ m^{-2} day^{-1}) in effluent from day 70 to 120 using Eq. 2.11. As described for the batch experiments, we are able to calculate Fe(II) reduction rates from changes in σ_b before day 120 in the column.

However, after day 120, σ_b increased by a factor of 3 (Fig. 2.4) while measured effluent chemistry did not change significantly. The cause of this σ_b increase that is unrelated to changes in effluent chemistry is not readily apparent. It is unlikely that methane bubbles formed within the column experiment or affected σ_b. The solubility of methane at 298 K under 1 atmosphere of pressure is about 35 mg/L (2.47 mM) [*Duan and Mao*, 2006]. The methane concentration was calculated from the flow rate (0.048 L/day) and the cumulative acetate consumption rate (40.8 mmol day^{-1}) assuming 0.60 moles methane produced per mole acetate (composite reaction IV, Table 2.1). The calculated methane concentration, 0.510 mM, was well below saturation. Furthermore, any gas bubbles that did form would be less conductive than the pore fluid and their presence would temporarily decrease the measured σ_b [*Knight*, 1991; *Wang et al.*, 2000; *Serra and Serra*, 2005]. Methane bubbles cannot explain the σ_b increase.

This result is surprising because deviation from Eq. 2.7 is sometimes associated with conductive minerals and the known Fe(II) precipitate siderite, is generally non-conductive [*Rzhevskii et al.*, 1965]. There are several other possible explanations for the measured increase in σ_b after day 120. Changes in porosity could affect electrical conductivity; however, ϕ, a or m would be required to change to unreasonable values of 0.87, 0.34 or 0.81, to match observations (see Eq. 2.7). It is impossible to keep all three parameters within acceptable bounds and still describe the measured increase in σ_b.

If geochemical gradients exist within the column it is possible that they are affecting σ_b. For example, a change in [$Fe(II)_{aq}$] or sorbed Fe(II) along the length of the column could affect surface conductance and thus σ_b. However, the gradient in sorbed Fe(II) as documented by our HCl extractions reported earlier is presumed to have been present, along with a gradient in $Fe(II)_{aq}$, from relatively early in the experiment and would not have caused changes in σ_b starting at day 120

In literature treatments, when measured σ_b is above the value predicted from fluid chemistry alone using Eq. 2.7, most conductivity models have been expanded to include either a surface conductivity term or a term for a secondary conductive phase as in Eqs. 2.8 or 2.9. For example, *Atekwana et al.* [2004b] used a variable surface conductivity term (σ_{surf} = 1 to 10 mS/m) (Eq. 2.8) to explain discrepancies between σ_b and σ_f in measurements in a borehole that passed through a zone of hydrocarbon contamination above an aquifer in Carson City, MI. They attributed the surface conductivity to changes in the electrical double layer around mineral surfaces caused by microbial activity. However, they did not present chemical or physical data such as measured changes in ionic strength, surface roughness or cation exchange capacity to support their hypothesis. *Slater et al.* [2009] took a conceptually different approach by modeling conductivity data with a parallel conductivity term that is mathematically similar to surface conductivity. The authors noticed an increase in σ_b measured in a flow-through column containing Se-reducing bacteria while effluent σ_f remained constant. *Slater et al.* [2009] were able to fit their data by adding a second conductivity term, similar to the surface term in Eq. 2.8, with variable values between 2 and 12 mS/m. They referred to their new term as a parallel conductivity path.

The largest changes in σ_b measured in our column can be modeled using Eq. 2.8 with σ_{surf} equal to about 127 mS/m. It is unlikely that this addition is due to a change in surface conductivity with time, however, because changes in surface conductivity are generally small when ionic strength is held constant. Similar to *Slater et al.* [2009], we attribute the σ_b increase in our column not to a surface conductivity, but to a new, parallel conductive pathway. The ionic strength in the column remained relatively constant throughout the experiment, increasing by only 0.75% (26.6 versus 26.8mM) despite extensive dissolution of iron oxides. Surface conductivity stops being affected by changes in ionic strength above 10 mM [*Revil and Glover*, 1997]; therefore, it is unlikely that we have developed significant surface conductivity

The concept of surface conductivity as described above is an unlikely explanation for increased σ_b, but it is possible that ferrous iron sorbed onto ferric oxide surfaces creates a unique type of surface conductivity that is not explicitly accounted for in previous publications [e.g. *Revil and Glover*, 1997]. Previous research has demonstrated that adsorbed ferrous iron is capable of transferring electrons onto ferric oxides [e.g. *Tronc et al.*, 1984; *Icopini et al.*, 2004; *Williams and Scherer*, 2004; *Crosby et al.*, 2005; *Handler et al.*, 2009]. While it is possible that this electron transfer affects macroscopic conductivity, no one has demonstrated this phenomenon conclusively. During our column experiment, the mass of adsorbed iron increased but the total mass of iron inside the column decreased by 16%. For these reasons we believe that ferrous sorption onto ferric oxides is not causing the σ_b increase measured in the column experiment.

In contrast to the decrease in total Fe in the column, the biomass grew in the column even after day 120. It is possible that this steady increase in biomass could increase surface conductivity by increasing the total surface area within the column. Increasing the surface area of a sample can increase its cation exchange capacity which in turn increases surface conductivity [e.g. *Revil and Glover*, 1998]. However, the sediment in the column had an initial surface area of 2,300 m^2 (= 1.48 m^2g^{-1} x 1552 g). Approximately 4.4 x 10^{12} cells were produced during the entire experiment, based on a γ value of 0.12 calculated as described previously (mass of one cell assumed = 1 x 10^{-12} g, [*Sundararaj et al.*, 2004]) If each cell has an average surface area of 6 x 10^{-12} m^2, then the total increase in surface area due to biomass production is 26 m^2, which is 1% of the total surface area inside the column. A 1% increase in surface area is unlikely to produce significant increases in cation exchange capacity and surface conductance since biomass has a similar sorption capacity to iron oxide minerals [*Urrutia et al.*, 1998].

Since the effect of iron sorption and biomass growth on surface conductivity is unlikely to be significant, we consider the possibility that cells connecting into biofilms by day 120 create a new conductive phase and cause a dramatic σ_b increase (Fig. 2.4). While we cannot confirm that biofilms are conductive, we use a theoretical approach to consider how the electrical conductivity of microbial biofilms might impact this experiment. This conceptual model is based on the assumptions about microbial growth from cumulative acetate and NH_4^+ consumption discussed above. The model does not require a massive increase in biomass after day 120. Instead, we hypothesize that day 120 represents the point at which a threshold is crossed such that sufficient numbers of discrete patches of biofilm become connected across the column. SEM analyses of the sediments reveal biofilm-like coatings on mineral grains (Fig. 2.5). While the column effluent was at steady state, the rate of biomass growth did not change. However, the amount of biomass connectivity was presumably increasing.

Because σ_b shows a threshold-type behavior (Fig. 2.4), we propose a theoretical model based on percolation theory to describe σ_b increases. This is only one of many possible ways to model the effect of biofilm growth and connectivity but is a first step in considering how biofilms might explain this data set. Percolation theory has been used to describe changes in hydraulic conductivity, micro-organism populations, and other properties [e.g. *Kirkpatrick*, 1973; *Deutsch*, 1989; *Thullner et al.*, 2002]. It incorporates a threshold that depends on the volume fraction of a new phase, assumed to be biomass in this case. By analogy to *Deutsch's* equation for hydraulic conductivity and Eq. 2.9, σ_b is assumed to follow Eq. 2.7 until the fraction, $f_{secondary}$, of secondary material with higher conductivity, $\sigma_{secondary}$, exceeds a critical fraction, $f_{critical}$, at which point a new term appears in the equation:

$$\sigma_b = a^{-1}\sigma_f \phi^m + (f_{\text{secondary}} - f_{\text{critical}})^{\omega} \sigma_{\text{secondary}} \,. \tag{2.14}$$

For hydraulic conductivity, the geometry of permeable zones is thought to control the values of $f_{critical}$ and ω ($1.5 < \omega < 2$) [*Deutsch*, 1989]. Interestingly, ω in Eq. 2.14 may be similar to p in Eq. 2.9 since both values can be attributed to tortuosity effects.

As argued above, $f_{critical}$ describes the critical volume fraction of biomass. Assuming a constant γ of 0.11 and the cumulative consumption of acetate we calculated $f_{secondary}$ for the volume fraction of biomass from the moles of $C_5H_7O_2N$, average cell volume ($1\text{x}10^{-9}$ mm^3), cell mass ($3.0 \text{ x}10^{-7}$ μg) [*Sundararaj et al.*, 2004], reactor volume (920 cm^3), and porosity (0.33). The calculated value of $f_{secondary}$ at 120 days, i.e., ~3%, was assumed equal to $f_{critical}$. Fitting the data to Eq. 2.7 for $f_{secondary} < f_{critical}$ before 120 days and to Eq. 2.14 for values above $f_{critical}$ after day 120 yields $\sigma_{secondary} =$ 5.5 S/m if $\omega = 1.5$ (Fig. 2.4). According to our hypothesis, this is an estimate for the conductivity of respiring biofilm in the reactor.

These $\sigma_{\text{secondary}}$ values for a biofilm, approximately 20 times that of σ_f, are reasonable. Many mechanisms might cause electrical conductivity in a biofilm. For example, it is well known that most soil bacteria can produce extracellular polymeric substances that affect hydrologic as well as chemical conditions in and around biofilms [e.g. *Little et al.*, 1991; *Or et al.*, 2007]. Furthermore, *Liermann et al.* [2000] demonstrated that [H$^+$] in biofilms grown on Fe-containing minerals is up to 10x higher than in the bulk fluid and *Marsili et al.* [2008] have argued for electron shuttles in biofilms. Either of those species in biofilms could increase conductivity. Nanowires could also contribute to biofilm conductivity if they are present [e.g. *Reguera et al.*, 2005; *Ntarlagiannis et al.*, 2007; *Nielsen et al.*, 2010] but, nanowires are not a pre-requisite for a conductive biofilm *Torres et al.* [2008] calculated a conductivity ≥0.05 S/m in biofilms and *Ramasamy et al.* [2008] observed a 40% decrease in kinetic impedance as biofilms grew inside fuel cells. As mentioned earlier, the analogous but much smaller increase in conductivity measured across a column containing Se(IV)-reducing bacteria [*Slater et al.*, 2009] was also attributed to biofilm growth, although without chemical evidence to eliminate other explanations such as changes in pore fluid chemistry.

Implications and Conclusions

Our observations have implications for interpreting σ_b in microbially active sediments. For example, in the aquifer in Carson City, MI, σ_b varied by 0.025 S/m with depth [*Atekwana et al.*, 2004b] . Using techniques outlined herein, a few co-located chemical and σ_b measurements versus depth could constrain composite reactions and be used to infer reaction rates using published approaches for interpreting chemistry versus depth in subsurface flow systems [e.g. *Bau et al.*, 2004]. However, if σ_b becomes decoupled from σ_f, reaction rates would be difficult to determine. Indeed, *Atekwana et al.* inferred that something other than ionic solutes contributed to σ_b because they needed to set σ_{surf} = 10 mS/m with Eq. 2.8 to describe the Carson City aquifer. Our work provides a framework for further investigations of the effect of biofilm growth on σ_b.

We suggest that models for biogeochemical reaction rates can in some cases be quantified using electrical conductivity and composite reaction stoichiometries – but not in those instances where thresholds in conductivity are crossed that necessitate the modification of Archie's Law. We propose a simple theoretical model that attributes a change in σ_b in our column experiments to a threshold that is crossed due to the increase in biomass. This research lays the groundwork for future investigations by presenting an iterative method that can be used to determine whether systems are above or below a threshold. More work on the electrical properties of biofilms is clearly needed. Future directions for this work include monitoring microbial activity and or chemical changes associated with contaminant plumes, enhanced oil recovery, and CO_2 sequestration.

Table 2.1. **Reaction Stoichiometries**

Individual reaction types that are summed into composite reactions	
A: Redox (metal reduction)	$\text{Reductant} + \text{MOOH} \rightarrow \text{Oxidant} + M^{2+} + 2OH^-$
B: Acid-Base[a]	$H_nA \rightarrow mH^+ + H_{(n-m)}A^{m-}$
C: Sorption	$\equiv SOH + M^{2+} \rightarrow \equiv SOM^+ + H^+$
D: Biosynthesis	$0.05\ NH_4^+ + 0.125\ CH_3COO^- + 0.075\ H^+ \rightarrow 0.05\ C_5H_7O_2N + 0.15H_2O$
E: Redox (methanogenesis)	$0.125\ CH_3COO^- + 0.125\ H_2O \rightarrow 0.125\ HCO_3^- + 0.125\ CH_4$
F: Dissolution / Precipitation	$M^{2+}_{(aq)} + HCO_3^- \rightarrow MCO_{3(s)} + H^+$
Composite reactions	
I: Abiotic	$9\ C_6H_8O_6 + 4\ \alpha\text{-}FeOOH_{(s)} + H^+ \rightarrow 4\ Fe^{2+} + 8\ H_2O + 7\ C_6H_7O_6^- + 2\ C_6H_6O_6$
II: *In Vitro*[b]	$HCOO^- + 2\ \alpha\text{-}FeOOH_{(s)} + x \equiv FeOH + (5\text{-}x)\ HL^- \rightarrow 4\ H_2O + (5\text{-}x)\ L^{2-} + x \equiv FeOFe^+ + CO_2 + (2\text{-}x)\ Fe^{2+}$
III: *In Vivo*[b]	$HCOO^- + 2\ \alpha\text{-}FeOOH_{(s)} + x \equiv FeOH + (5\text{-}x)\ HL^- \rightarrow 4H_2O + (5\text{-}x)\ L^{2-} + x \equiv FeOFe^+ + CO_2 + (2\text{-}x)\ Fe^{2+}$
IV: Column	$CH_3COO^- + 2.32\ \alpha\text{-}FeOOH_{(s)} + 0.044\ NH_4^+ + 0.0696 \equiv SOH + 2.3048\ HL^- + 0.8616\ HCO_3^- \rightarrow 0.6\ CH_4 + 0.2088\ Fe^{2+}_{(aq)} + 2.0416\ FeCO_{3(s)} + 0.0696 \equiv SOFe^+ + 0.044C_5H_7O_2N + 3.012H_2O + 2.3048L^{2-}$

[a] H_nA is the conjugate acid and $H_{(n-m)}A^{m-}$ the conjugate base, n: number of hydrogen atoms on acid, m: number of hydrogen atoms released.

[b] Here, x = fraction of reduced iron $[Fe(II)_{sorbed}]/([Fe(II)_{sorbed}]+[Fe(II)_{aqueous}])$ that sorbs to surfaces (denoted as ≡S or ≡Fe). L= HEPES ($C_8H_{18}N_2O_4S$) in batch experiments, or PIPES ($C_8H_{18}N_2O_6S_2$) in column.

Table 2.2 Experimental Conditions and Results[a]

	Abiotic		*In Vitro*			*In Vivo*		*Column*
Starting (Influent) pH	3.2		7.55			7.50		~7
Final (Effluent) pH	4.6		7.59			7.55		~7
Electron Donor	ascorbic acid $C_6H_8O_6$		formate $HCOO^-$			formate $HCOO^-$		acetate CH_3COO^-
Electron Acceptor	α-FeOOH		α-FeOOH			α-FeOOH		Ferric Oxide
Buffer	Ascorbic Acid		HEPES			HEPES		PIPES
Atmosphere	Air		N_2 (95%) H_2 (5%)			N_2 (95%) H_2 (5%)		Ar
[Electron donor][b]	0.01 (3)	0.1 (3)	0.001 (3)	0.01 (3)	0.1 (3)	0.01 (3)	0.1 (3)	0.001 (1)
% Fe Adsorbed[c]	<1%	<1%	97±3%	97±3%	97±3%	81±6%	78±2%	11 ±2%
% Fe precipitated[c]	--	--	--	--	--	--	--	80%
Surf. Area (m^2/g)	19.3	19.3	25.4	19.3	19.3	25.4	25.4	1.48
$d[Fe(II)]/dt$[d]	0.1	0.3	5.8	9.5	29.5	2.7	4.3	N.A.
$d\sigma_f/dt$[e]	1.18	4.25	2.63	10.5	37.6	2.0	3.0	N.A.
Rate[f] based on:								
$[Fe(II)_{aq}]$	0.10	0.30	10.4	18.5	43.5	4.8	7.6	0.0038
σ[g]	0.12	0.44	7.1	23.1	57.5	6.2	9.9	0.0041

[a] Rates calculated over the entire 5 hour batch experiments or steady state portion of column experiment.

[b] Molar. For each experiment, the number of replicates is shown in parentheses.

[c] Batch experiments: $[Fe(II)_{sorbed}]/([Fe(II)_{sorbed}]+[Fe(II)_{aq}])$ as calculated at the end of experiment. Column experiments: moles $Fe(II)_{sorbed}$/(moles $Fe(II)_{sorbed}$ + moles $Fe(II)_{siderite}$ + moles $Fe(II)_{aq}$)

[d] Rate $\times 10^{-6}$ M min^{-1} ;$[Fe(II)] = [Fe(II)]_{(aq)} + [Fe(II)]_{adsorbed}$ for batch experiments

[e] Batch experiments ($d\sigma_f/dt \times 10^{-5}$ S/m min^{-1})

[f] abiotic (nM m^{-2} min^{-1}); *in vitro* and *in vivo* (nmol (mg TM)$^{-1}$$m^{-2}$ min^{-1}); column (μmol $m^{-2}$$day^{-1}$)

[g] Rate based on σ_f and Eq. 5 (for abiotic (nM m^{-2} min^{-1}); *in vitro* and *in vivo* (nmol (mg TM)$^{-1}$$m^{-2}$ min^{-1} experiments); but based on σ_b and Eqs. 5 & 7 for column (μmol $m^{-2}$$day^{-1}$) from days 70 -120.

Table 2.3. Ionic Diffusion Constants and Mobilities.

Ion	Diffusion Constant $m^2 s^{-1} *10^{-5}$	Mobility[a] $m^2 (V s)^{-1} *10^{-7}$
H^+	9.311	3.626
Fe^{+3}	1.812	2.117
Fe^{+2}	1.438	1.120
OH^-	5.273	2.053
CHO_2^- (formate)	1.454	0.566
HCO_3^-	1.185	0.461
CO_3^{-2}	1.846	1.438
Na^+	1.334	0.519
Cl^-	2.032	0.791
K^+	1.957	0.762
Ca^{+2}	1.584	1.234
Mg^{+2}	1.424	1.100
$C_8H_{17}N_2O_4S^-$ (HEPES)	0.554	0.431
$C_8H_{17}N_2O_6S_2^-$ (PIPES)	0.467	0.364
$CH_3CO_2^-$ (acetate)	1.089	0.424
NH_4^+	1.957	0.762
$C_6H_7O_6^-$ (ascorbate)	0.687	0.267
$C_6H_6O_6$ (dehydroascorbic acid)	0.692	0.269

[a] Ion mobilities from published values [*Landolt-Bornstein*, 1969] or estimated from diffusion constants [*Schwarzenbach et al.*, 2003].

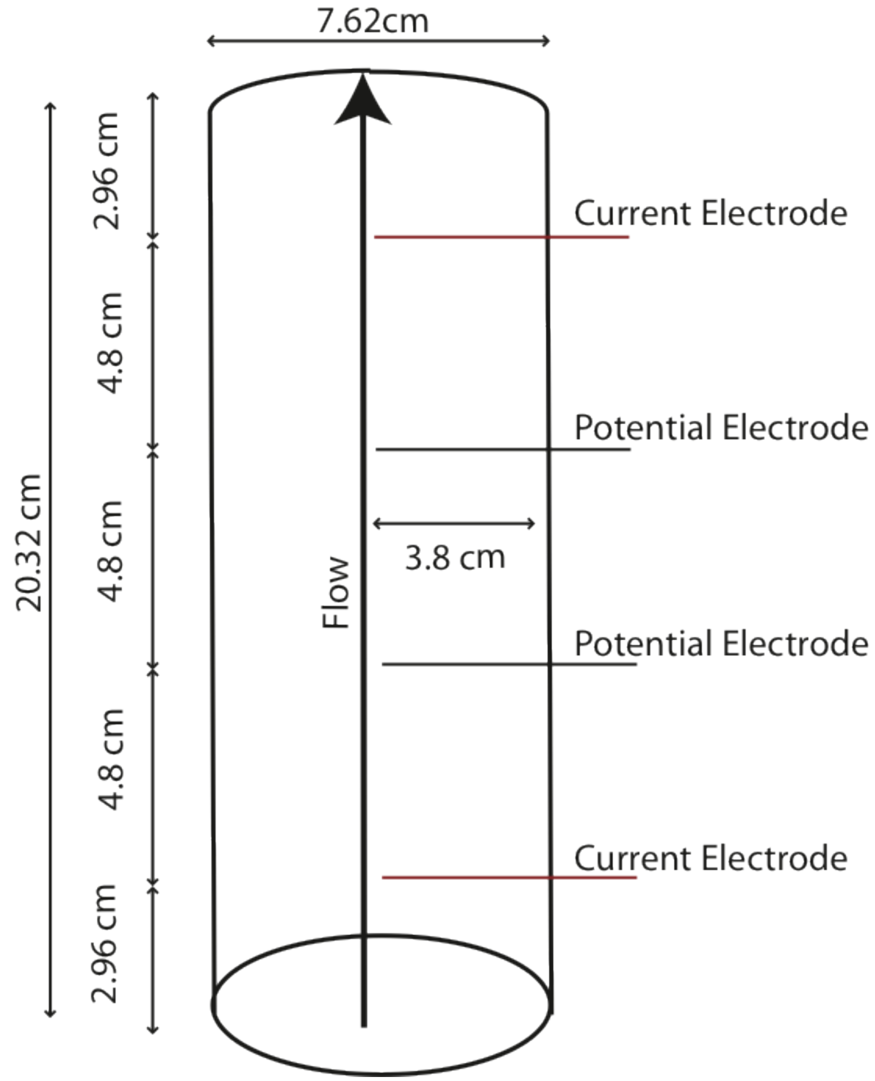

Figure. 2.1: Schematic of the column reactor. Electrodes were Ag/AgCl wires encased in glass tubes and were only conductive at the tip.

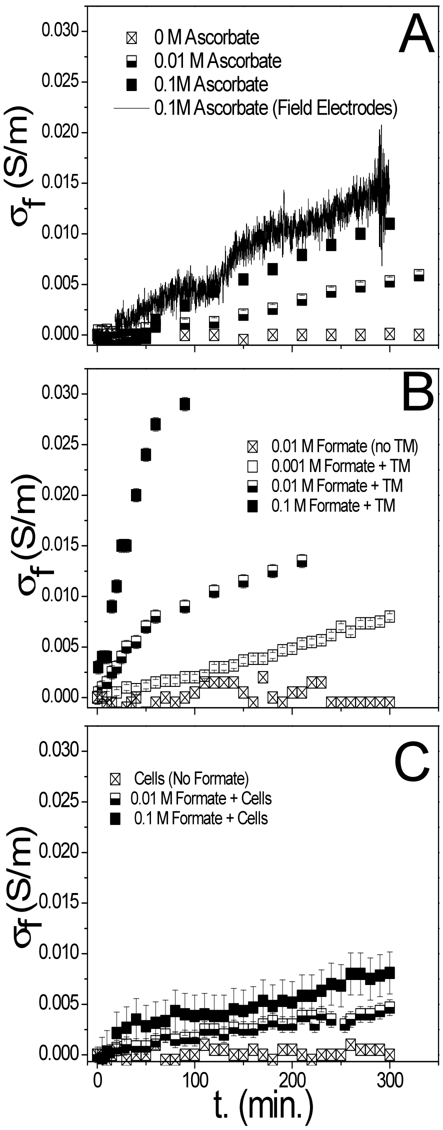

Figure. 2.2 Temporal evolution of measured fluid electrical conductivity (σf, S/m) during goethite reduction for abiotic (A), *in vitro* (B), and *in vivo* (C) batch experiments. All symbols represent data measured with laboratory conductivity meter unless otherwise indicated. The initial increases in conductivity observed in the abiotic experiments were from 1.18 – 4.25 x10^{-5} S min^{-1} changes *in vitro* were in the range 2.63 – 37.6 x10^{-5} S min^{-1}, while rates *in vivo* varied from 2.0 - 3.0 x10^{-5} S min^{-1}. Error bars indicate one standard deviation around the mean for replicate experiments; where no error bars are shown, standard deviations are smaller than symbols. *In vitro* rates were

measured with fragments of the total membrane, TM, fraction of *Shewanella* cells as described in text while *in vivo* rates were measured in the presence of cultures of *Shewanella*. No reduction was observed for controls without ascorbate (A), TM (B), or formate (C). Note that σ_f was adjusted to plot at 0 for time 0 in each experiment.

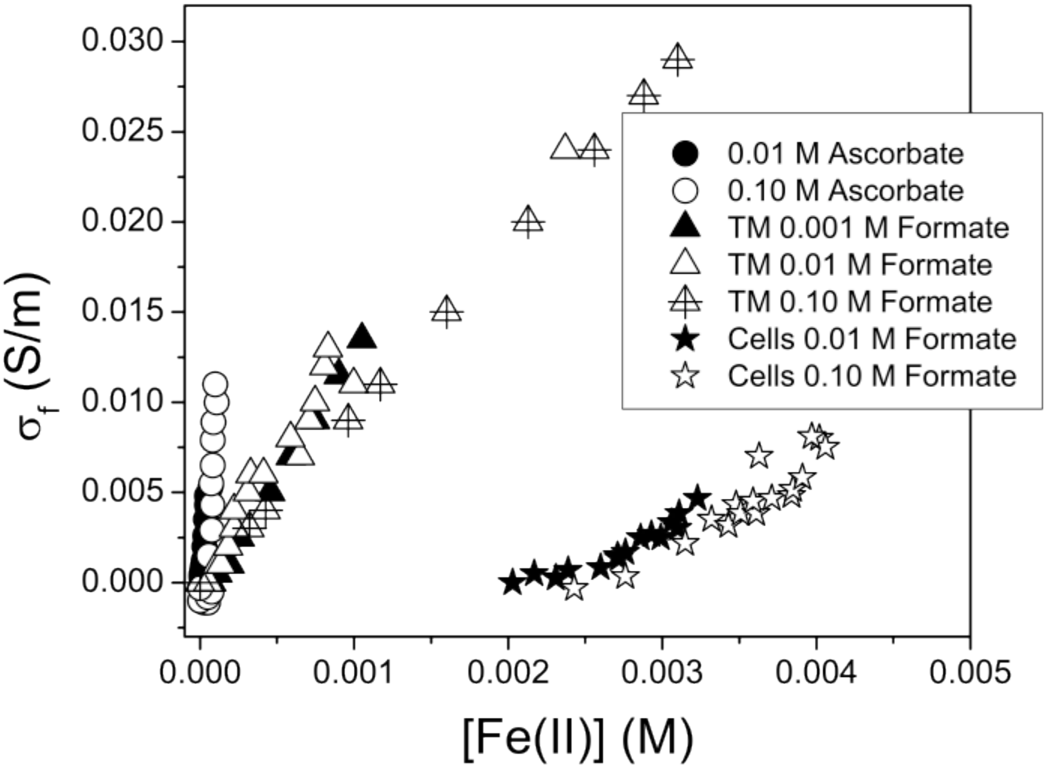

Figure. 2.3: σ_f increases as $[Fe(II)_{aq}]$ increases in abiotic (circles), *in vitro* (triangles), and *in vivo* (stars) batch experiments. The slope of σ_f (S/m) versus $[Fe(II)_{aq}]$ is a reflection of the reaction stoichiometry of each type of experiment (see equation 6). In all cases, σ_f measured at the start of the experiment has been corrected to start at 0.

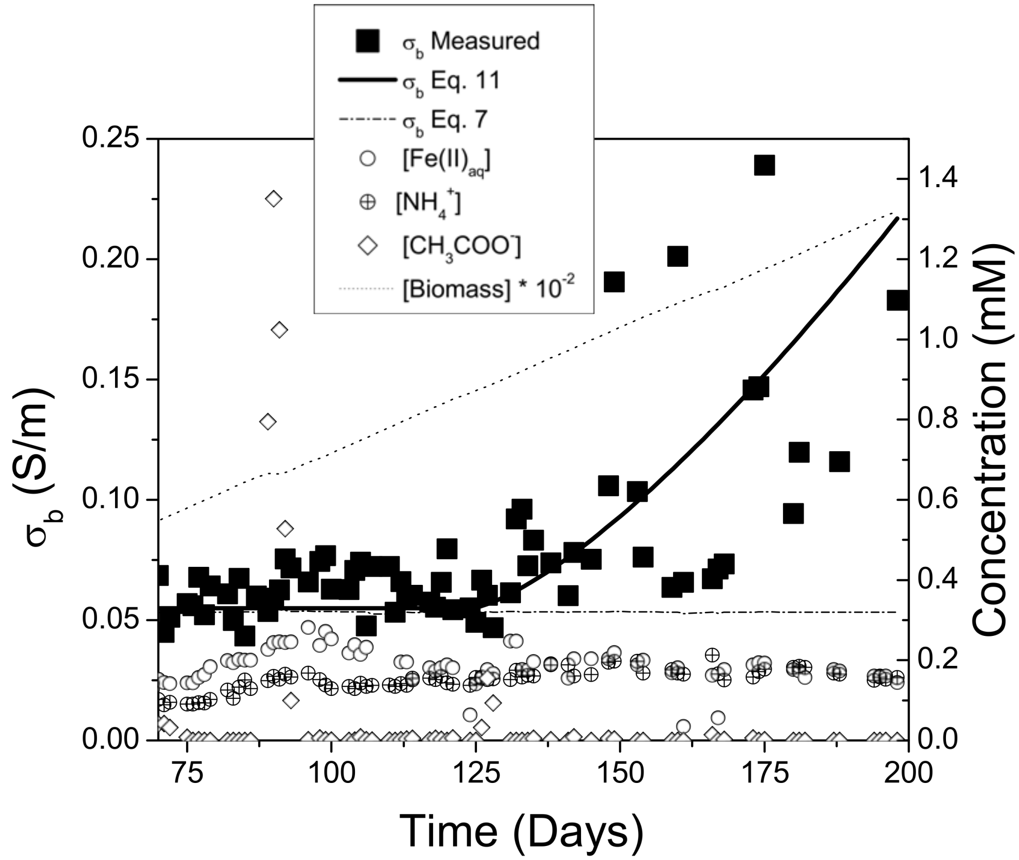

Figure. 2.4: Values of measured σ_b (Squares) plotted versus time for the column experiment. Also shown are measured effluent concentrations of NH_4^+ (crossed circles) acetate (open diamonds) and $Fe(II)_{aq}$ (open circles). Biomass concentration x 10^{-2} is also plotted versus time (dotted line) as calculated from the cumulative consumption of acetate and ammonia and Eq. IV in Table 1. Dash-dotted line indicates σ_b calculated from Eq. 7 based on known effluent chemistry. Solid line indicates σ_b calculated from Eq. 14 as described in the text.

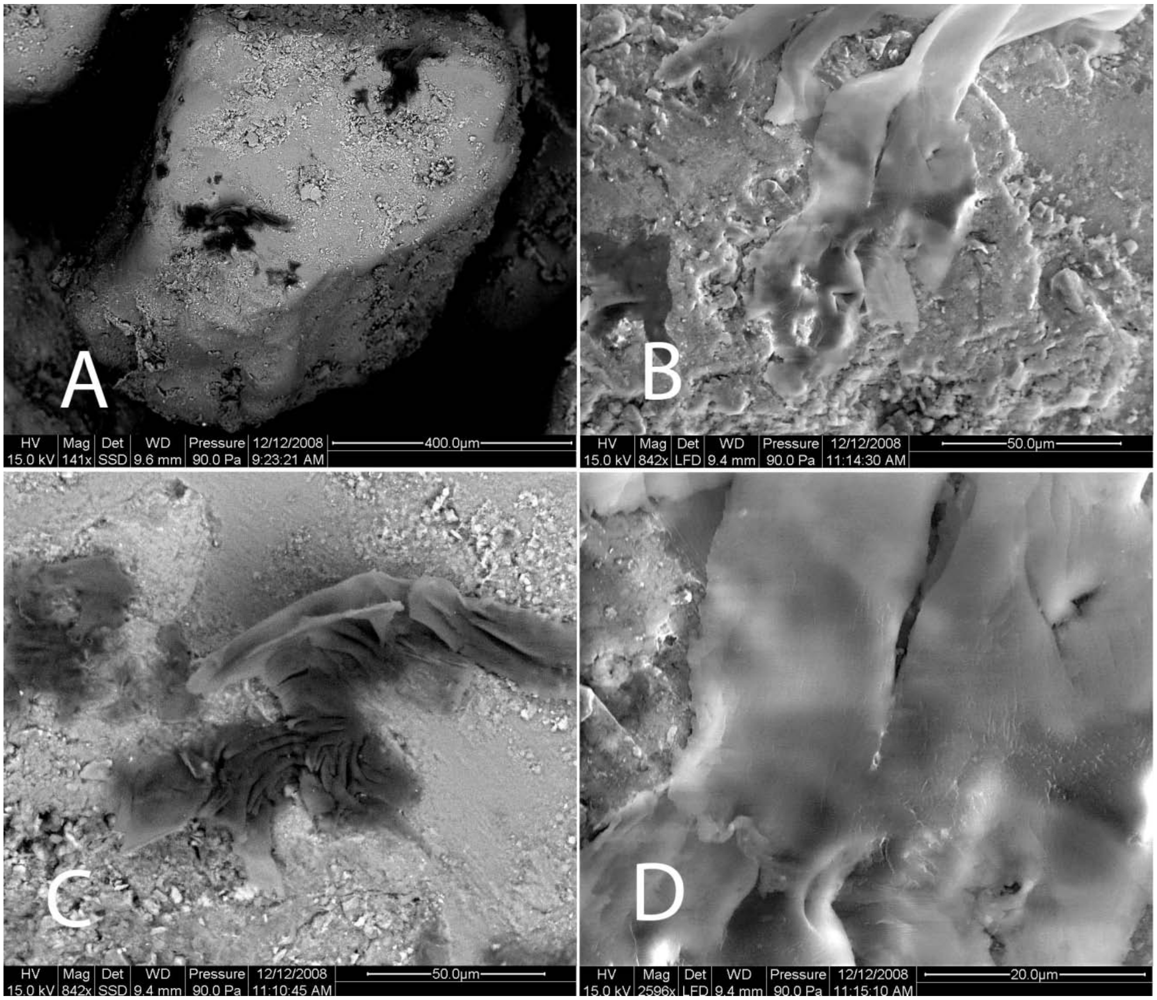

Figure. 2.5: Scanning electron microscope (SEM) images of biofilm patches on sediment grains from the column experiment. In back scattered electron mode, biofilms appear as dark patches (A) due to the high carbon content and low molecular weight. Enlargements of the upper patch (B and D) and the lower patch (C) reveal the surface texture of the biofilms.

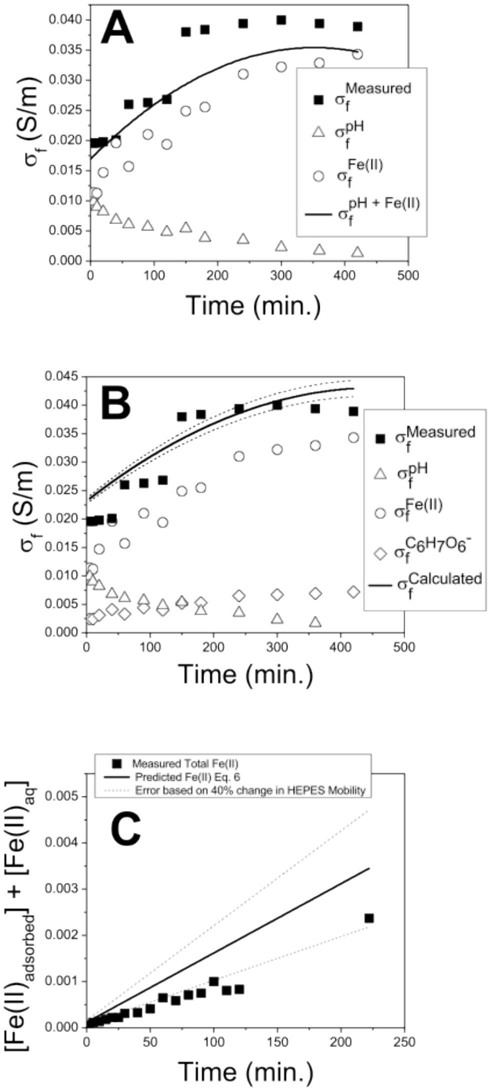

Figure 2.6: Measured σ_f (squares) versus time compared to calculated values (lines) during abiotic reduction of goethite by ascorbate (A,B). In (A), the line sums the contributions to σ_f calculated from changes in measured pH (triangles) and $[Fe(II)_{aq}]$ (circles) only. Calculated values differ slightly from measured values ($R^2 = 0.855$) due to ascorbate speciation, which is neglected in the calculations. A better estimate for σ_f ($R^2 = 0.947$) is shown in (B) when [ascorbate] (diamonds) is included assuming Composite Reaction I (Table 1). (C) Comparison of measured (squares) or calculated (line) $[Fe(II)]_{tot}$ for the *in vitro* experiment (for one replicate

with 0.01M Na-formate) versus time. The calculated value is based on reaction II (Table 1). Ion mobilities were derived from published values [*Landolt-Bornstein*, 1969] or estimated from diffusion constants [*Schwarzenbach et al.*, 2003] (see Table 3). Dashed lines (B, C) represent ±1 standard deviation in this estimate. Background σ_f measured before experiments was subtracted for (A) and (B).

Works Cited

Abdel Aal, G., E. Atekwana, S. Radzikowski, and S. Rossbach (2009), Effect of bacterial adsorption on low frequency electrical properties of clean quartz sands and iron-oxide coated sands, *Geophysical Research Letters*, *36*(L04403).

Abdel Aal, G. Z. G. (2004), Effects of microbial processes on electrolytic and interfacial electrical properties of unconsolidated sediments, *Geophysical Research Letters*, *31*(12).

Abrams, R., and K. Loague (2000), A compartmentalized solute transport model for redox zones in contaminated aquifers 2. Field-scale simulations, *Water Resour. Res.*, *36*(8), 2015-2030.

Allen, J. P., E. A. Atekwana, E. A. Atekwana, J. W. Duris, D. D. Werkema, and S. Rossbach (2007), The microbial community structure in petroleum-contaminated sediments corresponds to geophysical signatures, *Applied and Environmental Microbiology*, *73*(9), 2860-2870.

Archie, G. E. (1942), The electrical reisistivity log as an aid in determining some reservoir characteristics, *Petroleum Transactions of AIME*, *146*, 54-62.

Atekwana, E., E. Atekwana, F. Legall, and R. Krishnamurthy (2004a), Field evidence for geophysical detection of subsurface zones of enhanced microbial activity, *Geophysical Research Letters*, *31*(23), L23603.

Atekwana, E., E. Atekwana, R. Rowe, D. Werkema, and F. Legall (2004b), The relationship of total dissolved solids measurements to bulk electrical conductivity in an aquifer contaminated with hydrocarbon, *Journal of Applied Geophysics*, *56*(4), 281-294.

Atekwana, E. A. E., E. A. Atekwana, D. Werkema, J. P. Allen, L. A. Smart, J. W. Duris, D. P. Cassidy, W. A. Sauk, and S. Rossbach (2004c), Evidence for microbial enhanced electrical conductivity in hydrocarbon-contaminated sediments, *Geophysical Research Letters*, *31*(23), 20.

Balberg, I. (1986), Excluded-volume explanation of Archie's law, *Physical Review B*, *33*(5), 3618-3620.

Bau, M., B. Alexander, J. Chesley, P. Dulski, and S. Brantley (2004), Mineral dissolution in the cape cod aquifer, Massachusetts, USA: I. reaction stoichiometry and impact of accessory feldspar and glauconite on strontium isotopes, solute concentrations, and REY distribution, *Geochim. Cosmochim. Acta*, *68*(6), 1199-1216.

Bennett, P., F. Hiebert, and J. Rogers (2000), Microbial control of mineral–groundwater equilibria: Macroscale to microscale, *Hydrogeology Journal*, *8*(1), 47-62.

Caccavo Jr, F., D. Lonergan, and D. Lovley (1994), *Geobacter sulfurreducens* sp. nov., a hydrogen-and acetate-oxidizing dissimilatory metal-reducing microorganism, *Applied and Environmental Microbiology*, *60*(10), 3752-3759.

Christensen, T., P. Kjeldsen, P. Bjerg, D. Jensen, J. Christensen, A. Baun, H. Albrechtsen, and G. Heron (2001), Biogeochemistry of landfill leachate plumes, *Appl. Geochem.*, *16*(7-8), 659-718.

COMSOL (2008), COMSOL Multiphysics Modeling Guide, 1 - 518.

Cornell, R., and U. Schwertmann (2003), *The Iron Oxides: Structure, Properties, Reactions, Occurences and Uses*, 2nd ed., Wiley-VCH GmbH & Co. KGaA.

Crosby, H. A., C. M. Johnson, E. E. Roden, and B. L. Beard (2005), Coupled Fe(II)-Fe(III) electron and atom exchnage as a mechanism for Fe isotope fractionation during dissimilatory iron oxide reduction, *Environ. Sci. Technol.*, *39*(17), 6698-6704.

Davis, C. A., E. Atekwana, E. Atekwana, L. D. Slater, S. Rossbach, and M. R. Mormile (2006), Microbial growth and biofilm formation in geologic media is detected with complex conductivity measurements, *Geophysical Research Letters*, *33*(18), L18403.

Deutsch, C. (1989), Calculating effective absolute permeability in sandstone/shale sequences, *SPE Formation Evaluation*, *4*(September 1989), 343-348.

Duan, Z., and S. Mao (2006), A thermodynamic model for calculating methane solubility, density and gas phase composition of methane-bearing aqueous fluids from 273 to 523 K and from 1 to 2000 bar, *Geochemica et Cosmochimica Acta*, *70*(2006), 3369-3389.

Freeze, R. A., and J. A. Cherry (1979), *Groundwater*, 604 pp., Prentice Hall, Englewood Cliffs, NJ.

Glover, P., M. Hole, and J. Pous (2000), A modified Archie's law for two conducting phases, *Earth. Planet. Sci. Lett.*, *180*(3-4), 369-383.

Handler, R. M., C. M. Johnson, and M. M. Scherer (2009), Atom exchange between aqueous Fe(II) and goethite: An Fe isotope tracer study, *Environ. Sci. Technol.*, *43*(4), 1102-1107.

Heron, G., C. Crouzet, A. Bourg, and T. Christensen (1994), Speciation of Fe (II) and Fe (III) in contaminated aquifer sediments using chemical extraction techniques, *Environ. Sci. Technol.*, *28*(9), 1698-1705.

Holmes, R., A. Aminot, R. Kérouel, B. Hooker, and B. Peterson (1999), A simple and precise method for measuring ammonium in marine and freshwater ecosystems, *Canadian Journal of Fisheries and Aquatic Sciences*, *56*(10), 1801-1808.

Icopini, G. A., A. D. Anbar, S. S. Reubush, M. Tien, and S. L. Brantley (2004), Iron isotope fractionation during microbial reduction of iron: The importance of adsorption, *Geology*, *32*(3), 205-208.

Johnson, D., T. Plona, and H. Kojima (1987), Probing porous media with 1st sound, 2nd sound, 4th sound, and 3rd sound, *AIP Conference Proceedings*.

Juhasz, I. (1981), Normalized Qv - the key to shaly sand evaluation using the Waxman Smits equation in the absence of core data, *Transactions of the SPWLA 22nd Annual Logging Symposium*(Paper Z).

Kirkpatrick, S. (1973), Percolation and conduction, *Reviews of Modern Physics*, *45*(4), 574-588.

Kjeldsen, P. (1993), Evaluation of gas diffusion through plastic materials used in experimental and sampling equipment, *Water Res.*, *27*(1), 121-131.

Knapp, E., J. Herman, A. Mills, and G. Hornberger (2002), Changes in the sorption capacity of coastal plain sediments due to redox alteration of mineral surfaces, *Appl. Geochem.*, *17*, 387-398.

Knight, R. (1991), Hysteresis in the electrical resistivity of partially saturated sandstones, *Geophysics*, *56*(12), 2139 - 2147.

Knutsson, G. (1966), Tracers for groundwater investigations, paper presented at Groundwater Problems, Pergamon Press, Stockholm Sweden.

Kumler, W. D., and T. C. Daniels (1935), Titration curves and dissociation constants of l-ascorbic acid (vitamin C) and diethyl dihydroxymaleate, *J. Am. Chem. Soc.*, *57*, 1929-1930.

Landolt-Bornstein (1969), *Numerical data and functional relationships in science and technology*, Sixth Edition ed., Springer-Verlag.

Liermann, L., A. Barnes, B. Kalinowski, X. Zhou, and S. Brantley (2000), Microenvironments of pH in biofilms grown on dissolving silicate surfaces, *Chem. Geol.*, *171*(1-2), 1-16.

Little, B., P. Wagner, R. Ray, R. Pope, and R. Scheetz (1991), Biofilms: an ESEM evaluation of artifacts introduced during SEM preparation, *J. Ind. Microbiol. Biotechnol.*, *8*, 213-222.

Lovley, D., and E. Phillips (1986), Organic matter mineralization with reduction of ferric iron in anaerobic sediments, *Applied and Environmental Microbiology*, *51*(4), 683-689.

Lovley, D., and E. Phillips (1988), Novel mode of microbial energy metabolism: organic carbon oxidation coupled to dissimilatory reduction of iron or manganese, *Applied and Environmental Microbiology*, *54*(6), 1472.

Marsili, E., D. Baron, I. Shikhare, D. Coursolle, J. Gralnick, and D. Bond (2008), *Shewanella* secretes flavins that mediate extracellular electron transfer, *Proceedings of the National Academy of Sciences*, *105*(10), 3968.

Nielsen, L. P., N. Risgaard-Petersen, H. Fossing, P. B. Christensen, and M. Sayama (2010), Electric currents couple spatially separated biogeochemical processes in marine sediment, *Nature*, *463*(7284), 1071-1074.

Ntarlagiannis, D., N. Yee, and L. Slater (2005), On the low-frequency electrical polarization of bacterial cells in sands, *Geophysical Research Letters*, *32*(24).

Ntarlagiannis, D., E. Atekwana, E. Hill, and Y. Gorby (2007), Microbial nanowires: Is the subsurface “hardwired”?, *Geophysical Research Letters*, *34*(17), L17305.

Or, D., S. Phutane, and A. Dechesne (2007), Extracellular polymeric substances affecting pore-scale hydrologic conditions for bacterial activity in unsaturated soils, *Vadose Zone Journal*, *6*(2), 298-304.

Parkhurst, D. L., and C. Appelo (1999), User's guide to PHREEQC (Version 2) - A Computer program for speciation, batch-reaction, one-dimensional transport, and inverse geochemical calculations, *Water-Resources Investigations Report*, *99-4259*.

Penn, R. L., C. Zhu, H. Xu, and D. R. Veblen (2001), Iron oxide coatings on sand grains from the Atlantic coastal plain: High-resoltuion transmission electron microscopy, *Geology*, *29*(9), 843-846.

Ramasamy, R. P., Z. Ren, M. M. Mench, and J. M. Regan (2008), Impact of initial biofilm growth on the anode impedance of microbial fuel cells, *Biotechnol. Bioeng.*, *101*(1), 101-108.

Reguera, G., K. D. McCarthy, T. Mehta, J. S. Nicoll, M. T. Tuominen, and D. R. Lovely (2005), Extracellular electron transfer via microbial nano-wires, *Nature*, *453*(23).

Revil, A., and P. W. J. Glover (1997), Theory of ionic-surface electrical conduction in porous media, *Phys. Rev. B: Condens. Matter*, *55*(3), 1757-1773.

Revil, A., L. Cathles III, S. Losh, and J. Nunn (1998), Electrical conductivity in shaly sands with geophysical applications, *Journal of Geophysical Research-Solid Earth*, *103*(B10).

Revil, A., and P. Glover (1998), Nature of surface electrical conductivity in natural sands, sandstones, and clays, *Geophysical Research Letters*, *25*(5), 691-694.

Rittmann, B. E., and P. L. McCarty (2001), *Environmental Biotechnology: Principles and Applications*, 754 pp., McGraw Hill, Boston.

Roden, E., and D. Lovley (1993), Dissimilatory Fe (III) reduction by the marine microorganism *Desulfuromonas acetoxidans*, *Applied and Environmental Microbiology*, *59*(3), 734-742.

Ruebush, S., G. Icopini, S. Brantley, and M. Tien (2006), *In vitro* enzymatic reduction kinetics of mineral oxides by membrane fractions from *Shewanella oneidensis* MR-1, *Geochim. Cosmochim. Acta*, *70*(1), 56-70.

Rzhevskii, V. V., V. B. Dobretsov, and V. S. Yamshcikov (1965), Investigation of the effect of temperature on the physical properties of siderite ores for the purpose of selecting the parameters of low-frequency rock breaking, *Journal of Mining Science*, *1*(2), 116-118.

Sauck, W. (2000), A model for the resistivity structure of LNAPL plumes and their environs in sandy sediments, *Journal of Applied Geophysics*, *44*, 151-165.

Scheibe, T., Y. Fang, C. Murray, and E. Roden (2006), Transport and biogeochemical reaction of metals in a physically and chemically heterogeneous aquifer, *Geosphere*, *2*(4), 220-235.

Schwartz, L. M., P. N. Sen, and D. L. Johnson (1989), Influence of rough surfaces on electrolytic conduction in porous media, *Phys. Rev. B: Condens. Matter*, *440*(4), 2450-2458.

Schwarzenbach, R. P., P. M. Gschwend, and D. M. Imboden (2003), *Environmental Organic Chemistry*, 2nd. ed., 1313 pp., Wiley-Interscience, Hoboken.

Sen, P., and P. Goode (1992), Influence of temperature on electrical conductivity on shaly sands, *Geophysics*, *57*(1), 89-96.

Serra, O., and L. Serra (2005), *Well Logging Data Acquistion and Applications*, 674 pp., Serra Log, Corbon France.

Slater, L. D., F. D. Day-Lewis, D. Ntarlagiannis, M. O'Brien, and N. Yee (2009), Geoelectrical measurement and modeling of biogeochemical breakthrough behavior during microbial activity, *Geophysical Research Letters*, *36*.

Stookey, L. L. (1970), Ferrozine- a new spectrophotometric reagent for iron, *Anal. Chem.*, *42*(7), 779-781.

Sundararaj, S., A. Guo, B. Habibi-Nazhad, M. Rouani, P. Stothard, M. Ellison, and D. S. Wishart (2004), The cybercell database (CCDB): a comphrehensive, self-updating, relational database to coordinate and facilitate *in silico* modeling of *escherichia coli*, *Nucleic Acids Res.*, *32*, D293-D295.

Thullner, M., J. Zeyer, and W. Kinzelbach (2002), Influence of microbial growth on hydraulic properties of pore networks, *Transport in Porous Media*, *49*, 99-122.

Torres, C. I., A. K. Marcus, P. Parameswaran, and B. E. Rittmann (2008), Kinetic experiments for evaluating the Nernst-Monod model for anode-respiring bacteria (ARB) in a biofilm anode, *Environ. Sci. Technol.*, *42*, 6593-6597.

Tronc, E., J.-P. Jolivet, J. Lefebvre, and R. Massart (1984), Ion adsorption and electron transfer in spinel-like iron oxide colloids, *J. Chem. Soc.*, *80*, 2619-2629.

Urrutia, M. M., E. E. Roden, J. K. Fredrickson, and J. M. Zachara (1998), Microbial and surface chemistry controls on reduction of synthetic Fe(III) oxide minerals by the dissimilatory iron-reducing bacterium *Shewanella alga*, *Geomicrobiol. J.*, *15*(4), 269-291.

Vanhala, H., and H. Soininen (1995), Laboratory technique for measurement of spectral induced polarization response of soil samples, *Geophysical Prospecting*, *43*(5), 655-676.

Violier, E., P. Inglett, K. Hunter, A. Roychoudhury, and P. V. Capellen (2000), The ferrozine method revisited: Fe(II)/Fe(III) determination in natural waters, *Appl. Geochem.*, *15*, 785-790.

Wang, M., A. Dorward, D. Vlaev, and R. Mann (2000), Measurements of gas-liquid mix in a stirred vessel using electrical resistance tomography (ERT), *Chem. Eng. J.*, *77*, 93-98.

Waxman, M. H., and L. J. M. Smits (1968), Electrical conductivities in oil-bearing sands, *Society of Petroleum Engineers Journal*, *8*, 102-122.

Werkema, D. D., E. A. Atekwana, A. L. Endres, W. A. Sauck, and D. P. Cassidy (2003), Investigating the geoelectrical response of hydrocarbon contamination undergoing biodegradation, *Geophysical Research Letters*, *30*(12), 1647.

White, A., T. Bullen, D. Vivit, M. Schulz, and D. Clow (1999), The role of disseminated calcite in the chemical weathering of granitoid rocks, *Geochim. Cosmochim. Acta*, *63*(13/14), 1939-1953.

Williams, A. G. B., and M. M. Scherer (2004), Spectroscopic evidence for Fe(II)-Fe(III) electron transfer at the iron oxide-water interface, *Environ. Sci. Technol.*, *38*, 4782-4790.

Zinder, B., G. Furrer, and W. Stumm (1986), The coordination chemistry of weathering: II. Dissolution of Fe (III) oxides, *Geochim. Cosmochim. Acta*, *50*(9), 1861–1869.

Chapter 3

MODELING BIOFILM CONDUCTIVITY WITH REACTIVE TRANSPORT MODELS

Introduction

Recent experimental evidence is consistent with the hypothesis that biofilms have unique electrical properties. Several authors have suggested that microbial biofilms are more electrically conductive than their surroundings [e.g., *Atekwana et al.*, 2004; *Reguera et al.*, 2005; *Torres et al.*, 2008, *Regberg et al.*, in press]. Other researchers have noticed that biofilms affect surface conductivity and or the imaginary component of complex conductivity [*Davis et al.*, 2006; *Abdel-Aal et al.*, 2009; *Abdel-Aal et al.*, 2010]. If biofilms are more electrically conductive than their surroundings, it may be possible to monitor biogeochemical activity using measured changes in bulk electrical conductivity (σ_b). This would be helpful because measurements of σ_b are generally faster and cheaper than many geochemical sampling and analysis methods used to monitor changes in sub-surface biogeochemistry. However, direct measurements of the electrical conductivity of biofilms have been unsuccessful, because natural and laboratory grown biofilms are difficult to observe in a non-destructive manner [e.g., *Torres et al.*, 2008]. In Chapter 2, (see also *Regberg et al.* [in press]) we observed that σ_b measurements across a column reactor containing Fe-reducing bacteria began to increase after 120 days of continuous input of an acetate-containing artificial groundwater. After 198 days σ_b measurements had increased by a factor of 3 without any corresponding changes in ionic concentrations in the effluent from the column; we suggested that microbial biofilms and/or Fe(II) adsorption onto Fe(III) oxide coated sediments may have affected measured σ_b.

In this chapter we make similar measurements using a new flow-through column reactor and demonstrate that Fe(II) adsorption has little or no effect on σ_b. We use reactive transport modeling to constrain the processes described by the data set in Chapter 2 (*Regberg et al.* [in press]), and to better estimate the effect a conductive biofilm would have on macroscopic electrical conductivity measurements of a column reactor. The estimates of reaction rates, biomass production rates, and biofilm electrical conductivity in Chapter 2 were based on steady-state assumptions. Specifically, transient effects and concentration gradients along the length of the column were not explicitly incorporated into the conceptual model used in Chapter 2. Using a reactive transport model allows us to explicitly model concentration gradients and should result in better predictions of total biomass growth.

This new modeling treatment represents a next step in the use of changes in σ_b to monitor microbial activity. Specifically, we use reactive transport modeling to estimate the extent of biomass growth in a flow-through column reactor containing an environmental consortium of dissimilatory iron-reducing (DIRB) and methanogenic bacteria. Additionally, an electrical model is used to estimate the electrical conductivity of that biomass. While the models are non-unique, they provide a starting point for future research focused on quantifying the electrical conductivity of biofilms.

Methods

Fe-reducing column reactor

To investigate the effect of biofilm growth on σ_b we set up a flow-through column reactor inoculated with a mixed culture of bacteria from Dorn Creek in Madison, WI. Anaerobic influent pumped into the reactor was amended with 1 mM Na-acetate to encourage the growth of dissimilatory iron reducing bacteria (DIRB). This is the same reactor discussed in Chapter 2. The reactor was constructed and maintained by Flynn Picardal and Quanxing Zheng at Indiana University. The reactor, an acrylic tube 20.3 cm long with a 7.6 cm inner diameter and walls 1.27 cm thick was packed with 1552 g of air-dried, sieved, coastal-plain sediment from Oyster, VA. This sediment has been well characterized previously and shown to contain 77 wt. % quartz, 21 wt. % feldspar, and 2 wt. % Fe present primarily as iron-oxide coatings [*Penn et al.*, 2001]. Prior to packing the column the sediment was mixed in a 9:1 ratio by mass with a microbial inoculum of shallow-subsurface sediment from Dorn Creek in Madison, WI. The ends of the column were loosely packed with glass wool to inhibit the migration of fine particles out of the column [*Regberg et al.,* in press]. The initial effective porosity was calculated to be 0.33. Effective porosity was measured by pumping a NaBr tracer through the column at a known flow rate. The amount of time necessary for 50% of the tracer's mass to pass through the column was used to calculate the effective porosity [*Knutsson*, 1966; *Freeze and Cherry*, 1979]. A sterile, anoxic solution of PIPES-buffered artificial groundwater (PBAGW) containing NaCl (0.15 g L^{-1}), $CaCl_2$ (0.30 g L^{-1}), $MgCl_2$-$6H_2O$ (0.50 g L^{-1}), KH_2PO_4 (0.006 g L^{-1}), NH_4Cl (0.01 g L^{-1}), PIPES (3.35 g L^{-1}), trace elements and vitamins was amended with 1 mM Na-acetate. The PBAGW was pumped upwards through Teflon tubing into the reactor at 2 ml hr^{-1} using a glass, gas-tight syringe pump. The reactor was presumed to be gas tight and was maintained on the bench top. All the effluent from the reactor was collected daily in N_2-purged tubes and was used to confirm the flow rate by weighing each sample. Effluent samples were analyzed for concentrations of acetate ($[\text{acetate}]_{out}$), using high performance liquid chromatography; Fe(II) ($[Fe(II)_{(aq)}]_{out}$) using ferrozine [*Stookey*, 1970; *Violier et al.*, 2000]; and NH_4^+ ($[NH_4^+]_{out}$) using *o*-phthaldialdehyde [*Holmes et al.*, 1999].

At the conclusion of the 198-day experiment, adsorbed Fe(II) and Fe(II) precipitated within the column as siderite were measured using a 0.5 N HCl and a 1 N HCl extraction respectively. For the first extraction, three 10 g samples of the column sediments were taken from different sections along the length of the column. Each sample was incubated for 24 hours in the presence of 0.5 N HCl. The concentration of Fe(II) measured in the HCl solutions after this extraction was attributed to adsorbed Fe(II) following *Heron et al.* [1994]. To quantify the amount of siderite precipitated, an additional 10 g sample of sediment was taken from the sediment within 10 cm of the inlet, washed with acetone and was incubated with 10 ml of 1 N HCl for 24 hours in a sealed vessel under a N_2 atmosphere. The concentrations of Ca, Mg, P and Fe(II) were measured in the HCl solution and the concentration of CO_2 was measured in the head space. Details of this extraction can be found in Chapter 2 (*Regberg et al.* [in press]) as modified from *White et al.* [1999].

Non-invasively quantifying the amount of biomass produced in a column reactor is very difficult [e.g., *Characklis*, 1990; *Costerton et al.*, 1995; *Thullner*, 2010]. Here, we use chemical measurements of nutrient consumption to calculate a growth yield and estimate the rate and extent of biomass growth. The estimated biomass is used to calculate a biomass electrical conductivity necessary to explain the measured increase in σ_b. During this experiment, we measured an almost 3 fold increase in σ_b (0.055 S/m to 0.2 S/m) and we attributed this increase to either sorption of Fe(II) or biofilm growth [*Regberg et al.,* in press]. To test the first hypothesis we designed an abiotic column reactor experiment described below and used it to measure the effect of Fe(II) adsorption on σ_b.

Abiotic column reactor

The abiotic column reactor, made of PVC pipe 30 cm long with an inner diameter of 6 cm and walls 1 cm thick, was constructed and maintained at Penn State. The column was filled with 12/20 Accusand, a commercially available quartz sand with a uniform particle size of 1.1 ± 0.01 mm [*Schroth et al.*, 1996]. The Accusand was synthetically coated with goethite by repeatedly allowing a continuously stirred solution of dissolved 0.05 M $FeCl_2$ to oxidize in the presence of 665 g/L sand and 0.1M $NaHCO_3$ for 48 hours [*Schwertmann and Cornell*, 2000]. This procedure was repeated 6 times for each batch of sand. This coated Accusand is similar physically and mineralogically to the Oyster sediment (i.e. little or no organic matter, predominantly quartz mineralogy). The column was sealed with 50-mm diameter Teflon end caps (Omnifit, Inc.). The caps have butyl-rubber o-rings to form an air-tight seal and Teflon frits with a pore size of 10 μm to ensure uniform flow and prevent particle migration. This column reactor was assembled and maintained inside a Coy Labs anaerobic chamber under a 95% N_2, 5% H_2 atmosphere. The initial effective porosity of the abiotic column was 0.40 ± 0.02 as measured by repeatedly packing test columns with Accusand and measuring the mass of water needed to saturate the column.

No micro-organisms were added to the abiotic reactor. Every appropriate effort was made to limit introduction and or growth of such organisms within the column. The sand in this reactor was sterilized with UV light for 12 hours, but was not autoclaved in order to avoid altering the mineralogy of the synthetic goethite coatings. The autoclaved, PBAGW without Na-acetate was pumped upwards through Tygon tubing at 3 ml hr^{-1} with a Cole-Parmer peristaltic pump. Any organisms that were alive in the reactor despite the UV treatment must have been severely carbon-limited and unable to grow quickly or at all.

After 80 days of flow, when σ_b measurements along the column had remained constant (~ 0.05 S/m) for about 40 days, $FeCl_2$ was added to the PBAGW to attain 1.2 mM $FeCl_2$ to investigate the effect of iron adsorption on σ_b. All of the effluent was collected in sealed N_{2}-purged vials doped with 0.4 ml of 12 N HCl. Effluent was analyzed for $[Fe(II)_{(aq)}]_{out}$ using ferrozine and $[NH_4^+]_{out}$ using *o*-phthaldialdehyde [*Holmes et al.*, 1999]. Effluent fluid electrical conductivity (σ_f) was also measured daily with an in-line conductivity electrode from Microelectrodes Inc. A 1 ml aliquot was collected prior to acidification for pH measurements with an Orion pH electrode.

Electrical conductivity methods

Direct-current electrical conductivity was measured on the Fe-reducing column and complex conductivity was measured on the abiotic column. For these measurements, an electrical current of known magnitude is injected between two electrodes and the resulting voltage is measured between the other two electrodes. According to Ohm's law, the imposed current divided by the measured voltage is the conductance, *S*. Conductance can be converted to conductivity if the geometric factor κ is known for the system:

$$\sigma_b = \kappa^{-1} S \,. \tag{3.1}$$

Here, σ_b is the bulk electrical conductivity in a D.C. measurement measured in S/m, the geometric factor κ is measured in m, and the conductance S is measured in Siemens. For the Fe-reducing column, a value of κ = 10.7 m was determined by modeling the column with the software package COMSOL Multiphysics [*COMSOL*, 2008]. To calculate κ, a numerical model of the column was constructed in COMSOL and assigned a σ_b value of 1 S/m. The geometric factor calculated is independent of the σ_b of the model domain. We chose σ_b to simplify the calculation of κ. A 1-A current was induced across the current electrodes and the voltage drop was modeled across the voltage electrodes. Simulated conductances were compared to the known σ_b of the column to calculate κ. κ for the abiotic column was calculated in an identical manner and varied between 20 and 10 m for different voltage pairs (Fig. 3.1B).

The value of σ_b for a water-saturated, unconsolidated sediment is related to σ_f via the following empirical equation:

$$\sigma_b = a^{-1}\sigma_f\phi^m \tag{3.2}$$

where ϕ is the porosity and a and m are non-dimensional parameters related to tortuosity and cementation [*Archie*, 1942]. For unconsolidated sediments, a has been observed to vary between 0.62-3.5 and m between 1.37-1.95 [*Balberg*, 1986].

Measurements of D.C. conductivity depend upon the type of electrical current imposed. Despite the name, D.C. conductivity measurements use a very low-frequency alternating current (between 0.5 and 2 Hz) [*Binley and Kemna*, 2007]. In contrast, complex conductivity is measured using alternating current imposed at multiple frequencies. We measured the real component of the complex conductivity rather than the DC conductivity on the abiotic column to control for surface conductivity that may have been produced as Fe(II) sorbed onto mineral surfaces. Fe(II) adsorption affects the surface conductivity and thus imaginary component of the complex conductivity*[e.g.,'Lesmes and Frye, 2001],.*

To make the D.C. conductivity measurements in the Fe-reducing column reactor, four electrodes were inserted into the center of the column reactor containing the microbial inoculum (Fig. 3.1A). The electrodes consist of Ag/AgCl wire inside a glass tube filled with KCl saturated agar. σ_b was measured by injecting current (0.1-0.2 mA) across the outer two electrodes and measuring the resulting voltage across the inner two electrodes with an IRIS Syscal R2E resistivity meter. Measured voltage was converted to conductance in Siemens using Ohm's law. Conductance was then converted to σ_b using Eq. 3.1.

Complex conductivity was measured on the abiotic column with a Radic Research SIPLab II instrument. Current was injected at the following 24 frequencies: 12, 6, 3, and 1.5 kHz, 750, 375, 187.5, 93.75, 46.875, 23.437, 11.7188, 5.859, 2.927, 1.465, 0.732, 0.366, and 0.183 Hz, and 91.5, 45.8, 22.8, 11.4, 5.7, 2.8, and1.4 mHz. Voltage measurements were converted to conductivities using Ohm's law and Eq. 3.1. In the abiotic column, a spiral coil of Ag/AgCl wire was placed inside the reactor at the top and bottom of the column flush with the end-caps (Fig. 3.1B). These coils were used as current electrodes to obtain a more uniform current density necessary for complex conductivity measurements [*Sumner*, 1976; *Vanhala and Soininen*, 1995]. With this more uniform current density, it was not necessary to position the potential electrodes in the center of the column [*Sumner*, 1976; *Vanhala and Soininen*, 1995]. Instead, eight Ag/AgCl electrodes identical to those used in the Fe-reducing column were inserted into the abiotic column until they were just touching sediment. The electrodes were positioned in two rows on opposite sides of the column and were evenly spaced every 5 cm along the length of the column starting 7.5 cm from the inlet.

Yield coefficients

Biomass growth in the Fe-reducing column was estimated using the concept of yield coefficients [*Rittmann and McCarty*, 2001]. The yield coefficient, γ (unitless), is used for a substrate such as acetate that is consumed by cellular respiration and maintenance as well as for generating new biomass. The yield coefficient relates the amount of substrate consumed to the amount of biomass produced. The value can range from 0 when 100% of the substrate is used for cellular respiration and maintenance to a value closer to 1 when almost all of the substrate is used to produce new biomass. Here, the yield coefficient is estimated by comparing the relative rates of NH_4^+ and acetate consumption. Acetate is consumed for both cellular respiration and biomass growth, but NH_4^+ is consumed only for new biomass growth [*Rittmann and McCarty*, 2001]. For an experimental system with substrate concentration ([substrate], in this case, acetate) and biomass concentration, [biomass], the yield coefficient relates the rate of change in the concentration of the substrate, $R_{substrate}$, to the rate of change in concentration of biomass, $R_{biomass}$:

$$\begin{aligned} R_{biomass} &= \frac{d[biomass]}{dt} \\ R_{substrate} &= \frac{d[substrate]}{dt} \\ R_{biomass} &= -\gamma \nu R_{substrate} \end{aligned} \quad . \qquad (3.3\ \text{a,b})$$

Here *[biomass]* is expressed as moles $C_5H_7O_2N$ L^{-1}, and ν (dimensionless) is the stoichiometric coefficient relating biomass growth to substrate (acetate) consumption (i.e. $v = 0.05/0.125$ for Eq. 3.4) [*Rittmann and McCarty*, 2001]. We assume the following chemical reaction to represent biomass growth and acetate consumption [*Rittmann and McCarty*, 2001]:

$$0.05NH_4^+ + 0.125CH_3COO^- + 0.075H^+ \rightarrow 0.05C_5H_7O_2N + 0.15H_2O \ . \qquad (3.4)$$

To estimate a value for the yield coefficient we used the following method. In the Fe-reducing column, $R_{substrate}$ and $R_{biomass}$ are constant in time when the effluent concentrations of ammonia are constant. These rates for the entire column were estimated as follows:

$$\begin{aligned} R_{ammonia} &= Q([NH_4^+]_{out} - [NH_4^+]_{in}) \\ R_{acetate} &= Q([acetate]_{out} - [acetate]_{in}) \end{aligned} \quad . \qquad (3.5\ \text{a,b})$$

Here $R_{ammonia}$ and $R_{acetate}$ are the estimates of rates of ammonia and acetate consumption respectively (µmol day^{-1}), Q is the flow rate (L day^{-1}), and $[x]_{in}$ and $[x]_{\mathrm{out}}$ are the influent and effluent concentrations of species x (M). Since NH_4^+ is only consumed by biomass growth, and acetate is consumed by both biomass growth and respiration [*Rittmann and McCarty*, 2001], we can use the steady state rates of NH_4^+ and acetate consumption and the stoichiometry from Eq. 3.4 to estimate γ for the Fe-reducing column using equation 3.3b:

$$\gamma = \frac{R_{ammonia}}{R_{acetate}} \frac{0.125}{0.05} \qquad (3.6)$$

For example, using the steady-state rates for NH_4^+ and acetate consumption (1.8 μmol NH_4^+ day^{-1} and 39.1 μmol acetate day^{-1}) calculated in Chapter 2 (*Regberg et al.* [in press]), γ = 0.12 for the Fe-reducing column reactor. Every mole of acetate consumed produces 0.048 moles of biomass (5.42 g). However, this coefficient (γ = 0.12) is only an estimate based on the net rate expressions in Eqs. 3.6 a and b, and does not take into account how the rate and extent of reaction change along the length of the column.

Reactive transport modeling

Changes in chemistry within the column and their relationship to the amount of biomass produced were modeled using PHREEQC, an operator-splitting reactive-transport code that models equilibrium as well as kinetic reactions [*Parkhurst and Appelo*, 1999]. We demonstrated the consistency of the PHREEQC model by comparing measured $[Fe(II)_{(aq)}]_{out}$, $[acetate]_{out}$, and $[NH_4^+]_{out}$, total Fe(II) adsorbed and total Fe(II) precipitated as siderite to values calculated with PHREEQC. We used the default database in version 2.17 [*Ball and Nordstrom*, 1991] with the following modifications. Equilibrium redox reactions between $Fe(II)_{aq}$ and $Fe(III)_{aq}$ were removed from the database under the assumption that equilibrium was not attained between these aqueous species. Thirteen reactions were added to the database and are summarized in Table 3.1. Equilibrium conditions were assumed for all chemical reactions occurring within the column except for the five kinetic reactions discussed below.

Dissimilatory iron reduction was modeled with a multiplicative Monod-type rate law that included the concentration of biomass, the concentration of acetate, the availability of surface sorption sites on the sediment, and the Gibbs free energy of the system. The rate law used in our modeling was taken from *Scheibe et al.* [2006]:

$$R_{acetate}^{Fe(III)} = \frac{V_{\max,Fe(III)}[biomass_{DIRB}]([\equiv FeOH^{+}]-[Fe(II)_{adsorbed}])}{K_{m,Biomass}+[biomass_{DIRB}]}\left(\frac{[acetate]}{K_{m,Acetate}+[acetate]}\right) f(\Delta G_{rxn}) \; . \quad (3.7)$$

Here $R_{acetate}^{Fe(III)}$ is the surface area-normalized rate of iron reduction by DIRBs using acetate as an electron donor (moles day^{-1}), $V_{\max,Fe(III)}$ is the maximum surface-area-normalized value of $R_{acetate}^{Fe(III)}$ when the system is saturated with cells (moles (mole sites)$^{-1}$ day^{-1}), $K_{m,Biomass}$ (g cells (dm^3 bulk sediment) $^{-1}$) and $K_{m,Acetate}$ (moles acetate (dm^3 pore fluid)$^{-1}$) are the half-saturation constants for biomass and acetate respectively. Finally, $[biomass_{DIRB}]$ is the concentration of biomass of DIRBs (g DIRB biomass (dm^3 bulk sediment)$^{-1}$). $[acetate]$ is the concentration of acetate (moles acetate (dm^3 pore fluid)$^{-1}$). $[\equiv FeOH^{+}]$ is the concentration of surface sorption sites (mol sites (dm^3 bulk sediment^{-1})). $[Fe(II)_{adsorbed}]$ is the concentration of sorption sites occupied by Fe(II) (mol Fe(II) (dm bulk sediment^{-1})) assuming that each Fe(II) ion occupies one sorption site. The overall rate of reduction decreases as $([\equiv FeOH^{+}]-[Fe(II)_{adsorbed}])$ decreases due to increasing extent of sorption across sediment surfaces in the entire column with time. This is consistent with laboratory experiments that have demonstrated that sorption of Fe(II) onto Fe(III) surfaces can inhibit dissimilatory iron reduction [e.g., *Urrutia et al.*, 1998; *Zachara*, 1998; *Roden*, 2004; *Roden*, 2006]. The final term, $f(\Delta G_{rxn})$ models how the rate varies as function of chemical affinity. As the system approaches equilibrium the reaction rate decreases:

$$f(\Delta G_{rxn}) = 1-\exp((\Delta G_{rxn}-\Delta G_{\min})/RT) \; . \quad (3.8)$$

Here $\Delta G_{\min}$ is the minimum energy required for cellular respiration and is set equal to -20 kJ/mol [*Liu et al.*, 2001]. R is the gas constant (8.314 J K^{-1} mol^{-1}) and T is temperature (K). ΔG_{rxn} is the Gibbs free energy of reaction (kJ/mol):

$$\Delta G_{rxn} = \Delta G^0_{rxn} + RT\ln\left(\frac{\{Fe^{2+}\}^8\{HCO_3^-\}^2}{\{CH_3COO^-\}\{H^+\}^{15}}\right). \tag{3.9}$$

Here ΔG^0_{rxn} is the Gibbs free energy of reaction under biological standard state conditions (pH = 7, standard temperature and pressure), and $\{x\}$ is the activity of species *x* for the chemical reaction representing dissimilatory iron reduction via acetate oxidation:

$$CH_3COO^- + 8FeOOH + 15H^+ \rightarrow 8Fe^{2+} + 2HCO_3^- + 12H_2O. \tag{3.10}$$

As demonstrated in Chapter 2, and in *Regberg et al.* [in press], methanogenesis probably occurred in the column reactors, presumably because methanogens were present in the environmental inoculum. Therefore, another Monod-type rate law was used in PHREEQC to model the rate of acetate consumption via methanogenesis ($R^{CH_4}_{acetate}$) [*Watson et al.,* 2003*]:*

$$R^{CH_4}_{acetate} = \frac{-V_{\max,CH_4}[biomass_{Methanogen}][acetate]}{K_{m,acetate,CH_4} + [acetate]}. \tag{3.11}$$

Here $R^{CH_4}_{acetate}$ is the rate of methane production by methanogens using acetate as electron donor (moles day^{-1}), $V_{\max,CH_4}$ is the maximum rate (day^{-1}), $K_{m,acetate,CH_4}$ is the half saturation constant (mol acetate dm^{-3} pore fluid), and $[biomass_{Methanogen}]$ is the concentration of methanogenic biomass (mol $C_5H_7O_2N$ dm^{-3}).

Given the possibility of methanogenesis, methanogenic biomass growth was treated separately from DIRB. Growth of both microbial populations were modeled using the concept of yield coefficients presented in Eq. 3.6 [*Rittmann and McCarty*, 2001]. In addition to the growth term, a term describing biomass decay was added to Eq. 3.6, following standard practice to create a rate equation for net bacterial growth [e.g., *Parkhurst and Appelo*, 1999; *Rittmann and McCarty*, 2001; *Scheibe et al.*, 2006]:

$$R^{Net}_{biomass,Fe} = \left(-R^{Fe(III)}_{acetate}\gamma\nu\beta\right) - b[biomass_{DIRB}] \tag{3.12}$$

$$R^{Net}_{biomass,CH_4} = -R^{CH_4}_{acetate}\gamma\nu\beta - b[biomass_{Methanogen}]. \tag{3.13}$$

Here $R^{Net}_{biomass,CH_4}$ and $R^{Net}_{biomass,Fe}$ are the rates of methanogenic and iron-reducing biomass growth (g biomass day^{-1}). γ = 0.12 is the yield coefficient calculated using Eq. 3.6 (moles biomass (moles of substrate consumed)$^{-1}$), ν = 0.4 is the stoichiometry of biomass growth from Eq. 3.4, β is the molar mass of biomass expressed as $C_5H_7O_2N$ (113 g mol^{-1}), and *b* is the rate of cell death or inactivation (day^{-1}).

One additional kinetic rate law was used to describe siderite precipitation [*Van-Cappelen and Wang*, 1995; *Hacherl and Kosson*, 2003]:

$$R_{siderite} = k\left(\frac{\{Fe^{2+}\}\{CO_3^{2-}\}}{K_{Siderite}}\right) \tag{3.14}$$

where $R_{siderite}$ is the rate of siderite precipitation (moles day^{-1}), k is the rate constant for siderite precipitation (moles day^{-1}), $\{Fe^{2+}\}$ and $\{CO_3^{2-}\}$ are the activities of Fe(II) and CO_3^{2-} respectively, and $K_{Siderite}$ is the solubility product constant for siderite, $FeCO_3$. Using this equation, the rate of siderite precipitation decreases as conditions approach equilibrium with respect to siderite.

The constants for these kinetic rate laws were obtained from the literature. However, it is common that laboratory measurements of geochemical rate constants differ from those in column or field systems [e.g., *White and Brantley*, 2003]. Therefore, these constants were adjusted until calculated effluent chemistry matched measured effluent chemistry. The adjusted constants along with the literature values (Eqs. 3.7 - 3.14) are compiled in Table 3.2.

In addition, as described further below, a set of cation-exchange reactions was added to the model because without these reactions we were unable to predict the observed changes in $[NH_4^+]_{out}$ between day 0 and day 50. The rationalization for this addition is explained in the discussion section below. The cation-exchange reactions are also compiled in Table 3.1.

In PHREEQC, the column reactor was modeled as twenty cells of length 10.15 mm. Dispersivity parallel to flow was assumed to be 10% of the length of the column reactor, i.e., 0.0203 m. This assumption results in a model that is consistent with measured variations in effluent chemistry. The model was run for 198 days using an initial time step of 7.6 hours. PHREEQC automatically reduces this time step when needed to model dispersion and kinetic reactions [*Parkhurst and Appelo*, 1999].

To model time evolution of species in the reactor, we had to stipulate the initial values of $[biomass_{DIRB}]$ and $[biomass_{Methanogen}]$. The initial concentration of biomass in the reactor was treated as a fitting parameter. We compared model-calculated effluent concentrations from the twentieth column cell to the measured effluent concentrations and adjusted the initial [biomass] until predicted [acetate] for cell 20 was consistent with measured $[acetate]_{out}$ between day 1 and 75 when measured $[acetate]_{out}$ reached steady state. The best-fit initial concentrations equaled 8.7×10^{-4} g biomass $(dm^3 \text{ sediment})^{-1}$ for DIRBs and 1.3×10^{-3} g biomass $(dm^3 \text{ sediment})^{-1}$ for methanogens. These values were chosen on the basis of multiple model runs to achieve adequate simulations of the transient changes in effluent chemistry between days 0 and 70 (Fig. 3.2). In particular, changes in $[acetate]_{out}$ and $[Fe(II)_{aq}]_{out}$ were especially sensitive to initial biomass of DIRBs and $[acetate]_{out}$ was also sensitive to initial biomass of methanogens.

An initial attempt to model the system without including sorption of NH_4^+ or cation exchange between NH_4^+, Na^+ and Fe(II) was unsuccessful. Specifically, peaks in measured $[Fe(II)_{(aq)}]_{out}$ and $[NH_4^+]_{out}$ between days 0 and 70 (Fig. 3.2) were not reproduced when the model did not include NH_4^+ adsorption and NH_4^+, Fe(II) exchange. Therefore, the model was changed to allow both NH_4^+ and Fe(II) to adsorb onto sediment surfaces, and also to exchange Fe(II) for NH_4^+ and Na^+ as the concentration of $Fe(II)_{aq}$ increased. To account for these reactions in the model, it was necessary to model the NH_4^+ sorption/exchange sites separately from the Fe(II) sorption sites: the former were termed exchange sites and the latter termed sorption sites. The initial site densities were set to 0.0877 moles sorption site (dm^3 sediment)$^{-1}$ and 0.0877 moles exchange site (dm^3 sediment)$^{-1}$. The values were set equal to values obtained from previous modeling of sediments from Oyster, VA [*Scheibe et al.*, 2006]. The concentration of exchange sites was treated as an adjustable parameter. Model predictions of $[Fe(II)_{(aq)}]_{out}$ and $[NH_4^+]_{out}$ were compared to measured values of $[NH_4^+]_{out}$ and $[Fe(II)_{(aq)}]_{out}$ between day 0 and day 70 until a best fit value of [exchange sites] was found (Fig. 3.2).

Results

Fe-reducing reactor

The iron-reducing column experiment has already been reported in Ch. 2 [*Regberg et al.*, in press] and only a summary of the results is reproduced here. The measured chemical values have been reported previously. The results from the modeling represent new work. Measured $[Fe(II)_{(aq)}]_{out}$, $[acetate]_{out}$ and $[NH_4^+]_{out}$ in the Fe-reducing column reached constant values (steady state) by day 75. Influent $[Fe(II)_{(aq)}]$ was initially < 5 µM. Effluent $[Fe(II)_{(aq)}]$ was initially < 5 µM and increased to a maximum of 0.282 mM on day 30. By day 50 $[Fe(II)_{(aq)}]_{out}$ decreased to a steady state value of 0.18 mM. Influent [acetate] was 1 mM. Effluent [acetate] was consistently below detection (< 0.05 mM) after day 75.

Influent $[NH_4^+]$ was 0.190 mM. Initial $[NH_4^+]_{out}$ was 0.041 mM and increased to 0.295 mM on day 44. $[NH_4^+]_{out}$ then decreased to steady state values of 0.16 mM by day 75. Variations in $[Fe(II)_{(aq)}]_{out}$, $[NH_4^+]_{out}$, and $[acetate]_{out}$ around day 100 are due to an accidental increase in influent [acetate] from 1 to 10mM (Fig. 3.2).

At the end of the experiment sediment samples were taken from the column and extracted with 0.5 or 1 N HCl. The 0.5 N HCl extraction released 0.0067 mmol Fe(II) (g sediment)$^{-1}$ from the sample taken 4 cm from the inlet and 0.0050 mmol Fe(II) (g sediment)$^{-1}$ from the sample near the outlet of the column, 16 cm from the inlet. The 1 N HCl extraction released 0.0106 mmol Fe(II) (g sediment)$^{-1}$ and 0.039 mmol CO_2 (g sediment)$^{-1}$ for those same two samples respectively. As reported in [*Regberg et al.*, in press] these extractions lead to the conclusion that over the course of the 198 day experiment, an average of 2.05 ± 5.16 mmol sorbed Fe(II) accumulated in the column and 14.4 ± 5.16 mmol of Fe(II) precipitated as siderite. In comparison, the cumulative release of Fe(II) in the effluent over the entire 198 days of the experiment was 1.653 mmoles [*Regberg et al.*, in press].

Regberg et al. [in press] also described a series of mass balance calculations that lead to the conclusion that there was a significant amount of methanogenesis occurring in the Fe-reducing column reactor. In short, too much acetate was consumed and too little Fe(II) produced for dissimilatory iron reduction to be the only respiration pathway. Specifically, up to 60% of the electrons introduced to the column as acetate may have been utilized for methanogenesis.

Measured σ_b in the Fe-reducing column remained constant from day 70 until day 120 at 0.055 S/m. After day 120 σ_b, increased to 0.20 S/m by day 198 (Fig. 3.3). Effluent σ_f as calculated from measured concentrations of ions was constant at 0.281 S/m over the entire 198-day experiment. Influent σ_f calculated in the same manner was 0.281 S/m.

Abiotic column

In the abiotic column, $[Fe(II)_{(aq)}]_{out}$ was below detection until day 87. No $[Fe(II)_{(aq)}]$ was added to the influent before day 80. On day 80 we changed the influent solution by increasing the concentration of Fe(II) in the defined PBAGW to 1.2mM. On day 87 $[Fe(II)_{(aq)}]_{out}$ began to increase rapidly and reached 1.21 mM by day 120. $[Fe(II)_{(aq)}]_{out}$ then decreased to 0.50 mM by day 130 before increasing to 0.94 mM by day 163 (Fig. 3.4).

We also measured $[NH_4^+]_{out}$ to look for evidence of cation exchange involving Fe^{2+}, Na^+ and NH_4^+. Influent $[NH_4^+]$ was 0.190 mM. Initially $[NH_4^+]_{out}$ was ~ 0.010 mM. On day 17 $[NH_4^+]_{out}$ began to increase to 0.140 mM by day 26. After day 26 $[NH_4^+]_{out}$ continued to increase gradually to 0.175 mM by day 60. $[NH_4^+]_{out}$ remained constant around 0.170 mM until day 141 when it began to decrease to 0.032 mM by day 165 (Fig. 3.4). There was no change in $[NH_4^+]_{out}$ as $[Fe(II)_{(aq)}]_{out}$ increased. This result suggests that cation exchange sites may be associated with biofilms.

Real electrical conductivity (σ') measured with the complex conductivity instrumentation for all electrode pairs and frequencies in the abiotic column decreased from an initial value of 0.124 S/m to a steady state value of 0.051 S/m by day 49 (Fig 3.5A). Effluent σ_f showed a similar trend decreasing from initial values around 3500 μS/cm to steady state values around 1300 μS/cm by day 100 (Fig. 3.5). Adding the $FeCl_2$ to the influent on day 80 had no immediate effect on σ'. σ' began to decrease to 0.044 S/m on day 96. σ_f remained constant between 1300 and 1500 μS/cm during this period. There was no change in the imaginary component of the electrical conductivity, which would be sensitive to changes in surface conductivity (this is discussed further in Appendix B).

Discussion

Fe-reducing column

When using a column reactor it is important to note some of the assumptions inherent in interpreting changes in effluent concentrations as reaction rates. For example, we assume that flow rate is constant and uniform within the reactor and move with time. Additionally, reaction fronts that we cannot directly measure may exist inside the reactor. The conclusions that we draw about reaction rates inside the column reactor require inverse modeling and as such are non-unique [*Brantley and Conrad*, 2008]. These caveats do not preclude the use of column reactors, but it is important to be aware of the limitations.

We are able to match steady state effluent concentrations of $Fe(II)_{(aq)}$, NH_4^+ and acetate by using the modified PHREEQC database discussed above with kinetic reactions for acetate consumption via iron reduction (Eq. 3.7), acetate consumption via methanogenesis (Eq. 3.11), biomass growth with a 12% yield (Eqs. 3.12 and 3.13), precipitation of siderite (Eq. 3.14) and equilibrium Fe(II) sorption (Table 3.1). However, this model could not match the transient changes in $[Fe(II)_{(aq)}]_{out}$ and $[NH_4^+]_{out}$ from day 0 until day 75.

For example, the measured increase and subsequent decrease in $[Fe(II)_{(aq)}]_{out}$ between days 0 and 75 is not successfully modeled with the equations we have introduced so far. Most likely, this behavior is related to a nucleation barrier to siderite precipitation, which is not included in the equation for siderite precipitation (Eq. 3.14). Such nucleation initially inhibits mineral precipitation due to the energy required to form solid particles or crystal nuclei from an aqueous solution [e.g. *Steefel and Van-Cappellen*, 1990; *De-Yoreo and Vekilov*, 2003; *Fritz and Noguera*, 2009]. When a solution becomes super-saturated, the rate of generation of nuclei and their rate of growth increases to the extent that net precipitation occurs. For example, *Szramek and Walter* [2004] report that carbonate precipitation does not occur until the system is oversaturated by a factor of 100 (i.e., the saturation index (SI) $SI = \log\left(\frac{\{Fe^{2+}\}\{CO_3^{2-}\}}{K_{sp}}\right)$ = 2) where K_{sp} is the solubility constant for siderite) in a forested watershed in Michigan. Given such observations, we introduced a nucleation barrier such that the rate of siderite precipitation (Eq. 3.14) was set equal to zero for all values of the siderite SI < 1.7. The value of 1.7 was chosen because it resulted in a calculated value for [Fe(II)$_{(aq)}$] at cell 20 equal to 0.244 mM on day 29, which is similar to the measured maximum [Fe(II)$_{(aq)}$]$_{out}$ of 0.282 measured on day 30 (Fig. 3.2). Using lower SI values caused the calculated maximum [Fe(II)$_{(aq)}$]$_{out}$ to occur earlier be smaller than measured values. Using SI values > 1.7 caused no siderite precipitation to occur and thus the calculated steady-state [Fe(II)$_{(aq)}$]$_{out}$ values to be greater than measured values.

Even with the nucleation barrier for siderite, the transient increase and peak in [NH_4^+]$_{out}$ from day 0 until reaching steady state at day 75 was only adequately described by the model with the addition of three cation-exchange reactions described in Table 3.1. PHREEQC models cation exchange using the Gaines-Thomas convention [*Gaines and Thomas*, 1953; *Parkhurst and Appelo*, 1999] whereby the activity of the exchange site is defined as the moles of a species adsorbed onto the exchange site divided by the total moles of a species in solution. The model, with constants shown in Table 3.1, predicts a maximum [NH_4^+]$_{out}$ of 0.274 mM on day 38. The measured maximum [NH_4^+]$_{out}$ was 0.295 ± 0.001 mM on day 44 (Fig. 3.2). The PHREEQC model is consistent with measured [NH_4^+]$_{out}$ when these cation exchange reactions are employed in addition to reactions describing the adsorption of Fe(II) (Fig. 3.2). Furthermore, the model effluent chemistry is inconsistent with measured [NH_4^+]$_{out}$ and [Fe(II)$_{(aq)}$]$_{out}$ when only adsorption or only cation exchange reactions are considered. For example, using only cation exchange reactions fails to capture the transient peak in [Fe(II)$_{(aq)}$]$_{out}$. In contrast using only adsorption reactions fails to capture the transient peak in [NH_4^+]$_{out}$. The existence of two different sets of surface sites may explain the need for both cation exchange and Fe(II) adsorption reactions in our model. Fe-oxide surfaces may provide sites for Fe(II) adsorption while surface sites associated with organic matter and biomass may be available as cation exchange sites. Microbial biofilms are known to function as effective cation exchangers [*Christensen and Characklis*, 1990].

Results from the abiotic column support the hypothesis that Fe(II) cation exchange with NH_4^+ is associated with organic matter and biomass. In the abiotic-control column we observed no transient peak in $[NH_4^+]_{out}$ following the increase in $[Fe(II)_{(aq)}]_{out}$ (Fig. 3.5). The lack of a transient $[NH_4^+]_{out}$ peak indicates that Fe(II) was not replacing NH_4^+ from cation exchange sites in the abiotic control column. Although the abiotic column did not contain Na-acetate the PBAGW did still contain NaCl so Na^+ was still available to act as an exchangeable cation. The lack of a transient peak in $[NH_4^+]_{out}$ in the abiotic column, is consistent with NH_4^+ associated with sorption sites on organic matter. Since there was no carbon source or bacteria added to the abiotic column while all other influent chemistry was identical to the iron-reduction column, it is likely that this secondary set of cation-exchange sites were insignificant in that reactor.

For the Fe-reducing column, our reactive-transport model calculates 24.3 mmoles of siderite precipitated along the length of the column. This is greater than the 14.4 mmoles of siderite as measured with the 1N HCl extraction. Only one sample of sediment was used to measure the amount of siderite precipitated with the 1 N HCl extraction; it would have been unusual if this one sample had the average siderite composition of the entire column. Furthermore, this sediment sample came from a point 10 cm from the column inlet. The PHREEQC model calculated greater siderite precipitation nearer the column inlet (Fig. 3.6). The sediment sample used in the 1 N HCl extraction may have been too far from the inlet to record the average siderite precipitation. Additionally, the reactive transport model calculates that in total 2.42 mmoles of Fe(II) were bound to the adsorption sites and the exchange sites on day 198. This is consistent with 2.05 ± 5.16 mmoles adsorbed Fe(II) calculated with the results of the 1N and 0.5 N HCl extractions on day 198. The 0.5N HCl extraction was conducted on three samples from along the length of the column and probably obtained a more accurate average value.

Since our calculations of $[Fe(II)_{(aq)}]_{out}$, $[NH_4^+]_{out}$, and $[acetate]_{out}$ using PHREEQC are consistent with measured concentrations (Fig. 3.2), it can be concluded that the PHREEQC model is consistent with the biogeochemical reactions occurring within the Fe-reducing column. Therefore, we will use the model to calculate the amount of biomass grown within the column. Our reactive transport model is consistent with a rapid increase in total biomass from 0.0020 g to 0.65 g during the early portion of the experiment from day 0 to day 120. From day 120 on, the predicted amount of total biomass increased more slowly from 0.67 g to a final value of 0.74 g on day 198. The model also predicts that biomass growth will be greater towards the inlet of the column due to higher concentrations of acetate (Fig. 3.7 B)

This final value of 0.74 g of biomass is significantly lower than the value estimated in Chapter 2 [*Regberg et al.,* in press]. In Chapter 2 we used the cumulative consumption of acetate to estimate the amount of biomass produced based on a growth yield of 12%. Therefore, 0.048 moles of biomass (Eq. 3.13) as $C_5H_7O_2N$ were produced per mole of acetate consumed. The model in Chapter 2 is consistent with about 50 times greater biomass production (39.5 g over 198 days) than the PHREEQC model presented here (0.74 g over 198 days) despite using the same growth yield. The PHREEQC model captures transient effects in effluent chemistry and is able to explicitly account for concentration gradients along the length of the column. Using the PHREEQC model eliminates some of the assumptions made by *Regberg et al* [in press]. Namely, the PHREEQC model does not need to assume that reaction rates are constant across the length of the column. In fact, PHREEQC output of calculated Fe(II) adsorbed, Fe(II) bound to exchange sites, siderite precipitated and total Fe(III) dissolved demonstrates that reaction extent was greater towards the inlet of the column, especially for siderite precipitation. Most of the Fe(III) reduction and subsequent, adsorption, exchange and precipitation of Fe(II) occurred within 10 cm. of the inlet (Fig. 3.6). Another important difference between the model used in Chapter 2 and the PHREEQC model is the inclusion of a decay constant for biomass. Given these improvements the PHREEQC predictions are expected to more accurately portray the column than the model of *Regberg* et al. [in press].

Bacteria living under carbon-limited conditions like those found in the Fe-reducing column stop respiring and eventually oxidize if there is not enough energy available for cellular maintenance [e.g. *Pirt*, 1965; *Rittmann and McCarty*, 2001; *Scheibe et al.*, 2006]. The first-order decay constant *b* in Eqs. 3.14 and 3.15 accounts for this biomass loss in the PHREEQC model. The decay constant is a lumped parameter that describes the rate at which cells become inactive (i.e. stop respiring) with or without decomposing. Since a portion of the biomass is continuously decaying, the total amount of biomass calculated in the PHREEQC model is considerably lower than the amount predicted by Regberg et al. [in press]. *Thullner et al.* [2005] reported a similar discrepancy. Their model of a column reactor calculated a total mass of biomass three times less than what was estimated from measurements of protein bound to sediment within the column experiment. The protein assay may have been measuring dormant cells as well as active biomass. However, *Thullner et al.* remarked that the predicted pattern of biomass growth was consistent in extent although lower in magnitude than that estimated from the protein measurements. Both the PHREEQC estimate of biomass growth and that from *Regberg et al.* [in press] demonstrate constant increases in total biomass for the latter portion of the experiment after day 120 (Fig. 3.7). *Regberg et al.* [in press] calculate that the steady state biomass growth rate is 0.23 g biomass as $C_5H_7O_2N$ day^{-1}. The model created in PHREEQC calculates a biomass growth rate from day 120 to day 198 of 0.001 g biomass as $C_5H_7O_2N$ day^{-1}. It is possible to increase the biomass growth rate in the PHREEQC model by removing the decay coefficient from Eqs. 3.12 and 3.13. Removing the decay coefficient increases the total amount of biomass calculated by the model, but causes predictions of $[\text{acetate}]_{\text{out}}$ and $[\text{Fe(II)}_{(aq)}]_{\text{out}}$ to be inaccurate for the transient portion of the experiment (day 0 to day 70). Without a decay coefficient calculated $[\mathrm{Fe(II)}_{(aq)}]_{out}$ and $[\mathrm{acetate}]_{out}$ attain steady state values around day 50. This is 20 days before measured $[\mathrm{Fe(II)}_{(aq)}]_{out}$ and $[\mathrm{acetate}]_{out}$ reached steady state values. Removing the decay coefficient (*b*) from Eqs. 3.12 and 3.13 does not affect the magnitude of steady-state concentrations of Fe(II) and acetate, only the time scale at which those steady state values are achieved. It may also be possible to fit the data by varying the yield coefficient.

Abiotic column

Regberg et al. [in press] presented two possibilities for the anomalous increase in σ_b after day 120 in the Fe-reducing column reactor. One possible explanation was that sorption of Fe(II) created a conductive surface capable of increasing σ_b measurements. The results from our abiotic reactor do not support this hypothesis. Measured σ' across the abiotic reactor did not increase as Fe(II) adsorption occurred. In fact, σ', which is thought to be equivalent to D.C measurements of σ_b when surface conductivity is negligible [*Slater and Lesmes*, 2002], actually decreased by 14% (0.051 → 0.044 S/m) 19 days after the Fe(II) was introduced to the column. Since we measured no increases in σ' during the time period when $[\mathrm{Fe(II)}_{aq}]_{out}$ was increasing (day 86 to day 120) we conclude that Fe(II) adsorption has no effect on electrical conductivity under abiotic conditions *Regberg et al.* [in press] also argued for the presence of electrically conductive biofilms in the column experiment and used their estimate of biomass growth to model the anomalous increase in σ_b beginning on day 120. We can use the same equation adapted from percolation theory with the lower total biomass values predicted from PHREEQC to obtain a theoretical value for biofilm conductivity:

$$\sigma_b = a^{-1}\sigma_f \phi^m + (f_{\text{secondary}} - f_{\text{critical}})^{\omega}\sigma_{\text{secondary}} \,. \tag{3.15}$$

Here $f_{\text{secondary}}$ is the volume fraction of biomass, f_{critical} is some critical volume fraction occurring when a connected electrical pathway develops across the column, ω is a parameter that varies with tortuosity, and $\sigma_{\text{secondary}}$ is the electrical conductivity (S/m) of the new phase necessary to describe the measured increase in σ_b. As in *Regberg et al.* [in press], ω was assumed to equal 1.5 and f_{critical} was assumed to be the volume fraction of biomass present on day 120 when σ_b began to increase.

A calculated mass of biofilm can be converted to a volume using a reported value for the density of biofilm. *Regberg et al.* [in press] provided visual evidence for biofilm formation within the column reactor. Biofilms are significantly less dense than single cells (2.5 – 65 kg C m^{-3} vs. 561 kg C m^{-3}), because they are often dominated by less dense extracellular polymeric substances (EPS) [*Christensen and Characklis*, 1990; *Thullner*, 2010]. Using density values between 2.5 and 65 kg C m^{-3}, the living biomass produced in the column reactor could occupy between 1.8 and 47% of the available pore space within the column on day 120. This calculation is completed as follows. Each mole of biomass expressed as $C_5H_7O_2N$ has 60 g of carbon. If we assume that the biofilms produced in the Fe-reducing column had a carbon density of 65 kg C m^{-3}), the 0.67 g of biomass predicted on day 120 fills 1.8% (0.67 g biomass x (60g C/113 g biomass)/ 65,000 g C m^{-3} = 6.7 x 10^{-7} m^3) of the available pore space (2.97 x 10^{-4} m^3). By day 195 the biomass could occupy between 2 and 51% of the pore space. Using Eq. 3.15 with these assumptions of biofilm density, values of $\sigma_{\text{secondary}}$ between 2.75 and 220 S/m are consistent with the measured σ_b increase.

These values based on cells + extracellular polysaccharide are highly conductive but may be reasonable because they are within a factor of 2 of the conductivity of seawater. In contrast a biofilm composed entirely of cells with no extra-cellular material has a density of 531 kg C m^{-3}

[*Sundararaj et al.*, 2004]. If we assume that the biofilms produced in the Fe-reducing column had a carbon density of 531 kg C m^{-3}, the 0.67 g of biomass predicted on day 120 fills 0.22% of the column's pore space. By day 195 the predicted biomass fills 0.24% of the column's pore space. These very small pore-infilling values would require that biofilms are extremely conductive if they are to describe the measured increase in σ_b.

The model that is most consistent with the observations is that biomass inside the column reactor is not composed entirely of cells, but also contains some extra-cellular material and is thus less dense. As we have shown, a less dense biofilm could fill a larger fraction of the pores space and thus decrease the value of $\sigma_{\text{secondary}}$ in Eq. 3.15 needed to fit the measured increase in σ_b. Changing the values for f_{critical} or ω will not cause $\sigma_{\text{secondary}}$ to decrease to a more reasonable value.

Equations 3.12 and 3.13 model microbial decay with a lumped decay parameter that includes both the rate of oxidation of biomass and the rate of production of biomass that is dormant. While this is a commonly used convention [e.g., *Rittmann and McCarty*, 2001; *Scheibe et al.*, 2006] it seems likely that some of the biomass produced before [acetate]$_{\text{out}}$ approached 0 on day 70 (Fig. 2) became dormant instead of becoming oxidized. Dormant biomass may have similar electrical properties to respiring biomass, especially if the extracellular material is the dominant contributor to electrical conductivity. This is an area that requires further research.

Using a reactive transport model, we are able to calculate the processes driving chemical changes occurring in the effluent and inside the Fe-reducing column reactor. We have captured transient changes [Fe(II)$_{\text{aq}}$]$_{\text{out}}$, and NH_4^+ by adding precipitation reactions, adsorption-desorption reactions and cation exchange reactions. In a separate, abiotic column reactor we have demonstrated that Fe(II) adsorption reactions do not affect electrical conductivity measurements. Based on this, we were able to assume changes in bulk electrical conductivity were directly related to biofilm growth. Using the calculated rates of biomass growth from the PHREEQC model we are able to determine the necessary electrical conductivity of biomass to explain the measured increases in σ_b in the Fe-reducing column reactor. This work represents the first combination of reactive transport modeling with electrical geophysics and demonstrates how these two techniques can be combined to gain a greater understanding of biogeochemical processes.

Conclusions

The reactive transport code PHREEQC can be used to model changes in effluent chemistry for a column reactor containing a mixed culture of Fe-reducing and methane-generating microbes. It is necessary to add kinetic reactions for iron reduction, methane generation, siderite precipitation, and biomass growth/decay to produce a model that is consistent with measured changes in effluent chemistry. Furthermore, equilibrium reactions describing Fe(II) adsorption as well as cation exchange between $Na,^+$ Fe(II) and NH_4^+ were necessary to describe variations in effluent concentrations. This is the first time reactive transport modeling has been used to constrain electrical conductivity measurements. When the PHREEQC model was consistent with measured changes in effluent chemistry it also predicted an increase in total biomass within the column. There was no production of aqueous species predicted by the reactive transport model that could cause the measured increase in σ_b after day 120.

An abiotic column did not show a similar increase in σ_b even when Fe(II) was added to the influent to stimulate iron adsorption. This disproves the hypothesis that Fe(II) adsorption alone can create a conductive surface capable of driving the increases in measured σ_b. We hypothesize that the biomass generated within the Fe-reducing column may have electrical properties that are responsible for the measured increase in σ_b. This biomass and its associated extra-cellular compounds may occupy as much as 50% of the available pore space within the reactor. Using our modeling approach, an electrical conductivity for biomass between 2.75 and 220 S/m is consistent with the measured changes in σ_b after day 120.

This work advances our understanding of the relationship between biogeochemical reactions and changes in electrical conductivity of microbial biofilms by eliminating several potential causes for increased σ_b measurements. The chemical measurements here are consistent with the conclusion that sorption of the ammonium or ferrous cations is not consistent with changes in σ_b and therefore does not create the measured increase in σ_b measured in previous studies. More work is needed to confirm that microbial biofilms are indeed more conductive than their surroundings, such as directly measuring the electrical conductivity of respiring biofilms. If these biofilms are electrically conductive it may be possible to monitor biogeochemical activity using electrical geophysical techniques, which would be useful for monitoring the biogeochemical remediation of contaminated aquifers.

Table 3.1: Reactions Added to PHREEQC

Reaction	Parameter
$0.125CH_3COO^- + 1FeOOH + 1.875H^+ \rightarrow Fe^{2+} + 0.25HCO_3^- + 1.5H_2$	Eq. 3.7
$0.125CH_3COO^- + 0.125H_2O \rightarrow 0.125HCO_3^- + 0.125\ CH_4$	Eq. 3.11
$0.05NH_4^+ + 0.125CH_3COO^- + 0.075H^+ \rightarrow 0.05C_5H_7O_2N + 0.15H_2O$ (Fe reducing Bacteria)	Eq. 3.12
$0.05NH_4^+ + 0.125CH_3COO^- + 0.075H^+ \rightarrow 0.05C_5H_7O_2N + 0.15H_2O$ (Methanogenic)	Eq. 3.13
$Fe^{2+} + HCO_3^- \rightarrow FeCO_3 + H^+$	Eq. 3.14
$\equiv FeOH + Fe^{2+} \rightarrow \equiv FeOFe^+ + H^{+a}$	Log K = -1.65
$\equiv FeOH \rightarrow \equiv FeO^- + H^{+a}$	Log K = -8.93
$\equiv FeOH + H^+ \rightarrow \equiv FeOH_2^{+a}$	Log K = 7.29
$HCH_3COO \rightarrow H^+ + CH_3COO^-$	Log K = -4.76[c]
$C_8H_{18}N_2O_6S_2 \rightarrow H^+ + C_8H_{17}N_2O_6S_2^-$	Log K = -6.76[d]
$NH_4^+ + X^- \rightarrow NH_4X$ [b]	Log K = 1.2
$Fe^{2+} + 2X^- \rightarrow FeX_2$ [b]	Log K= 0.56
$Na^+ + X^- \rightarrow NaX$ [b]	Log K = -2

a: $\equiv FeO^+$ is a surface adsorption site

b: X is a cation exchange site.

c: [*Stumm and Morgan*, 1996]

d: [*Good et al.*, 1966]

Table 3.2 Kinetic Parameters

Name	Parameter	Units	Value	Literature Value
Maximum Fe(III) reduction rate	$V_{\max,Fe(III)}$	moles mole sites^{-1} day^{-1}	0.22	0.143[a]
Half saturation constant for biomass	$K_{m,Biomass}$	g cells (dm bulk sediment) $^{-1}$	0.00423	0.00423[a]
Half saturation constant for acetate	$K_{m,Acetate}$	moles acetate (dm pore fluid)$^{-1}$	0.0001	0.0001[a]
Concentration of surface sites	$[\equiv FeOH^{+}]$	mole sites (dm bulk sediment)$^{-1}$	0.00404	0.00404[a]
Gibbs free energy of reaction	ΔG_{rxn}^{0}	kJ mol^{-1}	-112.2	-112.2[a]
Gibbs free energy of cellular maintenance	$\Delta G_{\min}$	kJ mol^{-1}	-20	-20[b]
Maximum rate of methanogenesis	$V_{\max,CH_4}$	day^{-1}	12	0.069[c]
Half saturation constant for acetate	$K_{m,acetate,CH_4}$	Mol L^{-1}	5 x 10^{-4}	5 x 10^{-4}[c]
Growth Yield	γ	mol biomass as $C_5H_7O_2N$ (mol acetate consumed)$^{-1}$	0.12	N. A.
Biomass decay constant	b	g biomass as $C_5H_7O_2N$ day^{-1}	0.024	N. A.
Rate constant of siderite precipitation	k	moles (L day)$^{-1}$	2.4 x 10^{-7}	2.4 x 10^{-9}[d]
Solubility constant of siderite	$K_{Siderite}$		$10^{-10.89}$	$10^{-10.89}$ [e]

a: [*Scheibe et al.*, 2006]
b: [*Liu et al.*, 2001]
c: [*Watson et al.*, 2003]
d: [*Van-Cappelen and Wang*, 1995]
e: [*Ball and Nordstrom*, 1991]

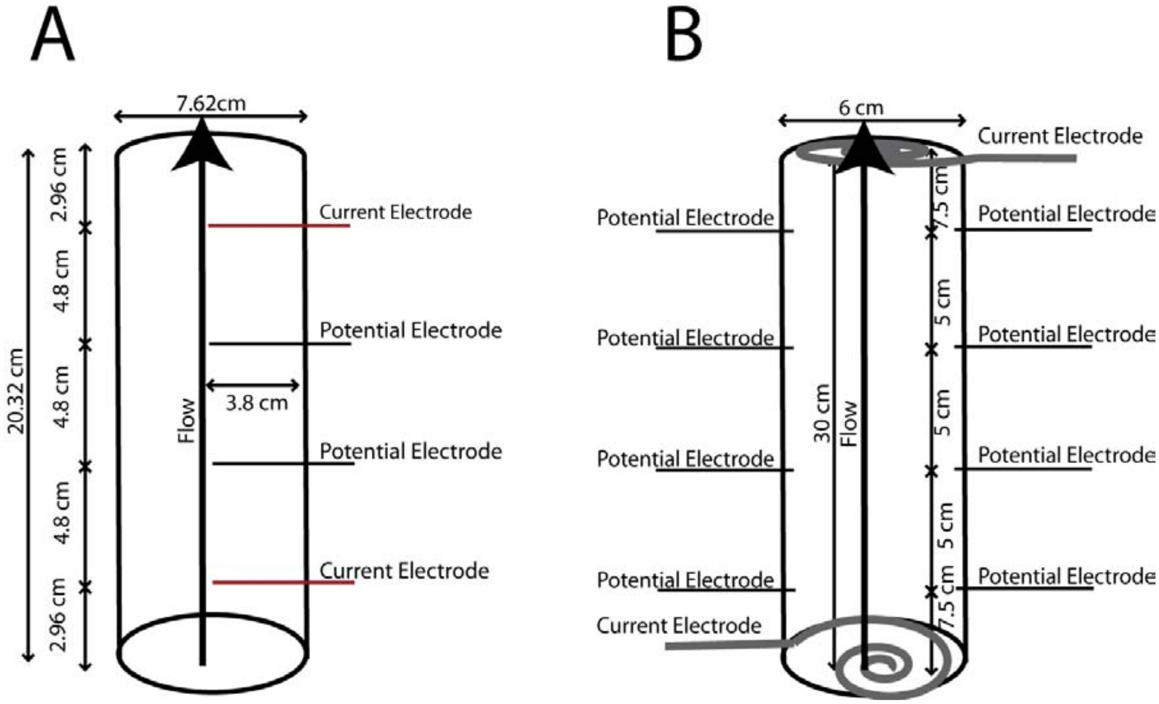

Figure 3.1: Schematic of the electrode configuration for the Fe-reducing column (A) and the abiotic column (B).

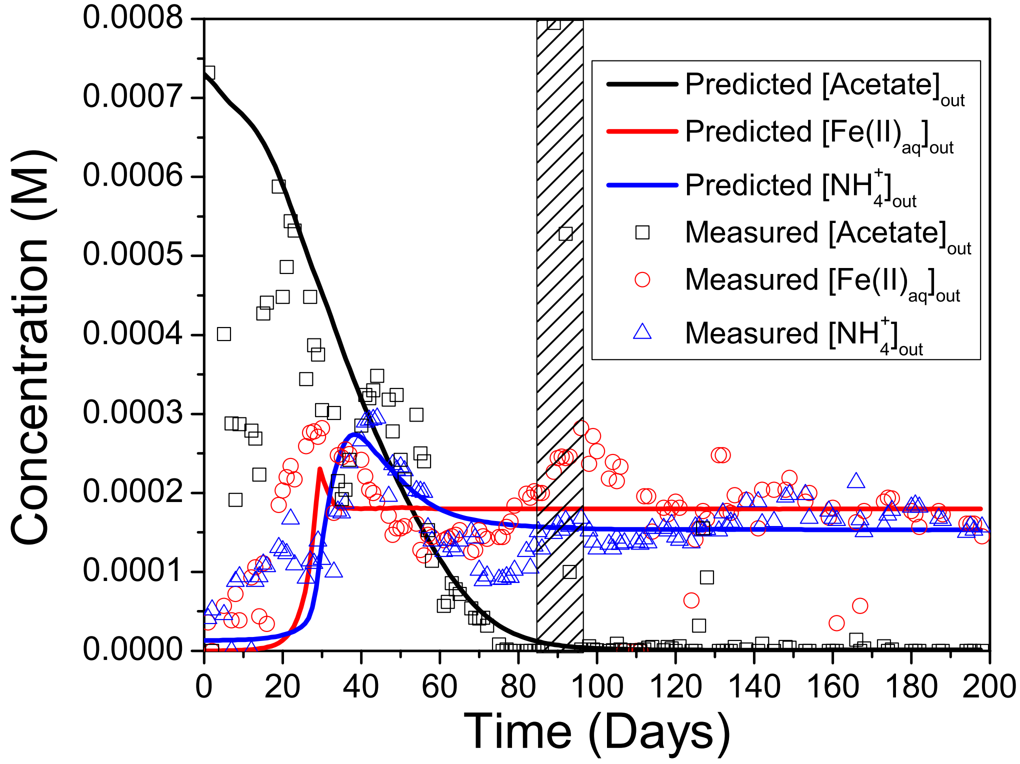

Figure 3.2: Model predictions of effluent chemistry (solid lines) are consistent with measured concentrations (open symbols) when the reactions summarized in Table 3.1 are added to the PHREEQC database. See text for details. Increases in $[\text{acetate}]_{\text{out}}$ around day 100 were due to a concentration fluctuation leading to an influent [acetate] of 2 mM for four days (hashed box). This extra acetate caused $[\text{Fe(II)}_{\text{aq}}]_{\text{out}}$ to temporarily increase due to increased Fe(III) reduction.

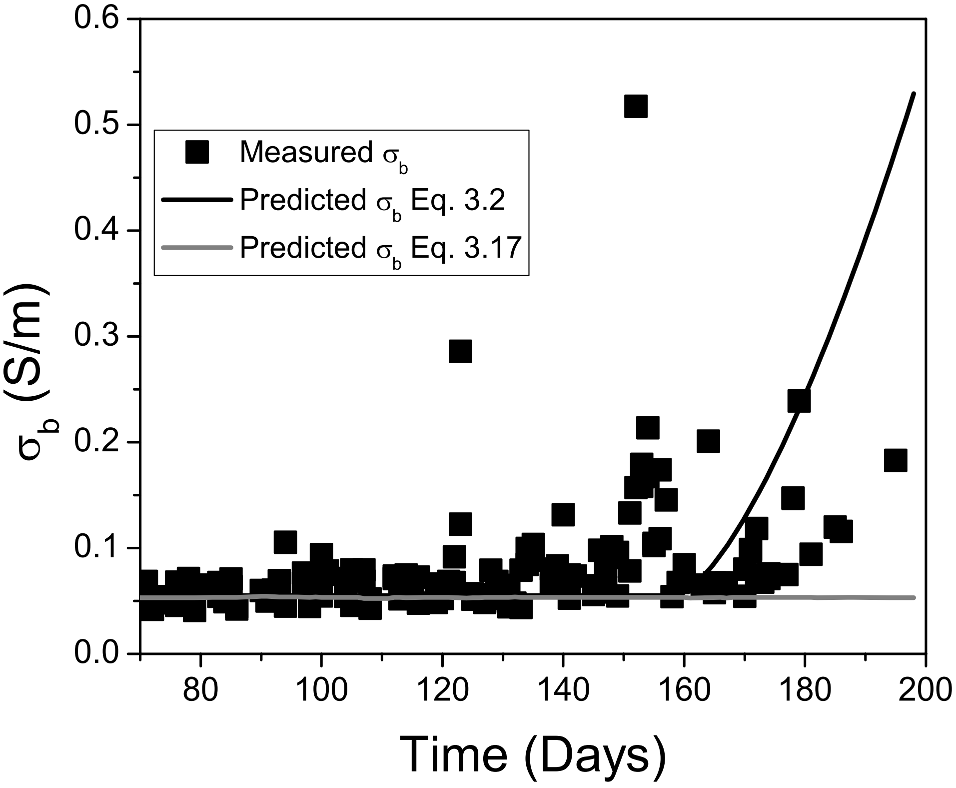

Figure 3.3: Measured values of σ_b (squares) are constant before day 120. After day 120 measured σ_b rapidly increases to a maximum value of 0.2 S/m. Calculated values of σ_b using Eq. 3.2 (grey line) are unable to describe this increase in measured σ_b. If Eq. 3.17 is used to calculate σ_b (black line) then depending on the amount of pore space occupied by the biomass, $\sigma_{secondary}$ must be between 2.75 - 220 S/m in order to describe the measured increase shown here.

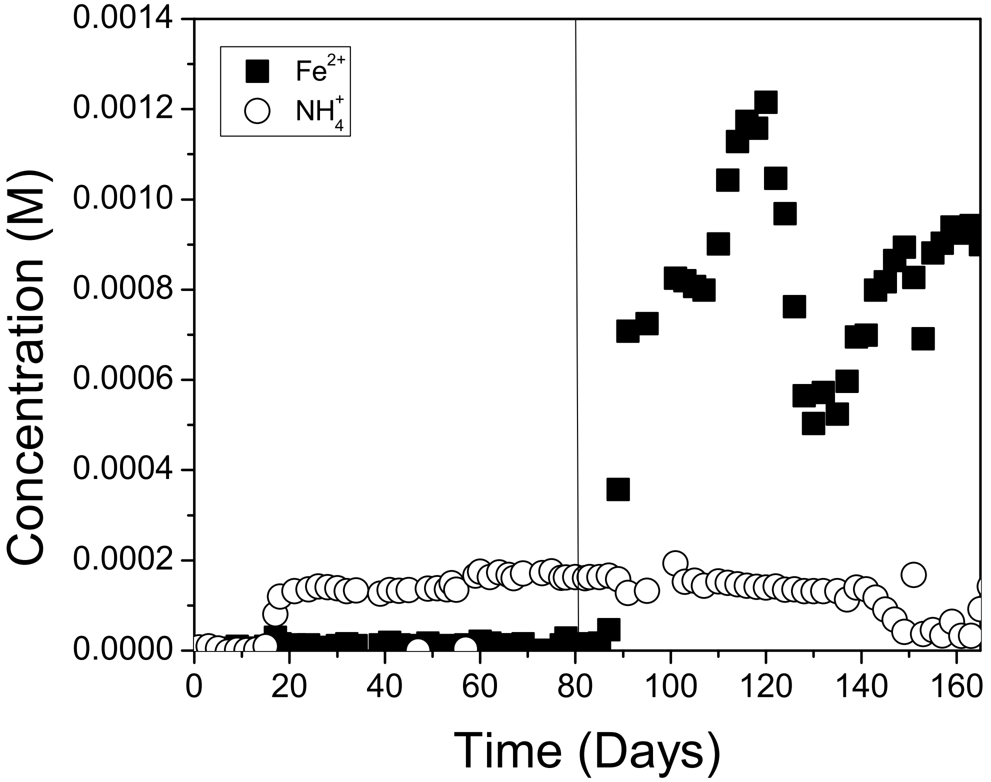

Figure 3.4: Effluent chemistry for the abiotic column. Increases in $[NH_4^+]_{out}$ (circles) are attributed to an initial period of NH_4^+ adsorption. Once sorption sites are saturated, the effluent ammonium cation returns to inlet values (190 μM). On day 80, 1.2 mM $FeCl_2$ was added to influent solution to test the effect of Fe(II) adsorption on σ_b. Effluent [Fe(II)] (squares) increased to values at or near the influent concentration by day 120. The lack of a corresponding increase in effluent of NH_4^+ is evidence for the lack of a cation exchange/ desorption reaction between Fe(II) and NH_4^+.

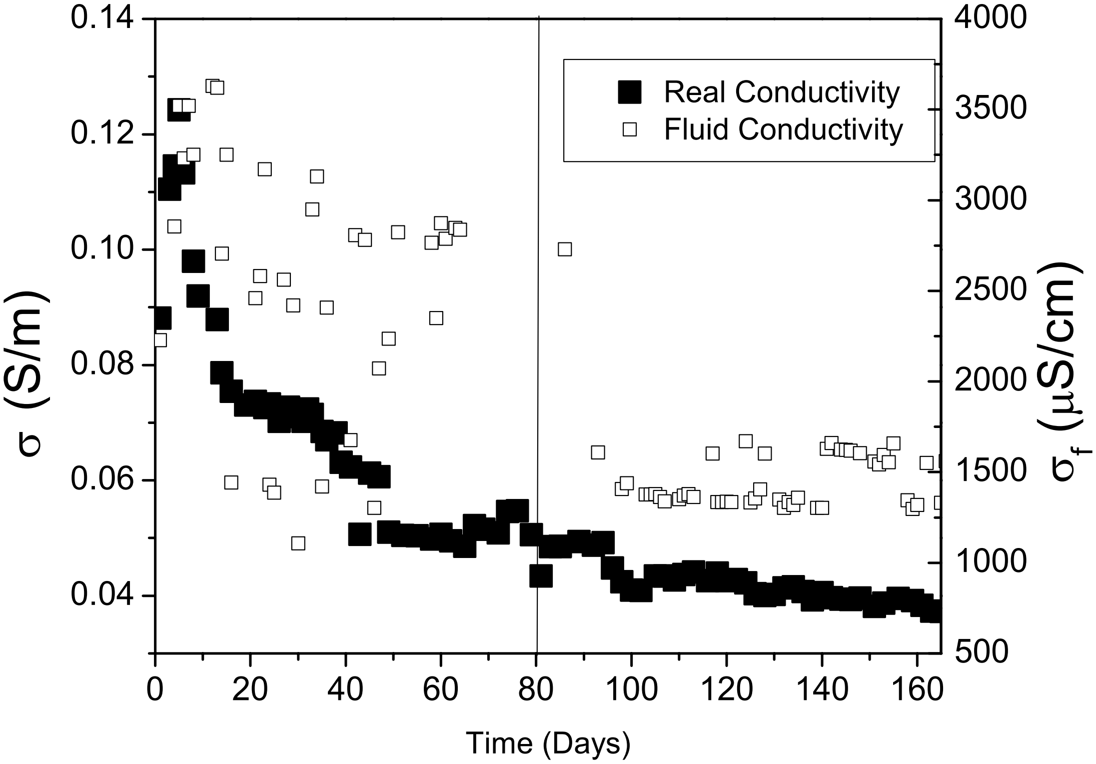

Figure 3.5: Plots of real electrical conductivity at 5.7 mHz for the abiotic column. There is no measurable increase in the real electrical conductivity due to the introduction of 1.2 mM $FeCl_2$ to the influent solution on day 80. The initial decrease in real conductivity (filled squares) is consistent with a measured decrease in fluid electrical conductivity (open squares) and is attributed to a decrease in the ionic strength of the pore fluid.

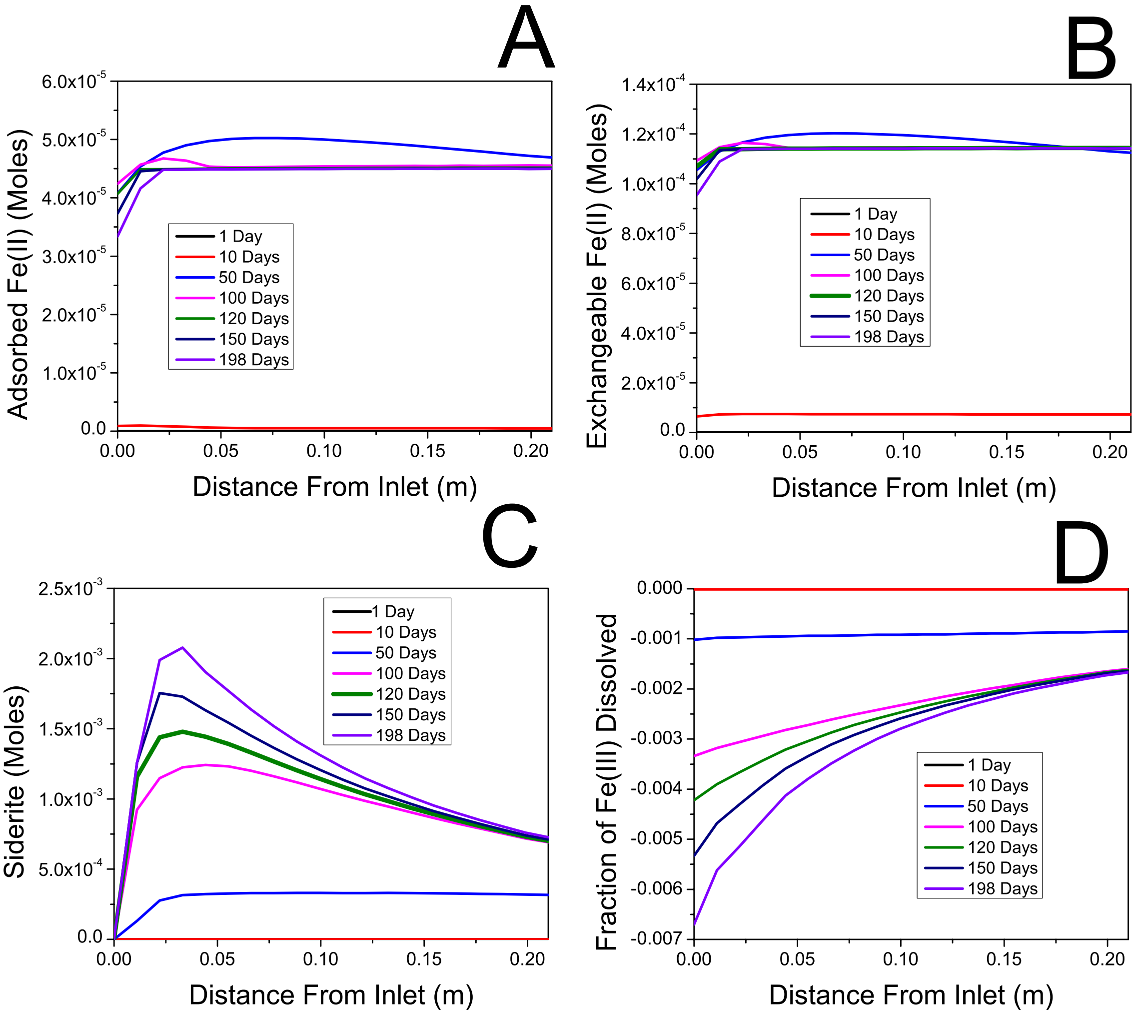

Figure 3.6: Output from PHREEQC showing the moles of adsorbed Fe(II) (A), moles of Fe(II) bound to exchanges sites (B), moles of Fe(II) precipitated as siderite (C) as a function of distance from the column inlet. Adsorbed Fe(II) and Fe(II) bound to exchange sites (A and B) increase from day 1 until day 50 when siderite precipitation begins. As siderite precipitation removes Fe(II) from solution the amount of adsorbed Fe(II) and exchangeable Fe(II) decreases. Panel D shows the extent of Fe(III) reduction as a function of distance along the column reactor. Values

of 0 indicate no reduction. A value of -1 indicates that 100% of the available Fe(III) was reduced. The extent of Fe(III) reduction is noticeably greater towards the column inlet where acetate concentrations were higher.

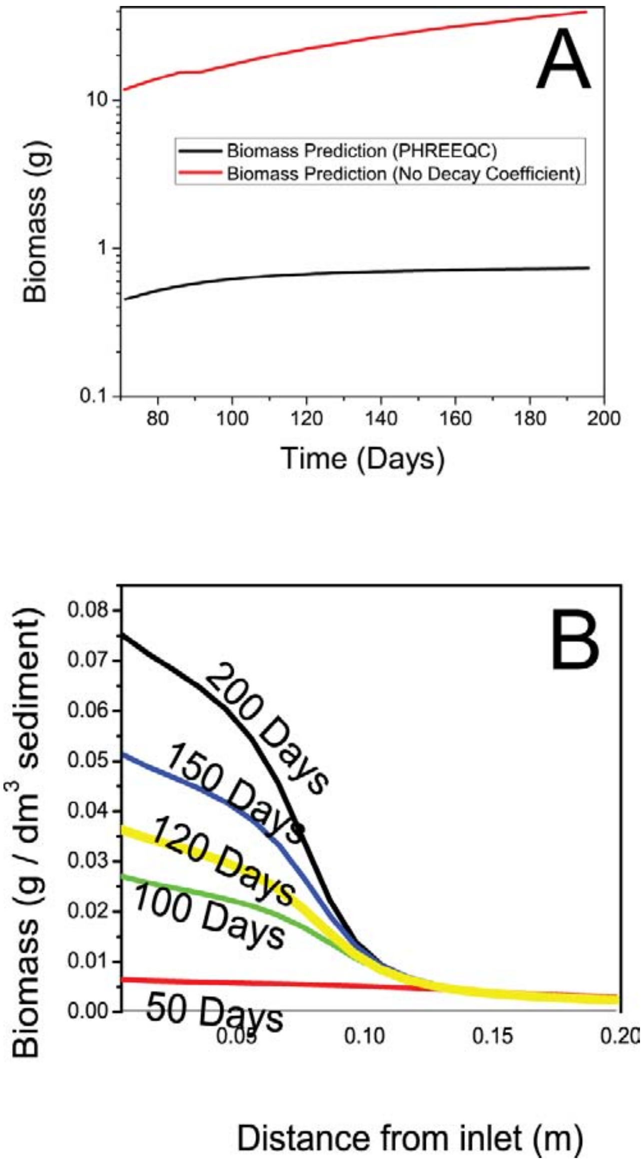

Figure 3.7: Predictions of total biomass (g) as $C_5H_7O_2N$ from PHREEQC (black line, A) are significantly less than predictions from chapter 2 [*Regberg et al.* in press] (red line, A) due to the inclusion of a decay coefficient in the PHREEQC model. Including a decay coefficient results in a more accurate model of biomass growth within the column. Panel B shows the spatial distribution of biomass as a function of time. Biomass in concentrated towards the column's inlet due to higher concentrations of acetate.

Works Cited

Abdel-Aal, G., E. Atekwana, S. Radzikowski, and S. Rossbach (2009), Effect of bacterial adsorption on low frequency electrical properties of clean quartz sands and iron-oxide coated sands, *Geophysical Research Letters*, *36*(L04403).

Abdel-Aal, G. Z., E. A. Atekwana, S. Rossbach, and D. D. Werkema (2010), Sensitivity of geoelectrical measurements to the presence of bacteria in porous media, *Journal of Geophysical Research-Biogeosciences*, *115*(G03017), 1-11.

Archie, G. E. (1942), The electrical reisistivity log as an aid in determining some reservoir characteristics, *Petroleum Transactions of AIME*, *146*, 54-62.

Atekwana, E. A. E., E. A. Atekwana, D. Werkema, J. P. Allen, L. A. Smart, J. W. Duris, D. P. Cassidy, W. A. Sauk, and S. Rossbach (2004), Evidence for microbial enhanced electrical conductivity in hydrocarbon-contaminated sediments, *Geophysical Research Letters*, *31*(23), 20.

Balberg, I. (1986), Excluded-volume explanation of Archie's law, *Physical Review B*, *33*(5), 3618-3620.

Ball, J. W., and D. K. Nordstrom (1991), User's manual for WATEQ4F with revised thermodynamic data base and test cases for calculating speciation of major trace and redox elements in natural waters, *U.S. Geological Survey Open File Report*, *91-183*, 1-59.

Binley, A., and A. Kemna (2007), DC Resistivity and Induced Polarization Methods, in *Hydrogeophysics*, edited by Y. Rubin and S. Hubbard, pp. 129-156, Springer, AA Dordrecht, The Netherlands.

Brantley, S. L., and C. F. Conrad (2008), Analysis of Rates of Geochemical Reactions, in *Kinetics of Water-Rock Interaction*, edited by S. L. Brantley, et al., pp. 1-38, Springer.

Characklis, W. G. (1990), Laboratory biofilm reactors, in *Biofilms*, edited by W. G. Characklis and K. C. Marshall, Jonh Whiley and Sons Inc., New York.

Christensen, B. E., and W. G. Characklis (1990), Physical and chemical properties of biofilms, in *Biofilms*, edited by W. G. Characklis and K. C. Marshall, John Wiley and Sons Inc., New York.

COMSOL (2008), COMSOL Multiphysics Modeling Guide, 1 - 518.

Costerton, J. W., Z. Lewandowski, D. E. Caldwell, D. R. Korber, and H. M. Lappin-Scott (1995), Microbial Biofilms, *Annual Review of Microbiology*, *49*(711-745).

Davis, C. A., E. Atekwana, E. Atekwana, L. D. Slater, S. Rossbach, and M. R. Mormile (2006), Microbial growth and biofilm formation in geologic media is detected with complex conductivity measurements, *Geophysical Research Letters*, *33*(18), L18403.

De-Yoreo, J. J., and P. G. Vekilov (2003), Principles of crystal nucleation and growth, in *Biomineralization*, edited by P. M. Dove, et al., pp. 57-93, Mineralogical Society of America

Geochemical Society, Chantilly, VA.

Freeze, R. A., and J. A. Cherry (1979), *Groundwater*, 604 pp., Prentice Hall, Englewood Cliffs, NJ.

Fritz, B., and C. Noguera (2009), Mineral precipication kinetics, in *Thermodynamics and kinetics of water-rock interaction*, edited by E. H. Oelkers and J. Schott, pp. 371-410, Mineralogical Society of America Geochemical Society, Chantilly, VA.

Gaines, G. L., and H. C. Thomas (1953), Adsorption studies on clay minerals II A formualtion of the thermondynamics of exchange adsorption, *The Journal of Chemical Physics*, *21*(714-718).

Good, N. E., G. D. Winget, W. Winter, T. N. Connolly, S. Izawa, and R. M. M. Singh (1966), Hydrogen ion buffers for biological research, *Biochem. Cell Biol.*, *5*(2), 467-477.

Hacherl, E. L., and D. S. Kosson (2003), A kinetic model for bacterial Fe(III) oxide reduction in batch cultures, *Water Resour. Res.*, *39*(4), 18.

Heron, G., C. Crouzet, A. Bourg, and T. Christensen (1994), Speciation of Fe (II) and Fe (III) in contaminated aquifer sediments using chemical extraction techniques, *Environ. Sci. Technol.*, *28*(9), 1698-1705.

Holmes, R., A. Aminot, R. Kérouel, B. Hooker, and B. Peterson (1999), A simple and precise method for measuring ammonium in marine and freshwater ecosystems, *Canadian Journal of Fisheries and Aquatic Sciences*, *56*(10), 1801-1808.

Knutsson, G. (1966), Tracers for groundwater investigations, paper presented at Groundwater Problems, Pergamon Press, Stockholm Sweden.

Lesmes, D. P., and K. M. Frye (2001), Influence of pore fluid chemistry on the complex conductivity and induced polarization responses of Berea Sandstone, *Journal of Geophysical Research*, *106*(B3), 4079-4090.

Liu, C., S. Kota, J. Zachara, J. Fredrickson, and C. Brinkman (2001), Kinetic analysis of the bacterial reduction of goethite, *Environ. Sci. Technol*, *35*(12), 2482-2490.

Parkhurst, D. L., and C. Appelo (1999), User's guide to PHREEQC (Version 2) - A Computer program for speciation, batch-reaction, one-dimensional transport, and inverse geochemical calculations, *Water-Resources Investigations Report*, *99-4259*.

Penn, R. L., C. Zhu, H. Xu, and D. R. Veblen (2001), Iron oxide coatings on sand grains from the Atlantic coastal plain: High-resoltuion transmission electron microscopy, *Geology*, *29*(9), 843-846.

Pirt, S. J. (1965), The maintenance energy of beacteria in growing cultures, *Procedeedings of the Royal Society B: Biological Sciences*, *163*(1965), 224-231.

Regberg, A., K. Singha, M. Tien, F. Picardal, J. Schieber, E. Roden, and S. L. Brantley (in press), Electrical conductivity as an indicator of iron reduction rates in abiotic and biotic systems, *Water Resour. Res.*

Reguera, G., K. McCarthy, T. Mehta, J. Nicoll, M. Tuominen, and D. Lovley (2005), Extracellular electron transfer via microbial nanowires, *Nature*, *435*(7045), 1098-1101.

Rittmann, B. E., and P. L. McCarty (2001), *Environmental Biotechnology: Principles and Applications*, 754 pp., McGraw Hill, Boston.

Roden, E. (2004), Analysis of long-term bacterial vs. chemical Fe (III) oxide reduction kinetics, *Geochim. Cosmochim. Acta*, *68*(15), 3205-3216.

Roden, E. (2006), Geochemical and microbiological controls on dissimilatory iron reduction, *Comptes rendus-Géoscience*.

Scheibe, T., Y. Fang, C. Murray, and E. Roden (2006), Transport and biogeochemical reaction of metals in a physically and chemically heterogeneous aquifer, *Geosphere*, *2*(4), 220-235.

Schroth, M. H., S. J. Ahearn, J. S. Selker, and J. D. Istok (1996), Characterization of Miller-Similar Silica Sands for Laboratory Hydrologic Studies, *Soil Science Society of America*, *60*, 1331-1339.

Schwertmann, U., and R. M. Cornell (2000), *Iron Oxides in the Laboratory: Preparation and Characterization*, 2nd ed., 188 pp., Wiley-VCH Verlag GmbH.

Slater, L., and D. Lesmes (2002), Electrical-hydraulic relationships observed for unconsolidated sediments, *Water Resour. Res.*, *38*(10), 1213.

Steefel, C. I., and P. Van-Cappellen (1990), A new kinetic approach to modeling water-rock interaction: The role of nucleation, precursors, and Ostwald ripening, *Geochim. Cosmochim. Acta*, *54*(10), 2657-2677.

Stookey, L. L. (1970), Ferrozine- a new spectrophotometric reagent for iron, *Anal. Chem.*, *42*(7), 779-781.

Stumm, W., and J. J. Morgan (1996), *Aquatic Chemistry: Chemical Equilibria and Rates in Natural Waters*, 3rd ed., 1022 pp., John Wiley and Sons Inc., New York.

Sumner, J. (1976), *Principles of Induced Polarization for Geophysical Exploration*, 1 ed., 277 pp., Elsevier Scientific Publishing Company, Amsterdam.

Sundararaj, S., A. Guo, B. Habibi-Nazhad, M. Rouani, P. Stothard, M. Ellison, and D. S. Wishart (2004), The cybercell database (CCDB): a comphrehensive, self-updating, relational database to coordinate and facilitate *in silico* modeling of *escherichia coli*, *Nucleic Acids Res.*, *32*, D293-D295.

Szramek, K., and L. M. Walter (2004), Impact of carbonate precipitaiton on riverine inorganci carbon mass transport from a mid-continent, forested watershed, *Aquatic Geochmeistry*, *10*(1-2), 99-137.

Thullner, M., P. V. Cappellen, and P. Regnier (2005), Modeling the impact of microbial activity on redox dynamics in porous media, *Geochim. Cosmochim. Acta*, *69*(21), 5005-5019.

Thullner, M. (2010), Comparison of bioclogging effects in saturated porous media within one-and two-dimensional flow systems, *Ecol. Eng.*, *36*(2), 176-196.

Torres, C. I., A. K. Marcus, P. Parameswaran, and B. E. Rittmann (2008), Kinetic experiments for evaluating the Nernst-Monod model for anode-respiring bacteria (ARB) in a biofilm anode, *Environ. Sci. Technol.*, *42*, 6593-6597.

Van-Cappelen, P., and Y. Wang (1995), Metal cycling in surface sediments: modeling the interplay of transport and reaction, in *Metal Contaminated Aquatic Sediments*, edited by H. E. Allen, Ann Arbor Press, Ann Arbor, MI.

Vanhala, H., and H. Soininen (1995), Laboratory technique for measurement of spectral induced polarization response of soil samples, *Geophysical Prospecting*, *43*(5), 655-676.

Violier, E., P. Inglett, K. Hunter, A. Roychoudhury, and P. V. Capellen (2000), The ferrozine method revisited: Fe(II)/Fe(III) determination in natural waters, *Appl. Geochem.*, *15*, 785-790.

Watson, I. A., S. E. Oswald, K. U. Mayer, Y. Wu, and S. A. Banwart (2003), Modeling kinetic processes controlling hydrogen and acetate concentrations in an aquifer-derived microcosm, *Environ. Sci. Technol.*, *37*, 3910-3919.

White, A., T. Bullen, D. Vivit, M. Schulz, and D. Clow (1999), The role of disseminated calcite in the chemical weathering of granitoid rocks, *Geochim. Cosmochim. Acta*, *63*(13/14), 1939-1953.

White, A. F., and S. L. Brantley (2003), The effect of time on the weathering of silicate minerals; why do weathering rates differ in the laboratory and field?, *Chem. Geol.*, *202*(3-4), 479-506.

Chapter 4

CHANGES IN ELECTRICAL CONDUCTIVITY ASSOCIATED WITH NITRATE REDUCTION

Introduction

Aquifers containing organic contaminants or low temperature petroleum reservoirs often include zones of increased microbial activity [e.g., *Bennett et al.*, 2000; *Christensen et al.*, 2001; *Röling et al.*, 2003]. In a contaminated aquifer, if organic carbon concentrations are high enough, micro-organisms will consume the available oxygen creating a zone of anoxia. Inside this anoxic zone, different microbiological communities can grow that are capable of using alternative terminal electron acceptors (TEAPs) to O_2. Previous researchers have documented changes in bulk electrical conductivity (σ_b) associated with microbiological activity under anoxic conditions, [e.g., *Atekwana and Atekwana*, 2005; *Ntarlagiannis et al.*, 2007; *Abdel-Aal et al.*, 2010] but no studies have focused on NO_3^- reduction. Nitrate reduction is an important environmental process for three reasons. Given equal concentrations, the most energetically favorable TEAP after O_2 is generally NO_3^- [*Christensen et al.*, 2001; *Rittmann and McCarty*, 2001] and is often abundant in contaminated aquifers [e.g., *Christensen et al.*, 2001]. Secondly, the reduction of NO_3^- to NO_2^- via the following half reaction releases 82.97 kJ/ e^- eq at pH = 7 under 1 atm pressure at 298 K:

$$\tfrac{1}{2}\, NO_3^- + H^+ + e^- \rightarrow \tfrac{1}{2}\, NO_2^- + \tfrac{1}{2}\, H_2O. \qquad (4.1).$$

For comparison, the ferric ferrous half reaction, another abundant alternative electron acceptor,

$$Fe^{3+} + e^- \rightarrow Fe^{2+}\,, \qquad (4.2)$$

only releases 74.29 kJ/ e^- eq [*Madigan et al.*, 2003]. Lastly, denitrifying bacteria are ubiquitous in the environment and zones where nitrate reduction occurs are often associated with contaminated aquifers [e.g., *Knowles*, 1982; *Christensen et al.*, 2001].

Our goal is to determine if rates of biogeochemical nitrate reduction can be determined from measured changes in σ_b. Measuring σ_b is faster and cheaper than traditional geochemical sampling, which often requires drilling multiple monitoring wells and many time-consuming rounds of sample collection followed by expensive laboratory analyses [e.g., *LeBlanc et al.*, 1991]. In contrast, electrical conductivity measurements can be collected quickly and efficiently, and in some cases, can be combined with a limited number of geochemical measurements to determine reaction rates [e.g., Regberg et al., in press].

We hypothesize that biologically catalyzed nitrate reduction will affect the σ_b of an aquifer in a quantifiable, predictable way and allow us to use measured changes in σ_b to calculate ongoing rates of nitrate reduction. To test this hypothesis we present the results of an experiment involving a column reactor inoculated with a mixed culture of bacteria from the environment. NO_3^- and acetate were added to the influent for this reactor to function as the TEAP and electron donor respectively. We measured effluent concentrations of NO_3^-, NO_2^-, Fe(II), acetate, and NH_4^+ to quantify the effects of NO_3^- reduction and biomass growth on measured changes in σ_b.

In an attempt to scale our findings from the laboratory to the field, we also present the results of a reactive tracer test conducted at the Massachusetts Military Reservation on Cape Cod, MA. A tracer containing $NaNO_3$ as a TEAP and NaBr as a chemically conservative marker was injected into a portion of the aquifer known to have conditions favorable for iron reduction (i.e. low concentrations of more energetically favorable TEAPs like O_2 and NO_3^-) to stimulate the reduction of NO_3^-. We suspected that bacterial respiration in the Fe-reducing zone was limited by the availability of TEAPs. Therefore, increasing the concentration of an energetically favorable TEAP (NO_3^-) should increase rates of bacterial growth and respiration. Conservative species like Br^- are not expected to chemically react as they are transported through the aquifer. A decrease in Br^- concentration $[Br^-]$ can therefore be used to quantify diffusion and dispersion [e.g., *Knutsson*, 1966]. The field research was conducted in collaboration with Doug Kent, Dick Smith and Deb

Repert and some of the observations have been treated with models developed by Doug Kent, USGS Menlo Park. The research in this chapter was informed by this collaborative effort.

Background

Relation between solute concentration and bulk electrical conductivity

Fluid electrical conductivity (σ_f) is a function of the concentration of ions in solution:

$$\sigma_f = F\sum_j \left|Z_j\right| C_j \mu_j . \tag{4.3}$$

Here σ_f is the fluid electrical conductivity (S/m), F is Faraday's constant (C/mol), C_j is the concentration of each ion (mol/m^3), Z_j is the charge of each ion and μ_j is the electrical mobility of each ion (m^2(V s)$^{-1}$). Changes in chemical concentration will affect σ_f in the following manner:

$$d\sigma_f = F\sum_j | Z_j | \mu_j dC_j . \tag{4.4}$$

In systems containing both sediments and an aqueous phase, measurements of electrical conductivity will reflect the electrical properties of both phases. The σ_b of a system containing sediments that are not conductive relative to the fluid phase can be described as a function of σ_f via an Archie's Law relationship:

$$\sigma_b = a^{-1}\sigma_f \phi^m = \frac{1}{\rho} \tag{4.5}$$

where ϕ is porosity, ρ is the apparent electrical resistivity in ohm-m, and *a* and *m* (dimensionless) are empirical parameters generally attributed to cementation and tortuosity [*Archie*, 1942]. The parameter *a* generally varies between 0.62-3.5 and *m* between 1.37-1.95 for unconsolidated sediments [*Balberg*, 1986].

Nitrate reduction

In contaminated aquifers, anoxic conditions are prevalent and nitrate reduction is a common pathway for bacterial respiration [*Christensen et al.*, 2001]. Previous work by Regberg et al. [in press] (Chapter 2) focused on changes in σ_b associated with dissimilatory iron reduction. Nitrate reduction in saturated aquifers is different from iron reduction in that most ferric iron is present as solid Fe(III)-oxides and that the reduction of Fe(III) usually involves dissolution and release of $Fe(II)_{(aq),}$ whereas NO_3^- is present as an aqueous species. In Chapter 2 we demonstrate that release of $Fe(II)_{(aq)}$ can increase the ionic strength of the pore fluid. In contrast, nitrate reduction does not necessarily change the ionic strength of a solution. Under optimal environmental conditions (i.e. low $[O_2]$ and ample concentrations of electron donor), NO_3^- will be completely reduced to N_2 gas in the series of sequential reactions (4.1, 4.6 – 4.8). Specifically, after NO_3^- is reduced to NO_2^- following the stoichiometry in Eq. 4.1, NO_2^- will then be reduced to NO:

$$NO_2^- + e^- + 2H^+ \rightarrow NO + H_2O. \tag{4.6}$$

NO will then be further reduced to N_2O:

$$NO + e^- + H^+ \rightarrow ½\, N_2O + ½\, H_2O. \tag{4.7}$$

Finally N_2O is reduced to $N_{2(g)}$:

$$½\, N_2O + e^- + H^+ \rightarrow N_{2(g)} + H_2O. \tag{4.8}$$

However, if conditions in an aquifer are suboptimal (i.e. dissolved $O_2 > 2.5$ mg/L [*Korner and Zumft*, 1989] or concentrations of electron donor are insufficient to fully reduce NO_3^-) only partial reduction will occur. If NO_3^- is completely reduced to N_2 or partially reduced to NO or N_2O, the ionic strength and σ_f decreases following Eq. 4.4. In contrast, partial reduction of NO_3^- to NO_2^- has little or no effect on σ_f since NO_3^- and NO_2^- have very similar molar conductivity values (7.15 S/m vs. 7.18 S/m respectively) [*Landolt-Bornstein*, 1969]. Previous research has focused on anomalous increases in σ_b that may be related to biotic activity in contaminated aquifers [e.g., *Atekwana et al.*, 2004]; here we hypothesized that it may be possible to monitor NO_3^- reduction using measured decreases in σ_b if NO_3^- is reduced to a non-ionic species like N_2O or N_2. If NO_3^- is fully reduced to N_2 or partially reduced to N_2O, the σ_f should decrease in a predictable manner.

Calculating the extent and amount of biomass growth

Directly measuring the rate and extent of biomass growth in a non-invasive manner is difficult [*Characklis*, 1990; *Christensen and Characklis*, 1990; *Thullner*, 2010]. Therefore, we use the concept of yield coefficients to calculate the amount and extent of biomass produced in our column reactor. Yield coefficients were originally developed to describe biomass growth in batch reactors. In a batch reactor, a yield coefficient relates changes in the concentration of substrate (in this case measured concentrations of acetate) over time to changes in the concentration of biomass produced and allows us to estimate biomass growth by measuring the amount of substrate consumed over time. We define the rates of growth of biomass and consumption of substrate in equations 4.9a and 4.9b and show how the growth of biomass can be written in terms of substrate using the growth coefficient in 4.9c [*Rittmann and McCarty*, 2001]:

$$\begin{aligned} R_{biomass} &= \frac{d[biomass]}{dt}, \\ R_{substrate} &= \frac{d[substrate]}{dt}, \\ R_{biomass} &= -\gamma \nu R_{substrate}. \end{aligned} \tag{4.9 a,b,c}$$

Here [*biomass*] (M) is the concentration of biomass and is expressed as $C_5H_7O_2N$, a simplified formula for biomass [*Rittmann and McCarty*, 2001]; [*substrate*] (M) is the concentration of substrate ; γ (unitless) is the yield coefficient and ν (unitless) is the stoichiometric coefficient of the biomass growth reaction. The primary assumption underlying Eq. 4.9c is that the substrate is only consumed for respiration and cell maintenance or the production of new biomass. γ can have values ranging between 0, indicating that no new biomass is produced, and 1, indicating that all of the available substrate is used to generate new biomass. For heterotrophic bacteria, γ values greater than 0.5 are not generally realistic [*Rittmann and McCarty*, 2001]. We use the following equation to describe biomass growth based on acetate consumption and obtain values for ν [*Rittmann and McCarty*, 2001]:

$$0.05NH_4^+ + 0.125CH_3COO^- + 0.075H^+ \rightarrow 0.05C_5H_7O_2N + 0.15H_2O. \qquad (4.10)$$

Using Eq. 4.10, $\nu = 0.05/0.125$. In a simple system γ can be calculated using a mass balance approach. For example, it is common to assume that NH_4^+ is only consumed for the generation of biomass and not for respiration or cellular maintenance [*Rittmann and McCarty*, 2001]. If this is true, we can use the stoichiometry from Eq. 4.10 to calculate γ based on the relative rates of NH_4^+ and acetate consumption. In this system it is possible that NO_3^- is being directly reduced to NH_4^+. The effects of this reaction on estimating γ are discussed later. For a flow-through reactor, the following equation is commonly used to calculate the net rate of reaction in the column:

$$R_x = ([x]_{out} - [x]_{in})Q \qquad (4.11)$$

Here R_x is the rate of consumption of species x (mol/day), Q is the flow rate (L/day), and $[x]_{out}$ and $[x]_{in}$ are the effluent and influent concentrations of species x (M). Strictly speaking, Eq. 4.11 is only accurate for concentration data from continuously stirred tank reactors or for zeroth-order reactions modeled from data for flow reactors [*Brantley and Conrad*, 2008]. When Eq. 4.11 is used for a column reactor, we are implicitly assuming that no significant concentration gradients that affect the reaction rate exist inside the column. While this assumption is unlikely to be true, treating the column this way allows the assessment of a net, column-integrated rate for systems where the stoichiometry of the reaction is unknown. For example, this general approach is often used to assess reaction rates for field systems where the complex stoichiometry of multiple reactions can be difficult to constrain. Here, we use the consumption rates from Eq. 4.11 in combination with the stoichiometry from Eq. 4.10 to calculate a net, column-integrated estimate for γ:

$$\gamma = \frac{R_{NH_4^+}}{R_{acetate}} \frac{0.125}{0.05} . \tag{4.12}$$

Here $R_{NH_4^+}$ and $R_{acetate}$ are the rates of NH_4^+ and acetate consumption calculated using Eq. 4.11 (μmol/day) and 0.125 and 0.05 are stoichiometric coefficients from Eq. 4.10. We test this approach for the column reactor, but note that in more complex experiments it may be necessary to estimate γ from previously published values for similar conditions. Nonetheless, inverse modeling of column experiments must start with an assumed yield coefficient, and the approach outlined herein may be useful to estimate the first value of this coefficient in an iterative modeling method.

Laboratory methods

Data collection

A column reactor (20.3 cm long, 7.6 cm I.D.) constructed of acrylic pipe was packed with 1552 g of dried, sieved iron mineral-bearing subsurface sediment (2 wt %. Fe) from Oyster, VA [*Penn et al.*, 2001]. These sediments are similar to those found at Oyster, VA and Cape Cod, MA; they are primarily quartz with minor amounts of feldspar and Fe-oxide coatings. These sediments are commonly used in flow-through column reactors to observe biologically mediated reduction kinetics [e.g. *Roden and Zachara*, 1996; *Jeon et al.*, 2005; *Scheibe et al.*, 2006]. The column was inoculated with a consortium of environmental micro-organisms by adding shallow subsurface sediment from Dorn Creek in Madison, WI in a 9:1 ratio by mass. The sediment from WI has abundant organic material and is more likely to contain a diverse population of micro-organisms than the organic-poor sediments from either the Cape Cod or Oyster sites. Sterile, anoxic, PIPES-buffered artificial ground water (PBAGW) containing NaCl (0.15 g L^{-1}), $CaCl_2$ (0.30 g L^{-1}), $MgCl_2$-$6H_2O$ (0.50 g L^{-1}), KH_2PO_4 (0.006 g L^{-1}), NH_4Cl (0.01 g L^{-1}), PIPES (3.35 g L^{-1}), trace elements and vitamins was amended with enough acetate and nitrate to obtain concentrations of 0.1 mM and 2 mM respectively. Acetate and nitrate were added to encourage NO_3^- reduction. A syringe pump was used to pump PBAGW upward through the column at a flow rate of 2 ml hr^{-1}. Fluid was pumped from a gastight, glass syringe through Teflon tubing into the column. Initial effective porosity was 0.33 as measured by injecting NaBr tracer at a known flow rate and measuring the amount of time necessary to recover 50% of the mass of the tracer from the column [*Knutsson*, 1966; *Freeze and Cherry*, 1979]. Effluent was collected in N_2-purged tubes and was analyzed for concentrations of aqueous species *i* in effluent, $[i_{(aq)}]_{out}$: $[acetate]_{out}$ (high performance liquid chromatography), $[Fe(II)_{(aq)}]_{out}$ (ferrozine) [*Stookey*, 1970], $[NH_4^+]_{out}$ (*o*-phthaldialdehyde) [*Holmes et al.*, 1999] and nitrate/nitrite (spectrophotmetry) [*Wetters and Uglum*, 1970]. Net column-integrated reaction rates were calculated using Eq. 4.11. In Eq. 4.11 a negative rate indicates consumption of a chemical species and a positive rate indicates production of a chemical species. The column was constructed and maintained by Flynn Picardal and Quanxing Zheng at Indiana University. I inserted the conductivity electrodes and was responsible for analyzing all of the electrical conductivity data.

Measurements of σ_b for the entire column were made by permanently inserting four electrodes into the center of the column. Each electrode, conductive only at the tip, was composed of a Ag/AgCl wire encased inside a glass tube filled with agar saturated with KCl. The first electrode was inserted at a point 2.96 cm from the inlet at the bottom of the column. Each subsequent electrode was inserted 4.8 cm higher along the column. An IRIS Syscal R2E resistivity meter measured σ_b twice daily by injecting a known current (0.1-0.2 mA) across the top and bottom electrodes and measuring the resulting voltage across the inner two electrodes.

The measured voltages were converted to conductances using Ohm's Law. Conductances were then converted to σ_b using the following equation:

$$\sigma_b = \kappa^{-1} S . \tag{4.13}$$

Here κ is the geometric factor (m) and S is the conductance (Siemens). A geometric factor of 10.7 m was calculated with COMSOL Multiphysics [*COMSOL*, 2008]. A model of the column was constructed in COMSOL and assigned a known σ_b of 0.01 S/m. The geometric factor is independent of σ_b and so the value of 0.01 S/m was chosen to simplify the model calculations. In the model, a 1 A current was injected across the current electrodes and the voltage was calculated across the voltage electrodes. These values were used to calculate the conductance and then Eq. 4.13 was solved for κ .

Reactive transport modeling

The reactive transport module in PHREEQC was used to model the effluent chemistry data from the column experiment [*Parkhurst and Appelo*, 1999]. PHREEQC is a computer code capable of equilibrium speciation as well as kinetic reactions and 1-D reactive-transport simulations. The column was modeled using the default database from version 2.17 [*Ball and Nordstrom*, 1991; *Parkhurst and Appelo*, 1999] with the following additions: reactions describing the deprotonation of acetate [*Stumm and Morgan*, 1996] and PIPES buffer [*Good et al.*, 1966] were added. The reactions for these two added species are summarized in Table 4.1. Additionally, equilibrium redox reactions for N were removed in order to treat these reactions kinetically. Nitrate reduction via acetate consumption was modeled as a kinetic reaction using the following dual Monod rate law [*Watson et al.*, 2003]:

$$R_{NO_3^-} = -k_{\max}[biomass]\frac{[acetate]}{K_{M\_acetate} + [acetate]}\frac{[NO_3^-]}{K_{M\_NO_3^-} + [NO_3^-]} . \tag{4.14}$$

In Eq. 4.14 $R_{NO_3^-}$ is the rate of nitrate consumption (mol L^{-1} sec^{-1}); $k_{\max}$, a first-order rate constant, is the maximum rate of acetate consumption (sec^{-1}); $[biomass]$ is the biomass concentration (mol L^{-1}). Biomass is represented with the generic formula $C_5H_7O_2N$. $K_{M\_acetate}$ is the Monod half saturation constant for acetate (M), and $K_{M\_NO_3^-}$ is the Monod half saturation constant for nitrate (M). Net biomass growth was modeled with the following rate law:

$$R_{biomass}^{net} = -R_{NO_3^-}\gamma\nu\beta - b[biomass] \tag{4.15}$$

where $R_{biomass}^{net}$ (g biomass hr^{-1}) is the rate of biomass growth. γ is the yield coefficient (moles biomass per mole substrate consumed), ν is the stoichiometry of biomass production as described by Eq. 4.10 (0.4), β is the molar mass of biomass as $C_5H_7O_2N$ (113 g mol^{-1}) and b is a decay constant used to account for the rate of death or inactivation of cells (hr^{-1}) [*Rittmann and McCarty*, 2001; *Scheibe et al.*, 2006]. The parameters used for these additional reactions are summarized in Table 4.1.

Site Description

The field-scale tracer studies were conducted on the Massachusetts Military Reservation (MMR) in the Northeastern Ashumet Valley, Falmouth, MA on Cape Cod (Fig. 4.1). Secondarily treated effluent pumped into infiltration beds associated with an on-base sewage treatment plant created a large plume of water contaminated with nitrate, phosphate, detergents and organic carbon at this site. The U.S. Geological Survey (USGS) has installed a large-scale array of multi-level sampling wells with more than 12,000 discrete sampling points [*LeBlanc et al.*, 1991]. The site is composed of unconsolidated glacial outwash containing sand and gravel sized particles of quartz (95 wt. %) and feldspar (5 wt. %). The outwash is approximately 35 m thick overlying unconsolidated Cretaceous sediments [*Oldale*, 1969]. The effective porosity has previously been measured at 0.39 and mean hydraulic conductivity is estimated to be 110 m day^{-1}. The water table is generally about 5 m below the land surface (BLS) [LeBlanc et al., 1991]. This portion of the Cape Cod aquifer is very homogenous [*LeBlanc*, 1984] and is considered to be one of the best-described aquifers in the world [e.g., *Repert et al.*, 2006; *USGS*, 2011].

For this experiment, we use one injection well (F625 M2) and multi-level samplers (MLS) located 1, 3 and 5 m down gradient from the injection well (Wells F625 M3, M5 and M10). Bulk electrical conductivity was measured in four wells (wells A, B, C and D) as described below (Fig. 4.1).

Field methods

Data collection

In the field-scale experiment, two reactive tracers were injected 6 days apart into the iron-reducing zone at well F625 M2 port 06WT, 1.64 m above sea level (ASL) (19.25 m below land surface (BLS)) (Figs. 4.1 and 4.2). The tracers were mixed in an N_2-purged, gas-impermeable bladder by adding $NaNO_3$, NaBr and B to 200L of groundwater pumped directly from the injection well. We assumed bromide was a conservative anion that did not react with the surrounding geologic media, and was carried through the aquifer with groundwater [*LeBlanc et al.*, 1991]. $NaNO_3$ was added as a reactive tracer to encourage nitrate reduction. Initial measured concentrations of Fe(II) and NO_3^- in samples from well F625 M2 at port 06 WT were 0.170 mM Fe(II) and less than 1 μM NO_3^-. This was consistent with previously reported measurements delineating the iron-reducing zone [e.g., *Walter et al.*, 1996; *Repert et al.*, 2006]. The first tracer contained 1.04 mM $NaNO_3$ and 1.16 NaBr. The second tracer, injected six days later, contained 1.12 mM $NaNO_3$, 1.26 mM NaBr and 0.520 mM B.

Water samples for chemical analysis were collected twice daily, from multi-level samplers (MLS) located 1, 3 and 5 m down gradient from the injection well (Wells F625 M3, M5 and M10 (Fig. 4.1). Samples from four discrete depths (19.05 m, 19.25 m, 19.46 m, and 19.66 m BLS) were collected at each MLS to sample the tracer. Concentration measurements are only reported for the wells located 1 m and 5 m downgradient (F625 M3 and F625 M10) of the injection well (Fig. 4.1) because the tracer did not clearly intersect any of the other MLSs. Concentrations of NO_3^-, NO_2^-, and N_2O, were measured at F625 M2 and F625 M10 to quantify the extent of NO_3^- reduction.

Anion, cation, and N_2O concentrations as well as fluid electrical conductivity and pH were measured on these samples. Samples were split into four fractions. The first fraction was filtered through a 0.45 μM filter and acidified with 2N HCl for cation analysis on a Thermo Jarrell Ash IRIS AP-DV_S Advantage (outfitted with a Sea-spray® nebulizer) inductively coupled plasma atomic emission spectrometer (ICP-AES) at the USGS lab at Menlo Park, CA (all analyses were supervised by Doug Kent, USGS). The second fraction was filtered and analyzed for anion concentrations on a Dionex model DX500 ion chromatograph (IC) with an AS15A-4 mm column. The third fraction was injected into a sealed serum vial that had been degassed with helium and spiked with 200 μL of 12 N NaOH. The headspace of this vial was subsequently injected into a gas chromatograph to determine N_2O concentrations [*Savoie and LeBlanc*, 1998]. IC measurements and N_2O measurements were made at Richard Smith's lab at the USGS office in Boulder, CO. σ_f and pH were measured in the field on the fourth fraction with Orion handheld conductivity and pH meters respectively. After measuring pH and σ_f, the fourth fraction was titrated with 0.01639 N H_2SO_4 to determine alkalinity [*Fishman and Friedman*, 1989].

Changes in σ_b were measured from monitoring wells located outside the predicted flow path (Wells A, B, C, and D) (Fig. 4.1). Twelve graphite electrodes (length = 5 cm) spaced 0.5 m apart were lowered down each well. In every well, the top electrode was located 16 m below land surface and the bottommost electrode 22 m BLS (Fig. 4.2). σ_b was measured on an IRIS Syscal Pro by injecting a known current across pairs of electrodes and measuring the resulting voltage across two different electrodes using a dipole-dipole array. This combination of four electrodes is commonly referred to as a quadripole. Six days before the first injection, combinations of two current electrodes and two voltage electrodes were used to make 1330 individual measurements of σ_b every hour. Measurements were collected where all four electrodes were located in a single well (in-well measurements) and measurements where the electrodes were located in two different wells (cross-well measurements). In-well measurements from well A, the well closest to the injection location, were the only ones that responded to the presence of the tracer. Several phenomena contribute to changes in ionic strength, and thus σ_f, in the experiment. For example, decreases in the concentration of Na^+ and Br^- due to dilution, dispersion and diffusion cause σ_f to decrease. Consumption of NO_3^- and production of N_2O via Eqs. 4.1, 4.6 and 4.7 will also cause σ_f to decrease. Measured changes in concentrations of aqueous species were used to calculate expected changes in σ_b following the method outlined in *Regberg et al.* [In Press]. Changes in σ_f due to changes in ionic concentrations can be related to changes in measured σ_b using Eq. 4.5 with $a = 1$ and $m = 1.7$ [*Singha and Gorelick*, 2005].

Numerical modeling

We created a reactive transport model of the first tracer injection in PHAST, a three-dimensional reactive-transport code [*Parkhurst et al.*, 2004] that can model both kinetic and equilibrium reactions to compare calculated changes in aqueous chemistry with field measurements. PHAST uses the same chemical databases as PHREEQC, and also calculates the fluid electrical conductivity (σ_f) for each node inside the model domain. Chemical reactions investigated at the column scale with PHREEQC can be directly imported into PHAST and used to calculate changes in chemical concentration at the field scale.

The model domain in PHAST was an 8-m cube with 2,560 individual voxels each having a volume of 0.2 m^3. The effective porosity was set equal to 0.39. Vertical and horizontal hydraulic conductivity was 80 and 40 m/day respectively [*LeBlanc et al.*, 1991]. The hydraulic gradient was defined as 0.015 and was set based on a 3-point measurement made prior to beginning the tracer experiment [LeBlanc, personal communication]. Dispersivity was defined as 0.0001 m. This small dispersivity value was set to match the measured [Br^-] at 19.25 m BLS at well F625 M3, 1 m down gradient from the injection well. PHAST is known to have high numerical dispersion [e.g., *Parkhurst et al.*, 2003], and using larger values for dispersion causes the predicted [Br^-] to be too low at well F625 M3. The model ran for 10 days with a 30-min time step. PHAST automatically subdivides this time step to model kinetic reactions and dispersion [*Parkhurst et al.*, 2004]. Additional model parameters for the PHAST simulations are outlined in Tables 4.2, 4.3, and 4.4.

We simulated three different scenarios for the field scale tracer in PHAST. In the first scenario, the tracer was allowed to transport conservatively through the system but NO_3^- was not consumed. This scenario represents a base case where the change in σ_b is due only to movement and dilution of the tracer. In the second scenario, we included cation-exchange reactions where a single divalent cation (e.g., Fe^{2+}, Ca^{2+}) exchanges from the aquifer materials with two monovalent cations (Na^+) in solution. Cation exchange was constrained by changes in total [$Fe_{(aq)}$] and [Ca^{2+}] measured at 1 m down gradient at F625 M3 (Fig. 4.3). In the third simulation we included transport, cation exchange, and conversion of NO_3^- to N_2 at a constant rate such that 30% of the initial [NO_3^-] was consumed over a 1 m transport distance, as observed for the [NO_3^-] measured at F625 M3 (Fig. 4.3).

Calculated σ_f values for each of the 0.2 m^3 voxels in the model domain were converted to σ_b using Eq. 4.5 with $a = 1$ and $m = 1.7$ as with the field data. A forward model was also used to predict σ_b measured with our in-well electrodes. We utilized the forward model in RESINVM3D [*Pidlisecky et al.*, 2007] to calculate expected σ_b values for the electrodes located inside well A.

Changes in measured σ_b for each quadripole are reported as a % difference using the following formula:

$$\% \text{ difference} = \left(\frac{\sigma_b^t - \sigma_b^o}{\sigma_b^o} \right) * 100 \tag{4.15}$$

where σ_b^t is the bulk conductivity at time t (S/m) and σ_b^o is the background bulk conductivity (S/m) calculated by averaging 144 individual σ_b measurements for each quadripole collected hourly for six days before the tracer was injected.

Results

Column geochemical measurements

The flow rate as determined by measuring mass of effluent each day remained constant at 2 ml hr^{-1} for the course of the 198 day experiment. Influent [NO_3^-] was 2 mM. Values of [NO_3^-]$_{out}$ initially dropped to 0.2-0.4 mM, presumably due to NO_3^- reduction, and then increased to a steady-state concentration of 1.2 mM by day 50 (Fig. 4.4). This corresponds to a steady-state reduction rate of 40 μmol/day based on Eq. 4.11 (Fig. 4.5 A). The large variability in measured [NO_3^-]$_{out}$ may be due to the development of zones of less-mobile porosity and will be discussed at length later.

Influent [NH_4^+] was 0.190 mM. [NH_4^+]$_{out}$ was initially below detection (<0.1 μM) and then increased to a maximum of 0.19 mM on day 56. By day 70, [NH_4^+]$_{out}$ reached a steady state value of 0.12 mM, corresponding to a steady-state consumption rate of 3 μmol/day (Fig. 4.5 C).

Influent [NO_2^-] was below detection limits (< 5 μM). [NO_2^-]$_{out}$ reached steady-state values of 0.11 mM by day 60, a steady-state production rate of 5 μmol/day. Influent [acetate] was 0.1 mM. [acetate]$_{out}$ was initially 0.22 mM and fell below detection limits by day 25, a steady-state consumption rate of 4.5 μmol/day. $[Fe(II)_{(aq)}]_{out}$ was below detection (<5 μM) after day 5 (Fig. 4.4).

Column electrical conductivity measurements

σ_b measured across the column beginning on day 70 was constant at 0.07 S/m until day 145. On day 146, σ_b began to increase rapidly. σ_b reached a maximum value of 7 S/m by day 181 (Fig. 4.6). We calculated σ_f from measured ionic concentrations using Eq. 4.3. These σ_f values remained between 0.276 and 0.288 S/m throughout the experiment, varying largely due to changes in $[NO_3^-]$. The calculated changes in σ_f could not account for the measured 10-fold increase in σ_b after day 150 (Fig. 4.6) using any values of *a* or *m* that are within the range described above.

Field Geochemical Measurements

Tracer concentrations were monitored in samples collected from wells F625 M3 and F625 M10, located 1 and 5 meters downgradient of the injection site, respectively (Fig 4.1). All concentrations are reported as normalized dimensionless values (measured concentration / initial concentration) where a value of 1 indicates no change in concentration of the injected tracer solution.

At the well 1 m from the injection point , F625 M3, $[Br^-]$ began to increase on day two. $[Br^-]$ reached a maximum of 0.9 ± 0.025 on day three and decreased to background values by day six (Fig. 4.7). NO_3^- followed a similar pattern at the F625 M3, increasing from background values on day two, reaching a maximum of 0.7± 0.025 on day five, and returning to background levels by day six. The lower maximum value of 0.7 indicates that 20 – 30% of the nitrate was consumed over the 1-meter transport distance between the wells.

Concentrations of N_2O were normalized to initial NO_3^- concentrations in the following manner:

$$[N_2O]_{norm} = \frac{2*[N_2O]}{[NO_3^-]_o}. \tag{4.16}$$

Here $[N_2O]_{norm}$ is the normalized concentration of N_2O (unitless), $[N_2O]$ is the measured concentration of N_2O (M), and $[NO_3^-]_o$ is the initial measured concentration of NO_3^- measured before the tracer was injected (M).

Elevated concentrations of N_2O measured in the same samples from well F625 M3 that showed an increase in [Br^-] and [NO_3^-] also showed evidence of NO_3^- reduction to N_2O Normalized N_2O concentrations began to increase on day 2 and reached a maximum of 0.2 ± 0.025 on day 6, i.e., one day after the maximum NO_3^- concentration was reached. This is consistent with reduction of most of the NO_3^- to N_2O (Fig. 4.7).

At the sampling well 5 m downgradient, F625 M10, the signal from the first tracer was attenuated relative to F625 M3 (1 m downgradient). At F625 M10, Br^- concentrations began to increase on day nine and reached a maximum of 0.4± 0.025 on day 12. This lower maximum value for Br^- at F625 M10 is consistent with dispersion of the tracer plume (Fig. 4.7). NO_3^- and N_2O followed a similar pattern reaching maxima of 0.15 ± 0.025 and 0.05± 0.025 on day 12. Solutions did not attain the original background concentrations until day 14.

The second tracer, injected on day six, showed larger changes in [NO_3^-] than the first. Br^- from the second tracer reached the well F625 M3 (1 m downgradient) on day seven and reached a maximum concentration of 0.9± 0.025 on day eight (Fig. 4.7). NO_3^- and N_2O reached maximum concentrations of 0.6± 0.025 and 0.3± 0.025 on day nine. In the second tracer experiment, 30-40% of the NO_3^- was reduced to N_2O over 1 meter. Br^- reached well F625 M10 (5 m downgradient) on day 15 and reached a maximum concentration of 0.5± 0.025 on day 19. No NO_3^- was measured from the second tracer at well F625 M10. A small amount of N_2O (0.05) was measured on days 18 and 19.

Using the physical and chemical parameters outlined in Tables 4.3, 4.4 and 4.5 for PHAST, we were able to match the measured breakthrough curves for Br^- and NO_3^- at the well 1-m downgradient (F625 M3) from the injection site (Fig. 4.3). The breakthrough curves for Br^- and NO_3^- were so small at the well 5m downgradient (F625 M10) that we did not try to directly match them. Therefore, the reactive transport model is consistent with the observations for the field tracer experiment.

Field electrical conductivity measurements

Geophysical monitoring well A was the closest well to the injection site (Fig. 4.1) and is the only well that recorded any changes in σ_b subsequent to the injection of the tracer. Stacking errors, on average, were 0.26% ± 0.078%.. As the tracer was injected, quadripoles centered between 19.25 and 23.75 m BLS, consistent with the 19.25 m BLS injection depth, recorded an increase in σ_b of 1 – 1.5% from background values (Eq. 4.15) (Fig. 4.8). This increase occurred during the first 20 hours of the experiment. After hour twenty, σ_b values slowly returned to background levels over the next 100 hours. This change in σ_b was observed for both tracers at the same electrodes and over similar time periods. Quadripoles centered above 19.25 m BLS did not record any significant changes in σ_b.

Geophysical monitoring wells B, C, and D did not record any significant changes in σ_b subsequent to injection of the tracer (Fig. 4.9). Measurements of σ_b between wells also failed to capture the presence of a conductive tracer. This lack of a measureable signal is consistent with the small changes that were recorded in the in-well measurements from well A. The cross-well measurements encompass a larger area than the in-well measurements and are less sensitive to small changes in σ_b. Notably, the measurements from well B were especially noisy; background measurements of σ_b fluctuated by as much as 20% from one another (Eq. 4.15). The electrodes in well B were not reliable.

Discussion

Column experiments

Additional organic carbon

Our conceptual model of the column experiment requires multiple chemical processes in order to be consistent with measured variations in effluent chemistry. The processes include anion adsorption reactions, cation exchange reactions, NO_3^- reduction reactions, biomass growth and the generation of less-mobile porosity. Initially, there were two sources of organic carbon in the column. One source, 0.1 mM acetate, was continuously pumped through the column. The steady-state consumption rate of NO_3^- from day 100 to day 198 is attributed to oxidation of this acetate. We believe that lower $[NO_3^-]_{out}$ from day 1 to day 50 is caused by the presence of an additional pool of organic carbon that was presumably bound to the sediments (This is discussed more fully below). Our model treatment attributes the attainment of steady-state $[NO_3^-]_{out}$ values to acetate consumption, but the initial transient is attributed to the sediment-bound organic matter. This additional pool of carbon spurred rapid rates of biomass production from day 1 to day 50. This new biomass may have created areas of less well-connected porosity as well as surface sites capable of adsorbing NO_3^- and NO_2^- and cation exchange sites capable of exchanging Na^+ for NH_4^+ [e.g., *Thullner et al.*, 2002]. Less-mobile pore space associated with surface sites and exchange sites can explain the slower than expected increase in $[NO_3^-]_{out}$ from day 50 to day 100. This conceptual model is further explained and justified below.

Over the course of the 198-day experiment in the column reactor, 0.584 mmoles of NH_4^+ were consumed based on the cumulative moles of NH_4^+ injected into the column minus the cumulative moles of NH_4^+ released in the effluent. We assume that NH_4^+ is only consumed during biomass growth and not for respiration and cellular maintenance [*Rittmann and McCarty*, 2001]. Using the stoichiometry from biomass growth (Table 4.5, Eq. C), we conclude that 0.2336 mmol of acetate or 1.869 meq e^- were necessary to produce 0.584 mmoles of biomass. This corresponds to a yield coefficient of 0.08, calculated by performing a mass balance calculation to account for all of the organic carbon consumed in a batch reactor, which is well below previously the reported value of 0.20 for denitrifying bacteria grown on acetate in batch experiments [*Watson et al.*, 2003]. However, many denitrifying organisms can convert NO_3^- directly to NH_4^+, so the true yield coefficient may be larger than what we calculated from NH_4^+ consumption [e.g., *Knowles*, 1982; *Korom*, 1992].

For the reactive transport model to be consistent with measured $[NH_4^+]_{out}$ between day 0 and day 70, it was necessary to add cation exchange reactions between Na^+ and NH_4^+ (Table 4.1). The reactive transport model was consistent with the transient increase in $[NH_4^+]$ when the logarithm of the equilibrium constant (log K) for NH_4^+ exchange was equal to 0.9. The log K for Na^+ exchange was set equal to -2. We assumed there were 0.00404 moles of exchange sites dm^{-3} sediment. This is consistent with the concentration of surface sites used to create prior reactive transport models for the Oyster sediments [*Scheibe et al.*, 2006].

The cumulative moles of NO_3^- injected into the column do not match the cumulative moles of NO_3^- plus the cumulative moles of NO_2^- released as effluent. In total, 18.117 mmoles of nitrate were injected into the column. Some of this nitrate was oxidized to nitrite (0.717 mmol) and some passed right through the column (6.09 mmol). The remaining 11.31 mmol of NO_3^- are unaccounted for. Many species of nitrate-reducing bacteria can reduce NO_3^- to NO, N_2O, NH_4^+ or even N_2 [e.g. *Korom*, 1992; *Rittmann and McCarty*, 2001; *Watson et al.*, 2003]. Given that we measured concentrations of some of these species it is likely that the remaining nitrate was further reduced to these species that we did not measure. However, there is a problem with this hypothesis: the organic carbon added as acetate does not have enough electron-donating capacity to reduce the 11.31 mmoles of NO_3^- consumed inside the column to NO_2^- let alone NO, NH_4^+ or N_2O. Acetate was the sole electron donor added to the column, and 0.827 mmoles of acetate were oxidized over 198 days. The consumption of acetate releases 8 eq e^- mol^{-1}. Therefore, 6.616 meq e^- were released from the 0.827 mmoles of acetate consumed. Based on the cumulative amount of nitrite produced (0.717 mmoles) and the stoichiometry of Eq. 4.1, only 1.43 meq of these available electrons were consumed by nitrite production. Biomass growth accounted for at least another 1.869 meq e^- based on the cumulative amount of NH_4^+ consumed. The remaining pool of electrons (3.313 meq) is not enough to fully reduce 11.31 mmol of nitrate.

According to the stoichiometries outlined in Eqs. 4.1, 4.6, 4.7, and 4.8, reduction of 1 mole of NO_3^- to NO requires 3 moles of electrons, reduction to N_2O requires 8 moles of electrons, and complete reduction to N_2 requires 10 moles of electrons. To reduce the remaining nitrate, somewhere between 33.93 and 113.1 meq e^- are needed. This discrepancy is attributed to the presence of labile organic carbon in the sediment that temporarily acted as an electron donor in addition to the acetate in the influent. For example, *Zhang et al.* [1998] measured an average of 417 ± 224 μg C/g sediment for sediments collected from the Oyster, VA site. *Musselwhite et al.* [2002] measured a similar average value of 587 ± 163 μg C/g sediment. We believe that there is an additional pool of organic carbon in the column reactor providing electron-donating capacity to reduce the NO_3^- to NO or N_2O.

The likely amount of labile organic carbon in present in the column is consistent with previous findings [e.g., *Zhang et al.,* 1998; *Musselwhite et al.,* 2002] If we assume, based on previous work, a generic formula of CH_2O for this organic matter and an electron-donating capacity of 4 eq e^-/mol [e.g., *Abrams and Loague*, 2000; *Parkhurst et al.*, 2003; *Watson et al.*, 2003], then there are between 21.6 and 30.3 mmol (86.4 – 121.2 meq e^-) of additional organic carbon present inside the column. Furthermore, this organic carbon must be assumed to have sufficient electron-donating capacity to reduce the missing nitrate to N_2O. As discussed above., the depletion of this organic carbon reservoir inside the column explains the decreasing rate of nitrate reduction with time (Fig 4.4). Nitrate reduction rates at the start of the experiment were twice as high as steady-state values obtained after day 50 (100 μmoles/day vs. 40 μmoles/day). In our model, once organic carbon in the column was consumed, nitrate reduction rates became limited by the flow of acetate into the reactor and decreased accordingly. This hypothesis allows us to explain the decreasing rate of nitrate reduction measured in the column's effluent.

Reactive transport modeling of the column experiment with PHREEQC confirms that another pool of organic carbon is necessary to match the consumption of NO_3^- from day 0 to day 50. Predicted $[NO_3^-]_{out}$ was consistent with measured $[NO_3^-]_{out}$ from day 0 to day 50 when 10 mmoles (6.44 μmol g^{-1} sediment) of organic carbon were added as a consumable substrate. This is slightly less than the reported range of organic carbon concentrations (13.91 – 19.52 μmol g sediment^{-1}) [*Zhang et al.,* 1998; *Musselwhite et al.,* 2002. A second rate law was added to the PHREEQC database to account for reduction driven by this pool of organic carbon (Table 4.1). The rate law had the same form as Eq. 4.14 and all of the same values for the reaction constants. However, a second biomass growth reaction was written to account for the different stoichiometry:

$$0.05NH_4^+ + 0.25CH_2O \rightarrow 0.05\ C_5H_7O_2N + 0.15H_2O + 0.05H^+ \quad . \qquad (4.17)$$

While adding a source of labile organic carbon to our model can explain the low $[NO_3^-]_{out}$ from day 0 to day 50 (Fig. 4.4), it cannot explain the slow increase in $[NO_3^-]_{out}$ from day 50 to day 100. In our reactive transport model, the sediment-bound organic carbon is completely consumed by day 50. At that point the calculated nitrate reduction rate decreases to a steady state value of 1.5×10^{-5} mol day^{-1}. This rate is limited by the complete consumption of the 0.1 mM acetate in the influent solution. The residence time of a pore volume in this column is about six days.

Therefore, the model predicts that $[NO_3^-]_{out}$ reaches steady-state values around day 56, not day 100.

There must be another process retarding the transport of NO_3^- through the column. It is possible that there is some sort of reactive surface adsorbing NO_3^- and causing $[NO_3^-]_{out}$ to increase more slowly than we would expect. It is unlikely that mineral surfaces like iron oxides or quartz contain these sorption sites, since the pH of the influent and effluent was ~7. At neutral pH these surfaces are usually negatively charged [*Schindler and Stumm*, 1987; *Davis and Kent*, 1990]. However, in sewage treatment facilities, NO_3^- is observed to be strongly sorbed to clays [*Cengeloglu et al.*, 2006], red mud and organic carbon [*Ozturk and Bektas*, 2004; *Wang et al.*, 2007]. The subsurface sediment from Dorn Creek that we used as a microbial inoculum contained some organic matter. Also, as micro-organisms consumed the nitrate they presumably generated new organic matter in the form of biofilms and extracellular polysaccharides (EPS). Organic matter could provide surface sites for NO_3^- adsorption. We therefore modeled nitrate adsorption using the following reaction:

$$\equiv S^+ + NO_3^- \rightarrow \equiv SNO_3 \tag{4.18}$$

where $\equiv S^+$ represents a generic surface site. We also included a sorption reaction for NO_2^- in an attempt to describe a similarly slow increase in effluent $[NO_2^-]$ (Fig. 4.4):

$$\equiv S^+ + NO_2^- \rightarrow \equiv SNO_2 \, . \tag{4.19}$$

The log K value for Eqs. 4.18 and 4.19 was set equal to 3. Adding Eqs. 4.18 and 4.19 to the reactive transport model affects when effluent $[NO_3^-]$ begins to increase, but it does not affect the rate of that increase. In our model, when all of the surface sites are filled, the effluent $[NO_3^-]$ increases to steady-state values over a period of six days. In contrast, measured $[NO_3^-]$ took 100 days to reach steady-state values (Fig 4.4). Changing the log K value for Eqs. 4.18 and 4.19 changes the total amount of nitrate adsorbed but does not affect the rate of NO_3^- increase.

Changing the surface site density has a similar effect compared to changing the log K. Therefore, nitrate adsorption alone cannot explain the retardation of nitrate within the column.

Dual porosity

The delayed arrival of a chemical tracer is often attributed to processes related to less-mobile pore space, such as rate-limited mass transfer [e.g., *Haggerty and Gorelick*, 1995]. Rate-limited mass transfer describes pore space that is decoupled from the advective flow path. This disconnected pore space is accessible via diffusion or some similar process that is considerably slower than the advection. Rate-limited mass transfer is often modeled as a dual porosity [e.g., *van Genuchten*, 1985]. In these dual-porosity models, some portion of the model domain is designated as immobile pore space. Transfer between the mobile and immobile domains is generally described by the following first-order rate expression:

$$\frac{dM_{immobile}}{dt} = \theta_{immobile}\Delta_{immobile}\frac{dC_{immobile}}{dt} = \alpha(C_{mobile} - C_{immobile}) \qquad (4.20)$$

where t is time (s), $M_{immobile}$ is the moles of a species in the immobile zone, $\theta_{immobile}$ is the immobile porosity (dimensionless), $\Delta_{immobile}$ is retardation in the immobile zone (dimensionless), C is concentration (M), and α is the first-order exchange constant (s^{-1}) [*van Genuchten*, 1985; *Parkhurst and Appelo*, 1999]. Conceptually, a chemical species could enter this disconnected porosity and slowly diffuse back into the advective flow path, and the rate of movement along the flow path would be slow, explaining the slow increase in concentration as in Fig. 4.4.

Therefore, we added dual-domain porosity to our reactive transport model to explain the delayed increase in $[NO_3^-]_{out}$. The reactive transport model is consistent with measured $[NO_3^-]_{out}$ when $\alpha = 8.5 \times 10^{-7}\ s^{-1}$, and $\theta_{immobile} = 0.1$, i.e., approximately 30% of the effective porosity. We hypothesize that biomass growth may be responsible for the formation of immobile porosity. This seems reasonable since biomass has been shown to reduce porosity in column reactors by up to 90% [*Thullner et al.*, 2002]. Additionally, we hypothesize that the biomass contains the surface sites capable of adsorbing NO_3^- and NO_2^- following the stoichiometry outlined in Eqs.

4.18 and 4.19 and the cation exchange sites capable of exchanging NH_4^+ (Table 4.1). Therefore, only the immobile pore space contained adsorption sites and cation exchange sites. The log K value for both adsorption reactions (Eqs. 4.18 and 4.19) was set equal to 3. The surface was described with a reactive site density of 0.580 mmoles of surface sites per g of sediment. The log K and surface site density values were chosen to allow the model to be consistent with measured $[NO_3^-]_{out}$ and $[NO_2^-]_{out}$.

Biomass growth can cause porosity reductions in filters and flow-through reactors [e.g. *Or et al.*, 2007]. Systems with ample concentrations of N have been shown to be especially susceptible to bioclogging via cellular growth and the production of extracellular polysaccharides [*Thullner*, 2010]. The sediment-bound organic carbon present in the column may have spurred an initial phase of rapid biomass growth consuming all of the influent NO_3^- and occluding some porosity, producing a zone of immobile porosity. The use of a syringe pump prevented the flow rate from changing as this pore space was segregated. Syringe pumps operate by increasing the pressure until the desired flow rate is achieved. Unless the increase in pressure due to the porosity decrease overwhelmed the capacity of the pump, it would not have been detected as a change in flow rate. When the sediment-bound organic carbon was consumed, NO_3^- reduction decreased to steady-state rates, but the surface sites associated with organic matter remained unsaturated, causing $[NO_3^-]_{out}$ to remain lower than expected until the surface sites became saturated (Fig. 4.4).

Biofilm electrical conductivity

Regberg et al. [in press] have demonstrated that increasing amounts of biomass may represent electrically conductive pathways in a similar column under iron-reducing conditions. Since none of the chemical changes discussed above could be used to generate a composite chemical reaction (Table 4.5) that explains the measured 10-fold increase in σ_b, we propose biofilm electrical conductivity as a possible explanation for the late stage σ_b increase in this column as well.

To match the calculated $[NO_3\text{-}]_{out}$ with measured $[NO_3\text{-}]_{out}$ at the early portion of the experiment (day 0-50), we had to increase γ from the calculated value of 0.08 to a value of 0.20. This value is reasonable because it was used to describe a similar experiment involving nitrate-respiring bacteria [*Watson et al.*, 2003] so that calculated $[NO_3\text{-}]_{out}$ was consistent with measured $[NO_3\text{-}]_{out}$ at the early portion of the experiment (day 0-50) Using the value of γ calculated with Eq. 4.12 caused the calculated $[NO_3^-]_{out}$ to be greater than what was measured. However, it is also possible that the micro-organisms in the column were synthesizing NH_4^+ from the NO_3^- thus rendering Eq. 4.12 incorrect. Many nitrate-respiring organisms are capable of synthesizing NH_4^+ from NO_3^- [*Knowles*, 1982; *Korom*, 1992]. Using a generic stoichiometry for biomass of $C_5H_7O_2N$ [*Rittmann and McCarty*, 2001], and a γ value of 0.20 [*Watson et al.*, 2003], the PHREEQC model calculates that 55 mg of biomass were generated over the 198 day experiment. This is consistent with the value calculated by measuring the cumulative consumption of NO_3^- and assuming a steady-state production rate of 4 μmoles biomass/day (66 mg of total biomass). The calculation from PHREEQC is more accurate than the steady-state prediction because it explicitly accounts for concentration gradients within the column and transient effects in the experiment from days 0 – 100.

If the biomass produced in the column is creating zones of immobile porosity it may be capable of affecting σ_b as well. Using the values from PHREEQC in conjunction with a model adapted from percolation theory outlined in *Regberg et al.* [in press], we can calculate a theoretical value for biomass electrical conductivity using the following equation:

$$\sigma_b = a^{-1}\sigma_f\phi^m + (f_{\text{secondary}} - f_{\text{critical}})^{\omega}\sigma_{\text{secondary}} \tag{4.21}$$

where $f_{\text{secondary}}$ is the volume fraction of the new conductive material (in this case biomass), f_{critical} is the critical volume fraction at which there is enough new material to represent a connected electrical pathway, $\sigma_{\text{secondary}}$ is the electrical conductivity of this new conductive phase (S/m) and ω is a parameter similar to *m* that is related to tortuosity. In this model we followed the example in Chapter 2 and chose to keep ω fixed at 1.5. The value of f_{critical} was set equal to the volume fraction of biomass present on day 145 when σ_b began to rapidly increase. The second term in Eq. 4.21 is only utilized when $f_{\text{secondary}} > f_{\text{critical}}$.

For calculations in Chapter 2, *Regberg et al.* [in press] (Chapter 2) a carbon density of 531 kg C m^{-3} was assumed to determine the volume filled by the biomass grown in an iron-reducing column similar to the one modeled here. With this density, one mole of biomass as $C_5H_7O_2N$ (i.e., 60 g of C) has a mass of 113 g and occupies 1.1 x 10^{-4} m^3. If we use this volume per mole for biomass in the nitrate-reducing column, the calculated 55 mg of biomass grown in the column only occupies 0.018 % (5.5 x 10^{-5} Kg biomass x (60/113) / 531 Kg C m^{-3} = 5.5 x 10^{-8} m^3) of the total pore space (0.000297 m^3). At first inspection, this is inconsistent with the results from the reactive transport model that required 30% of the pore space to be immobile in order to describe the measured $[NO_3^-]_{out}$. However, this biomass could have grown across pore throats, occluding porosity without infilling it entirely. However, using these density values the biofilm would have to be very conductive (~7 x 10^5 S/m) in order to cause the measured increase in σ_b. This conductivity value is unrealistic and, changing the values of f_{critical} or ω will not significantly decrease the value of $\sigma_{\text{secondary}}$ necessary for Eq. 4.21 to be consistent with measured σ_b. Thus we conclude that the biomass in this reactor must be less dense than the values assumed in Chapter 2.

If the biomass is less dense, then $f_{\text{secondary}}$ would have to increase in Eq. 4.21 and $\sigma_{\text{secondary}}$ would have to decrease for the modeled value of σ_b to be consistent with measured increases. The reactive transport model required an immobile pore space equivalent to ~30% of the total pore space for model predictions to match measured $[NO_3^-]_{out}$. This is much greater than the 0.018% of the pore space we estimated assuming a very dense biofilm.

The retardation of effluent $[NO_3^-]$ was attributed to the formation of immobile porosity due to bioclogging. This situation did not occur in the columns reported by *Regberg et al.* [in press]. Both *Thullner* [2010] and *Or et al*. [2007] suggest that EPS production is often more responsible for bioclogging than cellular growth. EPS-containing biofilms are much less dense than bacterial cells alone and have carbon densities varying between 2.5 and 65 kg C m^{-3} [*Thullner*, 2010]. Because we observed evidence of immobile porosity in the form of retardation of effluent $[NO_3^-]$ and because NO_3^--respiring bacteria are known to produce EPS when ample N is available [*Bielefeldt et al.*, 2002], we conclude that our initial estimate of biomass density is too great to explain the measured increase in σ_b. Using the lower carbon densities for EPS-rich biofilms reported by *Thullner [2010]*, we estimate that the 55 mg of biomass occupies between 1.5 and 38% of the pore space inside the column. This is consistent with our estimate of the amount of immobile pore space needed to explain the retardation of $[NO_3\text{-}]$. Using these values in Eq. 4.21, the model described by *Regberg et al.* [in press] results in an estimate of biofilm electrical conductivity between 350 and 35,000 S/m. These values are large, but more reasonable that the value (7.5 x 10^5 S/m) obtained by assuming the biomass was composed solely of cells.

In summary we have demonstrated that measured σ_b is consistent with changes in fluid chemistry using the composite reaction in Table 4.5 from day 0 to day 145 as modeled using PHREEQC. After day 145, σ_b becomes decoupled from fluid chemistry, which we attribute to its dependence on the growth of conductive biofilm in the column. This is similar to the scenario described by *Regberg et al.* [in press] for a column reactor under iron-reducing conditions.

Field experiment

We expected the field-scale tracer test to affect σ_b in the same manner as the column reactors. However, this did not occur. In the field σ_b did not become decoupled from aqueous chemistry. Instead, the measured changes in σ_b due to the injection of the tracer were smaller than expected based on the results of the column experiment.

We were able to match the breakthrough curves of Br^-, NO_3^- and σ_f at the well F625 M3 (1 m downgradient) from the injection well (Fig. 4.3) using the reactive transport model PHAST in conjunction with the parameters described in Tables 4.3 and 4.4. Values of σ_f calculated from the PHAST output were converted to σ_b using Eq. 4.5. These calculated σ_b values were used to predict measured σ_b. While there is a clear trend in the measured data from well A, the well closest to the injection site, in-well measurements at wells B, C and D and cross-well measurements recorded no consistent changes in σ_b; consequently, we focus on 15 in-well quadripoles in well A. After removing measured values with a repeatability error >2% the remaining values had a mean repeatability error of 0.26% ± 0.078%. We measured a 1% increase in σ_b from background values at quadripoles in well A centered between 22.74 and 24.74 m below land surface.

Predicted increases in σ_b at these electrodes were only 0.25%, compared to the 1-1.5% change seen in the field data (Fig. 4.10). The following processes could be added to the model to match the field data: surface conductance, cation exchange, or increasing dispersion.. To match the measured increase in σ_b, the tracer would have had to have a maximum σ_f 10 times greater than that recorded, or 900 L of tracer would have to be injected instead of the 200 L actually injected. We were unable to match the change in σ_b measured in the field with our numerical models by including surface conductance or cation exchange in our reactive transport model. Including cation exchange increased the σ_f values of the tracer by 0.5% (0.0546 S/m vs 0.0549 S/m). Including surface conductance based on the formula described by *Sen et al.* [1988] increased σ_f values of the tracer by 9.5% (0.0546 S/m vs. 0.0598 S/m). Neither of these changes is enough to increase the predicted σ_f by the factor of 10 necessary to have modeled values of σ_b match measured values.

It is possible that the tracer was more disperse than predicted in the numerical model. A more disperse tracer would place conductive fluid closer to electrodes in Well A, and thus increase the calculated change in σ_b. Electrical conductivity methods are more sensitive to changes that occur close to the electrodes [e.g., *Day-Lewis et al.*, 2005]. Additionally, electrical conductivity methods detect larger more disperse objects better than smaller objects even if those objects are more conductive [*Singha and Gorelick*, 2005]. However, increasing dispersion caused the predicted breakthrough curves at the 1 m monitoring well to be inconsistent with measured values. In this case our electrical model is limited by the numerical dispersion inherent in PHAST, the reactive transport model.

It is instructive to compare the size and electrical conductivity of our tracer experiment to one that was successfully monitored. At the same site, *Singha and Gorelick* [2005] injected a non-reactive NaCl tracer. They were successful in monitoring the migration of this tracer over a 10-m distance. A comparison of the size and concentration of the injected tracers (Table 4.6) reveals that their tracer had an ionic strength 36 times larger than our tracer, had a σ_f 11 times greater and a total injected volume 35 times larger. Despite the fact that their tracer was ~ 2500% more conductive than the background fluid, measured increases in σ_b were only 15% greater than background conditions. Field-scale measurements of conductive tracers require large contrasts in

σ_b to produce readily interpretable results [e.g., *Rugh and Burbey*, 2008; *Dafflon et al.*, 2010; *Wilkinson et al.*, 2010]. To successfully observe a reactive tracer in the field it will be necessary to have a larger, more conductive tracer, especially in the presence of electrical conductivity consumption, which was expected in the work here. While the volume we chose to inject was easily observed with chemical measurements it was too small to be tracked with electrical geophysics. Alternatively, using a continuous tracer instead of a single pulse might allow future researchers to observe deviations from steady-state conditions similar to those observed in the column scale experiments. These deviations were presumably due to the presences and growth of electrically conductive biofilms. If conductive biofilms form at the field scale they will have to have a large spatial extent and/or contrast in electrical properties to cause a measureable change in σ_b.

Conclusions

Changes in σ_f and σ_b due to dissimilatory NO_3^- reduction are difficult to observe at the laboratory and field scale because NO_3^- reduction is often incomplete and a decrease in electrical conductivity is predicted, which can be confused with dispersion processes. Complete reduction of NO_3^- to $N_{2(gas)}$ may be measurable as a decrease in σ_f but partial reduction to NO_2^- does little to affect σ_f. We may be able to measure reaction rates at the laboratory and field scales using geophysical techniques if and only if σ_b is controlled by changes in fluid chemistry. It is possible that the use of electrical conductivity to infer biogeochemical reaction rates may be more straightforward for iron reduction than for nitrate reduction.

However, large increases in σ_b that are not correlated to changes in chemical concentration may be attributable to the formation of EPS-rich conductive biofilms in some cases. Such large increases were observed in column experiments for both dissimilatory iron reduction

(Chapter 2) and nitrate reduction (described here). If these biofilms are electrically conductive, we can estimate the extent and rate of biofilm growth based on measured changes in σ_b. This increase in σ_b in the nitrate-reducing columns described in this chapter is greater than seen in similar iron-reducing experiments It is possible that biofilms inside the column experiment may be more conductive and occupy a larger fraction of the available pore space than those forming the in Fe-reducing column.

Despite the larger effect observed in the nitrate reduction column, were unable to measure change in σ_b and attribute this to nitrate reduction in a field experiment. This is at least partly because ionic species that are easily detected using traditional chemical methods are effectively invisible to electrical geophysics due to their small size and low contrast from background σ_b. Future work at the field scale should focus on imaging larger volume tracers or on continuous tracers so that steady-state conditions can be established and observed. The models described in this chapter could furthermore be used to determine how to set up a field experiment that should have a measurable biotic effect. Achieving steady-state conditions would allow more time for biomass to form and would increase the likelihood of observing situations where σ_b becomes decoupled from changes in aqueous chemistry. Application of these geophysical techniques at the field scale is complicated by the resolution of current electrical conductivity methods, but the pilot experiments here show potential for the use of electrical methods to monitor biogeochemical activity in subsurface aquifers.

Table 4.1: Parameters used in PHREEQC model of Laboratory Data

Name	Parameter	Units	Value
Maximum acetate consumption rate	$k_{\max}$	s^{-1}	2×10^{-6}
Half saturation constant for acetate	$K_{M\_Acetate}$	M	5×10^{-5}
Half saturation constant for NO_3^-	$K_{M\_NO_3^-}$	M	8.1×10^{-6}
Yield Coefficient	Y	moles biomass (moles acetate consumed)$^{-1}$	0.20
Decay Coefficient	b	hr^{-1}	0.00208
Mobile Porosity	ϕ_{mobile}		0.23
Immobile Porosity	$\phi_{immobile}$		0.1
Exchange constant	α	s^{-1}	$8.5x10^{-7}$
Acetate		$CH_4CO_2 \rightarrow H^+ + CH_3CO_2^-$	Log K = -4.75
PIPES		$C_8H_{18}N_2O_6S_2 \rightarrow H^+ + C_8H_{17}N_2O_6S_2^-$	Log K = -6.76
NO_3^- Adsorption[a]		$\equiv S^+ + NO_3^- \rightarrow \equiv SNO_3$	Log K = 3
NO_2^-Adsorption[a]		$\equiv S^+ + NO_2^- \rightarrow \equiv SNO_2$	Log K = 3
Na^+ Exchange[b]		$X^- + Na^+ \rightarrow XNa$	Log K = -2
NH_4^+ Exchange[b]		$X^- + NH_4^+ \rightarrow XNH_4$	Log K = 0.9

a: $\equiv S^+$ represents a positively charged adsorption site

b: X^- represents a cation exchange site

Table 4.2: Physical Conditions For Field Scale Tracer Experiment

Model Domain	8 m x 8 m x 8m
Voxel Size	0.2 m^3
Effective Porosity	0.39
Horizontal Hydraulic Conductivity	80 m/d
Vertical Hydraulic Conductivity	40 m/d
Dispersivity	0.0001 m
Hydraulic Gradient	0.015
Injection Well Location	(4.7 m, 3.6 m)
Injection Depth	5.7 m – 6.3 m
Injection Rate	100 L/hr for 2 hr
Model Duration	10 d
Time Step	30 min

Table 4.3: Chemical Composition of the Field Scale Tracer. Significant differences in concentration between the in situ fluids and the tracer are highlighted **in bold**.

	Background Conditions	Tracer
pH	6.6	6.55
Temp[a]	25	25
C[b]	1103	1152
Na[b]	580	**2741**
Ca[b]	170	78
Mg[b]	53	54
Fe(II)[b]	175	178
Mn[b]	2.2	2.2
Sr[b]	0.08	0.09
Ba[b]	0.03	0.025
Br[b]	0.1	**1160**
N[b]	0	**1044**
Cl[b]	483	467
S[b]	100	100
P[b]	63	61
B[b]	2.6	2.7
Si[b]	227	232

a: °C

b: μM

Table 4.4: Cation Exchange Reactions Included in PHAST Models

Reaction[a]	Log k
$H^+ + Y^- = HY$	0
$Na^+ + Y^- = NaY$	-4.65
$K^+ + Y^- = KY$	-3.63
$Ca^{2+} + 2Y^- = CaY_2$	-6.72
$Mg^{+2} + 2Y^- = MgY_2$	-6.72
$Fe^{+2} + 2Y^- = FeY_2$	-6.72
$Mn^{+2} + 2Y^-$	-6.72
$Sr^{+2} + 2Y^- = SrY_2$	-6.72
$Ba^{+2} + 2Y^- = BaY_2$	-6.72

a: Y represents a generic cation exchange site.

s

Table 4.5: Composite Reactions

A) Nitrate Reduction	$0.5NO_3^- + 0.125CH_3COO^- \rightarrow 0.5NO_2^- + 0.125\ OH^- + 0.25CO_2 + 0.125H_2O$
	$0.2NO_3^- + 0.125CH_3COO^- + 0.325H^+ \rightarrow 0.1N_2 + 0.35H_2O + 0.25CO_2$
B) CO_2 Dissolution	$CO_2 + H_2O \rightarrow HCO_3^- + H^+$
C) Biosynthesis	$0.05NH_4^+ + 0.125CH_3COO^- + 0.075H^+ \rightarrow 0.05C_5H_7O_2N + 0.15H_2O$
	$0.05NH_4^+ + 0.25CH_2O \rightarrow 0.05C_5H_7O_2N + 0.15H_2O + 0.05H^+$
D) PIPES Buffering	$C_8H_{18}N_2O_6S_2 + OH^- \rightarrow C_8H_{17}N_2O_6S_2^- + H_2O$
E) Composite Reaction[a]	$2.44NO_3^- + CH_3COO^- + 0.032NH_4^+ + 0.152C_8H_{18}N_2O_6S_2 \rightarrow$ $1.12\ NO_2^- + 0.512N_2 + 0.032C_5H_7O_2N + 0.152\ C_8H_{17}N_2O_6S_2^- + 1.84HCO_3^- + 0.76H_2O$

a: Composite reaction is valid only for the steady state portion of the experiment after the labile organic carbon (CH_2O) had been consumed.

Table 4.6: Tracer Comparison

	Singha and Gorelick	Tracer 1	Tracer 2	Background
Conc. (mM)	37.6 mM NaCl	1.040 mM $NaNO_3$ 1.160 mM NaBr	1.120 mM $NaNO_3$ 1.260 mM NaBr	
σ_f (S/m)	0.47	0.0426	0.0479	0.0176
σ_b (S/m)	0.094	0.00852	0.00959	0.00352
σ_b % increase	142	172	257	
Tracer Volume (L)	~7000	200	200	

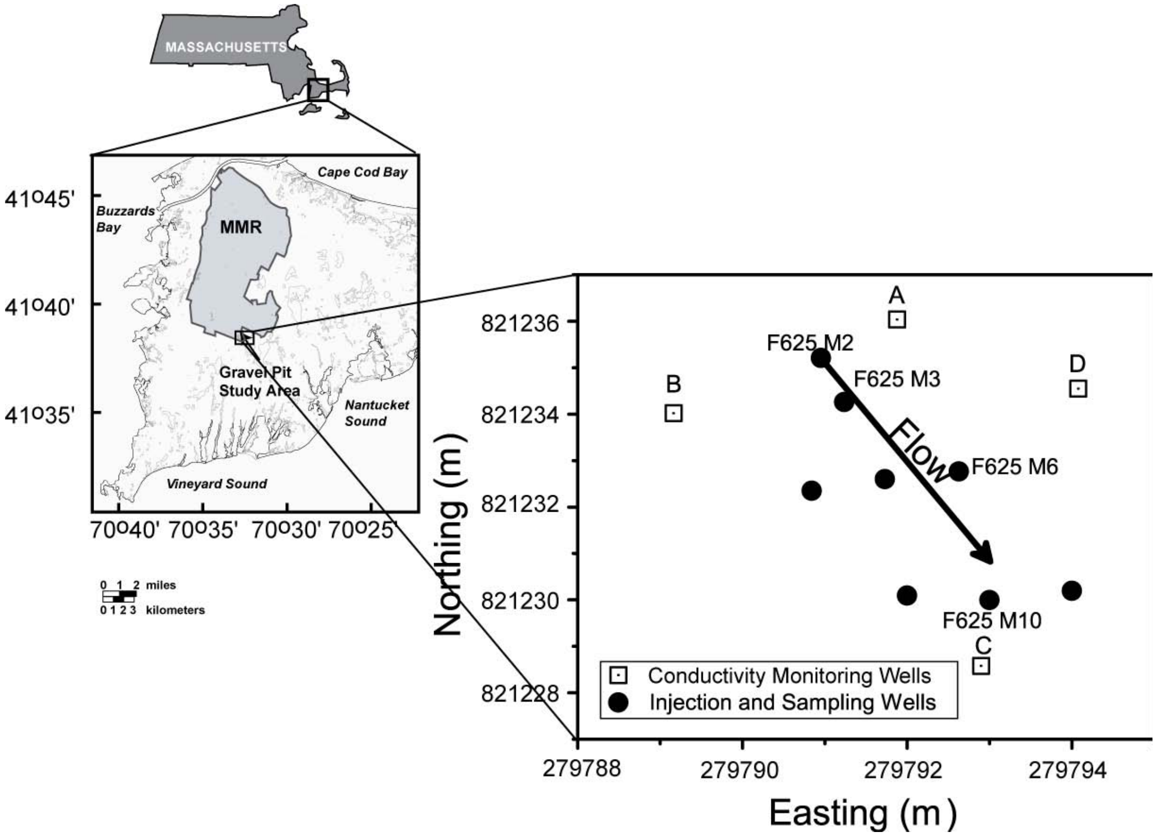

Figure 4.1: A map detailing the experimental setup at the Massachusetts Military Reservation (MMR) on Cape Cod. Conductivity monitoring wells (open squares) were located outside the flow path (arrow) and around the chemical monitoring wells (closed circles). The tracers were injected at the northernmost well (F625 M2) and flowed down gradient to the southeast. Chemical data was collected from all seven sampling wells but is only reported for two wells (F625 M3 and F625 M10) that were in the flow path of the tracer.

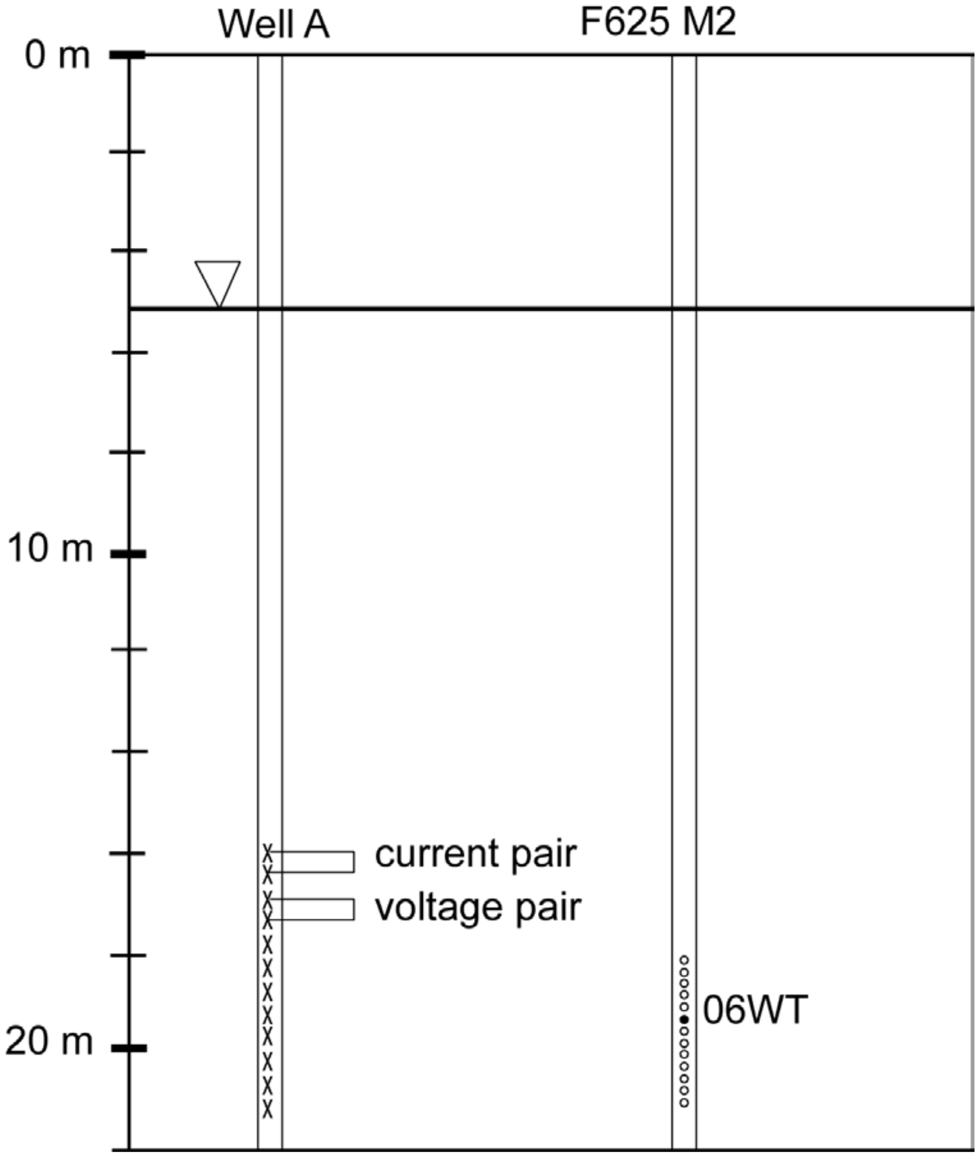

Figure 4.2: Schematic showing the electrode configuration in Well A and the sampling port configuration in well F625 M2. Electrodes are displayed as x's sampling ports are displayed as o's. The filled-in o represents the injection port. An example in well quadripole has also been highlighted.

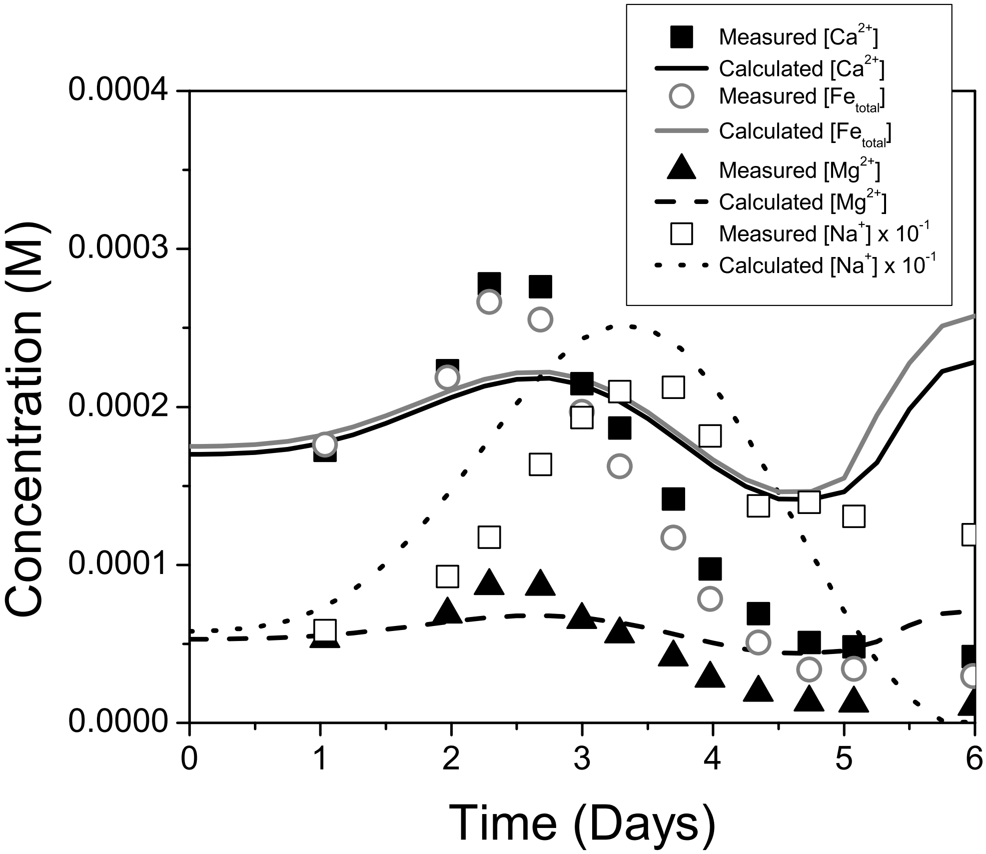

Figure 4.3: Chemical data (symbols) and PHAST predictions (lines) of the first reactive tracer passing the sampling well 1 m down gradient. The reactive transport model is consistent with the measured data for [Br$^-$] and [NO$_3^-$]. The predictions for the exchangeable cations are less consistent with measured concentrations due to poorly constrained cation exchange constants and high numerical dispersion inherent in the PHAST model.

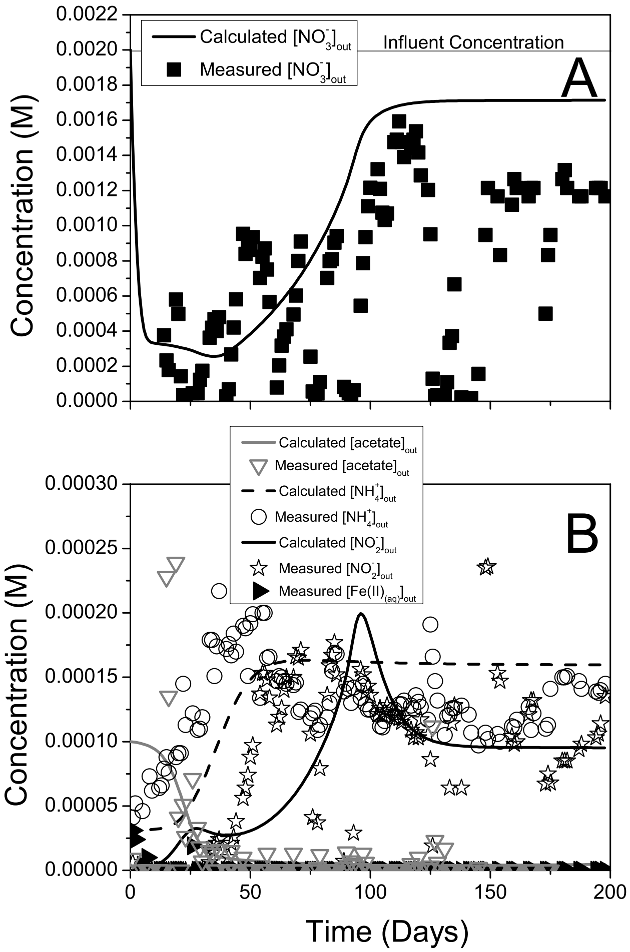

Figure 4.4: Effluent chemistry from the column experiment. (A) Influent $[NO_3^-]$ was 2 mM (thin line). Effluent $[NO_3^-]$ (squares = measured, black line = calculated) increases with time reaching a steady-state concentration around day 100. (B) $[NH_4^+]$ (open circles = measured, dashed line = calculated) and $[NO_2^-]$ (stars = measured, black line = calculated) also increase with time reaching steady state at 60 and 70 days respectively. Effluent [acetate] (triangles = calculated, grey line = calculated) decreases for the first 25 days until all of the acetate added is consumed within the column. There is no appreciable Fe(II) production (filled triangles). Lines represent predicted effluent concentrations from PHREEQC model.

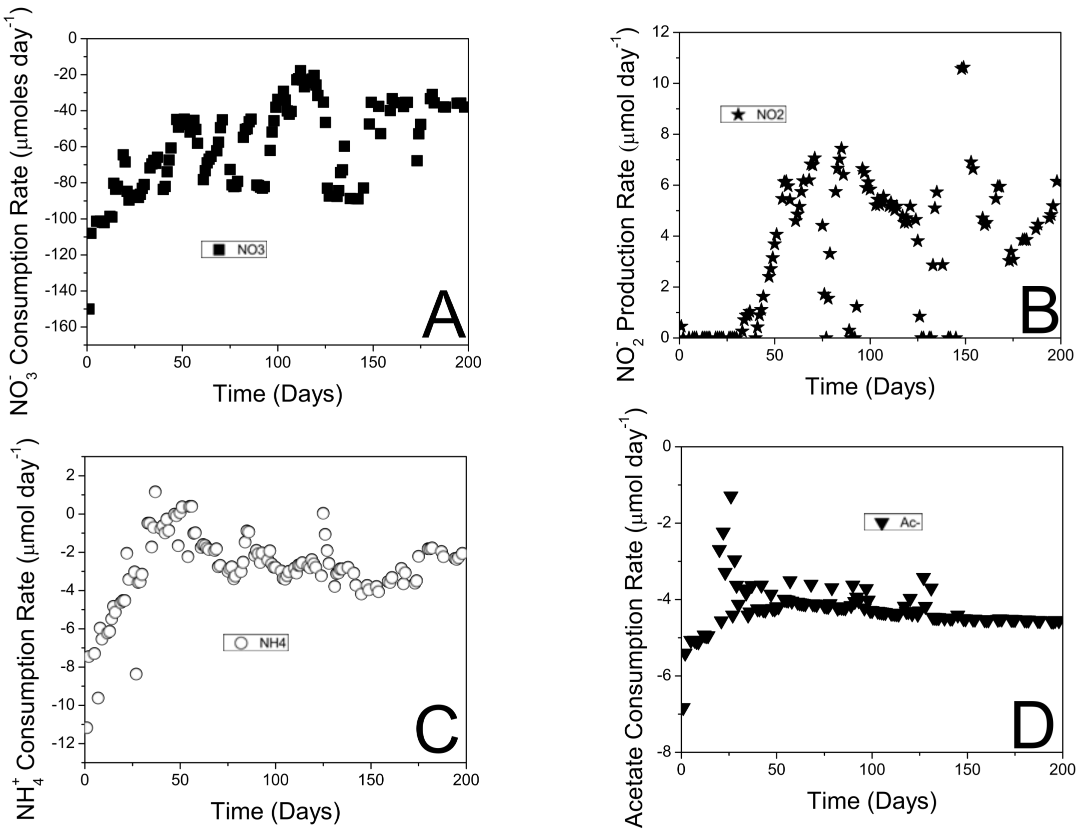

Figure 4.5: Instantaneous reaction rates versus time for the column experiment. Rates were calculated using Eq. 4.11. Positive rates indicate production of species (NO_2^- panel B); negative rates indicate consumption (NO_3-, NH_4^+ and acetate panels A, C and D). Note that the steady-state rate of nitrate consumption (squares, A) is much larger than the steady-state rate of nitrite production (stars, B). This observation is consistent with further reduction to N_2O or N_2.

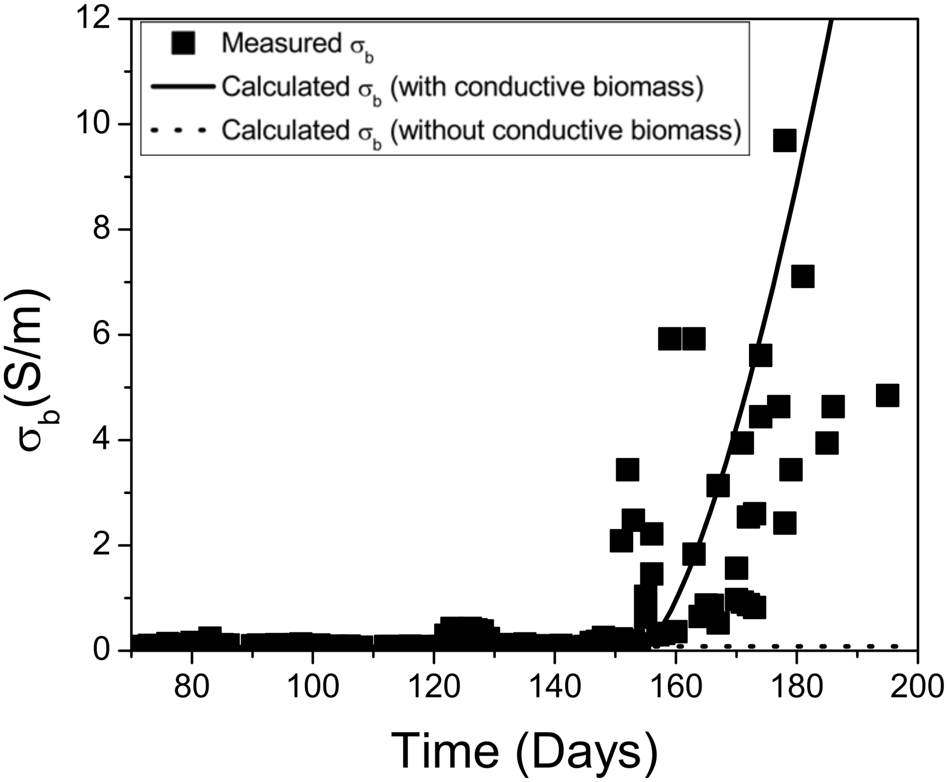

Figure 4.6: σ_b vs. time measured in the column experiment (squares). Measured σ_b increases from ~0.07 S/m to high values starting on day 150. This massive increase in conductivity can be modeled using Eq. 4.21 (solid line) if the new conductive phase has a σ_b between 350 and 35,000 S/m. The range is large due to the choice of C density of the biofilm material as described in the text. Measured σ_b is consistent with σ_b calculated from chemical concentrations (Eqs. 4.3 & 4.5) alone (dashed line) before day 150.

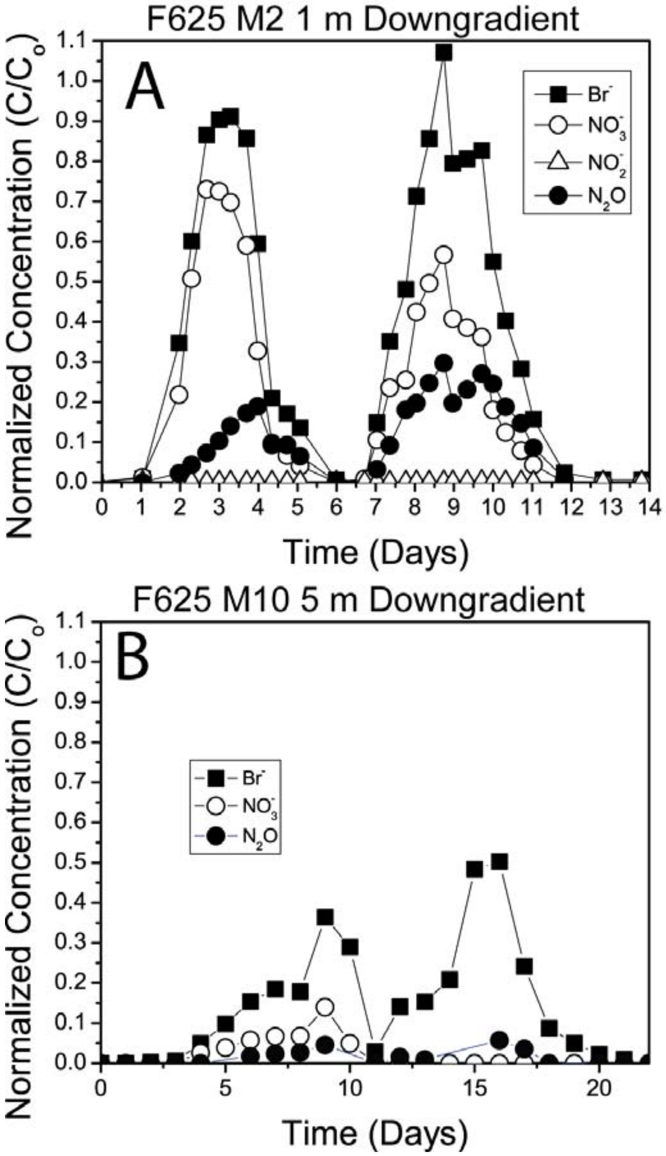

Figure 4.7: Breakthrough of Br^- (squares), NO_3^- (open circles), NO_2^- (open triangles), and N_2O (closed circles). All values are reported as normalized concentrations such that the measured concentration at the MLS is divided by the injected tracer concentration. NO_2^- and N_2O concentrations are normalized to the initial concentration of N as NO_3^- in the tracer (Eq. 4.16). Decreases in normalized concentrations of Br^- are attributed to dispersion. Decreases in normalized concentrations of NO_3^- are attributed to dispersion, consumption of NO_3^- and production of N_2O.

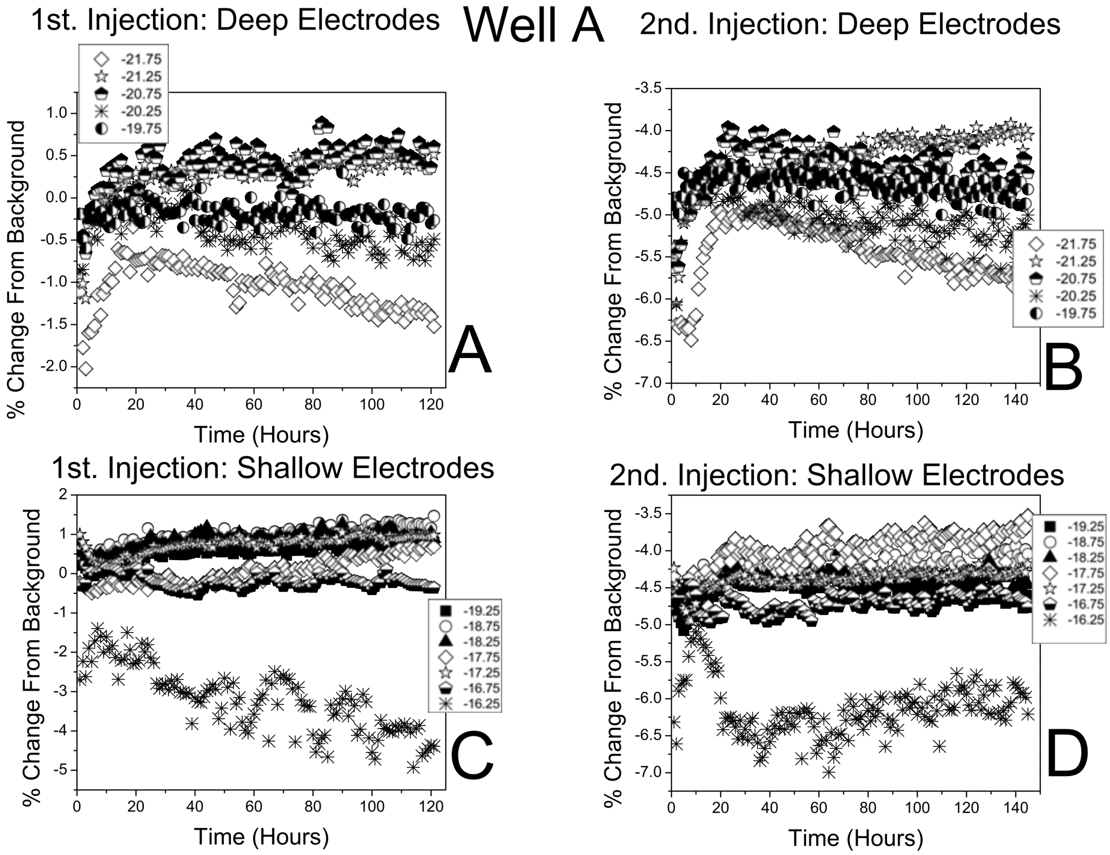

Figure 4.8: Electrodes located inside well A near the injection depth show a 1 – 1.5% decrease in apparent resistivity from background values concurrent with tracer injection (A, B). This decrease in apparent resistivity grows for the first 20 hours after injection and then slowly dissipates over the following 100 hours as the tracer moves down gradient. Electrodes located at shallower depths in well A (C, D) do not show this pattern because they are too far away from the tracer.

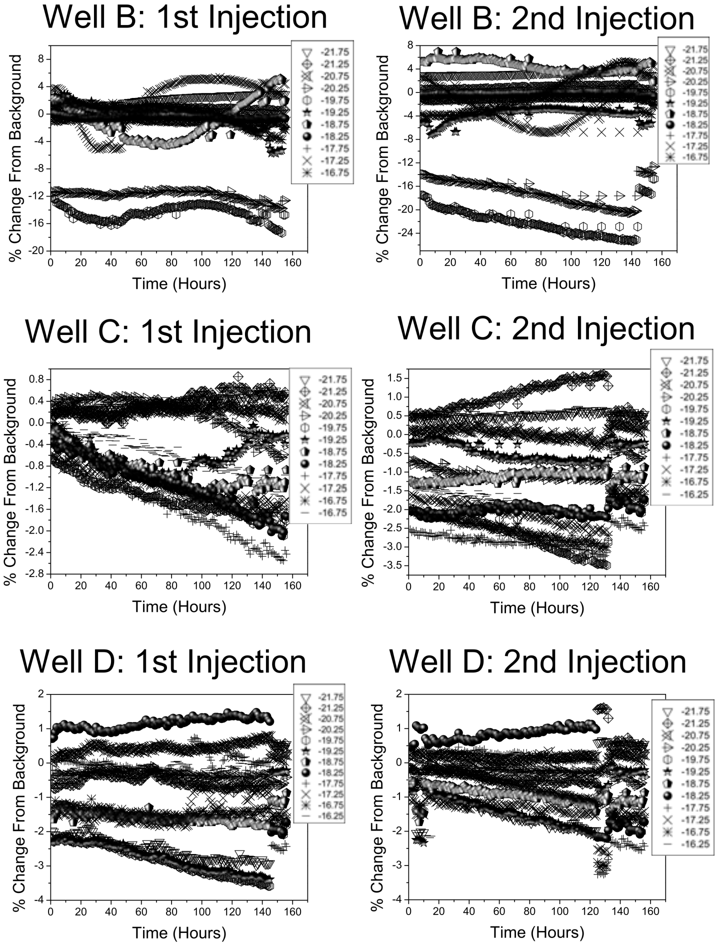

Figure 4.9: The percent change in apparent resistivity from background values versus time has no apparent correlation to the presence or absence of the conductive tracer for measurements made with electrodes located inside wells B, C, and D.

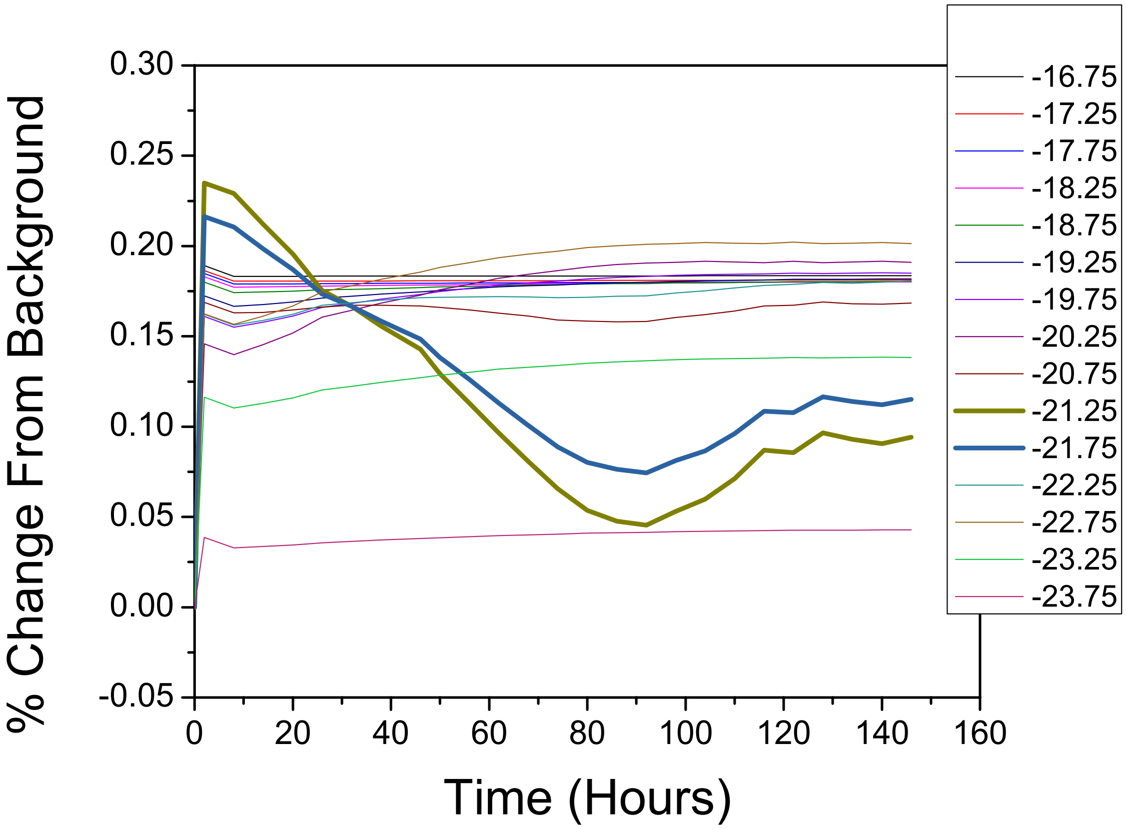

Figure 4.10: Predicted percent changes in apparent resistivity from the forward model of quadripoles located inside Well A are approximately 10 times smaller than measured changes in apparent resistivity. The deeper electrodes are affected more strongly and the calculated signal takes the same amount of time to dissipate (~ 100 hrs) as the measured signal.

Works Cited

.

Abrams, R., and K. Loague (2000), A compartmentalized solute transport model for redox zones in contaminated aquifers 2. Field-scale simulations, *Water Resour. Res.*, *36*(8), 2015-2030.

Archie, G. E. (1942), The electrical reisistivity log as an aid in determining some reservoir characteristics, *Petroleum Transactions of AIME*, *146*, 54-62.

Atekwana, E., E. Atekwana, F. Legall, and R. Krishnamurthy (2004), Field evidence for geophysical detection of subsurface zones of enhanced microbial activity, *Geophysical Research Letters*, *31*(23), L23603.

Balberg, I. (1986), Excluded-volume explanation of Archie's law, *Physical Review B*, *33*(5), 3618-3620.

Ball, J. W., and D. K. Nordstrom (1991), User's manual for WATEQ4F with revised thermodynamic data base and test cases for calculating speciation of major trace and redox elements in natural waters, *U.S. Geological Survey Open File Report*, *91-183*, 1-59.

Bennett, P. C., F. K. Hieberg, and J. R. Rogers (2000), Microbial control of mineral-groundwater equilibria: Macro-scale to microscale, *Hydrogeology*, *8*, 47-62.

Bielefeldt, A. r., T. Illangasekare, M. Uttecht, and R. LaPlante (2002), Biodegradation of propylene glycol and associated hydrodynamic effects in sand, *Water Res.*, *36*(2002), 1707-1714.

Brantley, S. L., and C. F. Conrad (2008), Analysis of Rates of Geochemical Reactions, in *Kinetics of Water-Rock Interaction*, edited by S. L. Brantley, et al., pp. 1-38, Springer.

Cengeloglu, Y., A. Tor, M. Ersoz, and G. Arslan (2006), Removal of nitrate from aqueous solution by using red mud, *Separation Purification Technology*, *51*(2006), 374-378.

Characklis, W. G. (1990), Laboratory biofilm reactors, in *Biofilms*, edited by W. G. Characklis and K. C. Marshall, Jonh Whiley and Sons Inc., New York.

Christensen, B. E., and W. G. Characklis (1990), Physical and chemical properties of biofilms, in *Biofilms*, edited by W. G. Characklis and K. C. Marshall, John Wiley and Sons Inc., New York.

Christensen, T., P. Kjeldsen, P. Bjerg, D. Jensen, J. Christensen, A. Baun, H. Albrechtsen, and G. Heron (2001), Biogeochemistry of landfill leachate plumes, *Appl. Geochem.*, *16*(7-8), 659-718.

COMSOL (2008), COMSOL Multiphysics Modeling Guide, 1 - 518.

Davis, J. A., and D. B. Kent (1990), Surface complexation modeling in aqueous geochemistry, in *Mineral-Water Interface Modeling*, edited by M. F. H. Jr. and A. F. White, pp. 178-260, MSA.

Day-Lewis, F. D., K. Singha, and A. M. Binley (2005), Applying petrophysical models to radar travel time and electrical resistivity tomograms: Resolution-dependent limitations *Journal of Geophysical Research*, *110*(B08206), 17.

Fishman, M. J., and L. C. Friedman (1989), A1 Methods for determination of inorganic subtances in water and fluvial sediments, in *Techniques of Water-Resources Investigations of the United States Geological Survey: Book 5 Laboratory Analysis*, edited, p. 466, United States Geological Survey, Washington D.C.

Freeze, R. A., and J. A. Cherry (1979), *Groundwater*, 604 pp., Prentice Hall, Englewood Cliffs, NJ.

Genuchten, M. T. v. (1985), A general approach for modeling solute transport in structured soils, *IAH Memoirs 17*(2), 513-526.

Good, N. E., G. D. Winget, W. Winter, T. N. Connolly, S. Izawa, and R. M. M. Singh (1966), Hydrogen ion buffers for biological research, *Biochem. Cell Biol.*, *5*(2), 467-477.

Haggerty, R., and S. M. Gorelick (1995), Multiple-rate mass transfer for modeling diffusion and surface reactions in media with pore-scale heterogenety, *Water Resour. Res.*, *31*(10), 1383-2400.

Holmes, R., A. Aminot, R. Kérouel, B. Hooker, and B. Peterson (1999), A simple and precise method for measuring ammonium in marine and freshwater ecosystems, *Canadian Journal of Fisheries and Aquatic Sciences*, *56*(10), 1801-1808.

Knowles, R. (1982), Denitrification, *Microbiological Reviews*, *46*(1), 43-70.

Knutsson, G. (1966), Tracers for groundwater investigations, paper presented at Groundwater Problems, Pergamon Press, Stockholm Sweden.

Korner, H., and W. G. Zumft (1989), Expression of denitrification enzymes in response to the dissolved oxygen level and respiratory substrate in continuous culture of *Pseudomonas stutzeri*, *Appl. Environ. Microbiol.*, *55*(7), 1670-1676.

Korom, S. F. (1992), Natural denitrification in the saturated zone: a review, *Water Resour. Res.*, *28*(6), 1657-1688.

Landolt-Bornstein (1969), *Numerical data and functional relationships in science and technology*, Sixth Edition ed., Springer-Verlag, Heidelberg.

LeBlanc, D. R. (1984), Sewage plume in a sand and gravel aquifer, Cape Cod, Massachusetts, *U.S. Geolgical Survey Water-Supply Paper*, *2218*.

LeBlanc, D. R., S. P. Garabedian, K. M. Hess, L. W. Gelhar, R. D. Quadri, Stollenwerk, K. G;, and W. W. Wood (1991), Large-scale natural gradient tracer test in sand and gravel, Cape Cod, Massachusetts; 1, Experimental design and observed tracer movement, *Water Resour. Res.*, *27*(5), 895-910.

Madigan, M. T., J. M. Martinko, and J. Parker (2003), *Brock Biology of Microorganisms*, 10th ed., 1019 pp., Prentice Hall, Upper Saddle River.

Musselwhite, C. L., M. J. Mcinerney, H. Dong, T. C. Onstott, M. Green-Blum, D. Swift, S. Macnaughton, D. C. White, C. Murray, and Y.-J. Chien (2002), The factors controlling microbial distribution and activity in the shallow subsurface, *Geomicrobiol. J.*, *20*, 245-261.

Oldale, R. N. (1969), Seismic investigations on Cape Cod, Martha's Vineyard, and Nantucket, Massachusetts, and a topographic map of the basement surface from Cape Cod Bay to the islands, *U.S. Geological Survey Professional Paper 650-B*, B122 - B127.

Or, D., S. Phutane, and A. Dechesne (2007), Extracellular polymeric substances affecting pore-scale hydrologic conditions for bacterial activity in unsaturated soils, *Vadose Zone Journal*, *6*(2), 298-304.

Ozturk, N., and T. E. Bektas (2004), Nitrate removal from aqueous solution by adsorption onto various materials, *J. Hazard. Mater.*, *B112*(2004), 155-162.

Parkhurst, D. L., and C. Appelo (1999), User's guide to PHREEQC (Version 2) - A Computer program for speciation, batch-reaction, one-dimensional transport, and inverse geochemical calculations, *Water-Resources Investigations Report*, *99-4259*.

Parkhurst, D. L., K. G. Stolenwerk, and J. A. Colman (2003), Reactive-Transport Simulation of Phosphorus in the Sewage Plume at the Massachusetts Military Reservation, Cape Cod, Massachusetts, *U.S. Geological Survey Water-Resources Investigations Report 03-4017*, 40.

Parkhurst, D. L., K. L. Kipp, P. Engesaard, and S. R. Charlton (2004), PHAST - A Program for Simulating Ground-Water Flow, Solute Transport, and Multicomponent Geochemical Reactions, *U.S. Geological Survey Techniques and Methods 6-A8*, 154.

Penn, R. L., C. Zhu, H. Xu, and D. R. Veblen (2001), Iron oxide coatings on sand grains from the Atlantic coastal plain: High-resoltuion transmission electron microscopy, *Geology*, *29*(9), 843-846.

Pidlisecky, A., E. Haber, and R. Knight (2007), RESINVM3D: A 3D resistivity inversion package, *Geophysics*, *72*(2), H1-H-10.

Regberg, A., K. Singha, M. Tien, F. Picardal, J. Schieber, E. Roden, and S. L. Brantley (in press), Electrical conductivity as an indicator of iron reduction rates in abiotic and biotic systems, *Water Resour. Res.*

Repert, D. A., L. B. Barber, K. M. Hess, S. H. Keefe, D. B. Kent, D. R. LeBlanc, and R. L. Smith (2006), Long-Term natural attenuation of carbon and nitrogen within a groundwater plume after removal of the treated wastewater source, *Environ. Sci. Technol.*, *40*, 1154-1162.

Rittmann, B. E., and P. L. McCarty (2001), *Environmental Biotechnology: Principles and Applications*, 754 pp., McGraw Hill, Boston.

Rugh, D. F., and T. J. Burbey (2008), Using saline tracers to evaluate preferential recharge in fractured rocks, Floyd County, Virginia, USA, *Hydrogeology Journal*, *16*(2008), 251-262.

Savoie, J., and D. R. LeBlanc (1998), Water-Quality data and method analysis for samples collected near a plume of sewage-contaminated ground water, Ashumet Valley, Cape Cod, Massachusets, 1993-94, U.S. Geological Survey Water-Resources Investigations Report 97-4269.

Scheibe, T., Y. Fang, C. Murray, and E. Roden (2006), Transport and biogeochemical reaction of metals in a physically and chemically heterogeneous aquifer, *Geosphere*, *2*(4), 220-235.

Schindler, P. W., and W. Stumm (1987), The surface chemistry of oxides, hydroxides and oxide minerals, in *Aquatic Surface Chemistry: Chemical Processes at the Paricle-Water Interface.*, edited by W. Stumm, John Wiley & Sons, New York.

Sen, P. N., P. A. Goode, and A. Sibbit (1988), Electrical conduction in clay bearing sandstones at low and high salinities, *J. Appl. Phys.*, *63*(10), 4832-4840.

Singha, K., and S. M. Gorelick (2005), Saline tracer visualized with three-dimensional electrical resistivity tomography: Field-scale spatial moment analysis, *Water Resour. Res.*, *41*(W05023), 1-17.

Stookey, L. L. (1970), Ferrozine- a new spectrophotometric reagent for iron, *Anal. Chem.*, *42*(7), 779-781.

Stumm, W., and J. J. Morgan (1996), *Aquatic Chemistry: Chemical Equilibria and Rates in Natural Waters*, 3rd ed., 1022 pp., John Wiley and Sons Inc., New York.

Thullner, M., J. Zeyer, and W. Kinzelbach (2002), Influence of microbial growth on hydraulic properties of pore networks, *Transport in Porous Media*, *49*, 99-122.

Thullner, M. (2010), Comparison of bioclogging effects in saturated porous media within one-and two-dimensional flow systems, *Ecol. Eng.*, *36*(2), 176-196.

USGS (2011), USGS Cape Cod site Bibliography, in *http://ma.water.usgs.gov/CapeCodToxics/*, edited.

Walter, D. A., B. A. Rea, K. G. Sollenwerk, and J. Savoie (1996), Geochemical and Hydrologic Controls on Phosphorus Transport in a Sewage Contaminated Sand and Gravel Aquifer Near Ashumet Pond, Cape Cod, Massachusetts, *United States Geological Survey Water-Supply Paper 2463*.

Wang, Y., B.-Y. Gao, W.-W. Yue, and Q.-Y. Yue (2007), Adsorption kinetics of nitrate from aqueous solutions onto modified wheat residue, *Colloids and Surfaces*, *308*(2007), 1-5.

Watson, I. A., S. E. Oswald, K. U. Mayer, Y. Wu, and S. A. Banwart (2003), Modeling kinetic processes controlling hydrogen and acetate concentrations in an aquifer-derived microcosm, *Environ. Sci. Technol.*, *37*, 3910-3919.

Wetters, J. H., and K. L. Uglum (1970), Direct spectrophotometric simultaneus determination of nitrite and nitrate in the ultraviolet, *Anal. Chem.*, *42*(3), 335-340.

Wilkinson, P. B., P. I. Meldrum, O. Kuras, J. E. Chambers, S. J. Holyoake, and R. D. Ogilvy (2010), High-resolution electrical tomography monitoring of a tracer test in a confined aquifer, *Journal of Applied Geophysics*, *70*(2010), 268-276.

Zhang, C., A. V. Palumbo, T. J. Phelps, J. J. Beauchamp, F. J. Brockman, C. J. Murray, B. S. Parsons, and D. J. P. Swift (1998), Grain size and depth constrains on microbial variability in costal plain subsurface sediments, *Geomicrobiol. J.*, *15*(3), 171-185.

Chapter 5

TOWARD NEW APPROACHES IN THE MEASUREMENT OF THE ELECTRICAL CONDUCTIVITY OF BIOFILMS

Previous work on electrical conductivity signals associated with microbial growth has suggested that microbial biofilms may be electrically conductive [e.g., *Liermann et al.*, 2000; *Ntarlagiannis et al.*, 2007; *Marsili et al.*, 2008b; *Torres et al.*, 2008; *Nielsen et al.*, 2010]. *Regberg et al.* [in press] and *Slater et al.* [2009] attributed increases in electrical conductivity in column reactors to the growth of biofilms and their subsequent connection into electrically conductive features If microbial biofilms are electrically conductive, it is important to quantify the magnitude of that conductivity so that changes in electrical conductivity can be interpreted with respect to the amount of biofilm present. While the idea of conductive biofilms has been postulated in numerous places, no known studies have directly measured the electrical conductivity of a respiring biofilm or demonstrated a definitive mechanism for this purported electrical conductivity. Here, we describe an attempt to grow a microbial biofilm in a controlled setting such that the biofilm's electrical properties can be measured. Without a definitive value for biofilm electrical conductivity, the interpretations of changes in electrical conductivity in the presence of microbial activity is difficult at best. Biofilms created by different bacterial species have distinct physical and chemical differences [e.g., *Christensen and Characklis*, 1990]. For example, *Liermann* et al. [2000] observed that some bacterial species produce pH gradients inside biofilms grown on Fe-containing minerals while others do not. Some bacterial species produce electron shuttles to aid respiration [e.g., *Marsili et al.*, 2008a]. Some researchers have suggested that microbial nano-wires cause electrical conductivity in biofilms [e.g., *Reguera et al.*, 2005; *Ntarlagiannis et al.*, 2007; *Nielsen et al.*, 2010], but not all bacteria are capable of producing these nano-wires. Chemical and physical differences inside biofilms are likely to cause differences in electrical conductivity as well. Therefore, we do not expect all microbial biofilms to have the same electrical conductivity.

We chose to focus on dissimilatory iron reducing bacteria because they are environmentally relevant [*Christensen et al.*, 2001]. Furthermore, we wish to elucidate the results of *Regberg et al.*, [in press] and *Slater et al.*, [2009] that described experiments involving metal-reducing bacteria where bulk electrical conductivity became decoupled from fluid electrical conductivity. The experiments described herein are presented as a first step in development of an approach to test the hypothesis that microbial biofilms are electrically conductive.

Recently, researchers have used electrochemical techniques like microbial fuel cells (MFC) to investigate the biochemical properties of biofilms composed of dissimilatory iron reducing bacteria [e.g., *Bond and Lovley*, 2003; *Min and Logan*, 2004; *Marsili et al.*, 2008b; *Meitl et al.*, 2009; *Richter et al.*, 2009]. In a MFC, current is generated by poising a working electrode either with a potentiostat or an oxygen cathode at a voltage similar to the redox potential of solid crystalline iron oxides (-0.2 V vs. Ag/AgCl reference electrode). When the MFC is inoculated with dissimilatory iron reducing bacteria, they are obßßserved to attach to the working electrode and utilize it as a terminal electron acceptor. Donating electrons to the working electrode creates electrical current that can be measured with the same potentiostat. Working electrodes have been successfully made with gold, graphite and glassy carbon [*Bond and Lovley*, 2003; *Marsili et al.*, 2008b; *Richter et al.*, 2008]. There are many advantages to using a poised electrode to grow microbial biofilms, including the ability to locate the biofilm and remove it from the system for additional investigation, with relative ease.

For our purposes, the most advantageous aspect of using a MFC is the ability to precisely locate the biofilm in space. In MFCs, the only available terminal electron acceptor is the working electrode. Therefore, actively respiring microbes must attach themselves to the working electrode to survive. In this chapter I describe an experimental system that takes advantage of this known location of biofilm in a fuel cell to probe the electrical properties of the biofilm. I describe three experiments: (1) a proof-of-concept experiment (Fig. 5.1) performed in Daniel Bond's lab at the University of Minnesota using a fuel cell, (2) a set of micro-electrode experiments where the micro-electrodes were suspended in an anaerobic reactor and, (3) a microfluidics experiment where the micro-electrodes were built into a microfluidic cell.

For the latter two experiments, we designed and built a set of six gold electrodes fixed to a glass microscope slide (Fig. 5.2). These micro-electrodes were used to grow microbial biofilms inside an anaerobic electrochemical cell. Additionally, some of the micro-electrodes were built into a micro-fluidics device that allowed us to optically image biofilm growth. These electrodes allowed us to use the current generated by an actively respiring biofilm to measure the electrical conductivity inside and outside the biofilm. Direct-current electrical conductivity measurements were collected by measuring the voltage drop across two electrodes when a known current was applied across two other electrodes. Ohm's Law states:

$$S = \frac{I}{V} = \frac{1}{R} \tag{5.1}$$

where S is the electrical conductance in Siemens (S), I is the current (A), V is the potential (V), and R is the resistance (ohms). In these experiments the current is generated by the micro-organisms donating electrons to the working electrode. The current was measured using the potentiostat. Electrical conductance can be converted to electrical conductivity if the geometry of the electrodes is known:

$$\sigma = \kappa^{-1} S \tag{5.2}$$

where σ is the electrical conductivity (S/m) and κ is a geometric factor (m). Laboratory values of κ are often determined by measuring the conductance of a standard solution with known electrical conductivity and then solving Eq. 5.2 for κ.

Methods

Proof-of-concept experiment

The first set of experiments was a proof-of-concept experiment using a fuel cell and larger set of electrodes than in the other two experiments. The design of the MFC is described in *Marsili et al.* [2008b]. A 1-cm^2 piece of unpolished carbon paper was used as the working electrode. The carbon paper was left unpolished and rough to increase the surface area and encourage the growth of thicker biofilms. A platinum wire served as the counter electrode and a saturated calomel electrode (SCE) was used as the reference. Two additional platinum wires were inserted into the system and positioned near the working electrode to measure potential changes as the biofilm grew (Fig. 5.1).

Micro-electrode experiment

The second set of experiments, the micro-electrodes experiments, used smaller electrodes patterned on a glass slide (Fig. 5.2). The micro-electrodes were placed in an anaerobic reactor and attached to a potentiostat. The micro-electrodes were produced using a photo-lithographic technique. This technique involves covering the surface (in this case, glass) with a photo-sensitive compound (a photo-resist) that becomes more soluble after being exposed to light. Sections of the surface are exposed to light so that the compound in those sections can be easily removed. After dissolving the exposed photo-resist, a layer of gold is applied to the surface. The gold adheres strongly to the exposed glass, but not to the remaining areas covered with photo-resist. Finally, the remaining photo-resist is dissolved to leave only the gold features bonded directly to the areas with exposed glass.

The gold electrodes were printed on a glass microscope slide from VWR (25 mm x 75 mm). A 2-mm diameter hole was drilled in the center of the slide for later use in the microfluidics device (Fig. 5.2). Initially, the glass slide was cleaned with acetone and rinsed with 2-propanol and DI water sequentially to ensure a clean surface. The slide was further cleaned with nanostrip at 65^{o} C for 30 min. Next, the glass slide was coated with hexamethyldisilazane (HMDS) to promote adhesion between a non-photosensitive compound and the glass. The HMDS was applied to the glass while spinning the slide at 4000 rpm for 20 s. Non-photosensitive material LOR-5A (MicroChem Corp.) was spun onto the glass slide coated with HMDS as a base at 4000 rpm for 60 s and the glass slide was then baked on a hotplate at 180°C for 10 min. The photo-resist 3012 (MicroChem Corp.) was mixed with the solvent Ethyl L-lactate (Alfa Aesar) at a ratio of 1:1 by volume. This mixture was spun onto the LOR 5A layer at 2000 rpm for 60 s and the glass slide was baked at 97°C for 60 s.

A prefabricated photo-mask, used to selectively expose parts of the photo-resist to light, was placed over the coated glass slide and aligned using a Karl Suss MA6/BA6 contact aligner. The unmasked portions of the slide were exposed to an unfiltered mercury lamp UV source with an output power of 12 mW/cm^{2} for 3.5s. The unmasked sections of the photo-resist become reactive to the developer (CD26) when exposed to UV radiation. After UV exposure, the resist was baked on a hotplate at 116°C for 1 min and developed in CD26 (0.1 N solution of tetra methyl ammonium hydroxide in water) for 90 s. The unmasked portions of the photo-resist and the underlying LOR dissolved in the CD26, forming an undercut feature. Gold thin films (500 Å thick) were deposited on top of chromium thin films (50 Å thick) in a Semicore Evaporator. Finally, the remaining photo-resist 3012 and non-photosensitive LOR were dissolved in Remover PG (MicroChem Corp.) to remove the excess metal. Only the metal deposited directly on the glass, inside the undercut feature remained (Fig 5.2).

The working electrode was designed to be 1 x 10 mm in dimension. The counter electrode is 5 mm away from the working electrode and is also 1 mm thick. The two pairs of potential electrodes were placed 1 mm away from each edge of the counter electrode and 5 μm and 25 µm away from the working electrode respectively. We expected the 5 µm electrodes to become enveloped by the growing biofilm before the 25 µm electrodes and to thus initially reveal larger conductivity values. The potential electrodes are 250 µm wide. The spacing between paired potential electrodes is 200 µm (Fig. 5.2).

The glass slides with electrodes printed on them were placed inside an anaerobic reaction vessel, connected to a potentiostat with gold plated steel alligator clips. The alligator clips were coated with silicone epoxy and wrapped in Teflon tape to prevent accidental electrical connections.

Microfluidics experiments

The third set of experiments, the microfluidics experiments, involved manufacturing a microfluidics device around the micro-electrodes. The microfluidics device was designed to be a self-contained system that allowed the bacteria to grow on the working electrode so as to be visible under optical microscopy. The microfluidics device was created by covering the central portion of the electrodes with a glass cover slip. A fluid reservoir for the growth medium was created by bonding another glass slide to the bottom of the electrode slide with polydimethylsiloxane (PDMS) (Fig. 5.3).

The PDMS monomer and a curing agent (Sylgard 184, Dow Corning) were mixed at a 10:1 ratio by weight and placed in a desiccator to evacuate any air bubbles. The evacuated mixture was poured into a polystyrene Petri dish (VWR) and cured at 45°C under vacuum. Once the PDMS had hardened it was peeled away from the Petri dish and cut into the desired shapes. A PDMS gasket 60 X 10 X 10 mm was used to join the two slides together to create a medium reservoir with a 6 ml capacity. The central portion of the electrodes and the hole was covered with a 18 X 18 mm cover slip bonded to the upper slide with another PDMS gasket ~ 0.7mm thick (Fig. 5.3).

Prior to bonding the PDMS gaskets, the glass slides and cover slip were placed in an ultra-sonic bath filled with acetone for 10 min and rinsed with 2-propanol and DI water sequentially. The thin gasket used to attach the upper slide to the cover slip was bonded under Oxygen plasma (100 standard cm^3 min^{-1}) in a Metroline M4L plasma etcher at 165 W for 10 s under an operating pressure of 300 mTorr. The thick gasket used to attach the glass slides to each other was bonded in the same fashion at 100 W for 60 s at 300 mTorr. Inlets and outlets to the fluid reservoir were created by inserting 21 ½ gauge needles into the large PDMS gasket and were reinforced with extra PDMS.

To connect the microfluidic device to the potentiostat, gold-plated alligator clips were attached to the square electrode pads outside the fluid reservoir (Fig. 5.2). The reference electrode was inserted into the system in one of the following two ways. A SCE was placed inside a 10 ml syringe containing 0.1M Na_2SO_4 and 1% (wt/wt) agar to act as a salt bridge [*Marsili et al.*, 2008b]. The end of the syringe was sealed with a Vycor frit and attached to one of the needles in the PDMS gasket. Alternatively, a 125 µm Ag/AgCl wire was inserted through one of the needles into the lower 6 ml media chamber.

Cells of *Geobacter sulfurreducens,* a known iron-reducing bacteria, were grown from a pure culture maintained on synthetic goethite as the terminal electron acceptor [*Cornell and Schwertmann*, 2003] suspended in Na fumarate-free ATCC 1957 *Geobacter* growth medium. Cells from these maintenance cultures were transferred into a growth medium containing the following ingredients (1.5 g/L NH_4Cl, 0.6 g/L NaH_2PO_4, 0.1 g/L KCl, 2.5 g/L $NaHCO_3$, 10 ml/L 100X Wolfe's Vitamin Solution, 10 ml/L Modified Wolfe's Minerals 30 mM Na-acetate and 50 mM Na-fumarate). These cultures were grown and transferred at least three times to remove all traces of the solid Fe oxides before use in experiments.

Cells were grown until the measured optical density was maximized [*Marsili et al.*, 2008b], i.e. absorbance of 600 nm light = 0.6. This is a standard technique. The cultures were then transferred into either the anaerobic reactor or microfluidics device at a 1:1 ratio by volume along with Na-fumarate free medium containing all the ingredients described above. The reactors and microfluidics devices were continuously bubbled with a 20% CO_2 - N_2 gas mix to maintain anaerobic conditions.

The working electrode was poised at -0.2 V vs. Ag/AgCl reference electrode using a Nuvant systems EZSTAT potentiostat attached to a Beckman Coulter Calomel pHree ® reference electrode. Both the working and the counter electrode were gold. The potential electrodes were attached to a Campbell Scientific CR1000 data logger programmed to record voltage across the two potential electrode pairs. The potentiostat recorded the potential at the working electrode surface and the current produced inside the system every second and output this data as a 1-min running average. The data logger collected potential data from the near and far electrode pairs (Fig. 5.2) at one-second intervals. Data were output as 1-min running averages as well. κ was calculated by measuring the conductance of the cell filled with a known conductivity standard and solving Eq. 5.2 for κ. We conducted six replicates of the micro-electrode experiments (A –F) and two replicates of the microfluidic experiment.

Results

Fuel cell experiment

In the proof-of-concept experiment the potentiostat maintained a constant voltage around -0.2 V vs. Ag/AgCl over 7 days (~10,000 min.) (Fig. 5.4). The current was measured before inoculation of *Geobacter* at background values equal to ~0.03 mA. The current increased to a maximum of 2.6 mA 3780 minutes after inoculation. The measured current oscillated between 2.6 mA and 0.9 mA for the next 4200 minutes. The oscillation was most likely due to evaporation inside the reaction vessel. As the volume of medium inside the reaction vessel decreased due to evaporation, the measured current also decreased. To compensate for this observed evaporation, anoxic DI water was added to the reactor. When the water was added measured current values increased to ~2 mA. At 7662 minutes, the measured current was observed to decrease. At this time, we assumed that acetate was mostly consumed in the reactor. We based this assumption on the amount of current produced in the reactor. Over the first 7662 minutes of the experiment the cumulative measured current production was 685 mA. This corresponds to 18 C of charge or 0.027 meq e^-. If each mole of acetate oxidized produces 8 electrons then the 0.027 meq e^- measured as current with the potentiostat corresponds to 0.216 mmoles of acetate. The reactor had a total volume of 20 ml and contained 30 mM Na-acetate or 0.2 mmoles. At 10902 minutes, the measured current returned to background values, ~0.14 mA, and the experiment was terminated (Fig. 5.4).

Changes in voltage measured with the conductivity electrodes in the proof-of-concept experiment behaved inversely to measured current. Initially measured voltage was 0.22 V vs. the reference electrode (Fig. 5.5). The measured voltage quickly decreased to 0.002 V vs. the reference electrode at 1500 min. Voltage measurements then oscillated inversely to current until increasing back to starting values as the experiment was terminated after 10902 min.

Electrical conductances were calculated with the measured values of current and voltage using Eq. 5.1. Conductance was converted to conductivity using Eq. 5.2. κ was calculated to be equal to 14.7 m using an algorithm available in the COMSOL Multiphysics software [*COMSOL*, 2008]. Consequently, we calculated an initial electrical conductivity around 1×10^{-5} S/m. By 1275 min., the electrical conductivity had increased to 2.2×10^{-3} S/m. The maximum conductivity was 7.9 x 10^{-3} S/m at 4305 s. At 7212 min., the conductivity began to decrease presumably due to decreases in acetate in the reactor (Fig. 5.6).

During the experiment, the maximum conductivity values were less than those previously published estimates of biofilm conductivity. *Torres et al.* [2008] predicted that biofilms growing in MFCs must have an electrical conductivity > 0.05 S/m. While the measured value is lower than the theoretical values discussed in *Torres et al.* [2008], *Regberg et al.* [in press] suggest that this may be because the conductivity electrodes were not inside the growing biofilm itself. In this proof-of-concept experiment, it was difficult to know exactly where the conductivity electrodes were in relation to the biofilm. Additionally these experiments utilized a single strain of bacteria while the column reactors contained multiple species. It is possible that mixed culture biofilms have different electrical properties than biofilms containing only a single species of bacteria. For these reasons, 2.2 x 10^{-3} S/m represents a minimum value for biofilm electrical conductivity.

Micro-electrode experiments

The micro-electrode experiments were less successful than the initial proof-of-concept experiment. When the micro-electrodes were used in the anaerobic reactor, the potentiostat maintained a constant voltage at the working electrode, but the amount of current produced in an individual replicate varied over 5 orders of magnitude (1 x 10^{-5} – 0.1 A) (Fig. 5.7). In earlier experiments using gold electrodes, measured current only varied by 0.1-0.5 A [*Richter et al.*, 2008]. We hypothesize that the variability in our measurements was due to corrosion of the gold-plated alligator clips used as connectors. The large variability in current produced at the micro-electrodes resulted in an equally large variability in measured bulk electrical conductivity (Fig. 5.8). Measured conductivity varied between 0.01 and 1 x 10^{4} S/m for different replicates. Calculated κ, as measured with the known conductivity standard, also varied between 1360 and 1 x 10^{6} m. Since the geometry of the electrodes did not change the 3 order of magnitude change in calculated κ is indicative of a problem with the electrical measurements. When the micro-electrodes were used in the anaerobic reactor it was necessary to submerge the gold-plated alligator clips, used to connect the electrodes to the potentiostat and the data logger, so that the micro-electrodes would be in contact with the medium containing the *Geobacter* cells. Despite covering the clips with silicone epoxy and wrapping them in Teflon thread tape, we observed evidence of corrosion on the alligator clips. Rust-colored precipitates were also found on the glass slides for replicates A, B, D and F. Conductivity values for those replicates are not shown. Corrosion reactions in the reactor can generate electrical current and obscure the current generated by the respiring microbes. Consequently, conductivity measurements of biofilms in these experiments are unreliable.

Micro-fluidics experiments

When the micro-electrodes were built into the micro-fluidic device, the results were also inconsistent. The potentiostat was unable to maintain a constant potential of -0.002 V vs. a normal hydrogen electrode (-0.2 V vs. Ag/AgCl) at the working electrode (Fig. 5.9). Changing the type of reference electrode to a smaller Ag/AgCl wire that we could position closer to the working electrode did not fix the problem. If the working electrode is not held at or near -0.2 V vs. Ag/AgCl, then the bacteria cannot pass electrons onto the working electrode and generate current. While we were able to measure current with the potentiostat (Fig. 5.9) and calculate an electrical conductivity (Fig. 5.10), the values obtained for electrical conductivity are not representative of microbial growth because the working electrode was not poised at the correct potential for electron transfer.

Discussion and Future Work

The conductivity measurements from the proof-of-concept experiment show promise for measuring the electrical conductivity of biofilms. However, we were unable to determine the precise location of the conductivity electrodes relative to the biofilm because the conductivity electrodes were not fixed in space relative to the working electrode. We may have measured the conductivity of the biofilm or merely the electrical conductivity at a point directly above the biofilm. Therefore, the measurements of electrical conductivity represent a minimum value for biofilm conductivity. The micro-electrodes were meant to solve this problem by fixing all the electrodes to the same surface. Problems with the gold-plated clips introduced a new source of error, because the steel underneath the gold plate corroded causing the formation of rust colored precipitates.

These attempts to measure the electrical conductivity of biofilm show promise, but several technical hurdles need to be overcome. When the micro-electrodes are used in the anaerobic reactor, the effect of corrosion is a confounding variable. We expected that replicate MFC experiments would produce consistent values of current within ±0.2 A [*Richter et al.*, 2008]. The gold-plated alligator clips used as connectors were expected to be non-reactive, but they were not. Covering the clips in silicone sealant and or Teflon pipe tape has not proven effective. The result of corrosion reactions occurring on the alligator clips is inconsistent current production at the working electrode. If current production cannot be replicated, there is little way of verifying the extent of microbial activity at the working electrode. Platinum wire is often used as a connector in electrochemistry. Using platinum as a connector is expensive but may allow us to avoid corrosion effects. Alternately, plastic clips might allow us to secure the platinum-connecting wires to the gold electrodes and to eliminate the precipitates caused by corrosion effects.

With the micro-electrodes built into the micro-fluidic device, we were unable to maintain the correct potential at the working electrode. Inability to maintain the proper potential may have been due to poor electrical coupling through the fluid with the reference electrode. In the microfluidic device, the reference electrode is in the lower chamber far away from the working and counter electrodes (Fig. 5.3). Inserting the SCE reference electrode into the system with a Vycor frit has been successful in previous work [e.g. *Marsili et al.*, 2008b], but it does not appear to work here because the resulting voltage measurements at the working electrode were highly variable (Fig. 5.9). We attempted to solve this problem by using a small Ag/AgCl wire as the reference electrode but this proved unsuccessful as well (Fig. 5.9). In future work, the reference electrode should be inserted into the upper chamber so that is in close proximity to the working and counter electrode. Ag/AgCl wires can be used as reference electrodes [e.g. *Luther et al.*, 2008] but if this proves ineffective, perhaps platinum reference electrodes should be used.

Conclusions

Initial proof-of-concept experiments using electrochemical methods to grow and maintain microbial biofilms were effective with iron-reducing bacteria. We were able to obtain measurements of changes in electrical conductivity as *Geobacter* biofilms grew and decayed. In the proof-of-concept experiments, a minimum conductivity value was measured for the biofilm. This value 0.0022 S/m was less than a previous estimates of conductivity (0.05 S/m) by Torres et al. [2008] and the value estimated in Ch. 2 (Regberg et al., 2011). Several devices were designed and tested to make more accurate biofilm conductivity measurements. These devices show promise but require further work to achieve consistent, repeatable results.

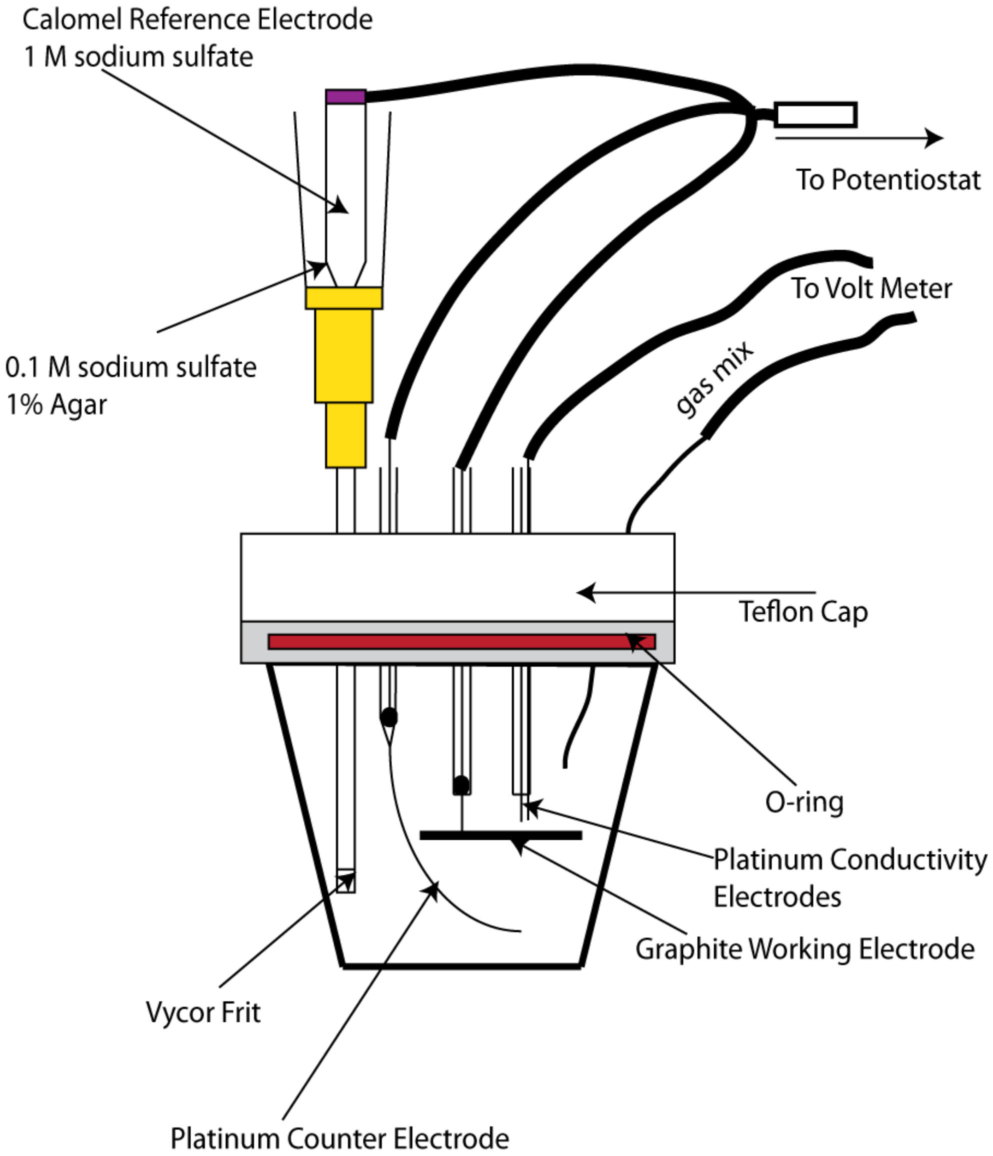

Figure 5.1: Schematic showing the construction of the proof-of-concept microbial fuel cell. Schematic adapted from *Marsili et al.,* [2008b]

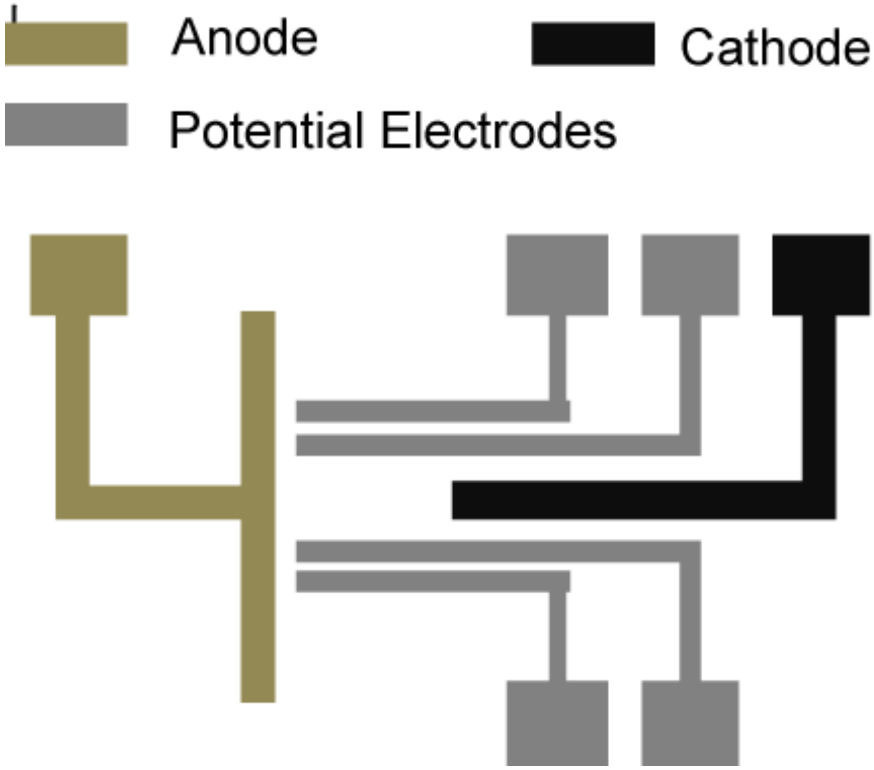

Figure 5.2: Schematic of gold microelectrodes on a glass slide for studying *Geobacter sulfurreducens*. Each pair of potential electrodes were 250 µm wide, with 200 µm or 500 µm spacing between two electrodes. Anode and cathode electrodes were 1 mm wide, with 5 mm spacing between two electrodes. Distance between potential electrodes and anode were 5 µm and 25 µm, respectively. Distance between potential electrodes and cathode were 1mm. The wide rectangular pads are areas where connections to the potentiostat or data logger can be made.

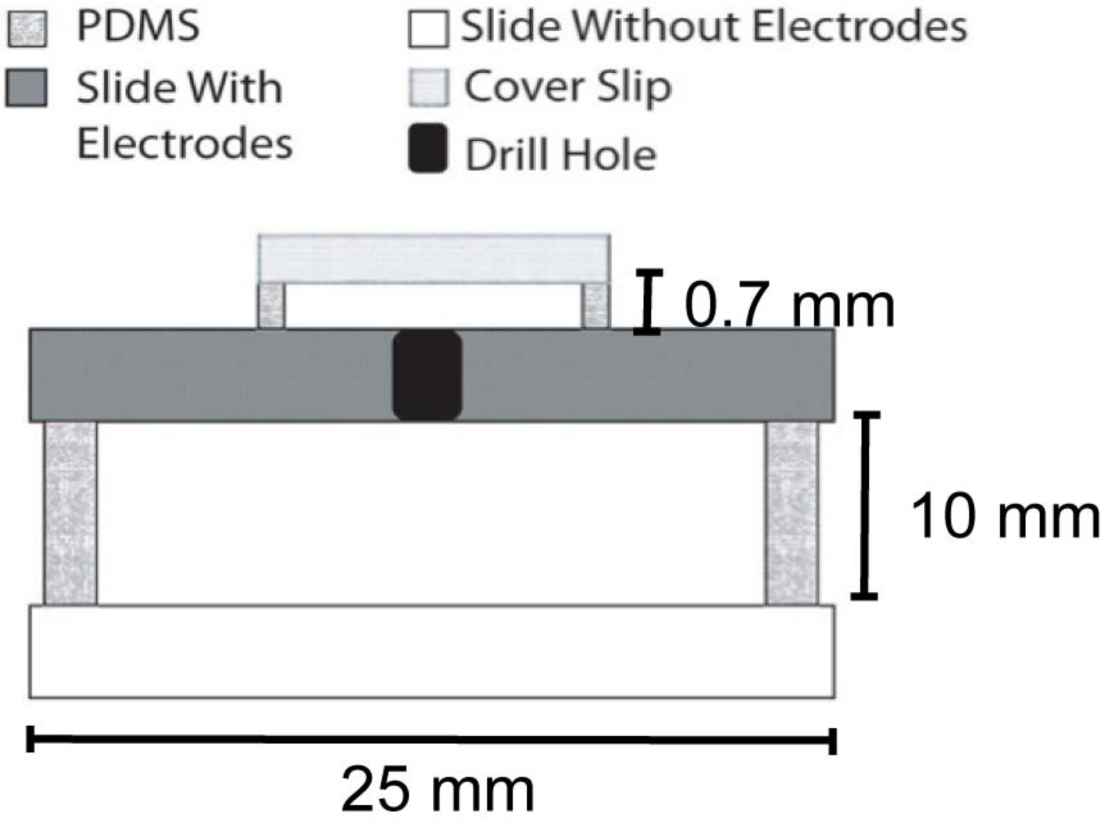

Figure 5.3: Cross section of the microfluidic chamber. The two glass slides were 10 mm apart. The glass cover slip was ~0.7mm above the upper glass slide. The drill hole was used to allow fluid exchange between the upper and lower reservoirs.

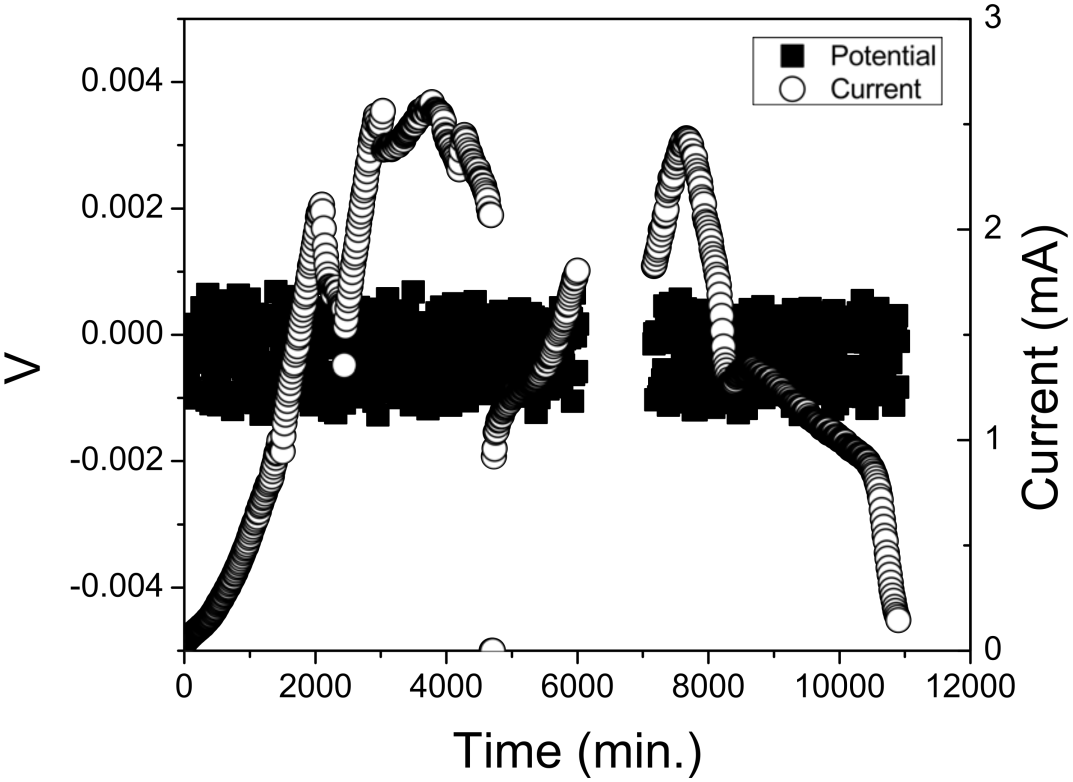

Figure 5.4: Imposed voltage remained constant (~ 0 V) vs. a standard hydrogen electrode (-0.2 V vs. Ag/AgCl) (squares). Measured current (open circles) increased to a maximum value of 2.5 mA as biofilms grew on the electrode before decreasing to background values as acetate was consumed inside the reactor.

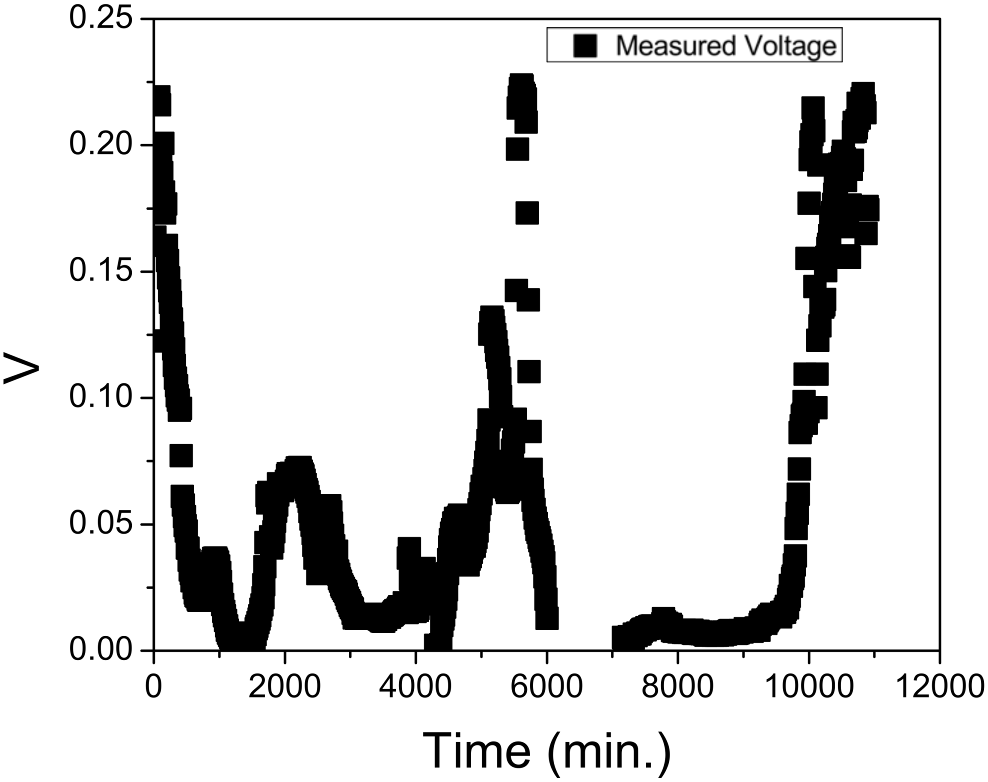

Figure 5.5: Measured voltage in the reactor behaves in the opposite manner to measured current. Measured voltage decreases as measured current increases. This is indicative of an increase in electrical conductivity.

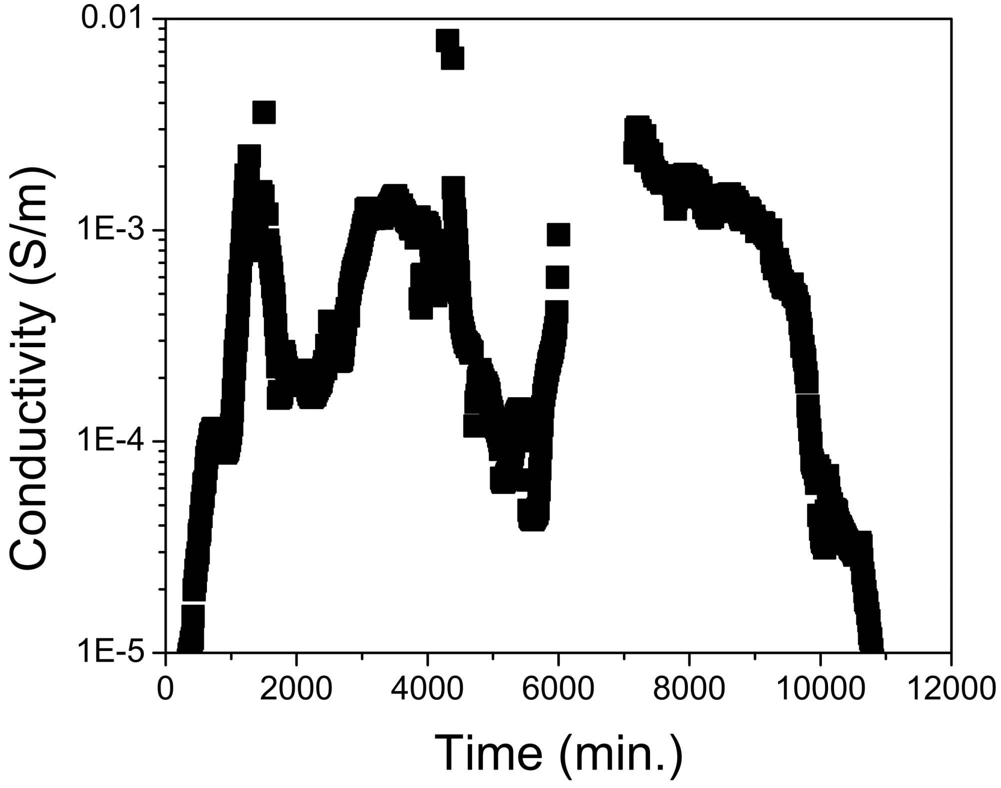

Figure 5.6: Electrical conductivity increased by 3 orders of magnitude as microbes grew on a graphite electrode inside an anaerobic vessel. Measured conductivity decreased as evaporation of the growth medium exposed the graphite electrode to the headspace. As all available acetate was consumed by the microbes, measured electrical conductivity decreased to background values.

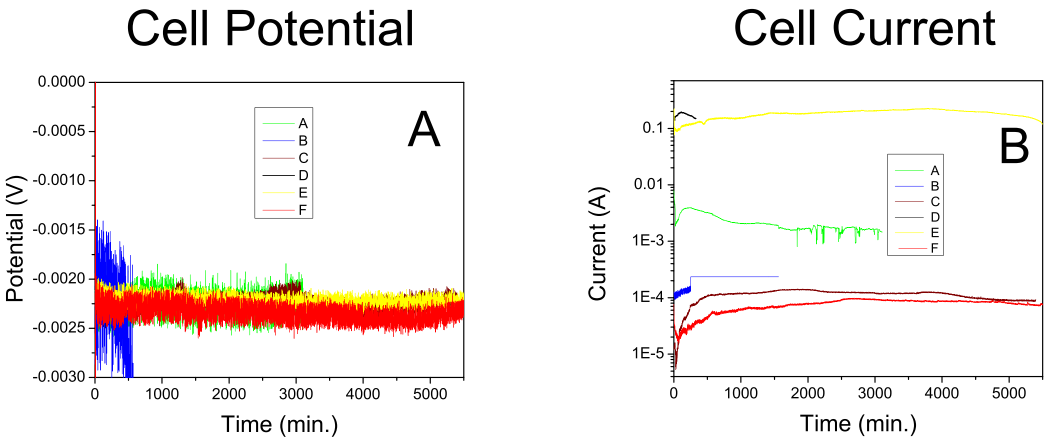

Figure 5.7: Imposed potential (A) and measured electrical current (B) from 6 replicate experiments using micro-electrodes in an anaerobic reactor. Imposed potential remains relatively constant for all the replicates except replicate D (blue line). The current generated by these experiments is highly variable due to corrosion reactions occurring on the gold-plated alligator clips used as connectors.

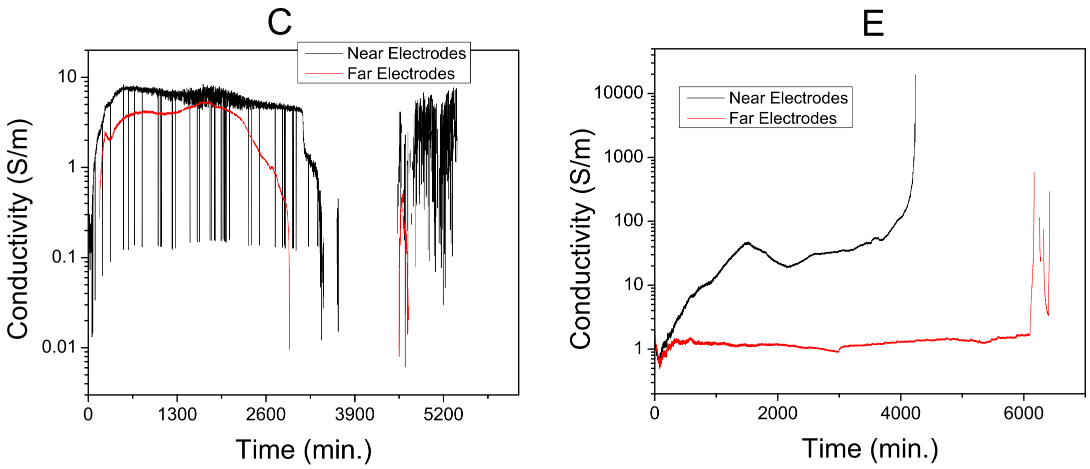

Figure 5.8: Calculated electrical conductivity for replicates C and E. Electrical conductivity was calculated using Eqs. 5.1 and 5.2. Induced current was measured with the potentiostat and voltages at the two pairs of electrodes were measured with the data logger. Because the current measured with the potentiostat is highly variable, the calculated electrical conductivity is highly variable as well.

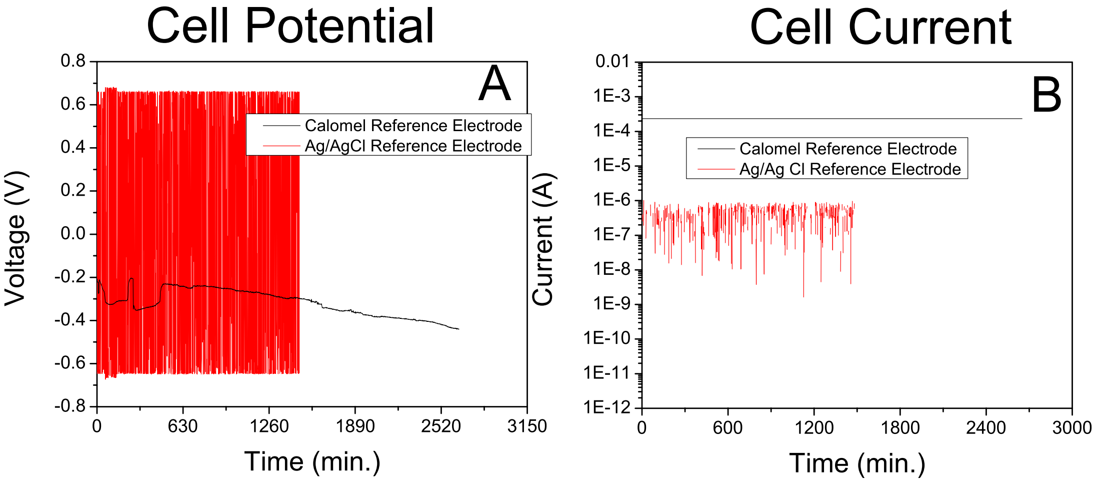

Figure 5.9: Imposed potential (A) and measured electrical current (B) for the micro-fluidics device. Imposed potential was inconsistent using either the Calomel reference electrode (black line) or the Ag/AgCl reference electrode (red line). Measured current was equally inconsistent.

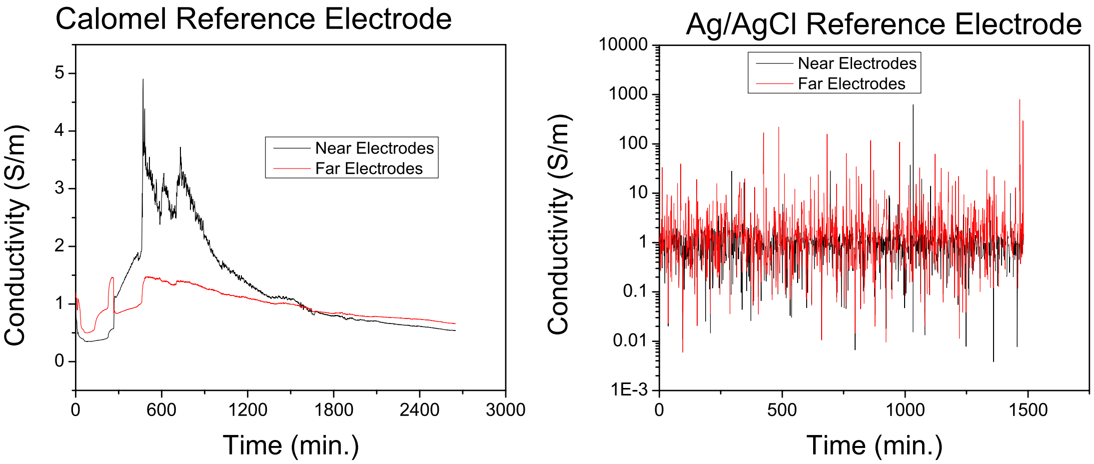

Figure 5.10: Calculated changes electrical conductivity for the microfluidics devices.

Works Cited

Bond, D. R., and D. R. Lovley (2003), Electricity Production by *Geobacter sulfurrducens* attached to electrodes, *Applied and Environmental Microbiology*, *69*(3), 1548-1555.

Christensen, B. E., and W. G. Characklis (1990), Physical and chemical properties of biofilms, in *Biofilms*, edited by W. G. Characklis and K. C. Marshall, John Wiley and Sons Inc., New York.

Christensen, T., P. Kjeldsen, P. Bjerg, D. Jensen, J. Christensen, A. Baun, H. Albrechtsen, and G. Heron (2001), Biogeochemistry of landfill leachate plumes, *Appl. Geochem.*, *16*(7-8), 659-718.

COMSOL (2008), COMSOL Multiphysics Modeling Guide, 1 - 518.

Cornell, R., and U. Schwertmann (2003), *The Iron Oxides: Structure, Properties, Reactions, Occurences and Uses*, 2nd ed., Wiley-VCH GmbH & Co. KGaA.

Liermann, L., A. Barnes, B. Kalinowski, X. Zhou, and S. Brantley (2000), Microenvironments of pH in biofilms grown on dissolving silicate surfaces, *Chem. Geol.*, *171*(1-2), 1-16.

Luther, G., B. Glazer, S. Ma, R. Trouwborst, T. Moore, E. Metzger, C. Kraiya, T. Waite, G. Druschel, and B. Sundby (2008), Use of voltammetric solid-state (micro) electrodes for studying biogeochemical processes: Laboratory measurements to real time measurements with an in situ electrochemical analyzer (ISEA), *Mar. Chem.*, *108*(3-4), 221-235.

Marsili, E., D. Baron, I. Shikhare, D. Coursolle, J. Gralnick, and D. Bond (2008a), *Shewanella* secretes flavins that mediate extracellular electron transfer, *Proceedings of the National Academy of Sciences*, *105*(10), 3968.

Marsili, E., J. B. Rollefson, D. B. Baron, R. M. Hozalksi, and D. R. Bond (2008b), Microbial biofilm voltammetry: Direct electrochemical characterization of catalytic electrode-attached biofilms, *Applied and Environmental Microbiology*, *74*(23), 7329-7337.

Meitl, L. A., C. M. Eggleston, P. J. S. Colberg, N. Khare, C. L. Reardon, and L. Shi (2009), Electrochemical interaction of *Shewanella* onedensis MR-1 and its outer membrane cytochromes OMcA and MtrC with hematite electrodes, *Geochemica et Cosmochimica Acta*, *23*(2009), 5292-5307.

Min, B., and B. E. Logan (2004), Continuous electricity generation from domestic wastewater and organic substrates in a flat plate microbial fuel cell, *Environmental Science & Technology*, *38*(21), 5809-5814.

Nielsen, L. P., N. Risgaard-Petersen, H. Fossing, P. B. Christensen, and M. Sayama (2010), Electric currents couple spatially separated biogeochemical processes in marine sediment, *Nature*, *463*(7284), 1071-1074.

Ntarlagiannis, D., E. Atekwana, E. Hill, and Y. Gorby (2007), Microbial nanowires: Is the subsurface “hardwired”?, *Geophysical Research Letters*, *34*(17), L17305.

Regberg, A., K. Singha, M. Tien, F. Picardal, J. Schieber, E. Roden, and S. L. Brantley (in press), Electrical conductivity as an indicator of iron reduction rates in abiotic and biotic systems, *Water Resour. Res.*

Reguera, G., K. McCarthy, T. Mehta, J. Nicoll, M. Tuominen, and D. Lovley (2005), Extracellular electron transfer via microbial nanowires, *Nature*, *435*(7045), 1098-1101.

Richter, H., K. McCarthy, K. P. Nevin, J. P. Johnson, V. M. Rotello, and D. R. Lovley (2008), Electricity generation by *Geobacter sulfurreducens* attached to gold electrodes, *Langmuir*, *24*(8), 4376-4379.

Richter, H., K. P. Nevin, H. Jia, D. A. Lowy, D. R. Lovley, and L. M. Tender (2009), Cyclic voltammetry of biofilms of wild type and mutant *Geobacter sulferreducens* on fuel cell anodes indicates possible roles of OmcB OmcZ, type IV pili, and protons in extracellular electron transfer, *Energy and Environmental Science*, *2*, 506-516.

Slater, L. D., F. D. Day-Lewis, D. Ntarlagiannis, M. O'Brien, and N. Yee (2009), Geoelectrical measurement and modeling of biogeochemical breakthrough behavior during microbial activity, *Geophysical Research Letters*, *36*.

Torres, C. I., A. K. Marcus, P. Parameswaran, and B. E. Rittmann (2008), Kinetic experiments for evaluating the Nernst-Monod model for anode-respiring bacteria (ARB) in a biofilm anode, *Environ. Sci. Technol.*, *42*, 6593-6597.

Appendix A

RESULTS FROM COLUMN REACTORS CONTAINING PURE CULTURES OF IRON-REDUCING BACTERIA

This appendix summarizes the current results of two ongoing flow-through column reactor experiments. The column reactors have been inoculated with pure cultures of iron-reducing bacteria and are maintained under anaerobic conditions favorable to iron reduction. The first column was inoculated with *Shewanella oneidensis* MR-1 and will be referred to as the *Shewanella* column (SC). The second reactor was inoculated with *Geobacter sulfurreducens* and will be referred to as the *Geobacter* column (GBC). Both reactors are instrumented with Ag/AgCl electrodes used to measure changes in complex conductivity as conditions within the reactors evolve. In addition to monitoring changes in complex conductivity, column effluent is collected and analyzed for changes in concentration of major cations and anions. The goal of these experiments is to determine the effect of dissimilatory iron reduction on complex conductivity. We expect to replicate the results discussed in Chapters 2 and 4 where changes in bulk electrical conductivity became decoupled from changes in fluid chemistry. To date this decoupling has not been observed in either reactor.

Methods

The two columns contained identical sediment and electrodes as the abiotic column reactor discussed in chapter 3. The SC was constructed out of a glass chromatography column from Omnifit Inc. The column was 25 cm long and had an inner diameter of 5 cm. The column was modified, by creating 16 sampling ports along the length of the column. Four sampling ports were placed in four rows at 0, 90, 180 and 280 degrees around the column. The sampling ports were 2.5, 7.5, 12.5, and 17.5 cm from the inlet respectively (Fig. A1). The ports were manufactured at the College of Earth and Mineral Sciences glass shop by epoxying the tops of Wheaton® serum vials to pre-drilled holes in the column. The ports were sealed with butyl-rubber stoppers and aluminum crimp seals.

The GBC was constructed of a PVC pipe 30 cm long with a 6 cm inner diameter. Two rows of sampling ports were constructed on opposite sides of the column by drilling 4 holes at points 7.5, 12.5, 17.5, and 22.5 cm. from the inlet of the column. Two additional ports were drilled at 7.5 cm from the inlet on opposite sides of the column 90^o away from the rows of ports (Fig. A1). These two holes were for the current electrodes. The ports were sealed with butyl rubber stoppers. Both columns were sealed with 50 mm Teflon endcaps from Omnifit. The endcaps have butyl rubber O-rings to ensure a water-tight fight with the column and Teflon filters with a 10 μm pore size to create even flow rates and prevent particle migration out of the reactors.

The columns were filled with 1310 g of 12/20 Accusand®. Accusand® is a commercially available well sorted quartz sand with very spherical particles having an average diameter of 1.1 ± 0.01 mm[*Schroth et al.*, 1996]. The Accusand® was coated with synthetic goethite by continuously stirring a solution of dissolved 0.05 M $FeCl_2$ with 0.1M $NaHCO_3$ with 665 g/L sand for 48 hours allowing the Fe(II) to oxidize and precipitate as goethite [*Schwertmann and Cornell*, 2000]. The effective porosity of both columns, determined by repeatedly packing the columns with sand and measuring the mass of water necessary to fully saturate the sand, is 0.40 ± 0.02.

A 250 ml pure culture of *Shewanella oneidensis* MR-1 was grown in an anaerobic growth medium adapted from *Myers and Nealson* [1988] containing 30mM lactate as an electron donor and 50 mM Na-fumarate as an electron acceptor. A similar 250 ml culture of *Geobacter* *sulfurreducens* was grown on a growth medium containing: 1.5 g/L NH_4Cl, 0.6 g/L NaH_2PO_4, 0.1 g/L KCl, 2.5 g/L $NaHCO_3$, 10 ml/L 100X Wolfe's Vitamin Solution, 10 ml/L Modified Wolfe's Minerals, 30 mM Na-acetate, and 50 mM Na-fumarate. When the cultures reached an optical density of 0.6 when measured with 600 nm light, the cells were pelleted by centrifugation and re-suspended in sterile anaerobic pipes-buffered artificial groundwater (PBAGW). PBAGW contains: NaCl (0.15 g L^{-1}), $CaCl_2$ (0.30 g L^{-1}), $MgCl_2$-$6H_2O$ (0.50 g L^{-1}), KH_2PO_4 (0.006 g L^{-1}), NH_4Cl (0.01 g L^{-1}), PIPES (3.35 g L^{-1}), 1 ml/L 100X Wolfe's Vitamin Solution and 1 ml/L Modified Wolfe's Minerals. Additionally, the PBAGW was amended with either Na-acetate or lactate to a final concentration of 10 mM. Lactate or acetate served as electron donors and carbon sources. The columns were assembled and maintained in Coy Labs anaerobic chamber under a 95% N_2, 5% H_2 atmosphere. The columns were wet-packed with the inoculated PBAGW and sealed with the Teflon endcaps. Omega PX30 pressure transducers were attached to the inlet and outlet tubing of both columns to measure variations in hydraulic head due to mineral dissolution and bacterial growth. Data from these transducers was collected and logged on a Cambpell Scientific CR1000 data logger.

Sterile, anaerobic PBAGW was pumped into each column through Tygon tubing with a Cole-Parmer peristaltic pump at 2-3 ml hr^{-1}. Effluent from each column was collected in a sealed N_2-purged serum vial doped with 0.4 ml of 12 N HCl to preserve the samples for later analysis. Effluent concentrations of Fe(II) ($[Fe(II)_{aq}]_{out}$) were analyzed with ferrozine [*Stookey*, 1970]. Effluent concentrations of acetate and lactate ($[acetate]_{out}$, $[lactate]_{out}$) were measured with a Dionex ion-chromatograph. Effluent NH_4^+ ($[NH_4^+]_{out}$) was measured using *o*-phthaldialdehyde [*Holmes et al.*, 1999]. Prior to acidification, 1 ml aliquots of effluent were collected and pH was measured with a Thermo-Orion five star pH meter.

In each column eight Ag/AgCl electrodes were inserted through the butyl-rubber stoppers until they were just touching the sediment. These electrodes were constructed by fixing a

Ag/AgCl wire inside a glass tube filled with KCl agar. The electrodes were designed to only be conductive at their tips and to be used as potential electrodes for complex conductivity measurements. Coils of Ag/AgCl wire were placed at the top and bottom of each column to act as current electrodes (Fig. A1). Using a coil of wire creates a uniform current density throughout the column while still allowing fluid flow [*Sumner*, 1976; *Vanhala and Soininen*, 1995]. Complex conductivity measurements were collected every other day at the following 24 frequencies: 12, 6, 3, and 1.5 kHz, 750, 375, 187.5, 93.75, 46.875, 23.437, 11.7188, 5.859, 2.927, 1.465, 0.732, 0.366, and 0.183 Hz, and 91.5, 45.8, 22.8, 11.4, 5.7, 2.8, and 1.4 mHz with a Radic Research SIPLab II instrument. Three pairs of potential electrodes were measured on each side of the column. The measurement using the two electrodes closest to the inlet is called the inlet electrode measurement. The measurement using the middle two electrodes is called the middle electrode measurement. Finally, the measurement using the electrodes closest to the outlet was designated the outlet electrode measurement (Fig. A1). All measurements involved electrode pairs from the same side of the column. No measurements were collected that used electrodes from opposite sides of the column at the same time (Fig. A1). Effluent fluid electrical (σ_f) conductivity was measured with an inline conductivity electrode from Micro-electrodes Inc.

Results

In the SC influent, [acetate] was 10 mM from day one to day 166. On day 166 the influent medium was modified to contain 10 mM lactate instead of acetate. The medium was changed to encourage increased bacterial growth because acetate is a poor electron donor for *S. oneidensis*. *Shewanella* species have been shown to grow faster when lactate is used as an electron donor [e.g., *Liu et al.*, 2001]. We were not able to distinguish acetate from lactate on the ion chromatograph. Therefore all effluent concentrations are reported as $[\text{acetate + lactate}]_{out}$.

[acetate + lactate]$_{out}$ was between 9.6 and 9.3 mM from day 0 until day 107. Between day 107 and day 165 [acetate + lactate]$_{out}$ decreased to 7.7 mM. On day 166 when the influent medium was modified to contain 10 mM lactate and 0 mM acetate, [acetate + lactate]$_{out}$ began to increase. On day 175 [acetate + lactate]$_{out}$ reached a maximum concentration of 13.6 mM. This concentration probably reflects a mixture of acetate and lactate. By day 194 [acetate + lactate]$_{out}$ had decreased to 6.0 mM. From day 194 on, [acetate + lactate]$_{out}$ increased to a value of 9.1mM on day 275 (Fig A2).

Influent Fe(II)$_{aq}$ in the SC was below detection (< 5 μM). [Fe(II)$_{aq}$]$_{out}$ was between 0.03 and 0.15 mM from day 1 until the medium was changed on day 166. On day 166 [Fe(II)$_{aq}$]$_{out}$ began to increase and reached a maximum of 1.22 mM on day 102. After day 102, [Fe(II)$_{aq}$]$_{out}$ decreased to a steady state value of ~0.4 mM from day 219 until day 303 (Fig. A2). Influent [NH_4^+] was 0.190 mM. [NH_4^+]$_{out}$ was initially 0.270 mM due to NH_4^+ associated with the medium the cells were grown in (the inoculum). [NH_4^+] in the growth medium was 18 mM. From day 1 [NH_4^+]$_{out}$ decreased to minimum value of 0.046 mM on day 46. After day 46 [NH_4^+]$_{out}$ increased to 0.190 mM on day 65. [NH_4^+]$_{out}$ remained between 0.190 mM and 0.150 mM from day 65 until day 124. From day 124 to day 133 [NH_4^+]$_{out}$ decreased to 0.024 mM. [NH_4^+]$_{out}$ remained around 0.024 mM until the medium was modified on day 166. As [Fe(II)$_{aq}$]$_{out}$ increased [NH_4^+]$_{out}$ also temporarily increased to 0.167 mM on day 175. By day 186 [NH_4^+]$_{out}$ had decreased to steady state values of ~0.034 mM (Fig. A2). The transient peak in [NH_4^+]$_{out}$ associated with the increase in [Fe(II)$_{aq}$]$_{out}$ may be due to Fe(II), NH_4^+ cation exchange.

The phase lag measurements in the SC showed a consistent maximum in phase lag at 0.005 Hz. Thus, all real and imaginary components are reported for this frequency. The real component of the complex conductivity (σ') for the SC was initially 0.13 S/m. This value steadily decreased to 0.09 S/m for the electrodes closest to the inlet to 0.07 S/m for the middle and outlet electrodes day 118. Between day 166 and 181 σ' increased from 0.08 to 0.1 S/m at the inlet electrodes and from 0.06 to 0.08 at the outlet and middle electrodes (Fig. A3). This increase in σ' corresponds to the increase in $[Fe(II)_{aq}]_{out}$ when lactate was added to the PBAGW in place of acetate (Fig. A2). σ' remained between 0.09 and 0.08 S/m (inlet electrodes) and 0.07 and 0.06 S/m (outlet and middle electrodes) for the rest of the experiment. Effluent fluid electrical conductivity, σ_f, followed a similar pattern as σ' decreasing from initial values of 0.559 S/m to steady values around 0.173 S/m by day 248 (Fig. A3).

The imaginary component of the complex conductivity (σ") was below detection ($< 1 \times 10^{-7}$) S/m for the outlet electrodes. σ" for the inlet electrodes varied between 0 and 2.3×10^{-4} S/m over the course of the experiment. σ" for the middle electrodes was $\sim 2 \times 10^{-6}$ S/m from day 1 until day 166. On day 166 σ" for the middle electrodes began to increase and reached a maximum value of 1.7×10^{-5} S/m on day 178. After day 178 σ" for the middle electrodes decreased to back to 2×10^{-6} S/m by day 222 (Fig. A3).

In the GBC influent, [acetate] was 10 mM. $[\text{acetate}]_{out}$ was initially 7.3 mM. By Day 10 $[\text{acetate}]_{out}$ had increase to 10 mM. $[\text{acetate}]_{out}$ then decreased to steady state values between 9.8 and 9.5 mM (Fig. A4). Influent $[Fe(II)_{aq}]$ was below detection (< 5 μM). $[Fe(II)_{aq}]_{out}$ was initially 1.5 mM. From day 1 until day 27 $[Fe(II)_{aq}]_{out}$ decreased from 1.7 mM to 0.4 mM. From day 27 until day 109 $[Fe(II)_{aq}]_{out}$ decreased from 0.4 mM to 0.09 mM. Influent $[NH_4^+]$ was 0.190 mM. $[NH_4^+]_{out}$ was below detection (< 1 μM) from day 1 until day 4. From day 4 to day 13 $[NH_4^+]_{out}$ increased from < 1 μM to 0.423 mM. From day 13 to day 24 $[NH_4^+]_{out}$ decreased from 0.423 mM to 0.222 mM. From day 24 to day 109 $[NH_4^+]_{out}$ slowly decreased to 0.104 mM (Fig. A4).

σ' for the GBC column was initially 0.21 S/m for the middle electrodes and 0.17 S/m for the inlet and outlet electrodes. From day 1 to day 110 σ' decreased from starting values to 0.05

S/m for the middle and outlet electrodes. σ' decreased to 0.09 S/m for the inlet electrodes. From day 215 on σ' was ~ 0.05 for all electrodes (Fig. A5). σ_f followed a similar pattern. On day 1 σ_f was 0.503 S/m. From day 1 to day 50 σ_f decreased from 0.503 S/m to 0.214 S/m. From day 50 onward σ_f was at steady state ~ 0.2 S/m. σ" for the GBC showed no consistent trend for any of the electrodes varying between 0 and 1 x 10^{-5} S/m (Fig. A5).

The flow rate as determined by measuring the mass of effluent collected for both the SC and the GBC have been increasing from 2 ml day^{-1} to 3 ml day^{-1} as the experiments progress (Fig. A6). This may be indicative of decreases in porosity due to biomass growth or mineral precipitation within the column.

Discussion/ Conclusions

The results of the two column experiments so far suggest that the bacteria are alive and actively reducing Fe(III) oxides in both columns. The incomplete consumption of acetate and NH_4^+ suggest that these are not limiting nutrients in the experiment. Rates of iron reduction may be controlled by the amount of available P in the PBAGW. Complex conductivity has not yet become decoupled from changes in aqueous chemistry although σ" did show a response to changing the carbon source from acetate to lactate in the SC. This transient increase in σ" in the SC may be due to an increase in the biomass in that reactor as the lactate was consumed. This is consistent with previous work reporting increases in σ" associated with microbial attachment to mineral surfaces [e.g., *Abdel-Aal et al.*, 2010].

The major difference between the experiments described in this appendix and the experiments discussed in chapters 2, 3 and 4 is the use of a pure strain of bacteria. Each column reactor in this appendix was inoculated with only one bacterial species. In chapters 2, 3 and 4 an environmental culture was used to inoculate the column. This environmental culture likely contained multiple bacterial species. It seems likely that the absence of these additional bacterial species caused the column reactors in this appendix to react differently than the reactors in chapters 2, 3 and 4. Perhaps, multiple bacterial species are needed to create biofilms with large electrical conductivities.

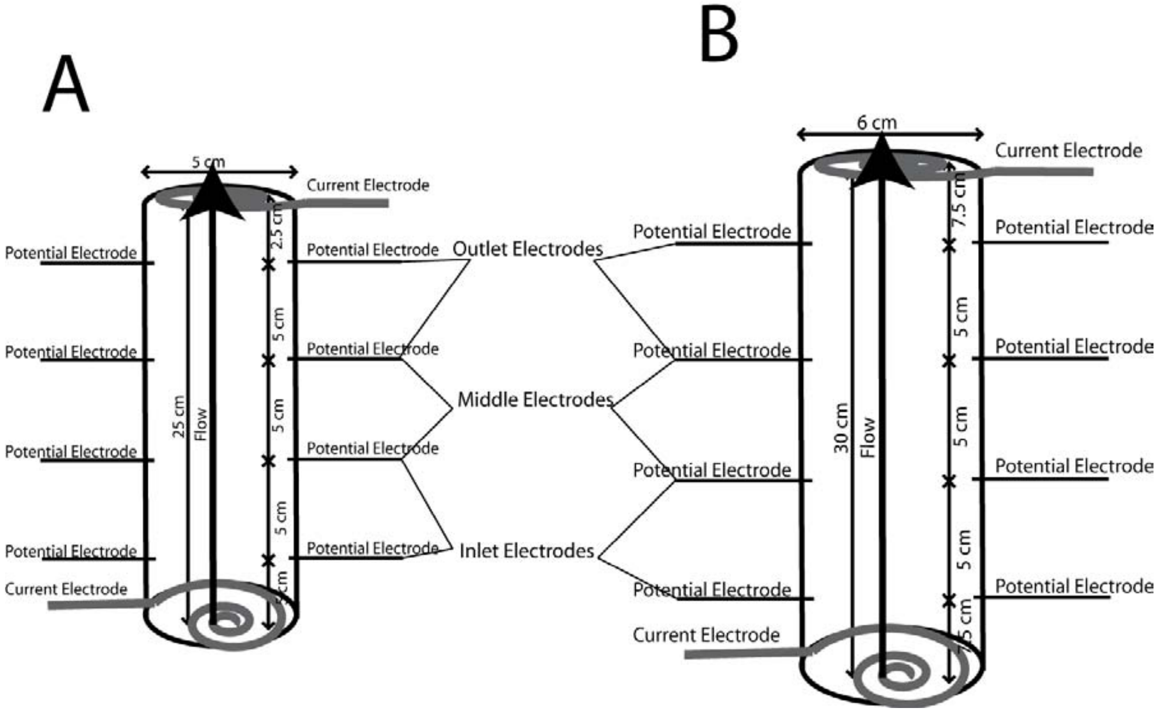

Figure A1: A diagram of the column reactors used for the reactor inoculated with *Shewanella oneidensis* MR-1 (A) and the reactor inoculated with *Geobacter sulfurreducens*. The spiral electrodes at the end of each column were always used as current electrodes. The potential electrodes were inserted until they were just touching the sediment.

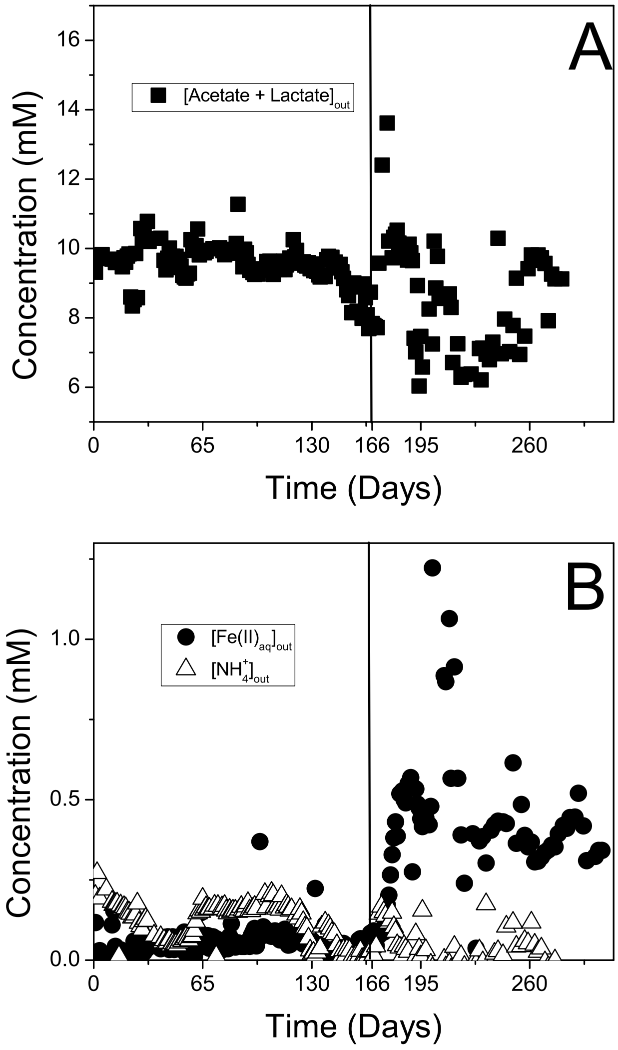

Figure A2: Effluent chemistry from the SC. [acetate + lactate]$_{out}$ (squares, A) decreased after day 166 when the influent medium was modified to contain 10 mM lactate instead of 10 mM acetate. Concurrent with this change in the medium [Fe(II)$_{aq}$]$_{out}$ (circles B) began to increase. [NH$_4$]$_{out}$ (open triangles, B) also increased concurrently.

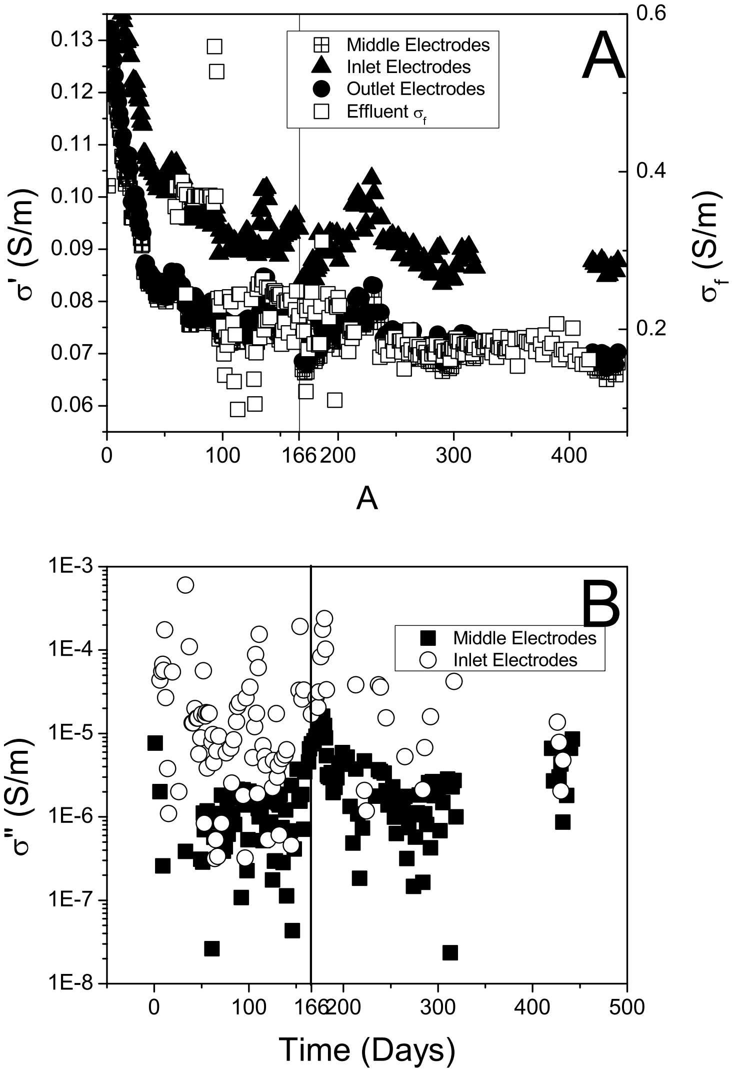

Figure A3: σ' (closed symbols, A) from all of the electrode pairs is coupled to changes in σ_f (open squares, A). σ" from the middle electrodes (squares, B) increases after day 166 concurrent with the change in inlet medium. σ" measurements from the other electrode pairs are highly variable due to their proximity to the current electrodes. The break in the data between day 120 and day 220 is due to the theft of the control computer

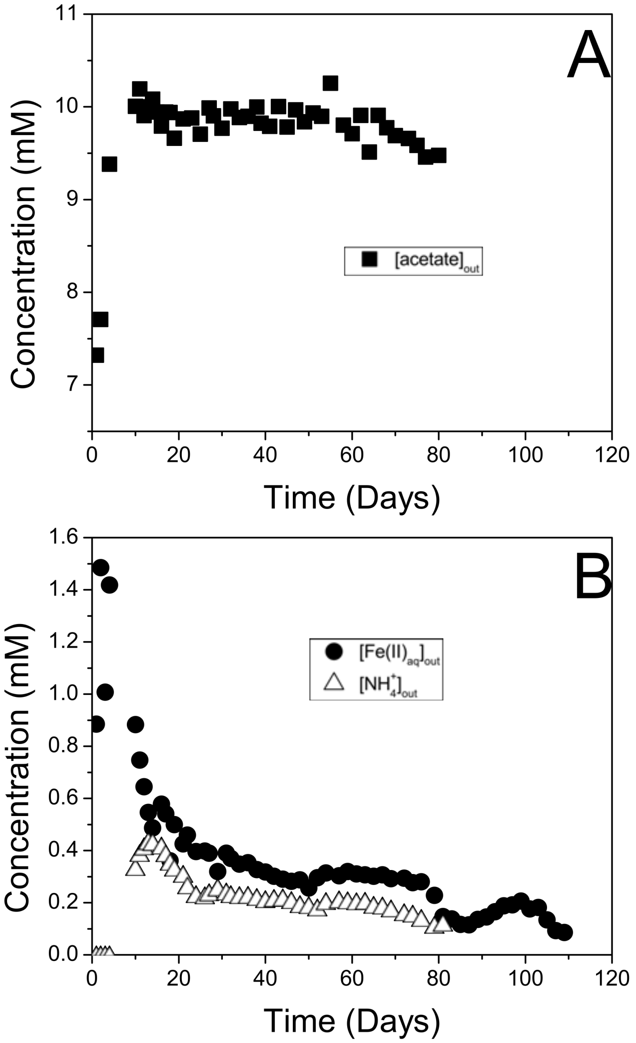

Figure A4: Plots of effluent chemistry from the GBC. [acetate]$_{out}$ (squares, A) increases over time. This corresponds to a decrease in [Fe(II)$_{aq}$]$_{out}$ (circles, B) and [NH$_4^+$]$_{out}$ (open triangles, B). This may be due to a decrease in bacterial activity.

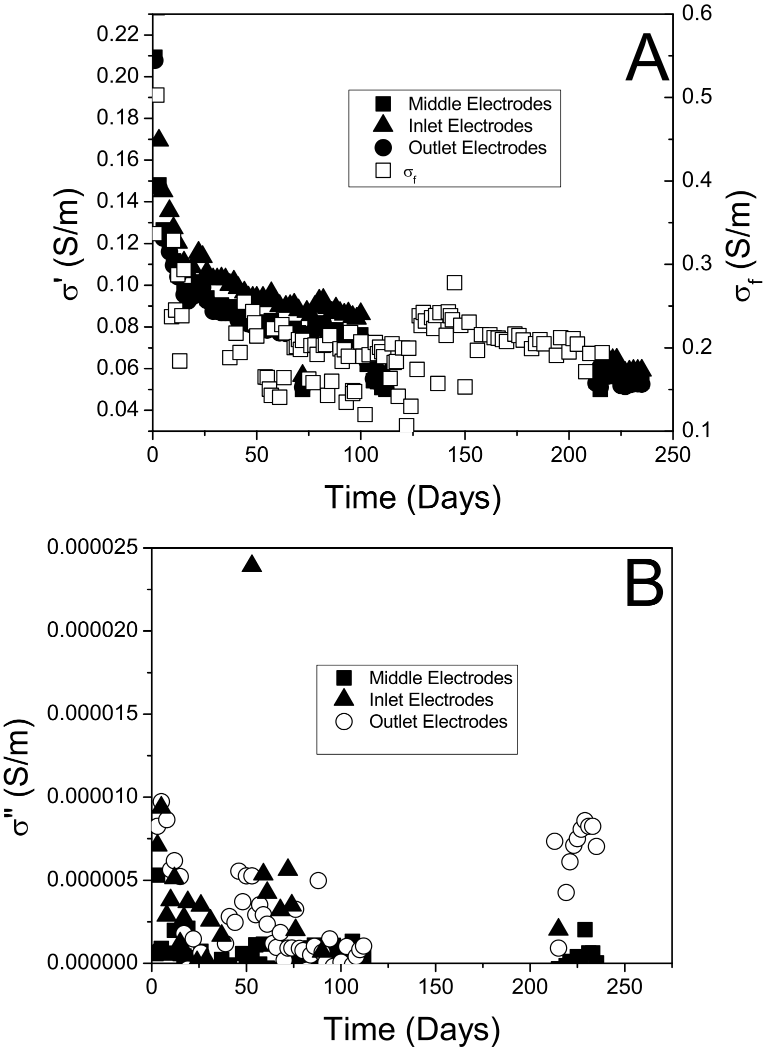

Figure A5: σ' for all electrode pairs (closed symbols, A) is coupled to changes in σ_f (open squares, A) for the GBC. σ" for all electrode pairs (B) shows no consistent trend with time. The break in the data between day 120 and day 220 is due to the theft of the control computer.

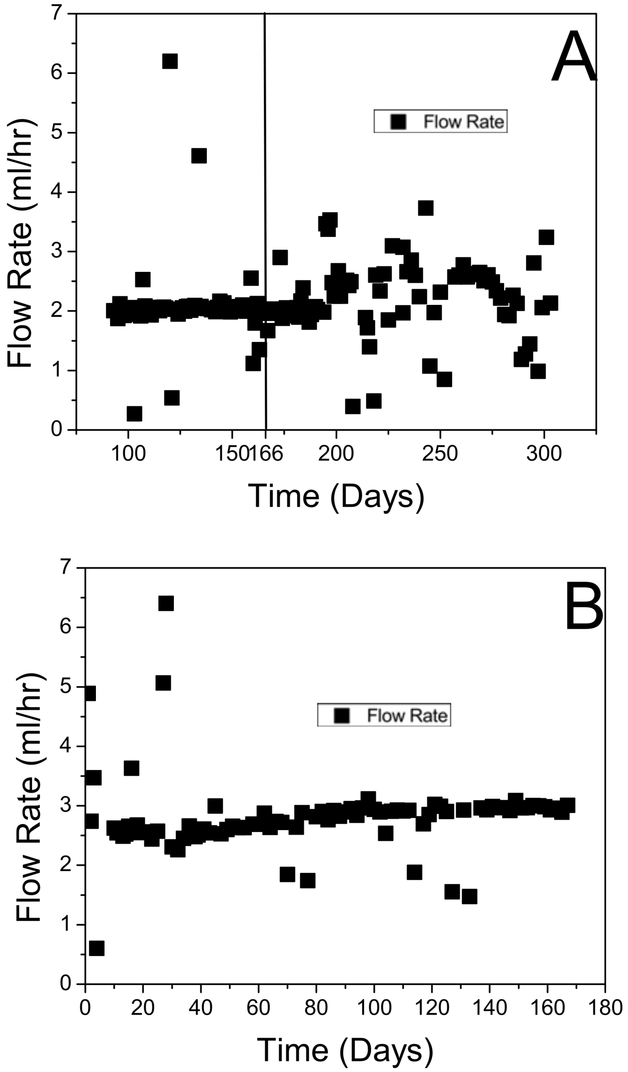

Figure A6: Flow rate as calculated by measuring the mass of effluent released each day increases for the SC (A) and the GBC (B) with time. This may be due to a porosity reduction caused by the precipitation of minerals or the growth of biomass.

Works Cited

Abdel-Aal, G. Z., E. A. Atekwana, S. Rossbach, and D. D. Werkema (2010), Sensitivity of geoelectrical measurements to the presence of bacteria in porous media, *Journal of Geophysical Research-Biogeosciences*, *115*(G03017), 1-11.

Holmes, R., A. Aminot, R. Kérouel, B. Hooker, and B. Peterson (1999), A simple and precise method for measuring ammonium in marine and freshwater ecosystems, *Canadian Journal of Fisheries and Aquatic Sciences*, *56*(10), 1801-1808.

Liu, C., S. Kota, J. Zachara, J. Fredrickson, and C. Brinkman (2001), Kinetic analysis of the bacterial reduction of goethite, *Environ. Sci. Technol*, *35*(12), 2482-2490.

Myers, C. R., and K. H. Nealson (1988), Microbial reduction of manganese oxides: Interactions with iron and sulfur, *Geochimica Et Chosmochimica Acta*, *52*(11), 2727-2732.

Schroth, M. H., S. J. Ahearn, J. S. Selker, and J. D. Istok (1996), Characterization of Miller-Similar Silica Sands for Laboratory Hydrologic Studies, *Soil Science Society of America*, *60*, 1331-1339.

Schwertmann, U., and R. M. Cornell (2000), *Iron Oxides in the Laboratory: Preparation and Characterization*, 2nd ed., 188 pp., Wiley-VCH Verlag GmbH.

Stookey, L. L. (1970), Ferrozine- a new spectrophotometric reagent for iron, *Anal. Chem.*, *42*(7), 779-781.

Sumner, J. (1976), *Principles of Induced Polarization for Geophysical Exploration*, 1 ed., 277 pp., Elsevier Scientific Publishing Company, Amsterdam.

Vanhala, H., and H. Soininen (1995), Laboratory technique for measurement of spectral induced polarization response of soil samples, *Geophysical Prospecting*, *43*(5), 655-676.

Appendix B

IMAGINARY CONDUCTIVITY MEASUREMENTS MADE ON THE ABIOTIC COLUMN REACTOR

Measurements of imaginary conductivity (σ”) were made on the electrodes in the abiotic-column reactor described in chapter 3 to investigate the effect of Fe(II) adsorption on imaginary conductivity. σ” is a component of the complex conductivity. Complex conductivity is measured by inducing an alternating current across a sample. The induced current is allowed to oscillate between two fixed values (e.g. 1 mA and -1 mA) at a predetermined frequency and measurements are repeated by varying this frequency across a wide range (mHz – kHz). Complex conductivity measurements can require minutes or even hours to collect depending on the range and number of frequencies sampled. Complex conductivity provides extra information that D.C. methods cannot such as the phase lag between induced current and measured voltage and the imaginary component of the complex conductivity. [e.g., *Binley and Kemna*, 2007].

A complex conductivity measurement requires measuring not only the voltage but also the lag between the induced current oscillations and the measured voltage oscillations. This lag, measured in degrees, is referred to as the phase lag (φ). The magnitude of this phase lag at low frequencies (< 1 Hz) is a measure of how polarizable a material is [e.g., *Slater and Lesmes*, 2002]. More polarizable materials behave somewhat like capacitors. They become slightly charged when current is imposed across them and release that charge when the current is reversed. The charge release causes the voltage curve to be out of phase with current curve creating a phase lag. More polarizable materials typically exhibit larger phase lags. Changes in the magnitude of the phase lag can correspond to changes in surface conductivity due to mineral precipitation [e.g., *Wu et al.*, 2005]. Measurement of the phase lag can be combined with the conductivity measurement (see Eq. 3.1) at each frequency to obtain a real and imaginary component of the complex conductivity. The real component of complex conductivity, σ' (S/m), is defined to be:

$$\sigma' = \left|\sigma\right| \cos(\varphi). \tag{B.1}$$

Here, σ is the complex conductivity obtained from the measured conductance as described in Eq. B.1 and φ is the phase lag in degrees. The imaginary component σ'' (S/m) is defined as:

$$\sigma'' = \left|\sigma\right| \sin(\varphi). \tag{B.2}$$

σ' is equivalent to D.C. conductivity and responds to changes in σ_f, the conductivity of mineral grains and surface conductivities according to Archie’s law (Eq. B.2) [e.g., *Slater and Lesmes*, 2002]. In contrast, σ'' is a measure of how polarizable a material is. Changes in this value have usually been attributed to effects at the mineral-water interface such as changes in the thickness of the electrical double layer, or to changes in grain size or attachment of bacteria at mineral surfaces [e.g. *Lesmes and Frye*, 2001; *Abdel-Aal et al.*, 2004]. We expected Fe(II) adsorption in abiotic reactor to affect σ'', but it did not

σ'' was measured using a Lab SIP instrument from Radic Research. The details of this measurement are described in Chapter 3. We expected σ'' to increase as Fe(II) adsorbed to the sediment surfaces, but this did not occur. The measured phase lag showed no consistent peaks at any particular frequency and thus imaginary conductivity (σ'') showed no trend throughout the course of the experiment varying between 0 and 2.8×10^{-6} S/m.

From these results we conclude that Fe(II) adsorption onto Fe(III) coated sediments does not affect σ". This supports our hypothesis that measured increases in bulk electrical conductivity in the Fe-reducing column reactor were caused by some processes like biofilm growth that was unrelated to Fe(II) adsorption.

Works Cited

Abdel-Aal, G. Z., E. A. Atekwana, L. D. Slater, and E. A. Atekwana (2004), Effects of microbial processes on electrolytic and interfacial electrical properties of unconsolidated sediments, *Geophysical Research Letters*, *31*(12).

Binley, A., and A. Kemna (2007), DC Resistivity and Induced Polarization Methods, in *Hydrogeophysics*, edited by Y. Rubin and S. Hubbard, pp. 129-156, Springer, AA Dordrecht, The Netherlands.

Lesmes, D. P., and K. M. Frye (2001), Influence of pore fluid chemistry on the complex conductivity and induced polarization responses of Berea Sandstone, *Journal of Geophysical Research*, *106*(B3), 4079-4090.

Slater, L., and D. Lesmes (2002), Electrical-hydraulic relationships observed for unconsolidated sediments, *Water Resour. Res.*, *38*(10), 1213.

Wu, Y., L. Slater, and N. Korte (2005), Effect of precipitation on low frequency electrical properties of zerovalent iron columns, *Environ. Sci. Technol*, *39*(23), 9197-9204.

Appendix C

INSTRUCTIONS FOR BUILDING NON-POLARIZABLE LABORATORY-SCALE ELECTRODES

1. Cut 5 mm O.D. glass tubing into 10 cm lengths

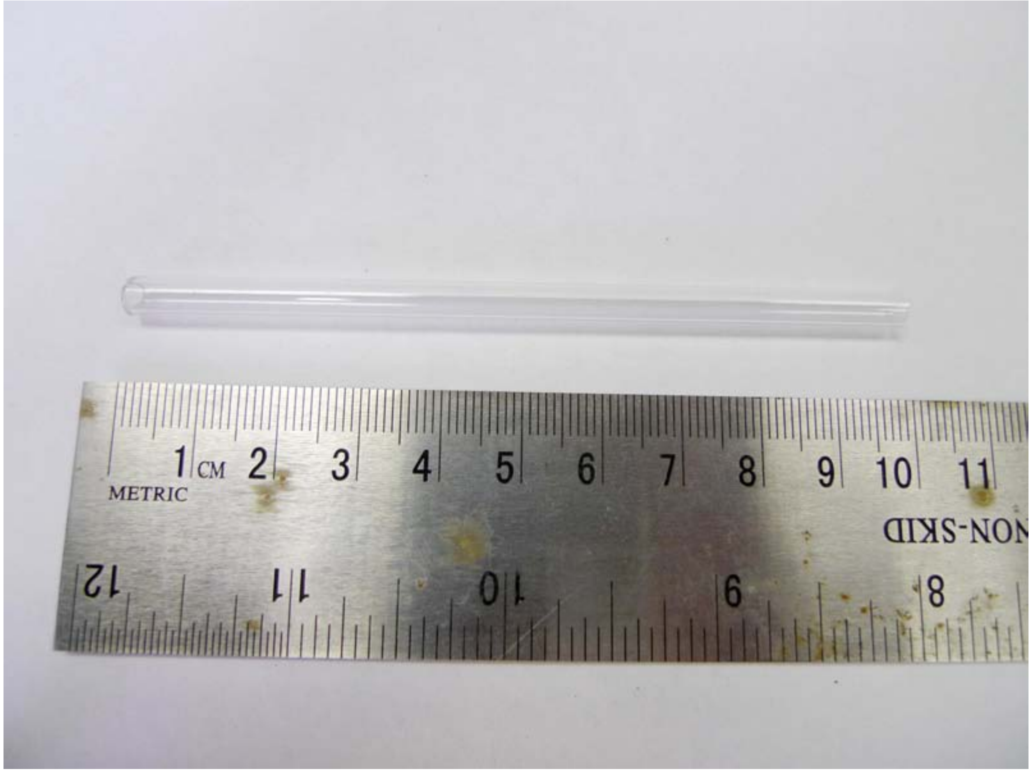

2. Fire polish one end of the tubing with a Bunsen burner. Use the Bunsen burner to narrow the opening on the other end of the tubing to approximately 1 mm.

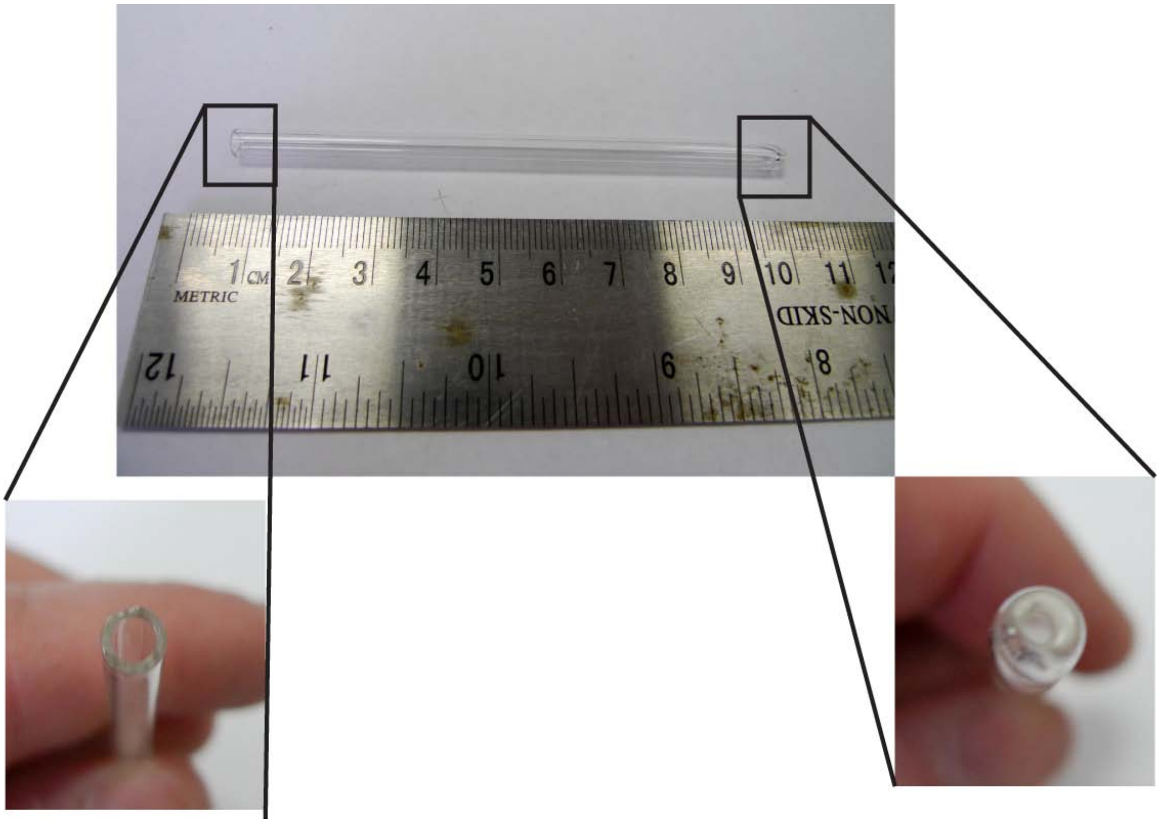

3. Cut 0.8 mm diameter Ag wire into 14 cm lengths

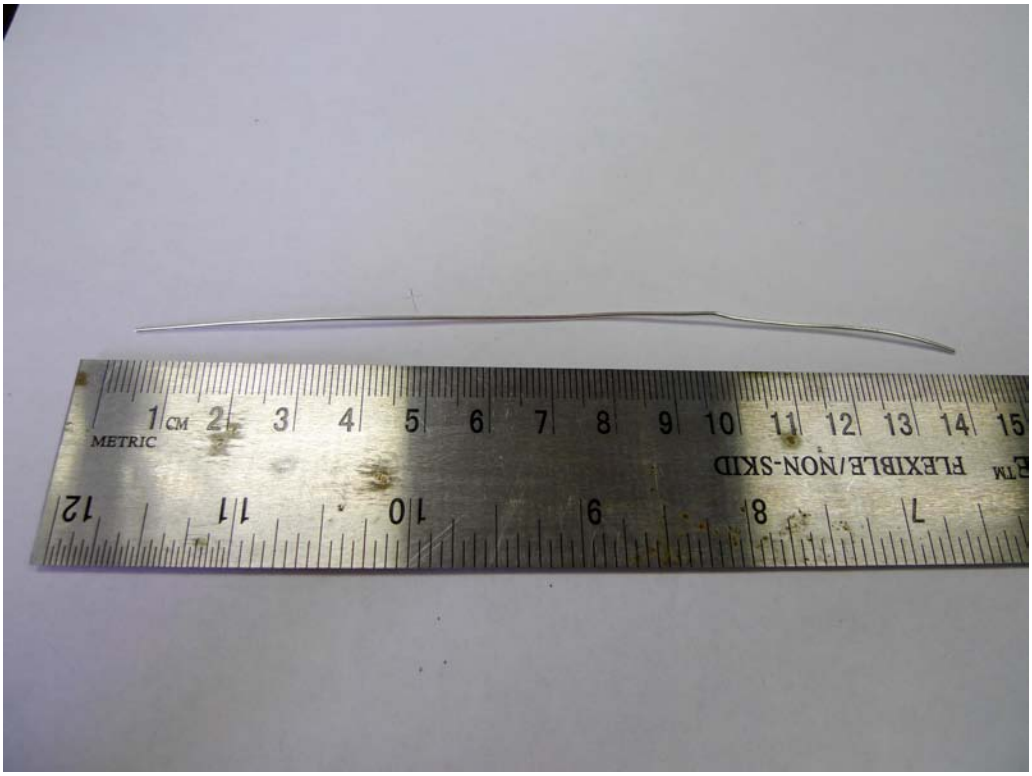

4. Twist the end of the silver wire back onto itself so that when the wire is inserted into the narrow end of the glass tube the end of the wire is at least 1 cm from the end of the glass tube.

5. Cut off the bottom third of a 3 ml syringe.
6. Fill the syringe with silicon epoxy.
7. Place the epoxy filled syringe over the wire and the small end of the glass tubing.

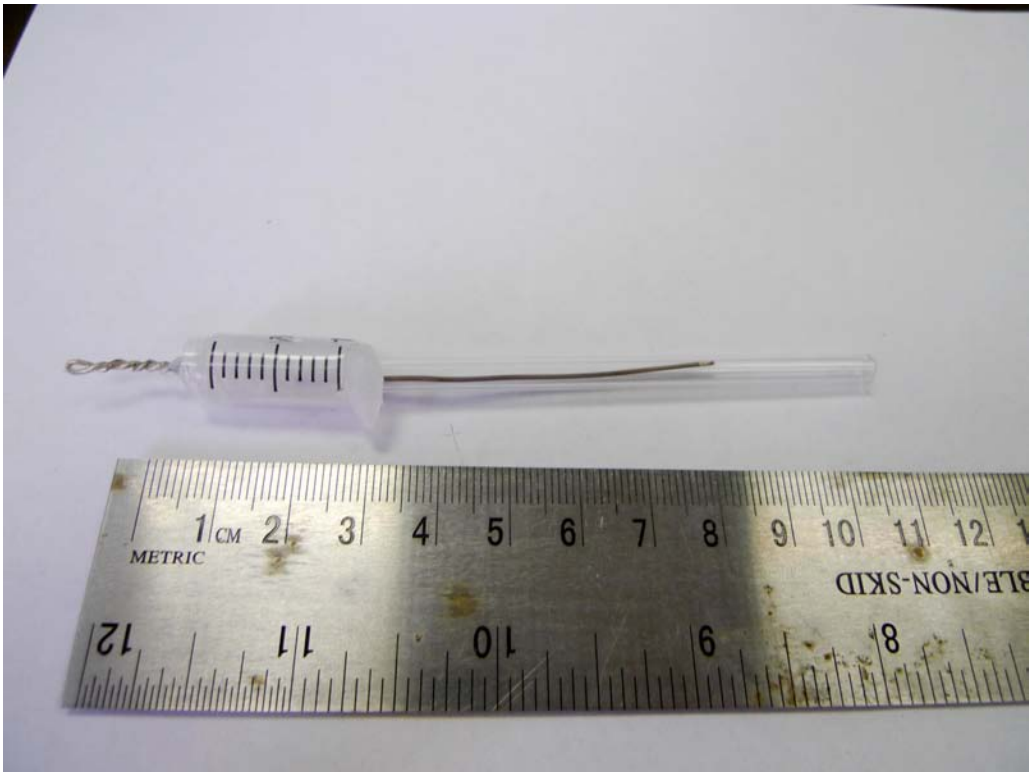

8. Allow epoxy to dry overnight.
9. Fill each glass tube with bleach and allow to react overnight.
10. If the amount of bleach in the tube is significantly less after 1 night the electrode is leaky and will need to be resealed with epoxy.
11. The Ag wire in the non-leaky electrodes will turn from a bright shiny metallic color to a dull purple / grey color.

12. Remove the bleach from the glass tubes and rinse each tube six times with distilled water.
13. Make a 3 M KCl solution.
14. Add 15 g/L Agar to the KC; solution
15. Heat the KCl and Agar solution until the agar dissolved (~ 10- 15 minutes).
16. Keep the KCl and Agar solution hot and use a 5 ml syringe with a long large gauge needle to fill the glass tube with Agar.
17. Try to avoid air bubbles in the glass tube by placing the large needle all the way at the bottom of the tube and filling it from the bottom up.

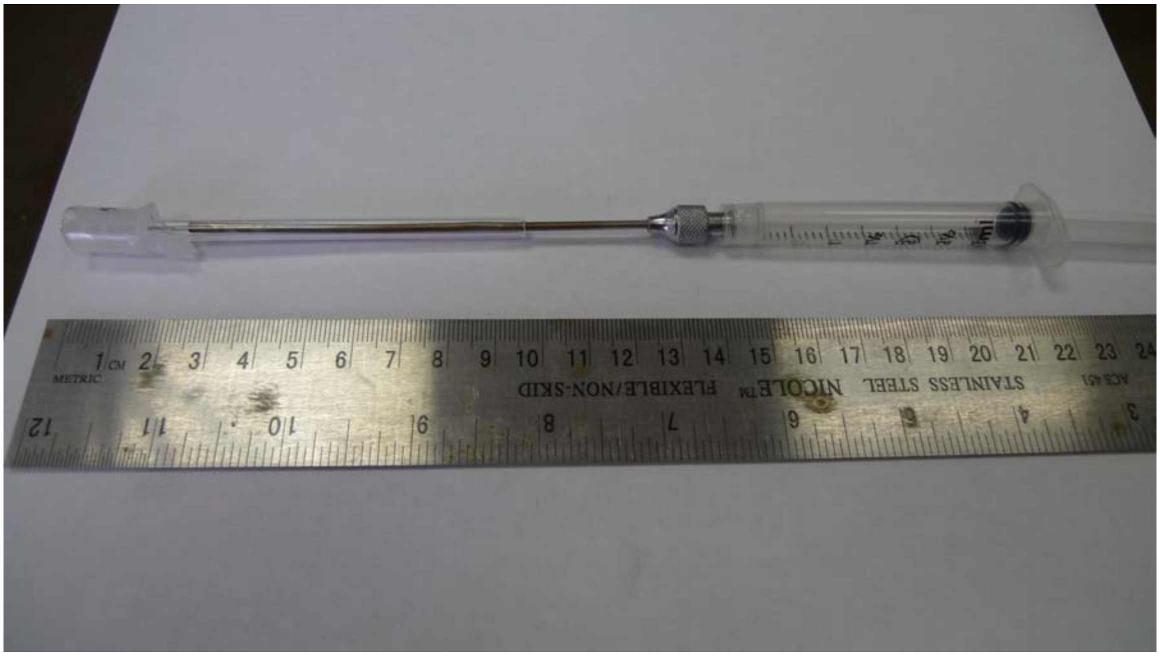

18. Seal the electrodes with a small piece of Vycor and heat shrink tubing.

    Try to avoid air bubble between the Vycor and the end of the glass.

19. Store electrodes in a 3 M KCl solution until ready to use.

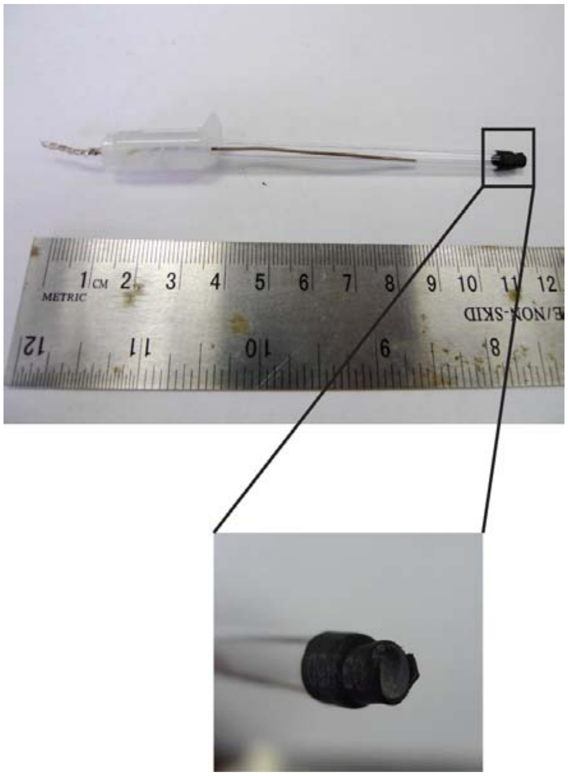

Vita

Aaron B. Regberg
315 Hosler Bldg. University Park, PA 16802
Phone: +1 814 863 8055 E-mail: aregberg@psu.edu

Education

8/05 to Present	**Pennsylvania State University (University Park)** PhD. Geosciences 2011 Interdisciplinary Program "Center For Environmental Kinetics Research" (CEKA)
8/01 to 4/05	**University of Michigan Ann Arbor** BS Geology Academic Minor History of Art Cumulative GPA 3.52/4.0 University Honors - Fall 2001, Winter 2002, Fall 2003, Winter 2004, Fall 2004
8/95 to 5/01	**Walnut Hills High School Cincinnati, Ohio** Graduated Cum Laude

Awards and Achievements

2008	Student Travel Grant for AGU Chapman Conference on Biogeophysics.
2008, 2010	Goldschmidt Student Travel Grant
2007	Parizek Graduate Fellowship
2007	Outstanding Student Paper Award - AGU
2006	ExxonMobil Quantitative Geosciences Fellow
2005	Anne C. Wilson Graduate Research Award
2004	Judith Turneaure Memorial Scholarship
2003	Geological Society of America Research Grant

Leadership Activities

2007	**Historically Black Colleges and Universities – Undergraduate Program National Research Conference** Judged undergraduate research in environmental chemistry
2005-2006, 2008	**Center For Environmental Chemistry and Geochemistry – Secretary** Helped organize annual student research symposium
2002 to 2005	**Michigan Pops Orchestra – Board Member** Treasurer 2003 to Present Managed a $40,000 annual budget Suggested and initiated orchestra growth
2004 to 2005	**Robert Owen Cooperative – President** Facilitated house meetings Oversaw general house operations